



Università
Ca' Foscari
Venezia

Dottorato di ricerca in Scienze Chimiche
Scuola di dottorato in Scienze e Tecnologie
Ciclo XXIV
(A.A. 2010 - 2011)

***Synthesis and characterization of
luminescent and magnetic materials for
biological applications***

SETTORE SCIENTIFICO DISCIPLINARE DI AFFERENZA: CHIM/02

Tesi di dottorato di ALVISE PARMA, matricola 955601

Coordinatore del Dottorato

Prof. Paolo Ugo

Tutore del dottorando

Prof. Pietro Riello

*To my mum Barbara
and my dad Ivano*

ABSTRACT

The following work focuses on the synthesis and characterization of luminescent and/or magnetic nanocomposite systems, that could be destined to a wide range of applications, for example in the biomedical field (e.g. bioimaging, DNA microarray, hyperthermal therapy, contrast-enhanced magnetic resonance imaging (MRI), combined optical and magnetic resonance bioimaging).

Red-emitting luminescent nanophosphors made of Eu^{3+} -doped zirconia nanocrystals were synthesized with the polyol method and embedded into a silica matrix by a Stöber route. A comparative study on different samples allowed to determine the optimum annealing temperature (700 °C) to maximize not only the optical properties, but also the nanostructural quality and the availability of superficial $-\text{OH}$ groups for efficient surface functionalization of the $\text{ZrO}_2:\text{Eu}^{3+}@\text{SiO}_2$ composites.

The use of mesoporous silica nanoparticles (ms- SiO_2 NPs) as a host structure became predominant in the following studies, since this material implied the possibility to load, via easy impregnation routes, a great variety and amount of materials (even more than one in the same host matrix) into the nanosized pores and to obtain efficient control of the final composition and easy surface functionalization of the systems. The ms- SiO_2 NPs were obtained through a micellar synthesis which implied the use of a cationic surfactant as pore template. Their impregnation with different rare-earth doped zirconia nanocrystals gave luminescent nanocomposites $\text{ZrO}_2:\text{RE}^{3+}@\text{ms-SiO}_2$ (RE = Eu, Tb, Er/Yb), which showed satisfying luminescent properties, morphological and structural regularity (the systems doped with Eu^{3+} and Tb^{3+}) and the possibility to obtain functionalizable nanocomposites with up-converting properties (the system co-doped with Er^{3+} and Yb^{3+}).

The ms- SiO_2 NPs were also impregnated with an optimized amount of $\text{Eu}(\text{DBM})_3\text{Phen}$ complex. Thanks to the peculiar properties of the organic complex, the resulting luminescent nanocomposite material showed a more intense red emission and a stronger absorption efficiency with respect to the previously studied luminescent materials, while retaining a high level of

mesoporosity. Therefore it resulted to be the most suitable material for a further production of a bifunctional luminescent and magnetic composite.

Lanthanide-doped luminescent materials were also studied during a PhD abroad stage at Turku University (Finland), in which the whole activity concerned the synthesis and characterization of $\text{Sr}_2\text{MgSi}_2\text{O}_7:\text{Eu}^{2+},\text{Dy}^{3+}$ persistent luminescence materials. These materials consisted of micro-sized powders that were synthesized with the simple solid state reaction. A comparative study allowed to determine an optimal composition of $(\text{Sr}_{0.97}\text{Eu}_{0.01}\text{Dy}_{0.02})_2\text{MgSi}_2\text{O}_7$, both for the strength and the duration (more than 25 h) of the persistent luminescence.

Parallel with the research activity on lanthanide-doped luminescent materials, magnetic nanocomposites were also investigated. The synthesis and characterization of magnetic composites made of iron oxide and cobalt-iron oxide embedded, via impregnation, into the ms-SiO₂ NPs were performed. A comparative study on a FeO_x@ms-SiO₂ series of samples with different loading levels allowed to determine the most recommended nominal fraction of loaded iron oxide (17%wt), in order to obtain the best structural and morphological homogeneity. The magnetic properties of the composite indicated superparamagnetic behavior, quite high magnetic anisotropy, large coercive fields and moderate density of magnetization and magnetic response to a magnetic field. The magnetic properties of the CoFe₂O₄@ms-SiO₂ composite were found to be superior to those of the FeO_x@ms-SiO₂ material. The higher density of magnetization in the former was attributed to a higher content of magnetic material in the crystalline phase and could justify the greater efficiency observed in the magnetic separation of this material.

A further investigation on the incorporation of metallic iron into a mesoporous silica matrix was made, in order to realize a nanostructured composite material with elevated magnetic properties. This goal has not been accomplished yet, due to the difficulties in avoiding iron oxidation during, or following, the preparation of the composite. Anyway, as a partial result, a promising material with a remarkable magnetic response was obtained, following an improvement in the synthetic procedure and in the employed

materials. However, the structural and morphological analysis indicated a nanostructural disorder and heterogeneity in the material. The presence of different crystalline phases (among which Fe_5C_2 iron carbide, which is known to have interesting magnetic properties) was demonstrated.

By selecting, among the investigated ones, the most suitable luminescent and magnetic species, especially in terms of desired coexistence, the production of a bifunctional luminescent and magnetic composite was obtained. This composite material consisted of magnetic iron oxide and luminescent Eu(III) complex embedded, via a multiple step impregnation route, into the APTES-functionalized ms- SiO_2 NPs. The $\text{FeO}_x/\text{Eu}(\text{DBM})_3\text{Phen}@ms\text{-SiO}_2$ composite material resulted to have regular morphology and nanostructure. Due to the strong correspondence between this bifunctional composite and the $\text{FeO}_x@ms\text{-SiO}_2$ system, the magnetic properties are expected to be almost identical to those of the latter. Notwithstanding the detrimental (to the optical properties) presence of the iron oxide nanocrystals, the bifunctional composite showed, as desired, a notable luminescent emission in the red range under UV excitation.

ESTRATTO IN LINGUA ITALIANA

Il seguente lavoro riguarda la sintesi e caratterizzazione di sistemi nanocompositi luminescenti e/o magnetici, che possono essere destinati ad un'ampia gamma di applicazioni, specialmente in campo biomedico (ad esempio in *bioimaging*, *DNA microarray*, terapie antitumorali di ipertermia, *imaging* di risonanza magnetica a contrasto avanzato, *bioimaging* combinato ottico-magnetico).

Nanofosfori luminescenti nel rosso e costituiti da nanocristalli di zirconia drogata con Eu^{3+} sono stati sintetizzati tramite il metodo dei polioli ed incorporati all'interno di una matrice di silice attraverso un processo Stöber. Uno studio comparativo su campioni in serie ha permesso di determinare la temperatura di trattamento termico ottimale ($700\text{ }^{\circ}\text{C}$) per massimizzare non solo le proprietà ottiche, ma anche la qualità nanostrutturale e la disponibilità di gruppi $-\text{OH}$ superficiali necessari per un'efficiente funzionalizzazione dei compositi $\text{ZrO}_2:\text{Eu}^{3+}@\text{SiO}_2$.

Negli studi successivi è stato fatto un utilizzo predominante di nanoparticelle di silice mesoporosa (ms-SiO_2) come struttura ospitante delle varie specie luminescenti o magnetiche. Tale materiale infatti ha implicato la possibilità di caricare, tramite semplici metodi di impregnazione, una notevole varietà e quantità di materiali (anche più di uno nella stessa matrice) dentro i pori di dimensione nanometrica, in modo da ottenere un efficiente controllo della composizione finale ed una facile funzionalizzazione superficiale dei sistemi compositi. Le nanoparticelle di silice mesoporosa sono state preparate sfruttando una sintesi di tipo micellare basata sull'utilizzo di un tensioattivo cationico come template per la porosità. La loro successiva impregnazione con fasi di zirconia nanocristallina drogata con differenti terre rare ha portato all'ottenimento di nanocompositi luminescenti $\text{ZrO}_2:\text{RE}^{3+}@\text{ms-SiO}_2$ ($\text{RE} = \text{Eu}$, Tb , Er/Yb), che hanno mostrato proprietà di luminescenza soddisfacenti, regolarità morfologica e strutturale (per quanto riguarda i sistemi contenenti Eu^{3+} e Tb^{3+}) e la possibilità di ottenere nanocompositi funzionalizzabili con proprietà di *up-conversion* (per quanto riguarda il sistema co-dopato con Er^{3+} e Yb^{3+}).

Le nanoparticelle di ms-SiO₂ sono state impregnate anche con una quantità ottimizzata di un complesso di Eu(III), ovvero Eu(DBM)₃Phen. Grazie alle proprietà ottiche peculiari di tale complesso organico, il materiale nanocomposito luminescente così prodotto è risultato essere caratterizzato da un'intensa emissione nel rosso ed un'elevata efficienza di assorbimento della radiazione di eccitazione rispetto ai materiali studiati in precedenza. Proprietà che, assieme all'alto livello di mesoporosità residua del prodotto finale, hanno contribuito a rendere questo materiale il più indicato in vista di un'ulteriore produzione di un composito bifunzionale luminescente e magnetico.

Lo studio di materiali luminescenti a base di lantanidi è proseguito con uno stage presso l'Università di Turku (Finlandia), durante il quale l'attività di ricerca ha riguardato la sintesi e caratterizzazione di materiali a luminescenza persistente (*long lasting*) di tipo Sr₂MgSi₂O₇:Eu²⁺,Dy³⁺. Questi materiali sono costituiti in polveri micrometriche ottenute tramite sintesi allo stato solido. Uno studio comparativo ha consentito di determinare la composizione ottimale del materiale, ovvero (Sr_{0.97}Eu_{0.01}Dy_{0.02})₂MgSi₂O₇, sia per l'intensità che per la durata della luminescenza persistente.

Parallelamente all'attività di ricerca sui materiali luminescenti a base di terre rare, sono stati studiati anche nanocompositi con proprietà magnetiche. In particolare sono state effettuate la sintesi e caratterizzazione di compositi magnetici costituiti da ossido di ferro oppure ossido di ferro e cobalto incorporati, tramite impregnazione, nelle nanoparticelle di silice mesoporosa. Uno studio comparativo su una serie di campioni FeO_x@ms-SiO₂ con differenti livelli di carica ha permesso di determinare la frazione nominale più indicata di ossido di ferro caricato (17% in peso), in modo da ottenere la migliore omogeneità strutturale e morfologica. Le proprietà magnetiche di tale composito hanno evidenziato un comportamento superparamagnetico, anisotropia magnetica e campi coercitivi abbastanza elevati, densità di magnetizzazione e risposta magnetica ad un campo magnetico applicato moderate. Le proprietà magnetiche del composito CoFe₂O₄@ms-SiO₂ sono risultate superiori rispetto a quelle del materiale precedente. La più alta densità di magnetizzazione in questo caso è stata attribuita al maggior contenuto di materiale magnetico

misurato nella fase cristallina, che ha potuto inoltre giustificare la superiore efficienza nella separazione magnetica osservata per questo materiale.

Uno studio ulteriore sulla possibilità di incorporare ferro metallico nella matrice di silice mesoporosa è stato effettuato con lo scopo di realizzare un materiale composito nanostrutturato con proprietà magnetiche più elevate. Tale obiettivo non è ancora stato conseguito, a causa delle difficoltà incontrate nell'evitare l'ossidazione del ferro durante, o dopo, la preparazione del composito. Tuttavia, dopo diverse prove e in seguito ad un miglioramento nella procedura di sintesi e nei materiali utilizzati, come risultato parziale è stato ottenuto un materiale promettente con notevole risposta magnetica. L'analisi strutturale e morfologica ha indicato tuttavia un disordine ed una eterogeneità nanostrutturali nel materiale. E' stata dimostrata la presenza di diverse fasi cristalline, tra le quali il carburo di ferro Fe_5C_2 , che possiede note proprietà magnetiche.

Selezionando, tra tutte quelle studiate, le specie luminescenti e magnetiche più adatte in termini di coesistenza reciproca nello stesso materiale, è stato prodotto un composito bifunzionale luminescente e magnetico. Tale materiale è costituito da ossido di ferro e complesso di $Eu(III)$ incorporati, mediante una preparazione di tipo multi-step basata su due impregnazioni in sequenza, all'interno di nanoparticelle di silice mesoporosa e funzionalizzata con APTES. Il materiale composito $FeO_x/Eu(DBM)_3Phen@ms-SiO_2F$ è risultato avere morfologia e struttura regolari ed omogenee. Data la stretta corrispondenza tra questo composito bifunzionale ed il sistema $FeO_x@ms-SiO_2$, le proprietà magnetiche del primo sono state ipotizzate essere del tutto analoghe a quelle del secondo. Nonostante la presenza dannosa (dal punto di vista delle proprietà ottiche) dei nanocristalli di ossido di ferro, il composito bifunzionale ha mostrato, come desiderato, una notevole emissione di luminescenza nel rosso se sottoposto ad eccitazione UV.

TABLE OF CONTENTS

CHAPTER I – INTRODUCTION	5
1.1 Structure of the thesis	6
1.2 Aim of the thesis	6
1.3 Luminescent and magnetic materials for biological applications	7
1.3.1 <i>The importance of nanosized materials</i>	11
1.3.2 <i>Silica as a host matrix in nanostructured materials</i>	12
1.3.3 <i>Rare earth doped silica nanoparticles: RE³⁺ ions as luminescent centers</i>	17
1.3.4 <i>Persistent luminescence materials</i>	22
1.3.5 <i>Magnetic mesoporous silica nanoparticles: iron based nanocomposites</i>	26
List of references	30
CHAPTER II – MATERIALS AND METHODS	39
2.1 Materials	40
2.2 Characterization methods	41
List of references	46
CHAPTER III – LUMINESCENT MATERIALS	47
3.1 ZrO ₂ :Eu ³⁺ @SiO ₂ nanophosphors	48
3.1.1 <i>Samples preparation</i>	49
3.1.2 <i>Results and discussion</i>	51

3.1.3	<i>Conclusions</i>	69
3.2	ZrO ₂ :RE ³⁺ @ms-SiO ₂ (RE = Eu, Tb, Er/Yb) nanophosphors	69
3.2.1	<i>Samples preparation</i>	71
3.2.2	<i>Results and discussion</i>	75
3.2.3	<i>Conclusions</i>	105
3.3	Eu(DBM) ₃ Phen@ms-SiO ₂ F nanocomposite	107
3.3.1	<i>Samples preparation</i>	108
3.3.2	<i>Results and discussion</i>	110
3.3.3	<i>Conclusions</i>	121
3.4	Sr ₂ MgSi ₂ O ₇ :Eu ²⁺ ,Dy ³⁺ persistent luminescence materials	122
3.4.1	<i>Samples preparation</i>	122
3.4.2	<i>Results and discussion</i>	123
3.4.3	<i>Conclusions</i>	145
	List of references	148

CHAPTER IV – MAGNETIC MATERIALS 153

4.1	FeO _x @ms-SiO ₂ , CoFe ₂ O ₄ @ms-SiO ₂ nanocomposites	154
4.1.1	<i>Samples preparation</i>	155
4.1.2	<i>Results and discussion</i>	157
4.1.3	<i>Conclusions</i>	184
4.2	Investigation on Fe(0)@ms-SiO ₂ nanocomposites	185
4.2.1	<i>Samples preparation</i>	186
4.2.2	<i>Results and discussion</i>	188
4.2.3	<i>Conclusions</i>	212
	List of references	214

CHAPTER V – LUMINESCENT AND MAGNETIC MATERIAL	217
<hr/>	
5.1 FeO _x /Eu(DBM) ₃ Phen@ms-SiO ₂ F nanocomposite	218
5.1.1 <i>Sample preparation</i>	219
5.1.2 <i>Results and discussion</i>	221
5.1.3 <i>Conclusions</i>	233
List of references	235
CHAPTER VI – GENERAL CONCLUSIONS	237
<hr/>	
ACKNOWLEDGEMENTS	245
<hr/>	
APPENDIX	249
<hr/>	
Publications in international journals	250

CHAPTER 1

INTRODUCTION

1.1 STRUCTURE OF THE THESIS

This doctoral thesis is composed of six chapters: the first is dedicated to the introduction of the main topics on which my PhD activities have been focused, *i.e.* photoluminescent rare earth-doped silica nanoparticles, persistent luminescence materials and magnetic nanostructured materials, with a particular attention to their potential applications in the biological field.

The second chapter contains the materials and methods section, in which the utilized materials and characterization methods are listed and described.

The third, fourth and fifth chapters are dedicated, respectively, to the luminescent, magnetic and both luminescent and magnetic materials. In each chapter, for every class of samples, the reason of the investigation, an accurate description of the followed procedures for the synthesis, the obtained results from the characterization and the conclusions about the study are presented.

The sixth chapter sums up the obtained results and contains some general conclusions and perspectives.

1.2 AIM OF THE THESIS

The thesis is focused on a study about the synthesis and characterization of luminescent and magnetic materials for biological applications.

The research project of my PhD activity mainly dealt with two topics of the PhD course in Chemical Sciences organized by the Graduate School of Ca' Foscari Venice University: micro and nanotechnologies and chemistry of the structured and functional materials.

In particular, being a starting guide line of my PhD project, most of my research activity was based on the development of innovative luminescent silica nanoparticles doped with lanthanides, whose properties and advantages are well known nowadays not only in the biomedical area and are becoming more and more interesting in a growing number of application fields. In the final part

of my studies I also dedicated time and efforts to the investigation on magnetic nanostructured silica-based materials, in order to expand the research field and the applicability of the studied materials, with a final look at a multifunctional composite material with both luminescent and magnetic properties.

1.3 LUMINESCENT AND MAGNETIC MATERIALS FOR BIOLOGICAL APPLICATIONS

Since many years, luminescent materials have attracted the attention and interest of researchers in the biological and biomedical fields. Their importance within these fields raised year after year when the progresses in science and medicine gave the possibility to employ the luminescent properties of different classes of materials in order to use them as labels for *in vitro* and *in vivo* applications. In recent years luminescent nanoparticles in particular have gained more and more interest in biosensing and bioimaging applications,^{1,2} such as the DNA microarray.³⁻⁵

Bioimaging (or biolabeling) is an analytical technique which is based on the formation of a selective bond between an easily detectable label and an analyte, so that the latter could be detected and identified through the detection of the label itself, which therefore acts as a biological marker.

In a typical example, a luminescent center is linked to an antibody which binds to a specific analyte or antigen; hence, the detection and quantification of the analyte are based on the intensity of the luminescent signal. Therefore it is clear that luminescent biomarkers need an optically active center, a biocompatible host matrix and suitable functional groups for the interaction with the analyte.

When luminescence is employed in a biological detection technique, the background autofluorescence (which can reduce the signal to noise ratio and therefore limit the detection capability) and the absorption by the biological system must be taken into account.

A possible way to overcome the problem of autofluorescence can be the use of labels with long radiative lifetimes, which allow time-delayed analysis in order to discriminate these long lifetimes against the short ones (typically of a few nanoseconds) of the fluorescence of the biological matrices. In fact, the radiative lifetime of organic molecules (especially when UV radiation is used to excite the phosphors) is short, since it relies on non-forbidden electronic transitions.

Another possibility to avoid autofluorescence is based on the use of up-converting phosphors, which, following the sequential absorption of two or more IR photons, are able to convert near infrared (NIR) radiation into a signal in the visible range. In the IR region, in fact, the biological materials show a window where their absorption is minimum, as depicted by Fig. 1.1, in which a typical absorption spectrum of some characteristic components of biological tissues is reported.⁶

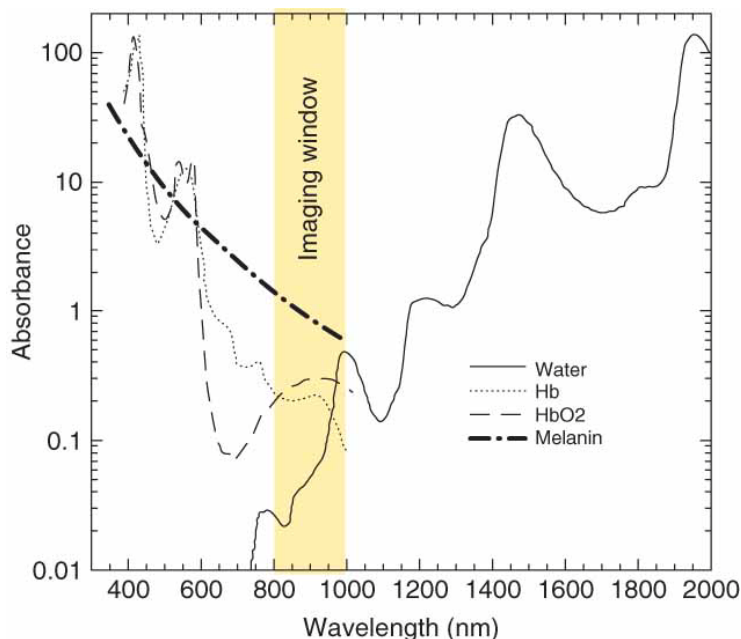


Figure 1.1 Absorption spectrum of some characteristic components of biological tissues.

In general, an efficient luminescent label is expected to produce an intense emission radiation with as little excitation as possible. From this point of view, for photoluminescent labels there are two factors of great importance: quantum yield and absorption cross section, the former indicating the efficiency of the conversion between the exciting and the emitted radiation, the latter being related to the ability of the label to absorb the exciting radiation.

Considering all these factors, several options are available for the choice of a candidate label. Different types of organic and inorganic phosphors, such as common dyes⁷ or quantum dots,^{8,9} have been successfully used as optical active center and incorporated, for example, into silica nanoparticles in order to make them luminescent. Although these approaches can lead to a strong photoluminescence emission, many of them require multiple processing steps and the use of expensive or toxic substances.

Moreover, organic dyes, which represent the standard choice for biomarking and bioimaging applications, suffer disadvantages such as a broad emission band, superposition of excitation and emission spectra, short fluorescent lifetimes and photobleaching. In contrast, as discussed later, rare earth ions present narrow emission bands, large Stokes shifts, long luminescence lifetimes and in some cases up-conversion.¹⁰ All these aspects can be used for increasing the signal to noise ratio in biological samples.

Therefore during my PhD studies on luminescent materials the attention was focused only on rare earth ions as inorganic luminescent centers. In particular, their incorporation into silica nanoparticles can give lanthanide doped nanomaterials that result very interesting and suitable for the aforementioned bioimaging applications. As an example, in Fig. 1.2 a schematic mechanism of the DNA microarray based on luminescent nanoparticles is depicted.¹¹

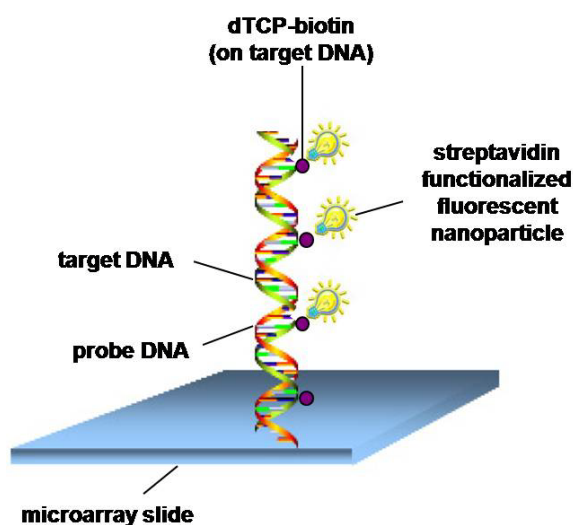


Figure 1.2 Schematic picture of the nanoparticle based DNA microarray.

The DNA microarray technology is a powerful tool for the parallel, high-throughput detection and quantification of many nucleic acid molecules and other molecules of biological interest.^{12–16}

Originally developed for the analysis of whole genome gene expression as a cDNA microarray, it is nowadays used also as oligonucleotide microarray, protein microarray and tissue microarray.^{17,18} Moreover, the applications have been expanded from gene expression analysis and profiling to genotyping, genetic screening, microbial diagnosis, environmental monitoring, immunoassay and protein assay.^{19,20}

A DNA microarray consists of an arrayed series of DNA molecules (cDNA or oligonucleotides), containing specific nucleotide sequences, which are used as probes to evaluate the presence of a target sequence in the sample, thanks to single strand DNA main feature to hybridize its complementary sequence under proper conditions. The hybridization event (probe–target interaction) is usually identified and quantified using optical methods, by fluorescence based detection.

In particular, a specific protocol optimization is needed for using nanoparticles within the mechanism of DNA microarray, since nanoparticles modify the kinetic of DNA hybridization process. The target DNA is

functionalized with biotin during Polymerase Chain Reaction (PCR) amplification and then the hybridization process takes place. Finally, the target DNA is marked with the streptavidin functionalized fluorescent nanoparticles, thanks to the very efficient and stable conjugation between biotin and streptavidin. In such a way, by means of the luminescent signal the target DNA can be detected and identified on the base of its position in the microarray.

In recent years, like the luminescent materials that were introduced above, also magnetic nanoparticles gained an increasing interest in the field of biomedical applications,²¹ among which: contrast-enhanced magnetic resonance imaging (MRI),^{22,23} hyperthermal therapy²⁴ and drug targeting. For this reason, part of my research activity concerned the study of iron based magnetic silica nanoparticles, with a final look also at their applicability together with the luminescent materials.

As a consequence of this purpose, the use of silica nanoparticles (see § 1.3.2), initially meant to function mainly as a vehicle and a protective coating for optically active centers, further resulted essential for the preparation of multifunctional and nanostructured systems, containing both luminescent and magnetic materials. The combination of luminescent and magnetic properties within a single nanocomposite system brought to a noticeable development in the sector of biological applications,²⁵⁻²⁸ since the double functionality makes these materials really interesting and suitable for several applications, such as, for example, combined optical and magnetic resonance (MR) bioimaging.²⁹

1.3.1 The importance of nanosized materials

With the exception of the persistent luminescence materials, my PhD research activities regarded nanomaterials, *i.e.* materials with nanometric size and properties. The term “nanotechnology” usually refers to a very vast field of science in which the common feature is represented by the possibility to control objects and materials on the atomic and molecular scale, in which, therefore, at least one dimension is included between 1 and usually 100 nanometers. But the

small size is not the only peculiar characteristic of nanomaterials, since also many of their chemical and physical properties in this dimensional range differ from the bulk ones. In particular, the high ratio between the surface area and volume of the nanoparticles considerably increases their driving force for diffusion at high temperatures, and the high value of specific surface area makes the nanoparticles suitable for catalysis applications. Moreover, their limited size allows the nanoparticles to pass through cell walls, giving room to a wide variety of uses and dangers in the field of biological applications.

Furthermore, a nanostructured system made of a limited number of atoms and/or molecules often presents features and properties that can only be described and studied by means of the quantum mechanical theory. Some examples of such quantistic effects are the modification of energy gaps between the valence and conduction bands in semiconductors due to quantum confinement effects,^{30,31} the variation of plasmon frequency that brings to the well known color changes in systems containing gold nanoparticles,³² the paramagnetic behavior of magnetic nanoparticles even below the Curie temperature of their bulk counterparts.³³

For all these reasons and so much more, nanomaterials and nanotechnologies are becoming subjects of greater and greater importance in our daily life.

1.3.2 Silica as a host matrix in nanostructured materials

In all the discussed materials of this thesis, with the exception of persistent luminescence materials, silica (SiO_2) has been chosen as the host matrix for the different luminescent and/or magnetic materials.

For applications of luminescent or magnetic materials involving, for example, DNA microarray, hyperthermal therapy and bio-imaging, and, more in general, for all *in vivo* applications, it is necessary to coat the lanthanide doped or magnetic nanoparticles with an inexpensive and non-toxic material. When the coating contains more than one functional nanoparticle, it can also be

considered as a matrix, with shape and size being dependent on the preparation method and on the inorganic or organic medium used. In any case, two main features are important when the purpose is to obtain a suitable coating: (i) a surface with accessible hydroxyl ($-OH$) groups, which can be readily functionalized and subsequently used for molecular recognition and (ii) a protective structure which can, for example, avoid the agglomeration and oxidation of small magnetic nanocrystals; or prevent the water molecules of the external environment from coming into contact with the lanthanide doped oxide nanoparticles. The latter would be strongly deleterious on the luminescence intensity and lifetime as a result of energy migration processes and non radiative recombination.

Thus far, silica has shown promise as an inorganic matrix in biological applications since it meets the aforementioned requirements. In fact, it is relatively inexpensive, demonstrates high thermal stability, low cytotoxicity and good chemical inertness.³⁴ Moreover, as the surfaces of silica coated nanoparticles are hydrophilic, they are readily modified with other functional groups.³⁵ Therefore, its properties make silica an optimal choice for coating luminescent and/or magnetic materials.

Among the huge variety of strategies and methods for the preparation of a silica coating, two different approaches were used during my research activity. A first way involved a classic sol-gel process based on the Stöber synthesis,³⁶ which was used in order to grow a silica shell onto colloidal luminescent nanocrystals, previously synthesized via a polyol method (see § 3.1.1).

The Stöber synthesis allows the production of monodispersed silica particles with spherical shape and controllable size. This synthesis is based on a sol-gel process that involves the reactions of hydrolysis and polycondensation of tetraethyl ortosilicate (TEOS), an organic precursor of silica. In general, such a sol-gel process can occur under acidic or basic conditions, depending on the used catalyst. As shown in Fig. 1.3, under acidic conditions the relative rate of the hydrolysis reaction exceeds that of the condensation (the single monomers formation occurs more rapidly than their polymerization), and in the resulting

fractal structure the silica network has grown in an uncontrolled and irregular way; on the other hand, under basic conditions, the condensation reaction is faster than hydrolysis (the growth of silica nuclei occurs more rapidly than the formation of new ones) and the process produces spheres with good density and regularity.

In the Stöber synthesis ammonia is used as a basic catalyst and such method allows a precise control in the size of silica spheres down to a diameter of 20 nm. Some parameters, such as, for example, the concentrations of the reagents (both absolute and relative to one another) or the molecular weight of the used alcohol, must be taken into account since they play an important role in determining the characteristics of the final product.

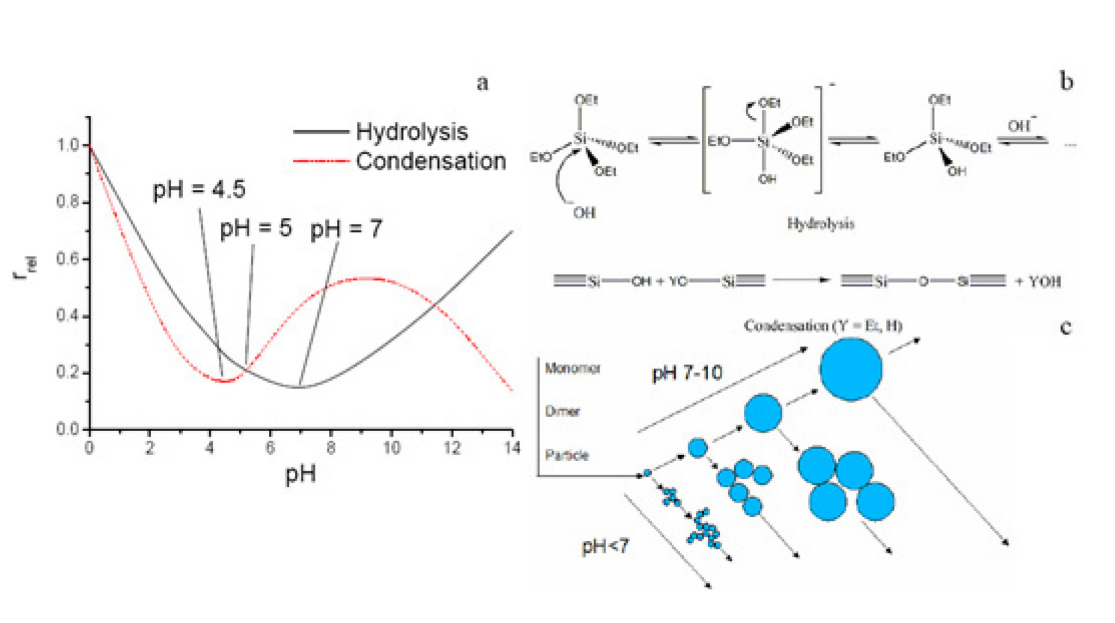


Figure 1.3 The hydrolysis and condensation reactions for TEOS: a) dependence of the relative rates of the reactions on the pH; b) reactions under basic conditions; c) morphological differences resulting from acid and basic catalysis.

The second approach that was followed in order to produce a protective and supporting silica matrix for the luminescent species as well as the magnetic nanocrystals, regarded the preparation of mesoporous silica nanoparticles to be impregnated with the desired functional material. This approach in particular

was the most employed for the preparation of the materials which are discussed in this thesis, for the easiness of the synthesis procedure and the advantages and opportunities that arise from using mesoporous silica nanoparticles as carriers of optical and/or magnetic markers in the biological field.

The synthesis of mesoporous³⁷ inorganic particles with control over their size distribution and pore diameter is of great importance in the field of materials science. Mesoporous inorganic particles are potentially interesting as catalytic supports, packing materials in high-resolution separation columns, robust host materials for sensors and photonic applications.³⁸ The importance of mesoporous silica in such applications is demonstrated by the numerous patents and literature publications. In particular, applications based on mesoporous silica nanoparticles have been thoroughly investigated and their utility demonstrated in the fields of catalysis, separation, ion exchange, molecular sieving and adsorption.³⁹⁻⁴² Other relevant application fields include environmental remediation,⁴³ drug release,⁴⁴ sensors and energy transfer devices⁴⁵⁻⁴⁸ and protein immobilization.⁴⁹

In the specific case of the work presented in this thesis, one of the main advantages brought by the utilization of mesoporous silica nanoparticles as carriers was the possibility to obtain a good compromise between the efficiency of the protective coating and the opportunity to embed a great variety of materials into the silica matrix, by impregnating the presynthesized mesoporous nanoparticles with desirable amounts of functional materials. Furthermore, applying this approach to a strategy based on multistep impregnations paved the way for the production of a multifunctional nanostructured material, which could also be easily functionalized thanks to the strong presence, even after annealing at high temperatures, of isolated and geminal silanols (which act as active sites for the functionalization) on the silica surface.

The synthesis of mesoporous silica nanoparticles was adapted from the procedure by Qiao et al.⁵⁰ The chemistry of the process is characterized by the utilization of a cationic surfactant as a templating agent for the mesoporosity; the surfactant, cetyltrimethylammonium chloride (CTAC) in the original paper or

bromide (CTAB) in my case, is included into the silica during the polycondensation reaction of nanoparticles and its further decomposition during calcination produces the formation of mesopores. This kind of synthesis can be considered as a co-operation between a classic sol-gel process (hydrolysis and condensation of TEOS) and a sort of autoassemblage of the silicate species with the surfactant. In fact, if the critical micellar concentration (CMC) inside the starting reaction mixture is reached, the surfactant molecules in a polar solution tend to organize into direct micelles, in which the hydrophobic tails of the surfactant are oriented towards the inner part while the hydrophilic heads remain outwards and face the interphase (Fig. 1.4).

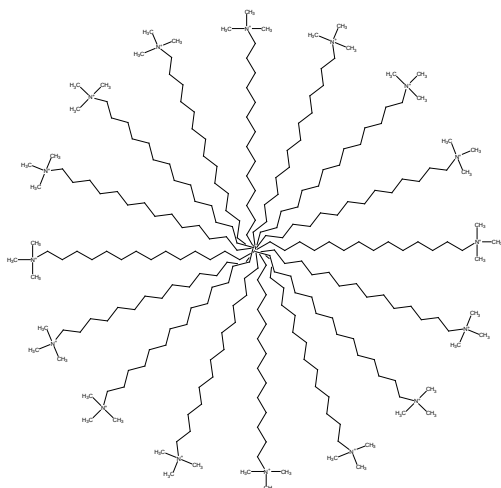


Figure 1.4 Schematic structure of a CTAB direct micelle in water solution.

Hence, these direct micelles have a positive surface charge, due to the hydrophilic heads and therefore the anionic silicate species are attracted and tend to concentrate all around them. With the hydrolysis and condensation reactions of silicon alcoxide and the growth of silica nuclei, the micelles are “trapped” inside the silica matrix and during the subsequent thermal treatment the organic fraction is burned away, leaving room to the mesoporous structure of silica nanoparticles, which are thus suitable for being impregnated with various materials.

1.3.3 Rare earth doped silica nanoparticles: RE³⁺ ions as luminescent centers

As mentioned before, rare earth ions can offer many advantages with respect to other luminescent centers as organic dyes, since they present narrow emission bands, large Stokes shifts, long luminescence lifetimes and in some cases up-conversion. The narrow emission bands are due to the shielding effect of 5d electrons on the inner 4f shell, whose energy levels host the electronic transitions that are responsible for the photoluminescence, while long emission lifetimes are made possible by the presence of forbidden f–f transitions once the selection rules are relaxed by the interaction with the surrounding environment. All these aspects can be used for increasing the signal to noise ratio in biological samples, where self-fluorescence is an important background noise and can overcome the signal under investigation, limiting the detection capability.

As an example, the trivalent europium ions (Eu³⁺), which were used, together with divalent europium (Eu²⁺), trivalent terbium (Tb³⁺) and erbium (Er³⁺) ions, as luminescent centers in the lanthanide doped materials presented in this thesis, can be efficiently excited at 393 nm, while their emission is far away peaked at 612 nm, therefore in the red region of visible light. This large Stokes shift allows an easy filtering of the light scattered by the sample and at the same time the narrow emission can be easily discriminated from the typically broad emission of self-fluorescence. For Eu³⁺ ions the main 612 nm emission is due to the ⁵D₀ – ⁷F₂ transition (see Fig. 1.5 for a scheme of Eu³⁺ energy levels and electronic transitions) and its lifetime is around one millisecond, much longer than self-fluorescence from biological samples which is of few nanoseconds. This allows time-delayed analysis that completely removes the biological noise.

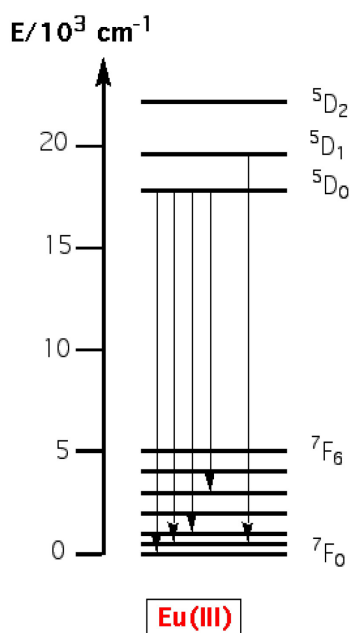


Figure 1.5 Scheme of the energy levels and electronic transitions of Eu^{3+} ion.

Instead, the main emission of trivalent terbium ions is peaked around 542 nm and therefore these luminescent centers are used for the preparation of green emitting phosphors, while the trivalent erbium ions are often employed in up-converting phosphors for their ability to absorb IR photons and emit visible light, though erbium(III) is more subject to quenching effects from hydroxide ions and non-radiative phonons emissions than europium(III).

However, one of the main drawbacks of lanthanides, especially in biological environments, is the luminescence quenching caused by water molecules and –OH groups in general. For this reason, a core-shell structure is desirable, with a lanthanide-doped core and a protective shell to screen the active centers from the water rich environment. This is one of the main role of the silica matrix, as explained in § 1.3.2. But silica by itself would not be an optimal host structure for lanthanide ions alone, because of the abundance of luminescence-quenching hydroxide groups (whose vibrational stretching overtones at 3200 cm^{-1} quench Eu^{3+} luminescence) and the tendency to form silicates with a high concentration of lanthanide, which would bring to undesirable concentration quenching effects. The concentration quenching is due to the energy migrations

in a crystal with a high concentration of lanthanide and the mechanism for quenching can either be cross-relaxation between ion pairs or energy migration to sinks depending mainly on the exact positions of energy levels in a specific host.

As a consequence, in order to avoid these effects and achieve a good dispersion of active centers, the lanthanide ions are usually employed in a solid solution (s. s.) with an appropriate crystalline oxide. Moreover, for Eu^{3+} -doped materials, the literature supports a beneficial contribution given by a crystalline nanostructure towards ${}^5\text{D}_0 - {}^7\text{F}_j$ emission properties. For such systems, the improved luminescence properties are mainly attributed to the influence of a confinement effect on resonant energy transfer in nanosized particles.⁵¹⁻⁶¹ In fact, in nanoparticles the energy transfer between luminescent centers is hindered by the particle boundary and the quenching centers (traps) could be confined in not all the particles. Hence, reducing the dimensions of Eu^{3+} -doped crystals help decreasing the probability of finding an energy sink spot on the same crystallite as an excited Eu^{3+} ion. In such conditions, the probability of trapping the excitation energy by impurities and defects is sensibly reduced and even doping levels of 10-15 mol% will not result in appreciable concentration quenching effects, while usually in the bulk counterpart the limit for concentration quenching is below 4%.

Another aspect that must be taken into account when thinking about a good host structure in a luminescent material, is that the excited lanthanide ions may relax (and hence compromise their luminescence) by releasing their energy to the host matrix as vibrations of the crystal lattice (phonons). Now, since the energy gap between an optical center's excited state and its ground state is much larger than the energy gap between adjacent modes of vibrations, a multi-phonon decay is required in order to dissipate an excited-state energy. For high-orders processes (when three or more phonons are required) the decay rate is found to be dependent on the number of phonons required to bridge the energy gap between the states and the probability of such a transition is reduced progressively as the number of required phonons grows,⁶² meaning

that a crystal lattice with a lower phonon energy is more desirable as a host matrix.

Among others, zirconium oxide (ZrO_2), a largely used material in today's industry⁶³⁻⁶⁷ due to its hardness, chemical stability, low thermal conductivity and optical transparency, is one of the best options as a host structure for trivalent rare earth ions (RE^{3+}),⁶⁸ thanks to its ability to form solid solutions with them and to its low phonon energy (470 cm^{-1}).

For all the aforementioned reasons the luminescent materials that are presented in this thesis, apart from the persistent luminescence materials, consist of nanosized RE^{3+} -doped zirconia crystals ($\text{RE} = \text{Eu}, \text{Tb}$ or Er/Yb) which are embedded in a protective amorphous silica matrix.

The only exception is represented by the $\text{Eu}(\text{DBM})_3\text{Phen}$ -doped silica nanoparticles, that were simply obtained by impregnating functionalized mesoporous silica nanoparticles with a solution containing an optimal concentration of tris(dibenzoylmethane)mono(1,10-phenanthroline)europium(III) (also known as $\text{Eu}(\text{DBM})_3\text{Phen}$). In such a structure, the rare earth ion is protected from surroundings by complex-forming ligands. Moreover, since, as mentioned before, the f-f transitions of rare earth ions are forbidden, in general they absorb very little excitation energy, while complex formation between lanthanide ions and ligands has a double beneficial effect of both protecting metal ions from vibrational coupling and increasing light absorption cross section by antenna effects.⁶⁹⁻⁷¹ It is well known that this luminescence mechanism is based on an efficient energy transfer from the triplet states of the absorbing coordinated ligands to the chelated lanthanide ions.⁷² As a consequence, lanthanide complexes have long been known to give intense emission lines and efficient luminescence upon UV light irradiation and the use of luminescent lanthanide complexes in imaging applications has also been reported in the literature.⁷³ In particular, a lot of attention has been paid to the β -diketonate complexes of trivalent europium.^{74,75}

Lanthanide β -diketonates are complexes of β -diketones (1,3-diketones) with rare earth ions. These complexes are the most popular and the most intensively

investigated rare earth coordination compounds. This popularity is partially due to the fact that many different β -diketones are commercially available and the fact that the synthesis of the corresponding rare earth complexes is relatively easy. To form the complex, β -diketonates ligands are deprotonated and their strong interaction with the metallic ion leads to the formation of hexa-coordinate complexes with high thermal stability. Since the coordination sphere of the rare earth ion is unsaturated in these kind of complexes, the rare earth ion can expand its coordination sphere by adduct formation with Lewis bases, such as water (which of course is not desired for its quenching role) or 1,10-phenanthroline, whose antenna effect is well known and can be used to this purpose. Moreover, the β -diketones with aromatic substituents, such as dibenzoylmethane (DBM), have a stronger light absorption than the β -diketones with only aliphatic substituents. Nevertheless, the instability of rare earth complexes under UV irradiation is one of the problems in their application. Since their stability depends on the vibrations of the complex after absorbing light, the more intense the vibrations are, the faster the decomposition of the complex will occur. It has been demonstrated that in (3-aminopropyl)triethoxysilane (APTES) functionalized mesoporous silica the strong hydrogen-bonding interactions of the rare earth complex with the APTES molecules limit the vibrations of the former and hence its decomposition is significantly slowed.⁷⁶

For the aforementioned reasons, the employed lanthanide complex in this thesis was $\text{Eu}(\text{DBM})_3\text{Phen}$ (see Fig. 3.38) and the host silica matrix was functionalized with APTES prior to its impregnation. This strategy allowed the preparation, via a facile synthesis, of a luminescent material with very efficient optical properties and an intense red emission. These strong optical properties were requested especially for the purpose of encapsulating into the same matrix a lanthanide doped species and an iron oxide phase, in order to obtain a multifunctional composite material with both luminescent and magnetic properties, since the presence in the same material of a typically dark magnetic

phase involves the drawback of its massive absorption of light that could weaken the luminescence from the optically active species.

For this reason, the aforementioned europium(III) complex was used in the preparation of the $\text{FeO}_x/\text{Eu}(\text{DBM})_3\text{Phen}@m\text{-SiO}_2\text{F}$ luminescent multifunctional material.

1.3.4 Persistent luminescence materials

As previously mentioned, the trivalent ions of the lanthanide series are involved in the preparation of luminescent materials which gained more and more importance not only in electronics but also in biomedical applications, such as biosensing and DNA microarray.

In addition to the trivalent ions, divalent Sm^{2+} ,⁷⁷⁻⁷⁹ Eu^{2+} ⁸⁰ and Yb^{2+} ⁸¹ yield commonly luminescence. For example Eu^{2+} is used in several commercial phosphors, e.g. for fluorescent tubes⁸² and X-ray detection.⁸³ Its emission and absorption spectra usually consist of broad bands due to transitions between the $^8\text{S}_{7/2}$ ($4f^7$) ground state and the crystal field components of the $4f^65d$ excited state configuration. The emission color varies from ultraviolet to red, depending on the host lattice. Divalent europium cation is also the most common emitting center used in the persistent luminescence materials.⁸⁴⁻⁸⁸ These materials have a varying number of possible applications, among which some of the most sophisticated belong to the biomedical field. The entire research activity of my PhD abroad stage in Turku (Finland) was dedicated to this class of materials.

Persistent luminescence, one of the most popular subjects of investigations in the storage phosphor field since the last decade,⁸⁹ is a phenomenon in which the material is emitting, usually in the visible range, for hours after the excitation source (visible light or UV, X-ray, or gamma radiation) has been switched off.⁹⁰ Although some details of persistent luminescence mechanism are still unclear, it is commonly known that this phenomenon is due to crystal defects which can act as energy storing traps. The depth of these traps makes possible the release of the energy stored by thermal excitation.

In many of conventional applications persistent luminescence is an unwanted phenomenon (also called afterglow), since, as a result of the formation of traps to store the excitation energy, the emission is retarded and, in many cases, also significantly weakened. Despite the usually undesired afterglow, persistent luminescence materials have already been used since decades in luminous paints,⁹⁰ since they resulted to be very useful in the applications in which light is needed in the dark without external energy sources (e.g. traffic and emergency signs, watches, clocks, and textile prints). More sophisticated applications of the persistent luminescence materials can be found in sensors⁹¹ and biomedical imaging.⁹²

The traditional ZnS:Cu,Co compounds were for a long time the only persistent luminescence materials in use, despite their weak and short afterglow and their sensitiveness to moisture. Such phosphors needed the addition of radioactive elements in order to prolong the afterglow and for these reasons alternative materials have been looked for.

Since the mid 1990's the alkaline earth aluminates doped with Eu^{2+} and co-doped with other rare earth ions ($\text{MAl}_2\text{O}_4:\text{Eu}^{2+},\text{R}^{3+}$; M = Ca, Sr; R = Nd, Dy) have been introduced as a new generation of persistent luminescence phosphors,^{85,86,93} with excellent properties such as high brightness, no radioactivity, long duration, excellent photoresistance and environmental capability. The Eu^{2+} ion acts as an emitting center with luminescence at the blue ($\lambda_{\text{max}} = 440 \text{ nm}$) and green (520 nm) regions for $\text{CaAl}_2\text{O}_4:\text{Eu}^{2+}$ and $\text{SrAl}_2\text{O}_4:\text{Eu}^{2+}$, respectively. Moreover, the Nd^{3+} and Dy^{3+} ions were found to increase the intensity and length of the persistent luminescence of these aluminate materials.⁸⁴ Unfortunately, the properties of these phosphors may be decreased greatly while exposed to water, which limited their application in the pigments, paints and other fields.

A new generation of materials has recently been introduced as alternatives for the alkaline earth aluminate based persistent luminescence materials.⁹⁴ These materials consist of alkaline earth magnesium disilicates doped with Eu^{2+} and co-doped with trivalent rare earth ions, $\text{M}_2\text{MgSi}_2\text{O}_7:\text{Eu}^{2+},\text{R}^{3+}$ (M = Ca, Sr,

Ba; R = Nd, Dy, Tm). They are chemically stable and they show very efficient persistent luminescence.

In particular, the best persistent luminescence material so far is $\text{Sr}_2\text{MgSi}_2\text{O}_7:\text{Eu}^{2+},\text{Dy}^{3+}$ ⁹⁵ which provides excellent stability against moisture and up to 24 hours of persistent luminescence with a reasonable price. Therefore, during my investigation on persistent luminescence the attention was focused on this material.

Persistent luminescence mechanism

In the recent past, a large number of different interpretations of the mechanism that leads to persistent luminescence has been given and some of them have been revised or considered unacceptable, thus bringing to the lack of a total agreement between researchers.

Nowadays, the persistent luminescence mechanism of the best phosphor $\text{Sr}_2\text{MgSi}_2\text{O}_7:\text{Eu}^{2+},\text{Dy}^{3+}$ is still not totally well defined to the detail. This phosphor emits blue light peaking at about 470 nm and its afterglow lasts several hours.

Generally, it is agreed that the Eu^{2+} ions act as the luminescent center while Dy^{3+} ions mostly act as the traps or create them in the host.^{96,97} The introduction of trivalent species as R^{3+} to the Sr^{2+} site inevitably creates strontium vacancies to balance the charges. The persistent luminescence should ascribe to the transition between 5d and 4f levels of Eu^{2+} ions and the afterglow should be due to the traps which are induced by Dy^{3+} ions.

Hölsä has suggested an interpretation of the persistent luminescence mechanism for $\text{Sr}_2\text{MgSi}_2\text{O}_7:\text{Eu}^{2+},\text{R}^{3+}$ phosphors.⁸⁹ Fig. 1.6 presents in a schematic way the proposed mechanism, according to which the irradiation of the material by blue light (or UV radiation) brings to the photoexcitation of Eu^{2+} through the $4f^7 \rightarrow 4f^65d^1$ transitions which overlap with the conduction band of $\text{Sr}_2\text{MgSi}_2\text{O}_7$. This leads to the creation of a free electron and a Eu^{3+} ion or a $\text{Eu}^{2+} - \text{h}^+$ (hole) pair. The capture of the excited electron by the conduction band may take place directly or may be assisted by thermal energy. Then the

electron can move in the conduction band until it returns to the europium center or is captured by the traps close to the bottom of the conduction band.

The actual persistent luminescence involves the temperature controlled gradual release of the trapped electrons followed by the migration of electrons through the conduction band to the hole trapped in Eu^{2+} ions. The recombination produces the typical emission of Eu^{2+} and makes persistent luminescence possible.

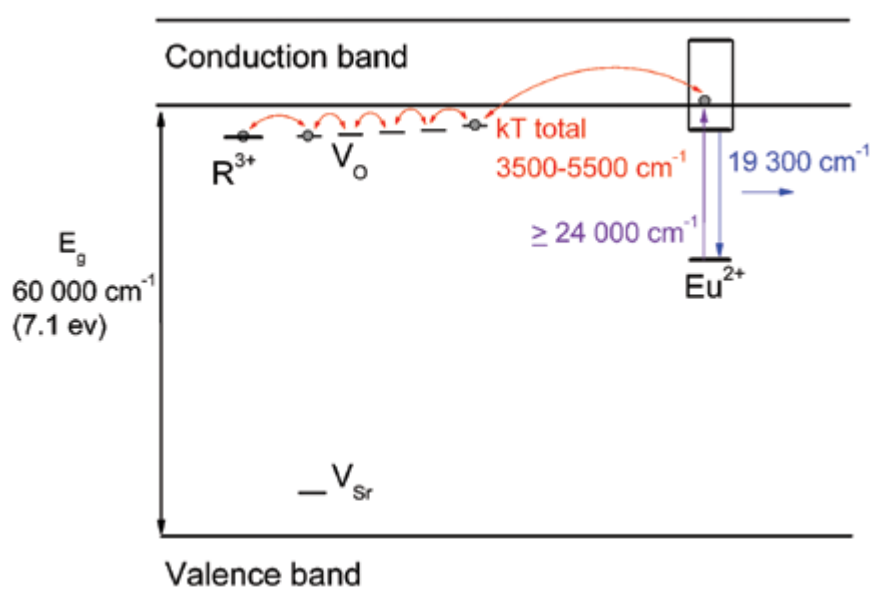


Figure 1.6 The persistent luminescence mechanism of the blue emitting $\text{Sr}_2\text{MgSi}_2\text{O}_7:\text{Eu}^{2+},\text{R}^{3+}$ phosphors.⁸⁹

Generally, the traps for holes or electrons of the phosphors are created by the lattice defects,⁹⁸ that can exist even without (co-)doping in the $\text{Sr}_2\text{MgSi}_2\text{O}_7$ structure. More disturbances in the crystal planes are observed in the $\text{Sr}_2\text{MgSi}_2\text{O}_7:\text{Eu}^{2+}$ structure. But it is with Dy^{3+} co-doping that a large number of small lattice domains centered around point defects and with different orientations are created. This fact implies that the doping of the rare earth ions increases the lattice defects which have existed already in the host. This may be the reason why the $\text{Sr}_2\text{MgSi}_2\text{O}_7:\text{Eu}^{2+}$ without co-doping Dy^{3+} or Nd^{3+} also has the afterglow, although the intensity is weak.

The Dy³⁺ ion, despite it fits rather well into the Sr²⁺ site, with its presence implies charge compensation effects which are very important in creating lattice defects. Therefore, the Dy³⁺ co-doping enhances the number of the lattice defects, which lead to an increase of the traps density and depth. As a consequence, the Dy³⁺ co-doping plays an important role in the persistent luminescence properties of the material, since the depth of the traps strongly influences the duration of the afterglow. In fact, a deeper trap releases the carriers slowly, resulting in a longer duration of the emission. However, too deep traps may not be emptied at all at room temperature.

1.3.5 Magnetic mesoporous silica nanoparticles: iron based nanocomposites

As previously mentioned, part of my research activity concerned the study of iron based magnetic silica nanoparticles, with a final look also at the coexistence of the magnetic phase with a luminescent species.

In recent years, nanocomposite magnetic materials have gained increasing interest due to their unique magnetic, catalytic and chemical properties.⁹⁹ Magnetic nanoparticles have already found use in magnetic recording and ferrofluid technologies, yet today they are also being explored for their use in biotechnological and medical applications,¹⁰⁰ such as DNA and RNA purification,¹⁰¹ cell separation,¹⁰² drug delivery,¹⁰³ magnetic recording and magnetic resonance imaging,^{104–108} and hyperthermia cancer treatments.^{24,109–111} The hyperthermal therapy is an *in vivo* application based on the interaction between an external alternating magnetic field with an appropriate frequency and the magnetic nanoparticles that have been placed in a desired area. Such an interaction produces a local heating that can destroy the tumoral cells or facilitate the release of a therapeutic drug previously loaded into the nanoparticles.

For all the aforementioned purposes, magnetic nanocrystals, including iron oxides as magnetite (Fe_3O_4) and maghemite ($\gamma\text{-Fe}_2\text{O}_3$), show promise due to their high magnetic susceptibility and good dispersibility.

In most applications the magnetic particles perform best when their size is below a critical value, which is typically around 10–20 nm depending on the material.¹¹² However, an inevitable problem associated with particles in this size range is their intrinsic instability over long periods of time. Such small particles tend to form agglomerates to reduce the energy associated with their high surface area to volume ratio. Moreover, naked metallic nanoparticles are chemically highly active and easily oxidized in air, leading to a general loss of magnetism and dispersibility.¹¹² For many applications it is thus crucial to develop protection strategies for chemical stabilization of the naked magnetic nanoparticles. In many cases the protecting shells not only stabilize the nanoparticles, but can also be used for further functionalization.¹¹²

The most important properties of magnetic materials for medical applications are non-toxicity and biocompatibility, combined with injectability, stability in physiological environments and high-level accumulation in the target tissue. Hence, for *in vivo* applications involving bio-imaging or hyperthermal therapy, it is highly desirable to coat the magnetic nanoparticles with a non-toxic material which is also a suitable host for the desired amount of magnetic phase.¹¹² A silica shell not only protects the magnetic phase, but can also prevent its direct contact with additional agents linked to the silica surface thus avoiding unwanted interactions.¹¹² Predominantly, methods developed for the coating of magnetic nanoparticles with silica have been based on the Stöber method and sol–gel processes.^{36,113–116} For instance, Xia et al.¹¹⁴ demonstrated that commercially available ferrofluids could be directly coated with silica shells by the hydrolysis of TEOS. Similarly, Ohmori and Matijević¹¹⁷ coated hematite ($\alpha\text{-Fe}_2\text{O}_3$) spindles via hydrolysis of TEOS in 2-propanol, while monodispersed amorphous cobalt nanoparticles coated with silica in an aqueous-ethanolic solution were prepared by Liz-Marzán et al.¹¹⁸ In the latter, the amorphous

cobalt core could be transformed by annealing in air to produce composites with crystalline metallic cores.

The reverse microemulsion technique has been used for the synthesis of α -Fe@silica nanostructured composites; by exploiting the micelles as nanocavities, Tartaj and Serna¹¹⁹ produced the superparamagnetic particles with a spherical morphology. Also via the reverse microemulsion approach, a method for coating CoFe_2O_4 and MnFe_2O_4 spinel ferrite nanoparticles with silica was developed by Zhang and Vestal.¹²⁰

As previously discussed, applications based on mesoporous silica nanoparticles have been thoroughly investigated and their utility demonstrated in many fields. In particular, mesoporous silica has also shown promise as an inorganic matrix in biological applications of magnetic materials. For example, Shi et al. prepared uniform nanospheres comprising a magnetic core and a mesoporous silica shell, and demonstrated their use as magnetic drug carriers for *in vitro* release.¹²¹ The approximately 270 nm sized particles were prepared via two sequential sol-gel steps. Synthesis of a thin silica coating on hematite nanoparticles by the Stöber process preceded a second coating, a mesoporous silica shell, produced by simultaneous sol-gel polymerization of TEOS and n-octadecyltrimethoxysilane.¹²¹ Zayat et al. prepared transparent and magnetic γ - Fe_2O_3 /Vycor-glass composites by impregnation of slices of porous Vycor-glass (VG) rods with an iron nitrate solution followed by a thermal treatment and a reduction process.¹²² These composites exhibited good mechanical, optical and magnetic properties. Therefore, in general an important consideration should be taken into account about the mesoporous nature of the silica matrix, which is suitably structured to provide ideal sites for nucleation of small magnetic nanocrystals, by limiting their aggregation and growth. The small pore dimensions could be exploited as nanocavities for the synthesis of the magnetic nanoparticles within the matrix. This approach was investigated during my PhD research activity. In particular, such studies include: the preparation and characterization of two nanocomposites comprising iron oxide and cobalt-iron oxide nanocrystals embedded (the former also together with a luminescent

species) within the pores of an amorphous SiO₂ matrix; an investigation on a similar nanocomposite which was meant to contain a magnetic phase made of metallic iron nanocrystals, whose strong magnetic properties are also well known and used in the biomedical field.^{123,124}

List of references:

- (1) Tansil, N. C.; Gao, Z. *Nano Today* **2006**, *1*, 28-37.
- (2) Seydack, M. *Biosens. Bioelectron.* **2005**, *20*, 2454-2469.
- (3) Wang, L.; Lofton, C.; Popp, M.; Tan, W. *Bioconjugate Chem.* **2007**, *18*, 610-613.
- (4) Taton, T. A.; Mirkin, C. A.; Letsinger, R. L. *Science* **2000**, *289*, 1757-1760.
- (5) Zhou, X.; Zhou, J. *Anal. Chem.* **2004**, *76*, 5302-5312.
- (6) Altinoğlu, E. I.; Adair, J. H. *Wiley Interdiscip. Rev. Nanomed. Nanobiotechnol.* **2010**, *2*, 461-477.
- (7) Sokolov, I.; Kievsky, Y. Y.; Kaszpurenko, J. M. *Small* **2007**, *3*, 419-423.
- (8) YinThai, C.; Zimmer, J. P.; Stroh, M.; Steckel, J. S.; Jain, R. K.; Bawendi, M. G. *Adv. Mater.* **2004**, *16*, 2092-2097.
- (9) Chan, W. C.; Nie, S. *Science* **1998**, *281*, 2016-2018.
- (10) Liu, G.; Jacquier, B. *Spectroscopic properties of rare earths in optical materials*; Springer: Berlin, 2005.
- (11) Enrichi, F.; Riccò, R.; Meneghello, A.; Pierobon, R.; Cretaio, E.; Marinello, F.; Schiavuta, P.; Parma, A.; Riello, P.; Benedetti, A. *Opt. Mater.* **2010**, *32*, 1652-1658.
- (12) Bilitewski, U. *Methods Mol. Biol.* **2009**, *509*, 1-14.
- (13) Sobek, J.; Bartscherer, K.; Jacob, A.; Hoheisel, J. D.; Angenendt, P. *Comb. Chem. High Throughput Screen.* **2006**, *9*, 365-380.
- (14) Jayapal, M.; Melendez, A. J. *Clin. Exp. Pharmacol. Physiol.* **2006**, *33*, 496-503.
- (15) Joos, T.; Bachmann, J. *Front. Biosci.* **2009**, *14*, 4376-4385.
- (16) Wingren, C.; Borrebaeck, C. A. K. *Methods Mol. Biol.* **2009**, *509*, 57-84.
- (17) Dufva, M. *Methods Mol. Biol.* **2009**, *509*, 135-144.
- (18) Chun, H.; Lee, D. S.; Kim, H. C. *Methods Mol. Biol.* **2009**, *509*, 145-158.

- (19) Andresen, H.; Bier, F. F. *Methods Mol. Biol.* **2009**, *509*, 123-134.
- (20) Andresen, H.; Grötzinger, C.; Zarse, K.; Kreuzer, O. J.; Ehrentreich-Förster, E.; Bier, F. F. *Proteomics* **2006**, *6*, 1376-1384.
- (21) Gao, J.; Gu, H.; Xu, B. *Acc. Chem. Res.* **2009**, *42*, 1097-1107.
- (22) Tanaka, T.; Matsunaga, T. *Anal. Chem.* **2000**, *72*, 3518-3522.
- (23) Magin, R. L.; Wright, S. M.; Niesman, M. R.; Chan, H. C.; Swartz, H. M. *Magn. Reson. Med.* **1986**, *3*, 440-447.
- (24) Ito, A.; Tanaka, K.; Kondo, K.; Shinkai, M.; Honda, H.; Matsumoto, K.; Saida, T.; Kobayashi, T. *Cancer Sci.* **2003**, *94*, 308-313.
- (25) Huh, Y.-M.; Jun, Y.-wook; Song, H.-T.; Kim, S.; Choi, J.-sil; Lee, J.-H.; Yoon, S.; Kim, K.-sup; Shin, J.-S.; Suh, J.-S.; Cheon, J. *J. Am. Chem. Soc.* **2005**, *127*, 12387-12391.
- (26) Giri, S.; Trewyn, B. G.; Stellmaker, M. P.; Lin, V. S.-Y. *Angew. Chem., Int. Ed.* **2005**, *44*, 5038-5044.
- (27) Kim, J.; Lee, J. E.; Lee, J.; Jang, Y.; Kim, S.-W.; An, K.; Yu, J. H.; Hyeon, T. *Angew. Chem. Int. Ed.* **2006**, *45*, 4789-4793.
- (28) Sen, T.; Sebastianelli, A.; Bruce, I. J. *J. Am. Chem. Soc.* **2006**, *128*, 7130-7131.
- (29) Kumar, R.; Nyk, M.; Ohulchanskyy, T. Y.; Flask, C. A.; Prasad, P. N. *Adv. Funct. Mater.* **2009**, *19*, 853-859.
- (30) Kayanuma, Y. *Phys. Rev. B: Condens. Matter.* **1988**, *38*, 9797-9805.
- (31) Volokitin, Y.; Sinzig, J.; de Jongh, L. J.; Schmid, G.; Vargaffik, M. N.; Moiseevi, I. I. *Nature* **1996**, *384*, 621-623.
- (32) Hodes, G. *Adv. Mater.* **2007**, *19*, 639-655.
- (33) Justin Joseyphus, R.; Narayanasamy, A.; Shinoda, K.; Jeyadevan, B.; Tohji, K. *J. Phys. Chem. Solids* **2006**, *67*, 1510-1517.
- (34) Iskandar, F.; Lenggoro, I. W.; Kim, T. O.; Nakao, N.; Shimada, M.; Okuyama, K. *J. Chem. Eng. Jpn.* **2001**, *34*, 1285-1292.
- (35) Ulman, A. *Chem. Rev.* **1996**, *96*, 1533-1554.

- (36) Stöber, W.; Fink, A.; Bohn, E. *J. Colloid Interface Sci.* **1968**, *26*, 62-69.
- (37) Rouquerol, J.; Avnir, D.; Fairbridge, C. W.; Everett, D. H.; Haynes, J. M.; Pernicone, N.; Ramsay, J. D. F.; Sing, K. S. W.; Unger, K. K. *Pure Appl. Chem.* **1994**, *66*, 1739-1758.
- (38) Büchel, G.; Unger, K. K.; Matsumoto, A.; Tsutsumi, K. *Adv. Mater.* **1998**, *10*, 1036-1038.
- (39) Ying, J. Y.; Mehnert, C. P.; Wong, M. S. *Angew. Chem., Int. Ed.* **1999**, *38*, 56-77.
- (40) Sayari, A.; Hamoudi, S. *Chem. Mater.* **2001**, *13*, 3151-3168.
- (41) Raja, R.; Thomas, J. M. *J. Mol. Catal. A: Chem.* **2002**, *181*, 3-14.
- (42) Grün, M.; Kurganov, A. A.; Schacht, S.; Schüth, F.; Unger, K. K. *J. Chromatogr. A* **1996**, *740*, 1-9.
- (43) Mercier, L.; Pinnavaia, T. J. *Adv. Mater.* **1997**, *9*, 500-503.
- (44) Vallet-Regi, M.; Rámila, A.; del Real, R. P.; Pérez-Pariente, J. *Chem. Mater.* **2001**, *13*, 308-311.
- (45) Yantasee, W.; Lin, Y.; Li, X.; Fryxell, G. E.; Zemanian, T. S.; Viswanathan, V. V. *Analyst* **2003**, *128*, 899-904.
- (46) Casasus, R.; Marcos, M. D.; Martinez-Manez, R.; Ros-Lis, J. V.; Soto, J.; Villaescusa, L. A.; Amoros, P.; Beltran, D.; Guillem, C.; Latorre, J. *J. Am. Chem. Soc.* **2004**, *126*, 8612-8613.
- (47) Walcarius, A.; Bessiere, J. *Chem. Mater.* **1999**, *11*, 3009-3011.
- (48) Hirano, T.; Yui, T.; Okazaki, K. I.; Kajino, T.; Fukushima, Y.; Inoue, H.; Torimoto, T.; Takagi, K. *J. Nanosci. Nanotechnol.* **2009**, *9*, 495-500.
- (49) Díaz, J. F.; Balkus, K. J. *J. Mol. Catal. B: Enzym.* **1996**, *2*, 115-126.
- (50) Qiao, Z.-A.; Zhang, L.; Guo, M.; Liu, Y.; Huo, Q. *Chem. Mater.* **2009**, *21*, 3823-3829.
- (51) Binnemans, K. *Chem. Rev.* **2009**, *109*, 4283-4374.
- (52) Williams, D. K.; Yuan, H.; Tissue, B. M. *J. Lumin.* **1999**, *83-84*, 297-300.

- (53) Zhang, W. P.; Xie, P. B.; Duan, C. K.; Yan, K.; Yin, M.; Lou, L. R.; Xia, S. D.; Krupa, J. C. *Chem. Phys. Lett.* **1998**, *292*, 133-136.
- (54) Pi, D.; Wang, F.; Fan, X.; Wang, M.; Zhang, Y. *Spectrochim. Acta. A Mol. Biomol. Spectrosc.* **2005**, *61*, 2455-2459.
- (55) Bender, C. M.; Burlitch, J. M.; Barber, D.; Pollock, C. *Chem. Mater.* **2000**, *12*, 1969-1976.
- (56) Ye, T.; Guiwen, Z.; Weiping, Z.; Shangda, X. *Mater. Res. Bull.* **1997**, *32*, 501-506.
- (57) Williams, D. K.; Bihari, B.; Tissue, B. M.; McHale, J. M. *J. Phys. Chem. B* **1998**, *102*, 916-920.
- (58) Tissue, B. M. *Chem. Mater.* **1998**, *10*, 2837-2845.
- (59) Tao Y.; Zhao G.; Shao X.; Ju X.; Zhang W.; Xia S. *Mater. Lett.* **1996**, *28*, 137-140.
- (60) Riello, P.; Bucella, S.; Brunelli, D.; Fossa, F.; Benedetti, A.; Trave, E.; Mazzoldi, P. *Opt. Mater.* **2006**, *28*, 1261-1265.
- (61) Silvestrini, S.; Riello, P.; Freris, I.; Cristofori, D.; Enrichi, F.; Benedetti, A. *J. Nanopart. Res.* **2009**, *12*, 993-1002.
- (62) Reisfeld, R.; Zelner, M.; Patra, A. *J. Alloy Compd.* **2000**, *300-301*, 147-151.
- (63) MacLeod, H. A. *Thin-film optical filters*; Hilger: Bristol, 1979; p. 519.
- (64) Armendariz, H.; Coq, B.; Tichit, D.; Dutartre, R.; Figueras, F. *J. Catal.* **1998**, *173*, 345-354.
- (65) Ansari, Z. A.; Karekar, R. N.; Aiyer, R. C. *Thin Solid Films* **1997**, *305*, 330-335.
- (66) Broscha, E. L.; Mukundan, R. et al. In *Proceedings of Volume Solid State Ionic Devices*, 99-13; Wachsman, E. D.; Akridge, J. R.; Liu, M.; Yamazoe, N., Eds.; 1999; pp. 374-381.
- (67) Thomas, I. M. In *Proceedings of SPIE*, 2288; 1994; p. 50.
- (68) García-Hipólito, M.; Martínez, R.; Alvarez-Fregoso, O.; Martínez, E.; Falcony, C. *J. Lumin.* **2001**, *93*, 9-15.

- (69) Bekiari, V.; Lianos, P. *Adv. Mater.* **1998**, *10*, 1455-1458.
- (70) Okamoto, Y.; Ueba, Y.; Dzhanibekov, N. F.; Banks, E. *Macromolecules* **1981**, *14*, 17-22.
- (71) Stewart, G. M.; Fox, M. A. *J. Am. Chem. Soc.* **1996**, *118*, 4354-4360.
- (72) Weissman, S. I. *J. Chem. Phys.* **1942**, *10*, 214.
- (73) Faulkner, S.; Pope, S. J. A.; Burton-Pye, B. P. *Appl. Spectrosc. Rev.* **2005**, *40*, 1-31.
- (74) Drake, S. R.; Lyons, A.; Otway, D. J.; Slawin, A. M. Z.; Williams, D. J. *J. Chem. Soc., Dalton Trans.* **1993**, 2379-2386.
- (75) Melby, L. R.; Rose, N. J.; Abramson, E.; Caris, J. C. *J. Am. Chem. Soc.* **1964**, *86*, 5117-5125.
- (76) Xu, Q.; Li, L.; Liu, X.; Xu, R. *Chem. Mater.* **2002**, *14*, 549-555.
- (77) Marium, I.; Feofilov, P. P.; Kaplyanskii, A. A. *Opt. Spektrosk.* **1962**, *12*, 493.
- (78) Aitasalo, T.; Dereń, P.; Hölsä, J.; Jungner, H.; Lastusaari, M.; Niittykoski, J.; Stręk, W. *Radiat. Meas.* **2004**, *38*, 515-518.
- (79) Hagemann, H.; Kubel, F.; Bill, H.; Gingl, F. *J. Alloy Compd.* **2004**, *374*, 194-196.
- (80) Blasse, G.; Grabmaier, B. C. *Luminescent Materials*; Springer-Verlag: Berlin, 1994.
- (81) Palilla, F. C.; O'Reilly, B. E.; Abbruscato, V. J. *J. Electrochem. Soc.* **1970**, *117*, 87.
- (82) Iwama, K.; Yamamoto, T.; Shibata, H.; Otaka, Y.; Takano, O.; Takahashi, M. Fluorescent lamp Jpn. Kokai Tokkyo Koho JP61254690 **1986**.
- (83) De Leeuw, D. M.; Kovats, T.; Herko, S. P. *J. Electrochem. Soc.* **1987**, *134*, 491-492.
- (84) Aitasalo, T.; Dereń, P.; Hölsä, J.; Jungner, H.; Krupa, J.-C.; Lastusaari, M.; Legendziewicz, J.; Niittykoski, J.; Stręk, W. *J. Solid State Chem.* **2003**, *171*, 114-122.

- (85) Matsuzawa, T.; Aoki, Y.; Takeuchi, N.; Murayama, Y. *J. Electrochem. Soc.* **1996**, *143*, 2670-2673.
- (86) Yamamoto, H.; Matsusawa, T. *J. Lumin.* **1997**, *72-74*, 287-289.
- (87) Katsumata, T.; Sakai, R.; Komuro, S.; Morikawa, T.; Kimura, H. *J. Crystal Growth* **1999**, *198-199*, 869-871.
- (88) Jiang, L.; Chang, C.; Mao, D. *J. Alloy Compd.* **2003**, *360*, 193-197.
- (89) Hölsä, J. *ECS Interface* **2009**, *18*, 42-45.
- (90) Newton Harvey, E. *A history of luminescence: from the earliest times until 1900*; American Philosophical Society: Philadelphia, 1957.
- (91) Aizawa, H.; Katsumata, T.; Takahashi, J.; Matsunaga, K.; Komuro, S.; Morikawa, T.; Toba, E. *Electrochem. Solid-State Lett.* **2002**, *5*, H17-H19.
- (92) le Masne de Chermont, Q.; Chanéac, C.; Seguin, J.; Pellé, F.; Maîtrejean, S.; Jolivet, J.-P.; Gourier, D.; Bessodes, M.; Scherman, D. *Proc Natl Acad Sci U S A.* **2007**, *104*, 9266-9271.
- (93) Murayama, Y. In *Phosphor Handbook*; Shionoya, S.; Yen, W. M., Eds.; CRC Press: Boca Raton, FL, USA, 1999; pp. 651-658.
- (94) Aitasalo, T.; Hölsä, J.; Laamanen, T.; Lastusaari, M.; Lehto, L.; Niittykoski, J.; Pellé, F. *Ceram.-Silik.* **2005**, *49*, 58-62.
- (95) Lin, Y.; Tang, Z.; Zhang, Z.; Wang, X.; Zhang, J. *J. Mater. Sci. Lett.* **2001**, *20*, 1505-1506.
- (96) Aitasalo, T.; Hölsä, J.; Kirm, M.; Laamanen, T.; Lastusaari, M.; Niittykoski, J.; Raud, J.; Valtonen, R. *Radiat. Meas.* **2007**, *42*, 644-647.
- (97) Lin, Y.; Zhang, Z.; Tang, Z.; Zhang, J.; Zheng, Z.; Lu, X. *Mater. Chem. Phys.* **2001**, *70*, 156-159.
- (98) Furusho, H.; Hölsä, J.; Laamanen, T.; Lastusaari, M.; Niittykoski, J.; Okajima, Y.; Yamamoto, A. *J. Lumin.* **2008**, *128*, 881-884.
- (99) Katz, E.; Willner, I. *Angew. Chem., Int. Ed.* **2004**, *43*, 6042-6108.
- (100) Pankhurst, Q. A.; Thanh, N. K. T.; Jones, S. K.; Dobson, J. *J. Phys. D: Appl. Phys.* **2009**, *42*, 224001.

- (101) Katz, E.; Weizmann, Y.; Willner, I. *J. Am. Chem. Soc.* **2005**, *127*, 9191-9200.
- (102) Wang, D.; He, J.; Rosenzweig, N.; Rosenzweig, Z. *Nano Lett.* **2004**, *4*, 409-413.
- (103) Arruebo, M.; Fernández-Pacheco, R.; Ibarra, M. R.; Santamaría, J. *Nanotoday* **2007**, *2*, 22-32.
- (104) Trivedi, P.; Axe, L. *Environ. Sci. Technol.* **2000**, *34*, 2215-2223.
- (105) Bucak, S.; Jones, D. A.; Laibinis, P. E.; Hatton, T. A. *Biotechnol. Prog.* **2003**, *19*, 477-484.
- (106) Moser, A.; Takano, K.; Margulies, D. T.; Albrecht, M.; Sonobe, Y.; Ikeda, Y.; Sun, S.; Fullerton, E. E. *J. Phys. D: Appl. Phys.* **2002**, *35*, R157-R167.
- (107) Wiltshire, M. C.; Pendry, J. B.; Young, I. R.; Larkman, D. J.; Gilderdale, D. J.; Hajnal, J. V. *Science* **2001**, *291*, 849-851.
- (108) Bomati-Miguel, O.; Morales, M. P.; Tartaj, P.; Ruiz-Cabello, J.; Bonville, P.; Santos, M.; Zhao, X.; Veintemillas-Verdaguer, S. *Biomaterials* **2005**, *26*, 5695-5703.
- (109) Rabias, I.; Tsi trouli, D.; Karakosta, E.; Kehagias, T.; Diamantopoulos, G.; Fardis, M.; Stamopoulos, D.; Maris, T. G.; Falaras, P.; Zouridakis, N. et al. *Biomicrofluidics* **2010**, *4*, 024111, DOI:10.1063/1.3449089.
- (110) Tartaj P.; Morales M. d. P.; Veintemillas-Verdaguer S.; González-Carreño T.; Serna C. J. *J. Phys. D: Appl. Phys.* **2003**, *36*, R182-R197.
- (111) Jordan, A.; Scholz, R.; Wust, P.; Föhling, H.; Felix, R. *J. Magn. Magn. Mater.* **1999**, *201*, 413-419.
- (112) Lu, A.-H.; Salabas, E. L.; Schüth, F. *Angew. Chem., Int. Ed.* **2007**, *46*, 1222-1244.
- (113) Tago, T.; Hatsuta, T.; Miyajima, K.; Kishida, M.; Tashiro, S.; Wakabayashi, K. *J. Am. Ceram. Soc.* **2002**, *85*, 2188-2194.
- (114) Lu, Y.; Yin, Y.; Mayers, B. T.; Xia, Y. *Nano Lett.* **2002**, *2*, 183-186.
- (115) Graf, C.; Vossen, D. L. J.; Imhof, A.; van Blaaderen, A. *Langmuir* **2003**, *19*, 6693-6700.

- (116) Philipse, A. P.; van Bruggen, M. P. B.; Pathmamanoharan, C. *Langmuir* **1994**, *10*, 92-99.
- (117) Ohmori, M.; Matijevic, E. *J. Colloid Interf. Sci.* **1992**, *150*, 594-598.
- (118) Correa-Duarte, M. A.; Giersig, M.; Kotov, N. A.; Liz-Marzán, L. M. *Langmuir* **1998**, *14*, 6430-6435.
- (119) Tartaj, P.; Serna, C. J. *J. Am. Chem. Soc.* **2003**, *125*, 15754-15755.
- (120) Vestal, C. R.; Zhang, Z. J. *Nano Lett.* **2003**, *3*, 1739-1743.
- (121) Zhao, W.; Gu, J.; Zhang, L.; Chen, H.; Shi, J. *J. Am. Chem. Soc.* **2005**, *127*, 8916-8917.
- (122) Zayat, M.; del Monte, F.; del Puerto Morales, M.; Rosa, G.; Guerrero, H.; Serna, C. J.; Levy, D. *Adv. Mater.* **2003**, *15*, 1809-1812.
- (123) Khurshid, H.; Tzitzios, V.; Colak, L.; Fang, F.; Hadjipanayis, G. C. *J. Phys.: Conf. Ser.* **2010**, *200*, 072049.
- (124) Kim, H.-J.; Ahn, J.-E.; Haam, S.; Shul, Y.-G.; Song, S.-Y.; Tatsumi, T. *J. Mater. Chem.* **2006**, *16*, 1617-1621.

CHAPTER 2

MATERIALS AND METHODS

2.1 MATERIALS

Diethylene glycol (DEG, Sigma-Aldrich, 99%)

Tetraethyl orthosilicate (TEOS, Aldrich, 98%)

(3-aminopropyl)triethoxysilane (APTES, Aldrich, 99%)

Absolute ethanol (J. T. Baker, 99.9%)

Ammonium hydroxide solution (Fluka, 28 wt% in water)

Zirconyl chloride octahydrate ($\text{ZrOCl}_2 \cdot 8\text{H}_2\text{O}$, Sigma-Aldrich, 98%)

Europium nitrate pentahydrate ($\text{Eu}(\text{NO}_3)_3 \cdot 5\text{H}_2\text{O}$, Aldrich 99.9%)

Sodium hydroxide (NaOH, Sigma-Aldrich, 98%)

n-propylamine ($\text{C}_3\text{H}_9\text{N}$, Aldrich, $\geq 99\%$)

Cyclohexane (Fluka, 99%)

Hydrochloric acid (HCl, Sigma-Aldrich, 37% in water)

n-hexane (C. Erba, 95%)

Cetyltrimethylammonium bromide (CTAB, Fluka)

Terbium nitrate pentahydrate ($\text{Tb}(\text{NO}_3)_3 \cdot 5\text{H}_2\text{O}$, Aldrich, 99.9%)

Erbium nitrate pentahydrate ($\text{Er}(\text{NO}_3)_3 \cdot 5\text{H}_2\text{O}$, Aldrich, 99.9%)

Ytterbium nitrate pentahydrate ($\text{Yb}(\text{NO}_3)_3 \cdot 5\text{H}_2\text{O}$, Aldrich, 99.9%)

Europium chloride hexahydrate ($\text{EuCl}_3 \cdot 6\text{H}_2\text{O}$, Aldrich, 99.9%)

Dibenzoylmethane (DBM, Aldrich, 98%)

1,10-Phenanthroline (Aldrich, $\geq 99\%$)

Dichloromethane (DCM, Fluka, $\geq 98\%$)

Strontium carbonate (SrCO_3 , 99.9%)

Magnesium nitrate hexahydrate ($\text{Mg}(\text{NO}_3)_2 \cdot 6\text{H}_2\text{O}$, 99.9%)

Europium oxide (Eu_2O_3 , 99.9%)

Dysprosium oxide (Dy_2O_3 , 99.9%)

Fumed silica (SiO_2 , 99.8%)

Iron(III) nitrate nonahydrate ($\text{Fe}(\text{NO}_3)_3 \cdot 9\text{H}_2\text{O}$, Aldrich, 98%)

Cobalt(II) nitrate hexahydrate ($\text{Co}(\text{NO}_3)_2 \cdot 6\text{H}_2\text{O}$, Acros Organics, 99%)

Trimethyl ethoxysilane (TMES, Aldrich, 98%)

Tetrahydrofuran (THF, Aldrich, $\geq 99.9\%$)

Iron pentacarbonyl ($\text{Fe}(\text{CO})_5$, Fluka, $\geq 97\%$ (Fe))

Distilled water

Diethylene glycol was freshly distilled to remove traces of water, while all the remaining reagents and solvents were used as received.

2.2 CHARACTERIZATION METHODS

Structural characterization

Morphology and structure of the nanocomposites were studied by X-ray powder diffraction (XRPD) and transmission electron microscopy (TEM). A Philips X'Pert vertical goniometer working in Bragg-Brentano geometry, connected to a highly stabilized generator, was used for the XRPD measurements. A focusing graphite monochromator and a proportional counter with a pulse-height discriminator were used. Nickel-filtered Cu $K\alpha$ radiation ($\lambda = 1.54056\text{\AA}$) and a step-by-step technique were employed (steps of 0.05° in 2θ values), with collection times of 10 s step^{-1} . The size of the crystallites was evaluated by Line Broadening Analysis (LBA) using a previously published method.¹

TEM images were taken with a JEOL 3010, operating at 300KV, equipped with a GATAN (Warrendale, PA, USA) multi-scan CCD camera and an Oxford EDS microanalysis detector. TEM specimens were prepared by ultrasonically dispersing the powdered samples in ethanol (approximately 10 mg mL^{-1}) and depositing several drops of the suspension on a holey carbon film grid.

Qualitative evaluation of the chemical composition of samples was obtained using diffuse reflectance infrared Fourier transform (DRIFT) spectroscopy (ThermoNicolet Magna-IR™). The powders were dispersed in KBr and the spectra were recorded in the range $4000\text{--}500\text{ cm}^{-1}$, at a resolution of 2 cm^{-1} using a KBr background.

Raman spectra were recorded with a Renishaw inVia microRaman spectrometer using a 50x magnification and the 633 nm line of a He-Ne laser as

exciting line. A low intensity, not exceeding 0.6 mW, was used to avoid the transformation of the synthesized phases.

Thermogravimetric analysis (TGA) was recorded using alumina as the inert standard (Netzsch STA 409). TGA analyses were collected consecutively, carried out with a temperature profile of 25 °C to 1000 °C, a heating rate of 10 °C min⁻¹, and an air (or N₂ + 5% H₂) to N₂ flow ratio of 1:2 (40:80 mL min⁻¹).

The structural changes as a function of temperature and atmosphere were investigated by in situ XRD measurements collected at the Materials Characterization by X-Ray Diffraction (MCX) beamline² at the Elettra Synchrotron source (Trieste, Italy). The instrument was coupled to a furnace that provides an atmosphere and temperature (RT to 1000 °C) controlled environment for sample powders contained in capillaries.

Porosimetric analysis was performed through N₂ adsorption/desorption measurements at the gas condensation temperature (77 K), using a Micromeritics ASAP 2010 instrument. Before the measurement samples were degased (10⁻³ torr) at 130 °C for 12 hours. Surface area was calculated from the adsorption isotherm according to B.E.T. method³. Specific pore volume was calculated at $p/p_0 = 0.98$ and the pore size distribution was determined by using the B.J.H. method.⁴

Optical characterization

Photoluminescence excitation, emission and time-resolved analysis were all performed on powdered samples and were carried out by using a Horiba-Jobin Yvon Fluorolog 3-21 spectrofluorimeter. A Xenon arc lamp was used as a continuous-spectrum source selecting the excitation wavelength by a double Czerny-Turner monochromator. Only for the up-converting erbium/ytterbium doped sample, the employed excitation source for the emission spectrum was a L980P030 single mode CW diode laser (30 mW).

The excitation spectra were recorded in the 250-550 nm range with 1 nm bandpass resolution. The detection system was constituted by a iHR300 single grating monochromator coupled to an R928 photomultiplier tube (PMT)

operating at 950 V. The excitation spectra were corrected by dividing the PMT signal by the intensity of the lamp, measured by using a calibrated photodetector. On the other hand, the emission spectra were recorded in the 450-750 nm range with 1 nm bandpass resolution.

Time-resolved analysis were performed in multi channel scaling modality (MCS) by using a 377 nm laser diode (SpectraLED-03) as a monochromatic source. This provided the possibility to set the duration of both illumination and dark periods long enough to let the system reach the equilibrium conditions, typically of the order of ten milliseconds, for the correct evaluation of the lifetime.

Photographs of the luminescent powders at different magnification under visible and/or UV light were collected using a Leica DM LM (reflected light or reflected/transmitted light) microscope equipped with: a digital photcamera, a mercury short arc (OSRAM HBO[®]) UV lamp for the excitation of the powders and a filtering optical system in the output optical path that was employed to cut the outgoing UV radiation, thus allowing only the passage of the emitted light in the visible range.

Magnetic characterization

Magnetic measurements were performed at the LA.M.M. of the Department of Chemistry at the University of Florence (Italy), using a superconducting quantum interference device (SQUID) magnetometer (Quantum Design MPMS) operating in the 3 K - 300 K temperature range with applied field up to 5.0 T. The measurements were performed directly on a pellet made with the dried powder of the sample in such a way to prevent preferential orientation of the nanocrystallites under the magnetic field. Zero-Field Cooling (ZFC) magnetization curves were obtained by cooling the sample under zero applied field to 5 K, then applying a small magnetic field (2.5 mT) and measuring while the temperature was increased to 300 K in presence of the magnetic field. Then, after cooling the sample to 5 K under applied field, Field Cooling (FC)

magnetization was measured by increasing the temperature in the presence of the magnetic field.

Characterization of persistent luminescence materials

Persistent luminescence materials were synthesized, characterized and studied at the Department of Chemistry of the University of Turku, Finland.

The solid state reaction involved in the preparation of the materials was studied between 25 and 1350 °C by thermogravimetry with a TA Instruments SDT 2960 Simultaneous DTA-TGA apparatus, with aluminium oxide sample pans. The heating rate was 5 °C min⁻¹ with a gas (N₂ + 10% H₂) flow rate of 100 cm³ min⁻¹. The sample weight was ca. 10 mg.

The structure and purity of the materials were investigated by X-Ray Powder Diffraction (XRPD). The patterns were collected at room temperature with a Huber G670 image plate Guinier-camera (CuK_{α1} radiation, λ = 1.54056 Å). The measurement range was from 4° to 100° in 2θ values. The image plate was scanned 10 times within a data collection time of 15 minutes.

The diffraction patterns were measured from powder samples attached to a Mylar film by Vaseline. The oscillation movement of the sample holder reduced the possible preferred orientation of the sample.

The UV excited and persistent luminescence spectra were measured at room temperature and at 77 K using a Varian Cary Eclipse Fluorescence Spectrophotometer. The excitation source of the emission measurements was a xenon lamp (λ_{exc} = 300 nm).

Prior to the persistent luminescence measurements by the Varian Cary Eclipse Fluorescence Spectrophotometer, the materials were exposed to radiation from a 4 W UVP UVGL-25 shortwave UV lamp (λ_{exc} = 254 nm) for 5 minutes. The delay between the initial excitation and the first persistent luminescence measurement was six minutes.

Excitation and emission spectra of the materials were measured using the beamline I at the SUPERLUMI station of HASYLAB at DESY (Hamburg, Germany), with a 15° Mc Pherson monochromator.

The excitation spectra, measured using a photomultiplier tube, and the emission ones, measured using a CCD camera, were collected at different temperatures and using different emission/excitation wavelengths. The excitation spectra were corrected for the incident flux of the excitation beam using the excitation spectrum of sodium salicylate.

X-ray absorption near edge structure (XANES) measurements were carried out by using the A1 beamline of HASYLAB at DESY (Hamburg, Germany). XANES spectra were measured at 10 and 300 K. The measurements were carried out in fluorescence mode using a PIPS (Passivated Implanted Planar Silicon) detector.

List of references:

- (1) Enzo, S.; Polizzi, S.; Benedetti, A. *Z. Kristallogr.* **1985**, *170*, 275-287.
- (2) Lausi, A.; Busetto, E.; Leoni, M.; Scardi, P. *Synchrotron Radiation in Natural Science* **2006**, *5*, 100-104.
- (3) Brunauer, S.; Emmett, P. H.; Teller, E. *J. Am. Chem. Soc.* **1938**, *60*, 309-319.
- (4) Barrett, E. P.; Joyner, L. G.; Halenda, P. P. *J. Am. Chem. Soc.* **1951**, *73*, 373-380.

CHAPTER 3

LUMINESCENT MATERIALS

3.1 ZrO₂:Eu³⁺@SiO₂ nanophosphors

The synthesis of two systems comprising luminescent Eu³⁺-doped zirconium oxide nanocrystals embedded in an amorphous SiO₂ matrix and their subsequent annealing at differing temperatures followed by surface functionalization were performed. The two systems have been prepared with the same overall wt% composition of SiO₂ (75%) and Eu_xZr_(1-x)O_(2-x/2) solid solution (s. s.) (25%). Variation of the crystalline phase composition to give $x = 0.03$ and 0.10 , respectively, provided the two systems for a comparative luminescence study. The incorporation of Eu³⁺ ions was achieved by the preparation of doped ZrO₂ nanoparticles through the polyol method,¹ whereby Eu³⁺ ions substituted Zr⁴⁺ ions in the solid solution.

The polyol method is a synthetic route that was developed in order to produce nano-sized metal oxide/hydroxide crystals, in which a polyalcohol (polyol), e.g. diethylene glycol (DEG), acts as solvent, reducing agent and surfactant. In fact, in a high-boiling solvent like DEG, the nucleation and growth of nanocrystals can occur at high temperatures, thus bringing to final materials with remarkable degrees of crystallinity. Moreover, the chelating effect of DEG on the solid nuclei during their growth can limit the latter (and therefore the nanocrystals' size) and avoid the agglomeration of nanoparticles.

The Eu(III)-doped ZrO₂ nanoparticles were subsequently embedded in the silica matrix via the Stöber process.²

Successively, the resulting two samples with differing crystalline phase composition were thermally annealed in the range of 135–1000 °C. In general, annealing is required to improve the quality of the matrix containing the rare earth oxide and to remove the –OH moieties which are responsible for luminescence quenching. Hence, careful consideration of a suitable temperature is required in order to reach a good compromise between the reduction of quenching centers while maintaining accessible –OH groups on the silica surface which can be functionalized. In fact, surface functionalization

would be necessary in applications such as biolabeling, in which further immobilization of biological molecules is required.

Therefore, the influence of the annealing temperature of the two sample series on the: i) nanostructure, ii) luminescence properties and iii) available superficial –OH groups have been thoroughly investigated, in order to determine the optimum value of the temperature.

3.1.1 Samples preparation

Synthesis of europium-doped zirconia nanoparticles: E03, E10

Samples E03 and E10, consisting of $\text{Eu}_x\text{Zr}_{(1-x)}\text{O}_{(2-x/2)}$ s. s. where $x = 0.03$ and 0.10 , respectively, were prepared by the polyol method. The resulting colloid was estimated to contain a theoretical mass yield of 2.5 g for both s. s. samples in DEG. The synthesis of sample E10 and its successive silica coating are described in detail in the following paragraph. The same procedure was used for sample E03.

Zirconyl chloride octahydrate (5.758 g, $17.5 \cdot 10^{-3}$ mol) and europium nitrate pentahydrate (0.845 g, $1.94 \cdot 10^{-3}$ mol) were added to DEG (97.2 mL) in a 3-necked flask while stirring. The flask was fitted with a reflux condenser and flushed with N_2 . Stirring was continued while the temperature was raised to 140 °C and held for 1 h. Subsequently, the temperature was raised to 180 °C, which was followed by the addition of an aqueous NaOH solution (15 mL, 5 M) to effect precipitation of the mixed oxide/hydroxide nanopowder. After 4 hours at 180 °C, the flask was cooled to ambient temperature and the product was recovered and purified by repeated centrifugation (30 min at 6 krpm), redispersion in distilled water and sonication (3 cycles). The obtained wet solid was divided in two portions. One portion was used to estimate the europium:zirconium ratio, while the other was suspended in ethanol in order to be coated with SiO_2 .

The first portion was dried overnight at 135 °C in order to calculate its water content and crystallites' size by XRD analysis and then it was calcined (12 h at 1000 °C) for determination of the europium:zirconium ratio.

Synthesis of $ZrO_2:Eu^{3+}@SiO_2$ samples

Following determination of the colloid's water content, 6.86 g of wet colloid (*i.e.* E03 or E10) was suspended in ethanol (50 mL) by sonication (30 min). The remaining ethanol required (513.4 mL), ammonia solution (4.3 mL) and distilled water (42.2 mL) were added to the suspension under vigorous stirring. A solution of TEOS in ethanol was then added dropwise over the course of 30 min. The resulting solution contained 1.25 g of Eu^{3+} -doped ZrO_2 , $6.2 \cdot 10^{-2}$ mol of TEOS, $6.2 \cdot 10^{-2}$ mol of ammonia and 2.5 mol of water in a total of 563.4 mL of ethanol. This gave a TEOS:water:ammonia molar ratio of 1:40:1 with a TEOS concentration of 0.1 M. Theoretically, 3.75 g of silica were expected, therefore giving a 1:3 weight ratio between crystalline and amorphous phases. Stirring was continued for two days at ambient temperature to produce sample E10S. E10S was recovered and purified by repeated (3 times) centrifugation (30 min at 6 krpm), ethanol washing and sonication (30 min).

Samples E10S and E03S were each divided into eight portions and annealed individually at the eight different temperatures, 135, 300, 500, 600, 700, 800, 900 and 1000 °C, for 12 h. This also allowed for complete transformation of any hydroxides formed by the polyol method to oxides. Each sample obtained was named E10S-x (where x = temperature of calcination, *e.g.* E10S-135).

Synthesis of reference sample $Eu^{3+}@SiO_2$

A sample containing the same theoretical Eu^{3+} ion content as E10S but alternatively dispersed in a SiO_2 matrix, *i.e.* in the absence of ZrO_2 , was prepared via the sol-gel method. TEOS (14.3 mL, 62.8 mmol) was dissolved in EtOH (11.9 mL) while stirring in an ice-bath. $Eu(NO_3)_3 \cdot 5H_2O$ (0.6 g, 1.3 mmol) and HCl (0.7 mL, 8.4 mmol) were dissolved in deionized H_2O (4.5 mL), then

added slowly to the TEOS solution. The ice-bath was removed and the reaction allowed to proceed stirring until gelation and subsequent formation of the glass-like solid occurred. The obtained solid was annealed in air at 500, 600, 700, 800, 900, and 1000 °C.

Synthesis of “bulk” s. s. reference sample $\text{Eu}_{0.1}\text{Zr}_{0.9}\text{O}_{1.95}$ (micrometric size powder)

The “bulk” sample $\text{Eu}_{0.1}\text{Zr}_{0.9}\text{O}_{1.95}$ with the same theoretical Eu^{3+} ion content as the E10 nanoparticles was obtained by a coprecipitation method (rather than polyol method). $\text{Eu}(\text{NO}_3)_3 \cdot 5\text{H}_2\text{O}$ (0.78 g, 1.8 mmol) and $\text{ZrOCl}_2 \cdot 8\text{H}_2\text{O}$ (5.22 g, 16.2 mmol) were dissolved in deionized H_2O (80 mL). A separate solution containing 28% NH_3 (3.6 mL) was prepared in deionized H_2O (80 mL) and subsequently introduced to the salt solution. The co-precipitated hydroxide, containing $\text{Eu}(\text{OH})_3$ and $\text{ZrO}(\text{OH})_2$, was calcined at 1000 °C for 24 h, thus giving the corresponding mixed oxide s. s.

General procedure for functionalization of $\text{ZrO}_2:\text{Eu}^{3+}@\text{SiO}_2$ with APTES

The functionalization procedure is described for a selected sample (E10S-700). By adaptation of the method by Chen and Brauer,³ surface grafting of APTES was achieved by addition of a cyclohexane (5 mL) solution containing 2% v/v APTES and 2% v/v *n*-propylamine to 0.1 g of the powdered sample E10S-700. The suspension was stirred at ambient temperature for 2 h, after which it was recovered and purified by repeated (3 times) centrifugation (30 min at 6 krpm), hexane washing and sonication (30 min). The obtained sample, E10S-700F was dried under reduced pressure (10^{-1} mbar for 1 h).

3.1.2 Results and discussion

Influence of the annealing temperatures on the nanostructures

The XRD patterns of the sample E10 dried at 135 °C and calcined at 1000 °C are shown in Fig. 3.1. The pattern of the dried sample indicates the typical

peaks of the cubic zirconia crystalline structure. The crystallites' size was evaluated by Line Broadening Analysis (LBA) to be around 1.5 nm in diameter. In the calcined sample E10, the XRD pattern clearly shows the presence of the same crystalline structure (Fig. 3.1).

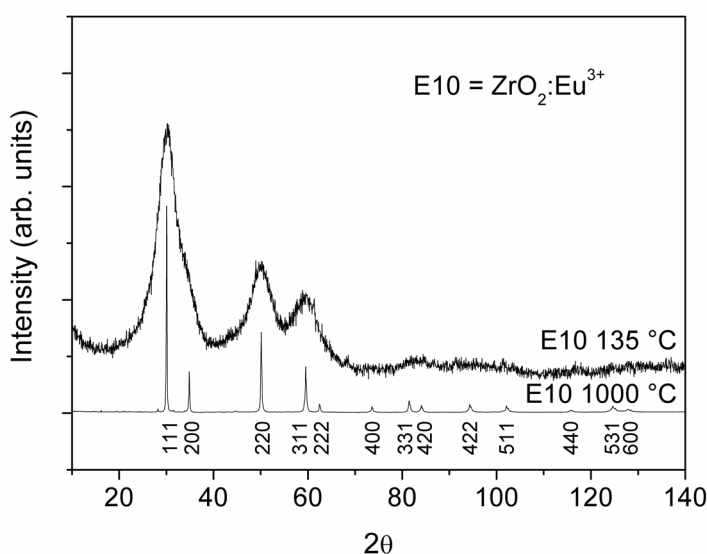


Figure 3.1 XRD patterns of the sample E10 dried at 135 °C and calcined at 1000 °C.

The Rietveld analysis method led to an accurate evaluation of the unit cell of the crystalline phase. From the cell volume, the related solid solution (s. s.) composition was obtained.⁴ The europium mole fraction was calculated to be 10.6 ± 0.3 wt%, a value very close to the theoretical 10%. It is important to note that the annealing temperature promoted the crystallites' growth for the ZrO_2 - Eu_2O_3 s. s. and, as expected, the peaks became narrower at higher temperatures without altering their angular positions. This structural trend, which is related to the thermal treatment, was evidenced by analysis of the XRD patterns for the E10S-x series reported with the E10 sample calcined at 1000 °C as a standard (Fig. 3.2a). The Rietveld analysis of E10S-900 is shown as a representative sample in Fig. 3.2b.

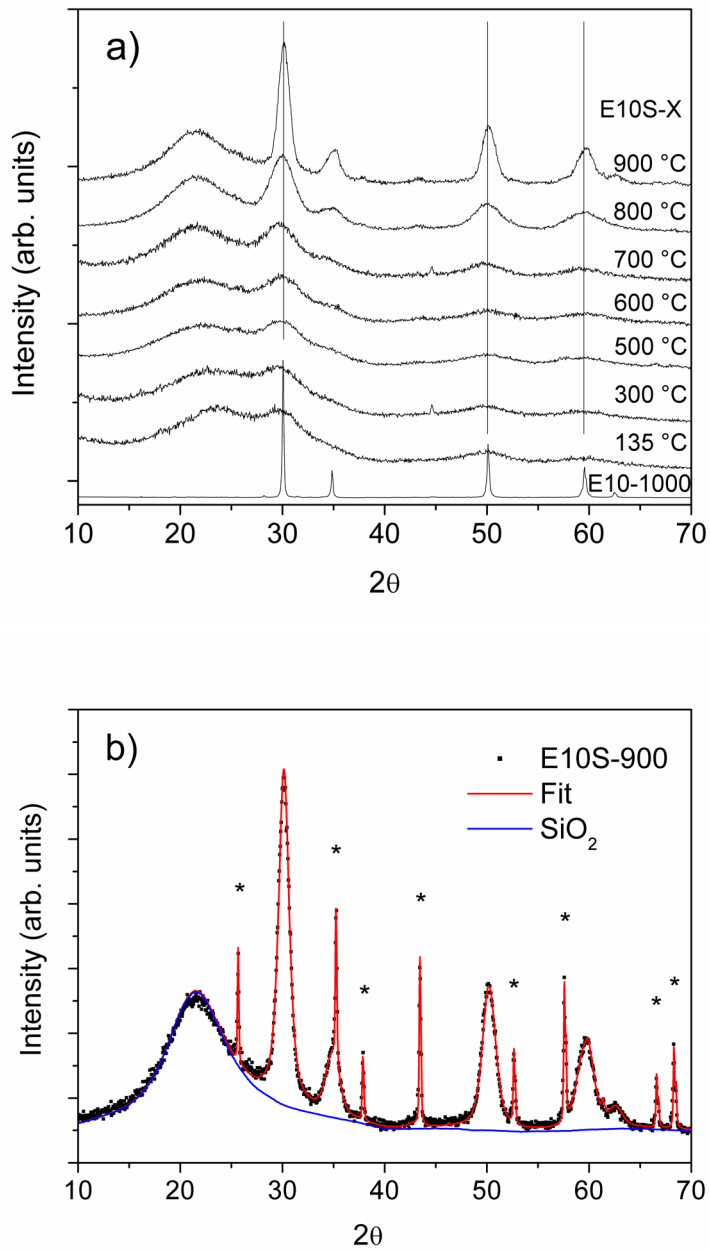


Figure 3.2 a): XRD patterns of the E10S-x series; b): example of Rietveld analysis: the narrow peaks marked by * belong to Al₂O₃ that was added to the sample as angular internal standard in order to reduce the error during the refinement of the unit cell parameters of the ZrO₂-Eu₂O₃ solid solution due to the broadness of its peaks.

From the refined cell the europium mole fraction was determined to be 10.3 ± 0.3 wt%, that quantitatively confirms the constancy of the nanoparticle composition during the thermal treatment. This was found to be consistent for the E03S-x series.

The crystallites' size of the Eu^{3+} -doped ZrO_2 nanoparticles versus the annealing temperature for both series is illustrated in Fig. 3.3. The size of the crystallites, obtained via XRD LBA, shows a constant value of ca. 2 nm up to 700 °C, after which it grows remarkably with an increase in temperature. The europium amount has no influence on the crystallites' size since the growth associated with the two different series almost coincided (Fig. 3.3).

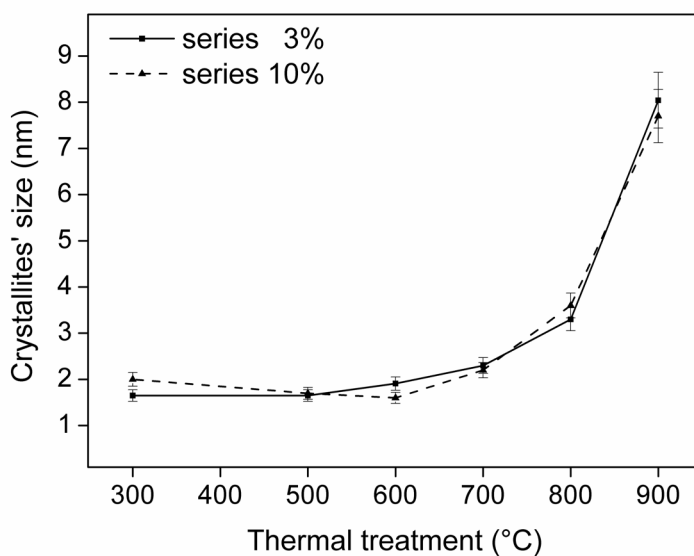


Figure 3.3 Trend of the crystallites' size with the temperature of thermal treatment for both of the series of samples.

TEM analysis corroborates the results obtained by XRD analysis in terms of the crystallites' size. As an example, representative micrographs of the sample E10S-800 (Fig. 3.4) at different resolutions evidence a fine regularity in shape and size for the Eu^{3+} -doped ZrO_2 nanoparticles.

Fig. 3.4 reveals the difficulty in controlling morphological regularity and size of the silica matrix, resulting in an agglomeration of silica particles.

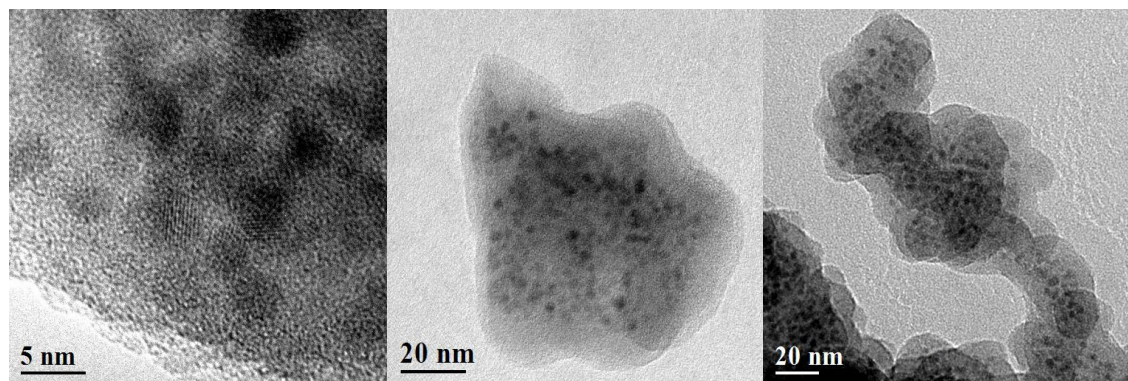


Figure 3.4 TEM micrographs of sample E10S-800.

The luminescence properties as influenced by annealing in the range 135–1000 °C

After establishing a relationship between annealing temperature and crystallite size of the $\text{ZrO}_2:\text{Eu}^{3+}@\text{SiO}_2$, the luminescence properties of the samples were examined.

The photoluminescence (PL) emission spectra measured for several representative samples of the E10S-x series are reported in Fig. 3.5 (x = 300, 700 and 900 °C).

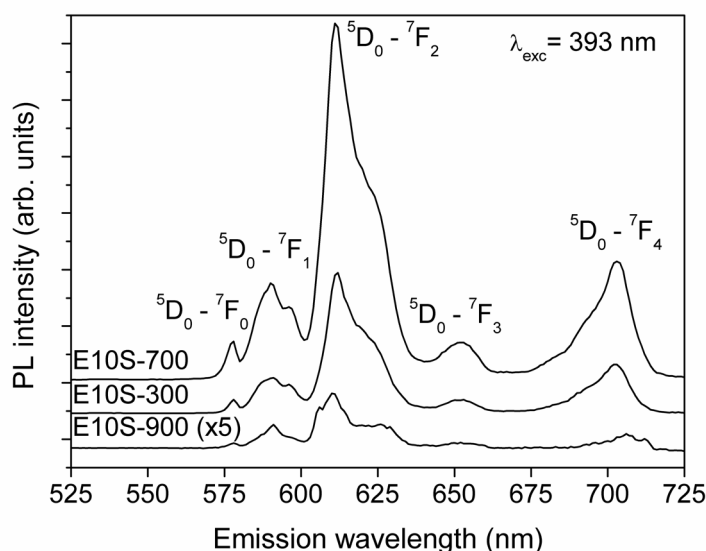


Figure 3.5 Luminescence emission spectra under 393 nm excitation for representative samples of the E10S-x series.

The emission peaks observed at 577, 590, 612, 650 and 700 nm are those related to the energy level structure of the Eu^{3+} ions and correspond to the ${}^5\text{D}_0 \rightarrow {}^7\text{F}_j$ ($j = 0, \dots, 4$) transitions. In particular, the peak assigned to ${}^5\text{D}_0 \rightarrow {}^7\text{F}_2$ is due to an electric dipole transition, while the ${}^5\text{D}_0 \rightarrow {}^7\text{F}_1$ is a pure magnetic dipole transition.

The index R defined as

$$R = \frac{I({}^5\text{D}_0 \rightarrow {}^7\text{F}_2)}{I({}^5\text{D}_0 \rightarrow {}^7\text{F}_1)}$$

represents the ratio between the integrated intensity of the ${}^5\text{D}_0 - {}^7\text{F}_1$ (580-601 nm) and the ${}^5\text{D}_0 - {}^7\text{F}_2$ (601-640 nm) transitions. In this kind of materials R can be used to give an indicative measure of the asymmetry of the coordination polyhedron of the Eu^{3+} ion. In particular, the former transition is a pure magnetic dipole transition, impervious to the effects of the surrounding crystal field, while the latter one is a hypersensitive forced electric dipole transition allowed only at

low symmetries with no inversion center^{5,6}. Therefore, a lower R value corresponds to an higher site symmetry of the Eu^{3+} ion. This relationship between R and the symmetry of the site is not strictly true, in fact in Eu^{3+} doped non-centrosymmetric fluorides (for example $\text{K}_5\text{Li}_2\text{LnF}_{10}$), in which Eu^{3+} occupies a site with C_s symmetry, a low intensity of the electric dipole emission (${}^5\text{D}_0 - {}^7\text{F}_2$) has been observed. This behavior of fluorides can be explained with the high ionicity of the Eu-F bond which allows a little admixture of the opposite parity Eu^{3+} f-states, so their electric-dipole transition becomes less favorable as compared to the oxides⁷⁻⁹. Principally, the spectra show an inhomogeneous broadening of the emission lines that denote the disorder of the sites in which the Eu^{3+} ions are accommodated. This disorder is attributed to the significantly small size of the luminescent nanoparticles. It is worth noting that apart from the intensities there are no other significant differences in the spectra of the two series, E03S-x and E10S-x, annealed at different temperatures. Hence, PL emission spectra for the E03S-x series are not shown.

According to Crystal Field Theory, the electron energy levels for lanthanide ions in nanoparticles may vary with respect to the bulk materials because of change in the strength of the local electrostatic field in the site. In nanocrystals, the structural disorder and the interactions with the surface and with the matrix beyond the particle boundaries are inevitable and therefore introduce an additional important inhomogeneous line broadening with respect to bulk crystals. For example, the case study of $\text{Eu}^{3+}@\text{LaCl}_3$ indicated that for nanocrystals with a size less than approximately 5 nm, the crystal fields potential is size dependent.^{10,11}

This would suggest that in the samples which are discussed in the present study the Eu^{3+} ions are located a few nm from the surface of the particles, therefore are influenced by the structure of the silica matrix. This explains the large inhomogeneous broadening and the small variability of the PL patterns observed in the samples. Only the nanocomposites annealed at elevated temperature (900 and 1000 °C) revealed a small peak at 606 nm which is typical of the Eu^{3+} -doped cubic bulk ZrO_2 (Fig. 3.6). In this latter case, there are

large particles embedded within the SiO_2 matrix, and the Eu^{3+} ions near the central "core" are therefore not influenced by the presence of the SiO_2 matrix outside the boundary of the nanocrystal. Consequently, the PL patterns showed some of the typical features of the cubic form (Fig. 3.6).

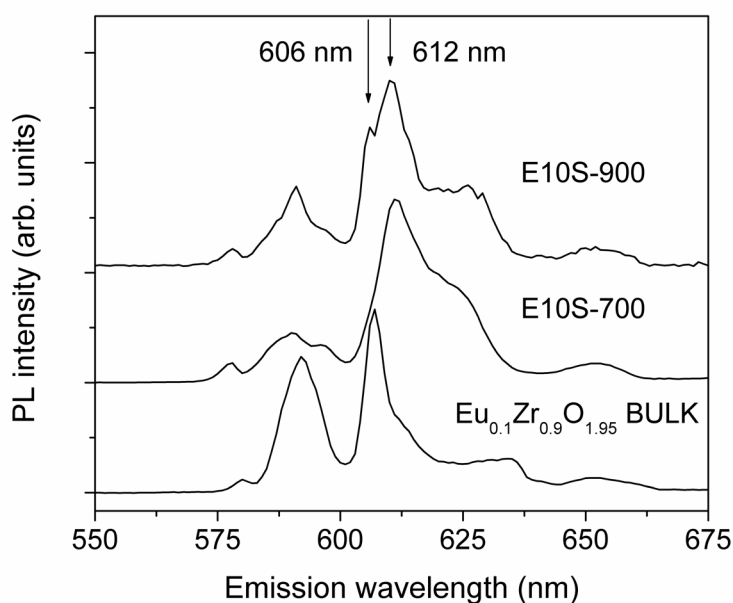


Figure 3.6 Comparison of the PL emission spectra under 393 nm excitation of two E10S samples and the emission spectra of $\text{Eu}_{0.1}\text{Zr}_{0.9}\text{O}_{1.95}$ bulk.

It is interesting to compare the PL emission of a sample containing Eu^{3+} ions embedded in a SiO_2 matrix with the samples of the E10S-X series. The PL pattern of a representative sample, E10S-700, is shown in Fig. 3.7 with $\text{Eu}^{3+}@SiO_2$ treated at the same temperature ($\text{Eu}^{3+}@SiO_2$ -700).

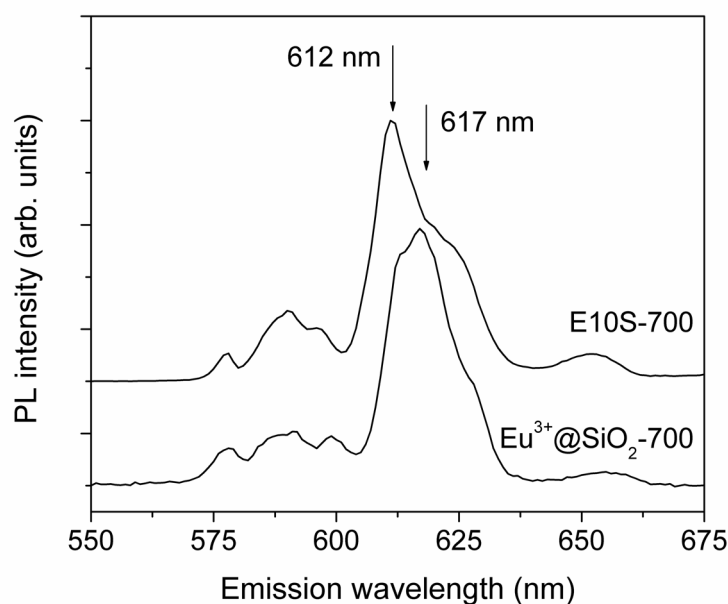


Figure 3.7 Comparison of the PL emission spectra under 393 nm excitation of E10S-700 sample and the emission spectra of $\text{Eu}^{3+}@SiO_2$ treated at the same temperature.

The patterns of the two materials showed a different overall shape of their PL spectra and a difference in the position of the maxima: at 612 nm for the E10S-X sample and at 617 nm for $\text{Eu}^{3+}@SiO_2$. This finding was observed at all annealing temperatures.

In Fig. 3.8, the variation of the R index with the annealing temperature is evident and confirmed that the symmetry is substantially independent of the temperature for the $\text{Eu}^{3+}@SiO_2$ sample while the R index decreases for the E10S-X samples when annealed at high temperatures. A decrease of the R index takes place specifically when the size of the $\text{Eu}_2\text{O}_3\text{-ZrO}_2$ s. s. nanoparticles become larger. Hence, the possibility of Eu^{3+} ions diffusing from the nanoparticles to the matrix was excluded, as corroborated by XRD analysis, so the PL spectra result to be mostly influenced by the size of the nanoparticles.

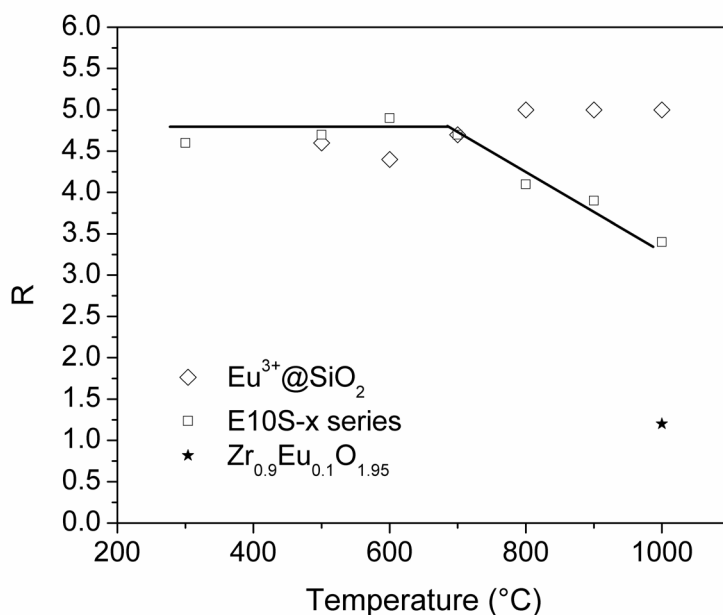


Figure 3.8 R index variation with the thermal treatment of the E10S and $\text{Eu}^{3+}@SiO_2$ series. The continuous line evidences the overall trend of the R index of the E10S series.

The PL excitation spectra for the same three representative samples are shown in Fig. 3.9. They displayed the typical Eu^{3+} absorption peaks and hence confirmed the aforementioned findings for PL emission.

An overall comparison of the relative PL emission intensities between the two systems (measured under identical experimental conditions) of the different samples after annealing is demonstrated in Fig. 3.10. As expected, the calculated values for the E10S-x series were higher than those obtained for the E03S-x series, as attributed to the higher Eu^{3+} content, even if emission intensity and Eu^{3+} content are not in linear relationship. As a general trend, the PL intensity increased with the increase in annealing temperature, reaching a maximum within the range of 600–700 °C, followed by a drastic reduction. This trend is best explained by considering the data in combination with the lifetime analysis of the photoluminescence emission.

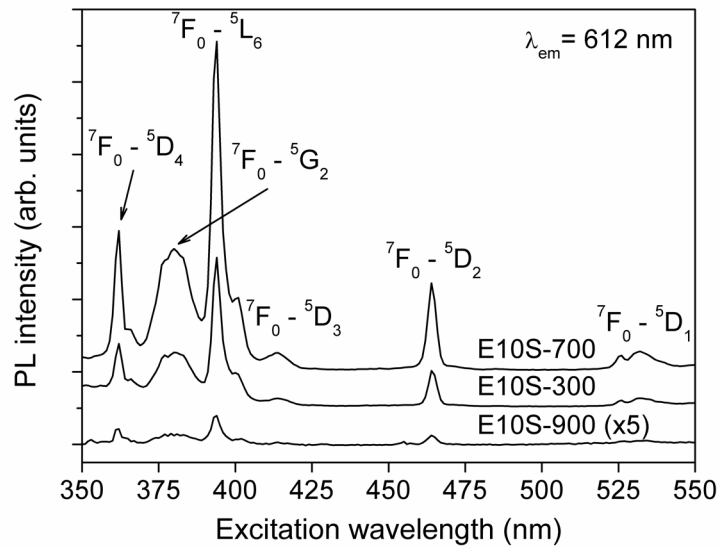


Figure 3.9 Luminescence excitation spectra at 612 nm emission for representative samples of the E10S-x series.

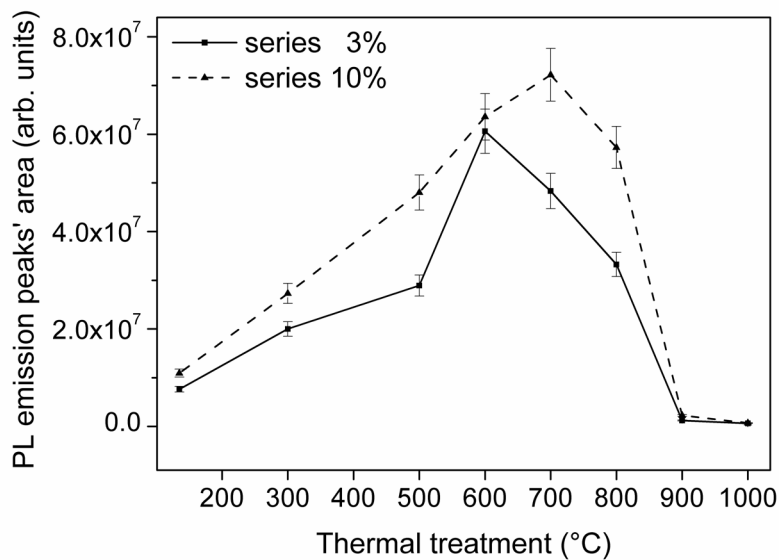


Figure 3.10 Comparison between the PL intensities (integral sum of the mean emission peaks' area under excitation at 393 nm) of E03S-x and E10S-x series of samples obtained after the thermal treatments.

The room temperature decay curves of the PL emission showed a non-exponential shape. Therefore, a double exponential fitting equation, which takes into account both the fast and the slow component of the decay, was applied:

$$I(t) = B + A_1 e^{-t/\tau_1} + A_2 e^{-t/\tau_2}$$

where B (background), A_1 , A_2 , τ_1 and τ_2 are the fitting parameters. It is worth mentioning that this provides a mathematical strategy, useful for the calculation of a representative effective lifetime τ_{obs} for each system, according to the following equation:

$$\tau_{obs} = \frac{\int_0^{\infty} t[I(t) - B]dt}{\int_0^{\infty} [I(t) - B]dt} = \frac{A_1 \tau_1^2 + A_2 \tau_2^2}{A_1 \tau_1 + A_2 \tau_2}$$

The non-exponential behavior of the luminescence decay curves could be reasonably attributed to the high degree of disorder, affecting the sites in which the Eu^{3+} ions are accommodated and as a consequence, to the different local crystalline field to which each of them would be exposed or to the presence of traps which act as quenching centers.

Fig. 3.11 reports some experimental decay curves and their fit.

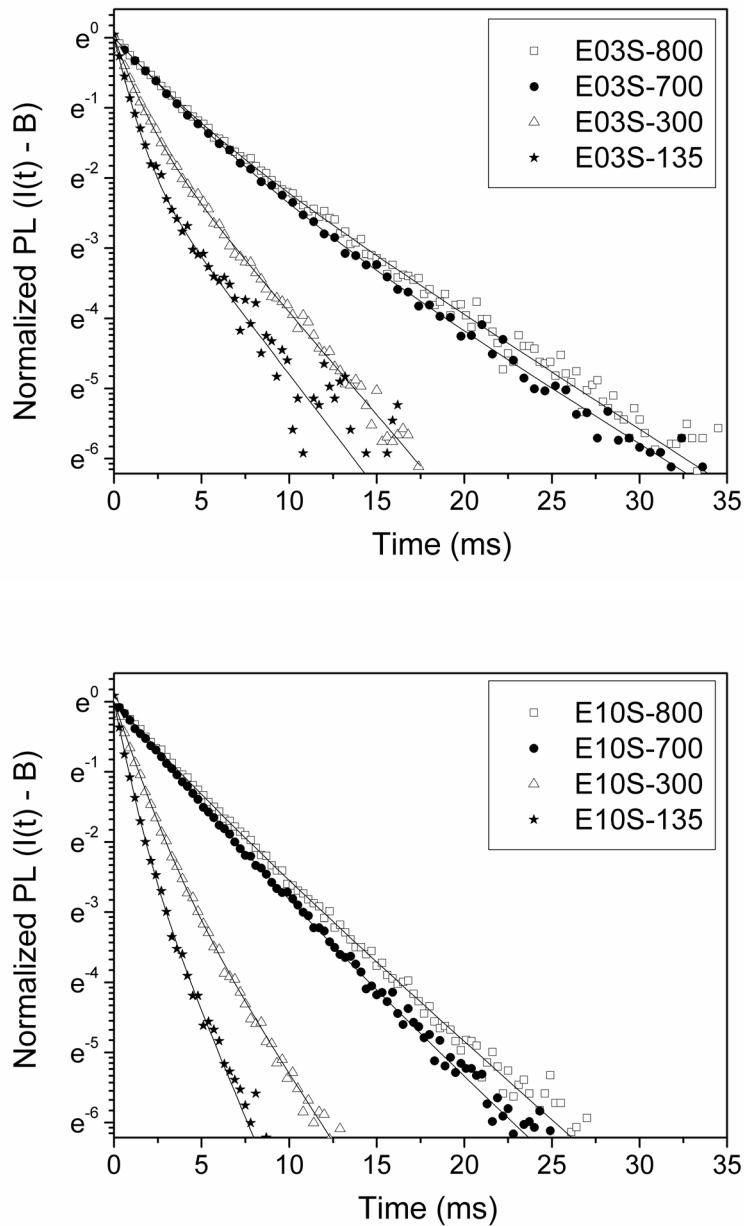


Figure 3.11 Time decay curves (MCSPC) of representative sample for both $\text{ZrO}_2:\text{Eu}^{3+}@\text{SiO}_2$ series (top: 3%, bottom: 10%), showing a monoexponential trend at 600-700 °C. Intensity corrected using the background.

The observed effective lifetimes (τ_{obs}) versus treatment temperature are depicted in Fig. 3.12. The results indicated that the E03S-x series showed

longer lifetimes with respect to the E10S-x series up to $x = 800$ °C. The reduced concentration quenching in the E03S-x series accounts for this phenomenon.

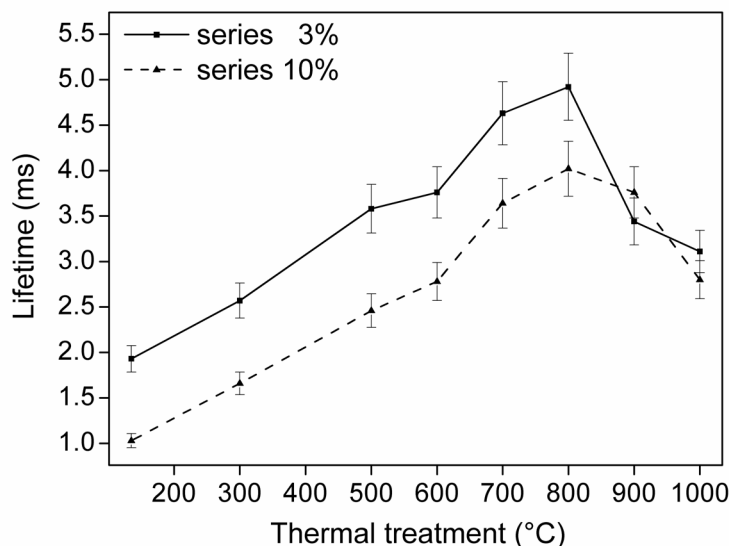


Figure 3.12 Comparison between the luminescence lifetimes (emission 612 nm, excitation 377 nm) of the two series (E03S-x and E10S-x).

As a general behavior, τ_{obs} increases with thermal treatments up to 800 °C for both series, reaching maximum values of about 4 – 5 ms. These high lifetimes are very close to the effective times measured for Eu doped bulk tetragonal zirconia ($\text{Eu}_{0.01}\text{Zr}_{0.99}\text{O}_{1.995}$)¹² and much longer than the lifetimes measured in silica that are 2 – 2.5 ms.¹³

This trend was in close agreement with the luminescence intensity values and hence ascribed to an improvement of the host material matrix up to 800 °C with regards to the reduction of defects or traps, *i.e.* the –OH groups that can provide non-radiative recombination paths.

For both series, E03S-x and E10S-x, the highest values were obtained for samples treated at 800 °C, nevertheless, long PL lifetimes were also observed for the samples treated at 700 °C, the temperature which corresponds with their highest emission intensity. Most importantly, at the optimal annealing

temperature (700 °C) the decay curves were very close to a single exponential function, and this is possibly explained not only by an improved homogeneity of the active sites for the rare earth ions but also by a reduction in quenching centers (defects, –OH groups) within the host matrix accounting for the high emission intensity.

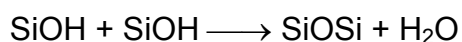
At a slightly higher temperature, this beneficial effect appeared to have been counterbalanced by an increase in particle size. Several authors^{14–16} observed an increase of the luminescence efficiency as a result of confinement effect on the migration of the long lifetime excitation between adjacent Eu^{3+} ions. Confining the excitation within a nanocrystal reduces the probability of the excitation coming into the vicinity of a quenching site. The steep growth of the particles size as the annealing temperature exceeds 800 °C can explain the drop of the luminescence and lifetime efficiency.

Concurrently, 700 °C was also established as the most suitable annealing temperature with regards to surface functionalization, as described in greater detail in the following part.

Influence of annealing temperature on the available superficial –OH groups for post-functionalization

Embedding the Eu^{3+} -doped ZrO_2 nanocrystals within an amorphous SiO_2 matrix not only creates a protective coating for the luminescent core particles, but also provides a layer of superficial hydroxyl groups, silanol groups, which may be further functionalized via a suitable post-grafting method. The availability and type of such superficial silanol groups varies according to the thermal treatment to which the samples are subjected. The surface of amorphous silica is known to contain three types of silanols: isolated, geminal and hydrogen-bonded.¹⁷ Activation of amorphous silica by thermal treatment in the range 100–180 °C removes the hydrogen-bonded water molecules from the surface,¹⁸ thus rendering the surface more reactive towards functionalization by exposing the isolated and geminal silanols which can form covalent linkages with silane coupling agents. Further treatment of silica at extremely high temperatures

(more than 727 °C) promotes complete dehydroxylation of the surface silanols according to reaction:¹⁷



thus producing siloxane groups on the surface.

In the case of the discussed samples, complete dehydroxylation would be undesirable for the following reasons: (1) the silica surface would lose its ability to undergo further modification in the absence of superficial silanols; and (2) the luminescence efficiency would be compromised if the thermal treatments were to exceed 800 °C, as discussed before. Therefore, the present study demonstrated that annealing at 700 °C for 12 h was suitable for the production of samples of optimal luminescence efficiency without causing complete surface dehydroxylation.

The presence of silanol groups (which represent the active sites for functionalization) on the samples' surface was monitored by DRIFT IR spectroscopy following the varying thermal treatments since isolated, geminal and hydrogen-bonded groups can be distinguished from their stretching vibrations. Fig. 3.13 depicts the area of interest in the IR spectra of several samples belonging to the E10S-x series. The presence of free silanols, which includes isolated and geminal groups, is evident from the sharp peak observed at 3750 cm⁻¹ in the samples treated between 135–800 °C. Exceeding this temperature showed a notable decrease in the presence of silanol groups (Fig. 3.13).

Hence, the presence of free silanols which can be functionalized, *i.e.* isolated and/or geminal silanol groups, is evident from the sharp peak observed at 3750 cm⁻¹ in the IR spectra of sample E10S-700 (Fig. 3.14), supported by the literature.^{17–19}

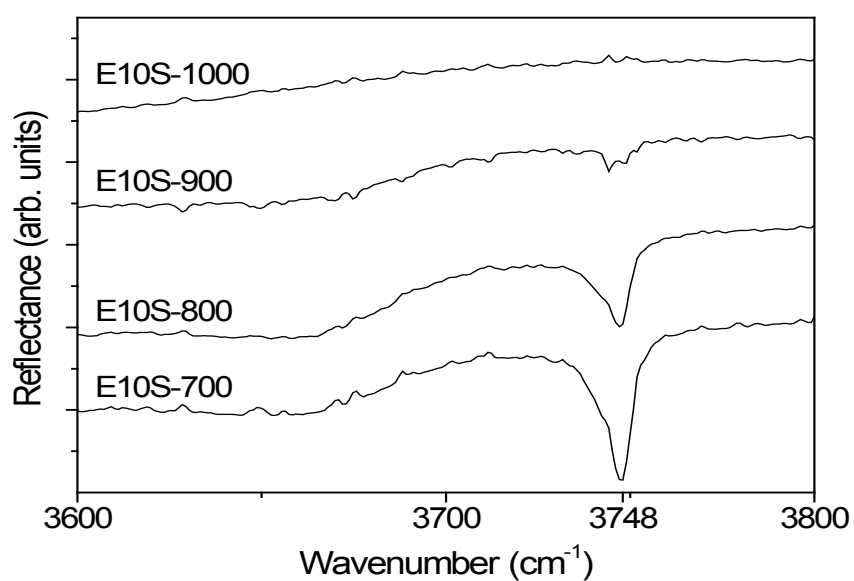


Figure 3.13 DRIFT IR of representative samples of the E10S-x series. Expansion of the region between 3600-3800 nm⁻¹ indicating the available silanol groups by varying annealing temperature.

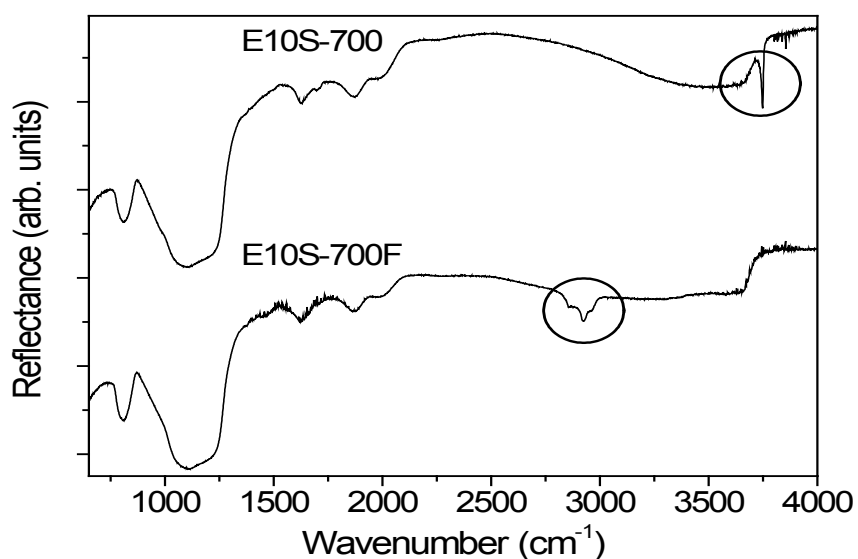


Figure 3.14 DRIFT spectra before and after functionalization with APTES (samples E10S-700 and E10S-700F respectively). Circled areas point out the sharp signal of active sites for functionalization (left) and the weak signals of aliphatic groups introduced with APTES (right).

The additional signals observed for the sample treated at 700 °C are in accordance with the expected spectral features of a calcined silica substance^a. These signals include the absorption bands in the region of 400–1600 cm⁻¹ which are attributed to the vibrational modes of the siloxane links.^{19,20} The asymmetric stretching (AS) vibrational mode of the siloxane bridges is visible in the region 1000–1200 cm⁻¹, while the symmetric stretching (SS) of the O atom along a line which bisects an axis formed by two Si atoms is notable at 810 cm⁻¹ (as opposed to 802 cm⁻¹ which would characterize the SS vibrational mode in un-activated silica sample).^{19,20}

In order to functionalize the silica surface for potential immobilization of biological molecules, the widely used silane coupling agent which contains a terminal amine group, (3-aminopropyl)triethoxysilane (APTES) was selected. APTES has already demonstrated broad utility for the covalent coupling of proteins onto the surface of silica materials.^{21–25}

Surface functionalization of the sample E10S-700 with APTES was achieved using the *n*-propylamine catalyzed method proposed by Chen and Brauer.³

The attachment of APTES on the silica surface was qualitatively confirmed by IR, whereby the sharp peak at 3750 cm⁻¹ was no longer present in the curve of sample E10S-700F providing evidence for functionalization (Fig. 3.14). It should be noted that these “free” silanol groups provide the point of attachment for APTES molecules. Furthermore, the introduction of aliphatic groups was clearly evidenced by the appearance of three signals at 2975 cm⁻¹, 2930 cm⁻¹ and 2900 cm⁻¹. The samples were thoroughly washed via repeated centrifugation and redispersion in organic solvent in order to remove any residual or unbound APTES, and subsequently dried *in vacuo* prior to IR measurements being recorded.

^a It should be noted that the presence of the luminescent material in the composite nanostructured system cannot be detected through IR spectroscopy.

3.1.3 Conclusions

This study was performed in order to investigate the influence of the thermal treatments on the: i) nanostructure, ii) luminescence properties, and iii) availability of superficial –OH groups for efficient surface functionalization on two systems comprising luminescent Eu^{3+} -doped zirconium oxide nanocrystals embedded in an amorphous silica matrix.

The two systems have been prepared with the same overall wt% composition of SiO_2 (75%) and $\text{Eu}_x\text{Zr}_{(1-x)}\text{O}_{(2-x/2)}$ s. s. (25%). Variation of the s. s. concentration to give $x = 0.03$ and 0.10 , respectively, provided the two systems for a comparative luminescence study. The incorporation of Eu^{3+} ions was achieved by the preparation of doped ZrO_2 nanoparticles, by the polyol method,¹ whereby Eu^{3+} ions substituted Zr^{4+} ions in the s. s., and were subsequently embedded in the silica matrix via the Stöber process.² Each system was treated at eight different temperatures, 135, 300, 500, 600, 700, 800, 900 and 1000 °C, for 12 h.

By a detailed X-ray diffraction analyses and transmission electron micrographs, combined with infrared spectroscopy and luminescence spectroscopy data, the optimum calcination temperature was found to be 700 °C for each series in terms of luminescence emission intensity, lifetime efficiency and post-functionalization efficiency with APTES.

3.2 $\text{ZrO}_2:\text{RE}^{3+}@ms\text{-SiO}_2$ (RE = Eu, Tb, Er/Yb) nanophosphors

The synthesis, annealing and surface functionalization of lanthanide doped luminescent nanoparticles with different rare earths as active optical centers were performed, in order to study and compare the structural and luminescence properties of three different systems, containing trivalent europium, terbium and erbium/ytterbium (as activator/sensitizer respectively) cations as active species

for the luminescence. The luminescent nanocomposite materials ($\text{ZrO}_2:\text{RE}^{3+}@ms\text{-SiO}_2$) were obtained by embedding, via a wet impregnation route, RE^{3+} -doped ZrO_2 nanocrystals into an amorphous silica matrix made of previously synthesized mesoporous nanoparticles. Therefore, here a different synthetic strategy was followed with respect to the $\text{ZrO}_2:\text{Eu}^{3+}@SiO_2$ nanophosphors obtained by means of the polyol method and the Stöber process (see § 3.1.1), even though the final materials will result quite similar.

A first series of four Eu(III)-doped samples ($\text{ZrO}_2:\text{Eu}^{3+}@ms\text{-SiO}_2$) was prepared: each sample of the series was meant to have the same nominal composition of the crystalline phase, with a 8% molar fraction of europium, *i.e.* $\text{Eu}_{0.08}\text{Zr}_{0.92}\text{O}_{1.96}$. This composition was selected on the basis of the results that were obtained in the previous study about the $\text{ZrO}_2:\text{Eu}^{3+}@SiO_2$ nanophosphors²⁶ (see also § 3.1.2), in which in a similar material good luminescent properties emerged both from the two europium molar fraction of the crystalline phase that were investigated, *i.e.* 3% and 10%. For this reason, an in-between value of 8% was chosen here. Hence, the varying parameter among the four samples of the series was the nominal fraction of crystalline phase on the total weight of the composite material, *i.e.* the amount of loaded Eu^{3+} -doped zirconia inside the silica matrix; a comparative investigation on the morphological, structural and luminescent properties of the red emitting nanocomposites was made through XRD, TEM and porosimetric analyses, photoluminescence measurements and IR spectroscopy. The four established nominal fractions were 0.1, 0.18, 0.25 and 0.33, to give samples named EuA, EuB, EuC and EuD respectively. These nominal fractions were quite similar to those that were employed on an analogous study on the same mesoporous silica host matrix loaded with magnetic nanocrystals²⁷ (see also § 4.1). The preparation of the four Eu(III)-doped samples is described afterwards, together with the surface functionalization with APTES of a selected sample of the series (EuB), in order to make it suitable for bio-labeling applications.

The same study was conducted on a second series of four Tb(III)-doped samples ($\text{ZrO}_2:\text{Tb}^{3+}@ms\text{-SiO}_2$), in which the only difference from the previous

series is represented by the presence of terbium instead of europium, which brings to a green, rather than red, emission. The same nominal composition ($\text{Tb}_{0.08}\text{Zr}_{0.92}\text{O}_{1.96}$) and nominal weight fractions of the crystalline phase for each sample (0.1, 0.18, 0.25 and 0.33 to give samples named TbA, TbB, TbC and TbD respectively) were used and an analogous characterization was performed.

Finally, a third system containing up-converting $\text{Er}^{3+}/\text{Yb}^{3+}$ -doped zirconia nanocrystals in a silica matrix was prepared. The nominal composition of the crystalline phase ($\text{Er}_{0.04}\text{Yb}_{0.1}\text{Zr}_{0.86}\text{O}_{1.93}$) was determined on the basis of previous studies conducted by my research group on an analogous nanocomposite system containing a 13% weight fraction of the same crystalline phase,²⁸ since the best luminescent properties came out from the aforementioned composition of the mixed oxide. However, since the up-converting properties of the previously studied nanocomposite material resulted to give a quite weak emission intensity, the nominal fraction of crystalline phase on the total weight of the sample was here increased from 13% to a very high value of 60%, in order to enhance the intensity of the emission. Even for the resulting sample (named Er/Yb), the morphological, structural and luminescent properties, together with its surface functionalizability were investigated.

3.2.1 Samples preparation

Synthesis of mesoporous SiO_2 nanoparticles (ms- SiO_2)

The synthesis of mesoporous silica nanoparticles was adapted from the procedure by Qiao et al.²⁹

Distilled water (145.2 mL, 8.07 mol), EtOH (22.8 mL, 0.39 mol) and CTAB (5.73 g, 15.72 mmol) were stirred at 60 °C. Following the complete dissolution of CTAB, as indicated by the transparency of the solution, 1.25 mL (18.08 mmol) of a 28 wt% NH_3 solution were added into the mixture under continued stirring and heating. After 30 minutes, TEOS (14.6 mL, 64.56 mmol) was added dropwise. Stirring at 60 °C was continued for 2 h, during which the clear solution gradually turned into a white suspension. The suspension was cooled to room

temperature and the solid product was recovered and repeatedly washed (initially in water and finally in EtOH) with five cycles of centrifugation (30 min at 9 krpm). The dried product was finally calcined in air for 2 h at 500 °C in order to remove the organic pore template, to give a final product consisting of ca. 3.5 g of mesoporous silica nanopowders.

Synthesis of $ZrO_2:Eu^{3+}@ms-SiO_2$ series: samples EuA-D

Four different samples were prepared with varying nominal fractions of impregnated luminescent mixed oxide inside the silica pore network. These fractions (respectively, 10, 18, 25 and 33% for samples EuA, EuB, EuC, EuD) correspond to the calculated nominal weight % (on the total weight of composite material) of $Eu_{0.08}Zr_{0.92}O_{1.96}$ which is expected to form following the thermal treatment.

Each sample was obtained by impregnating mesoporous SiO_2 nanoparticles (0.3 g) with an aqueous solution (4 mL) of $Eu(NO_3)_3 \cdot 5H_2O$ and $ZrOCl_2 \cdot 8H_2O$ salts, calculated according to the desired nominal composition and fraction of the crystalline phase. After stirring the mesoporous SiO_2 nanoparticles in salts solution overnight, the samples were dried by removing the solvent under reduced pressure. The impregnated silica powders were then annealed at 700 °C for 12 hours in air. The temperature was established on the basis of the results of previous investigation on the optimal annealing temperature for similar systems involving the same luminescent materials²⁶ (see also § 3.1.2) or the same protective silica matrix²⁷ (see § 4.1.2).

The respective quantities of $Eu(NO_3)_3 \cdot 5H_2O$ and $ZrOCl_2 \cdot 8H_2O$ salts used for the impregnation of SiO_2 to produce samples EuA-D are reported in Tab. 3.1.

Table 3.1 Total amount of $\text{Eu}(\text{NO}_3)_3 \cdot 5\text{H}_2\text{O}$ and $\text{ZrOCl}_2 \cdot 8\text{H}_2\text{O}$ used during impregnation for each sample of the $\text{ZrO}_2:\text{Eu}^{3+}@ms\text{-SiO}_2$ series.

sample	nominal %wt of $\text{Eu}_{0.08}\text{Zr}_{0.92}\text{O}_{1.96}$	total amount of $\text{Eu}(\text{NO}_3)_3 \cdot 5\text{H}_2\text{O}$	total amount of $\text{ZrOCl}_2 \cdot 8\text{H}_2\text{O}$
EuA	10%	0.009 g, 0.02 mmol	0.079 g, 0.24 mmol
EuB	18%	0.018 g, 0.04 mmol	0.156 g, 0.47 mmol
EuC	25%	0.027 g, 0.06 mmol	0.237 g, 0.72 mmol
EuD	33%	0.039 g, 0.09 mmol	0.351 g, 1.07 mmol

Synthesis of $\text{ZrO}_2:\text{Tb}^{3+}@ms\text{-SiO}_2$ series: samples TbA-D

The previously described procedure was exactly repeated for the preparation of the four Tb(III)-doped sample of the $\text{ZrO}_2:\text{Tb}^{3+}@ms\text{-SiO}_2$ series (with the only variation represented by the different lanthanide precursor, *i.e.* $\text{Tb}(\text{NO}_3)_3 \cdot 5\text{H}_2\text{O}$ in this case), and therefore is not reported again. In Tab. 3.2 the respective quantities of $\text{Tb}(\text{NO}_3)_3 \cdot 5\text{H}_2\text{O}$ and $\text{ZrOCl}_2 \cdot 8\text{H}_2\text{O}$ salts used for the impregnation of SiO_2 to produce samples TbA-D are shown.

Table 3.2 Total amount of $\text{Tb}(\text{NO}_3)_3 \cdot 5\text{H}_2\text{O}$ and $\text{ZrOCl}_2 \cdot 8\text{H}_2\text{O}$ used during impregnation for each sample of the $\text{ZrO}_2:\text{Tb}^{3+}@ms\text{-SiO}_2$ series.

sample	nominal %wt of $\text{Tb}_{0.08}\text{Zr}_{0.92}\text{O}_{1.96}$	total amount of $\text{Tb}(\text{NO}_3)_3 \cdot 5\text{H}_2\text{O}$	total amount of $\text{ZrOCl}_2 \cdot 8\text{H}_2\text{O}$
TbA	10%	0.009 g, 0.02 mmol	0.079 g, 0.24 mmol
TbB	18%	0.018 g, 0.04 mmol	0.155 g, 0.47 mmol
TbC	25%	0.027 g, 0.06 mmol	0.236 g, 0.72 mmol
TbD	33%	0.040 g, 0.09 mmol	0.349 g, 1.06 mmol

Synthesis of $ZrO_2:Er^{3+}/Yb^{3+}@ms-SiO_2$: sample Er/Yb

The Er(III)/Yb(III)-doped sample was prepared with a 60% nominal fraction of impregnated luminescent mixed oxide inside the silica pore network. This fraction correspond to the calculated nominal weight % (on the total weight of the composite material) of $Er_{0.04}Yb_{0.1}Zr_{0.86}O_{1.93}$ which is expected to form after the thermal treatment.

The sample was obtained by impregnating mesoporous SiO_2 nanoparticles (0.775 g) with an aqueous solution (10 mL) of $Er(NO_3)_3 \cdot 5H_2O$ (0.154 g, 0.35 mmol), $Yb(NO_3)_3 \cdot 5H_2O$ (0.391 g, 0.87 mmol) and $ZrOCl_2 \cdot 8H_2O$ (2.459 g, 7.48 mmol) salts, calculated according to the desired nominal composition and fraction of the crystalline phase. After stirring the mesoporous SiO_2 nanoparticles in salts solution overnight, the sample was dried by removing the solvent under reduced pressure. The impregnated silica powder was then annealed at 1000 °C for 1 hour in air. The temperature was established on the basis of the results of previous investigation conducted by my research group on the optimal annealing temperature for similar systems involving the same luminescent material.²⁸ In fact, with respect to europium and terbium ions, erbium ions are much more sensitive to moisture and -OH groups, whose presence can produce undesirable quenching effects, and therefore an elevated annealing temperature (more than 700 °C which is enough for europium or terbium doped samples) is necessary to reduce as much as possible their presence in the material in order to preserve the luminescence; on the other hand, such a high temperature, as previously demonstrated (see § 3.1.2), could strongly reduce or completely hinder the presence on the silica surface of isolated or geminal silanols, which act as active sites for the functionalization. To avoid or limit this drawback, the duration of the thermal treatment was decreased from 12 to 1 h.

Surface functionalization of $ZrO_2:RE^{3+}@ms-SiO_2$ with APTES

The general procedure for surface functionalization with APTES,²⁶ which has already been described (see § 3.1.1), was here applied to samples EuB, TbB

(selected as most suitable samples of their respective series) and Er/Yb, to give functionalized samples EuBF, TbBF and Er/YbF.

3.2.2 Results and discussion

Mesoporous SiO₂ nanoparticles (ms-SiO₂)

Thermogravimetric analysis was performed in an air atmosphere for the as obtained dry SiO₂ nanoparticles in order to establish the ideal calcination temperature for removal of the organic pore directing template. From the TG curve (Fig. 3.15), 500 °C was chosen as optimal since most of the weight loss occurred prior, suggesting significant oxidative removal of the organic template. Hence, treatment at 500 °C was expected to give a high degree of mesoporosity in the SiO₂.

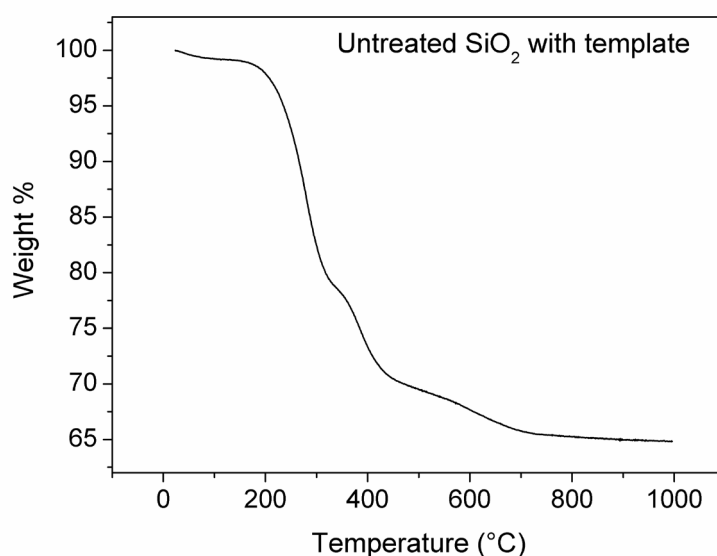


Figure 3.15 TG analysis in air atmosphere of dried SiO₂ nanoparticles containing CTAB organic surfactant as a pore template.

The thermograph (Fig. 3.15) indicates that increasing the calcination temperature above 500 °C (*i.e.* 800 or 1000 °C for example) would promote

complete oxidative removal of the template; however, detrimentally it would also initiate a sinterization process that would strongly decrease the mesoporosity of the material by pore shrinkage. Therefore, calcination at 500 °C was considered to be a good compromise for significant decomposition of the organic template whilst avoiding potential sinterization.

TEM micrographs (Fig. 3.16) of the calcined SiO₂ showed nanoparticles with a spheroidal shape. The sample depicted in Fig. 3.16 indicates the presence of both isolated and aggregated particles with relative sizes of around 60-70 nm in diameter. The mesoporosity of the SiO₂ nanoparticles calcined at 500 °C, clearly visible in TEM micrographs, was further characterized and corroborated by N₂ adsorption/desorption measurements.

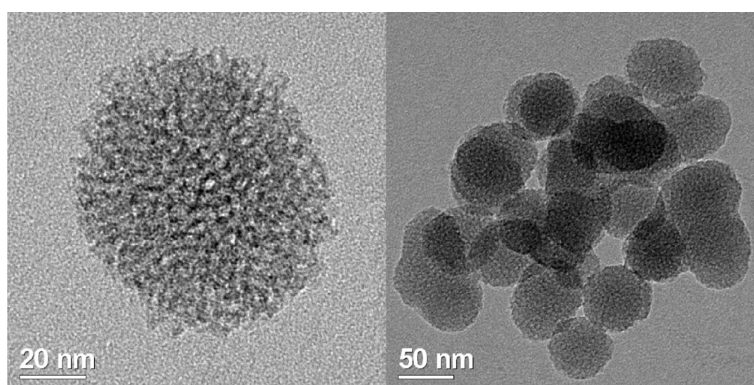


Figure 3.16 TEM micrographs of calcined mesoporous SiO₂ nanoparticles.

The N₂ adsorption/desorption isothermal curve of the ms-SiO₂ (Fig. 3.17) featured the typical shape of a mesoporous material (type IV isothermal according to IUPAC classification³⁰). From the same measurement, the surface area of the material could be evaluated through the B.E.T. method.³¹ The measured surface area resulted to be 980 ± 10 m²/g, which corresponds to a relevant level of mesoporosity in the material.

The pore size distribution for the calcined SiO₂ was determined by using the B.J.H. method.³² The corresponding curve (Fig. 3.18) showed a relatively narrow distribution of pore diameter, with the peak maximum centered at 2.8 nm, herein considered as the average value for pore diameter. The total pore

volume of the material was found to be *ca.* 1.3 cm³/g. This latter value further confirmed the very high mesoporosity of the material, and therefore the extensive availability of accessible internal surface area for potential embedding of various materials via impregnation methods.

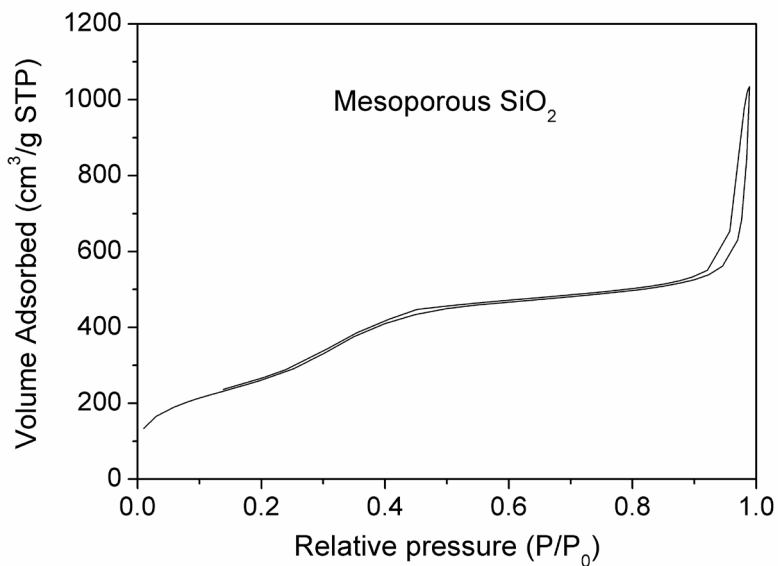


Figure 3.17 N₂ adsorption/desorption isothermal curves of calcined mesoporous SiO₂ nanoparticles.

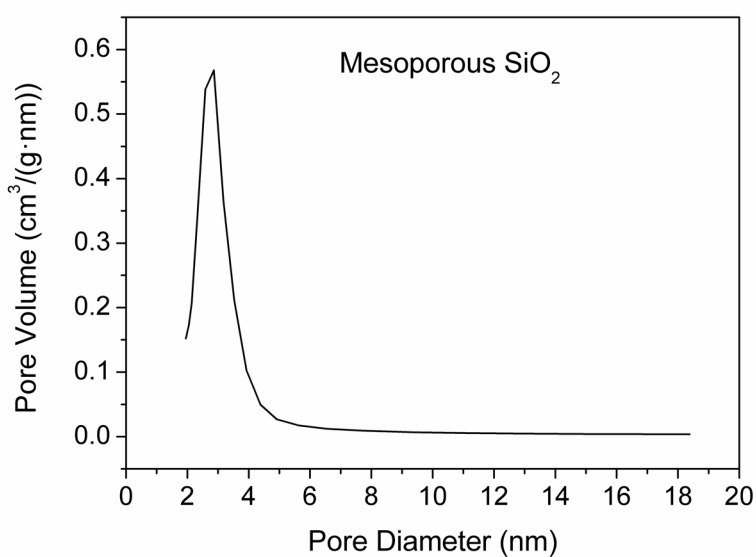


Figure 3.18 Pore size distribution curve of calcined mesoporous SiO₂ nanoparticles.

ZrO₂:Eu³⁺@ms-SiO₂ series: samples EuA-D

The ZrO₂:Eu³⁺@ms-SiO₂ series of samples was prepared with varying nominal weight fractions of ZrO₂:Eu³⁺ impregnated in mesoporous SiO₂ (see Tab. 3.1). On the basis of pore volume availability, four samples (EuA-D) were obtained by varying the amount of salts in the impregnating solutions, thereby filling the pores to varying degrees.

XRD analysis was performed on the samples EuA-D after the thermal treatment at 700 °C (Fig. 3.19). Hereby, the efficiency of the impregnation method was evaluated through the structural investigation of the resulting composite material, comprising, for all the four samples, amorphous SiO₂ and a crystalline cubic/tetragonal zirconia phase, as depicted by the aforementioned figure. This figure shows the XRD patterns of the four samples together with the amorphous curve of the undoped ms-SiO₂ and the pattern of cubic zirconia crystalline structure correspondent to sample E10-1000 in the previous study on Eu³⁺-doped zirconia in silica (see Fig 3.2a in § 3.1.2) as reference.

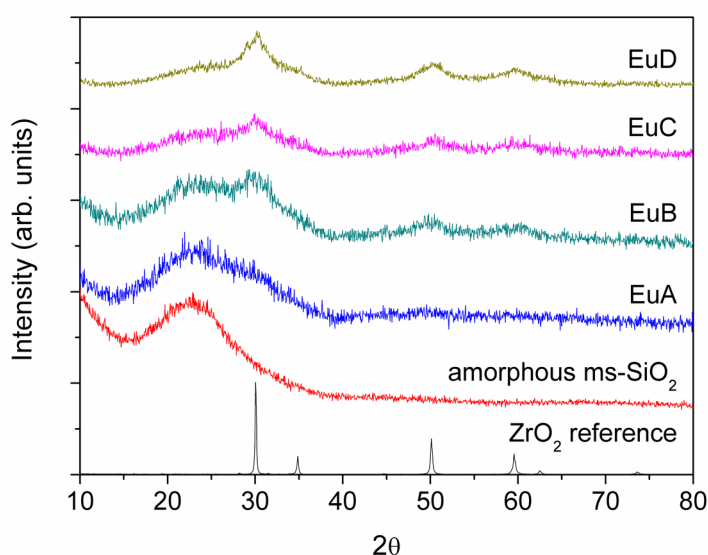


Figure 3.19 XRD patterns of: ZrO₂:Eu³⁺@ms-SiO₂ series of samples, calcined mesoporous SiO₂, cubic ZrO₂ reference from sample E10-1000 (see § 3.1.2).

Hence, as expected, all the samples presented the same crystalline structure, in agreement with the unvaried nominal composition ($\text{Eu}_{0.08}\text{Zr}_{0.92}\text{O}_{1.96}$) of the crystalline phase along the series. The cubic/tetragonal zirconia, which is the host matrix for the europium ions, showed the same reflections that appeared in the previously discussed $\text{ZrO}_2:\text{Eu}^{3+}@\text{SiO}_2$ samples (see Fig. 3.2a), being the rare earth molar fractions quite similar (8 and 10%) in the two cases. In theory, a rare earth fraction of 8% is a threshold value, for which the zirconia could be stabilized both in the tetragonal and in the cubic form, but these two different forms cannot be distinguished in such small nanocrystals due to the very similar diffraction patterns of the pure bulk phases and to the broadness of the peaks in the composite and therefore the experimental XRD patterns of the composites are consistent with the presence of one or both the phases.

The only change among the series of samples EuA-D is therefore related to the peaks' intensity, which follows the gradual increase in the weight fraction of crystalline material in the composite from sample EuA to sample EuD. Moreover, a qualitative comparison of the main peaks' width can provide useful information about the nanostructural quality of the examined composites, as for the analogous investigation on the $\text{FeO}_x@\text{ms-SiO}_2$ series of samples (see § 4.1.2). In fact, apart from the less doped EuA sample which showed very weak crystalline signals that hardly emerge from the amorphous background curve and whose analysis is therefore rendered difficult, all the samples seem to be characterized by a constant width of the main crystalline peaks, which appear quite broad with respect to those in the reference pattern of cubic zirconia. This result indicates that the crystallites' size, which is inversely proportional to the FWHM (Full Width at Half Maximum) of the peaks, is relatively small. Considering that the same thermal treatment was applied to each sample, the small dimensions of the crystallites would also be consistent with the presence of the crystalline luminescent phase inside the silica pores, that would evidence a good structural quality of the composite. In fact, the average pore size determined by B.E.T. was 2.8 nm. Therefore, assuming adequate impregnation

of the salts solutions, the small pores can limit the growth of the crystals within them, to give a regularly structured nanocomposite material. Hence, despite the different nominal levels of loaded material into the silica host matrix, the XRD analysis suggests a nanostructural homogeneity and regularity in all the series of samples (in contrast with the findings of the investigation on the $\text{FeO}_x@ms\text{-SiO}_2$ series, in which the most doped samples presented a fraction of loaded material that remained outside the silica matrix).

The nanostructural regularity that seems to characterize the whole series of samples was confirmed by the TEM analysis. Some representative TEM micrographs at different magnifications are reported in Fig. 3.20a-f. Impregnated silica nanoparticles with small (*ca.* 3 nm) embedded nanocrystals were observed in the four samples EuA-D, of course with an increasing density of nanocrystals inside the silica nanoparticles from sample A to sample D (Fig. 3.20c-f). The EDS elemental analysis that was performed on some impregnated nanoparticles (Fig. 3.20g and h) confirmed the nature of the observed nanocrystals, since both the spectra showed the typical signals of Si, O, Zr and Eu (the latter was weak due to the low fraction of europium in the material), which are attributed to the amorphous SiO_2 matrix and the Eu^{3+} -doped zirconia nanocrystals. Samples EuC and EuD presented also a few isolated structure (not shown) which appeared as foreign bodies with respect to the silica matrix. The EDS analysis identified the presence of Ca, Al and Si and therefore these irregular structures were considered as impurities that should not affect the overall quality of the samples. Most importantly, no traces of Zr and Eu were found externally to the silica nanoparticles in any of the four composite samples, as a confirmation of their nanostructural regularity and hence as a proof of the good efficiency of the impregnation method.

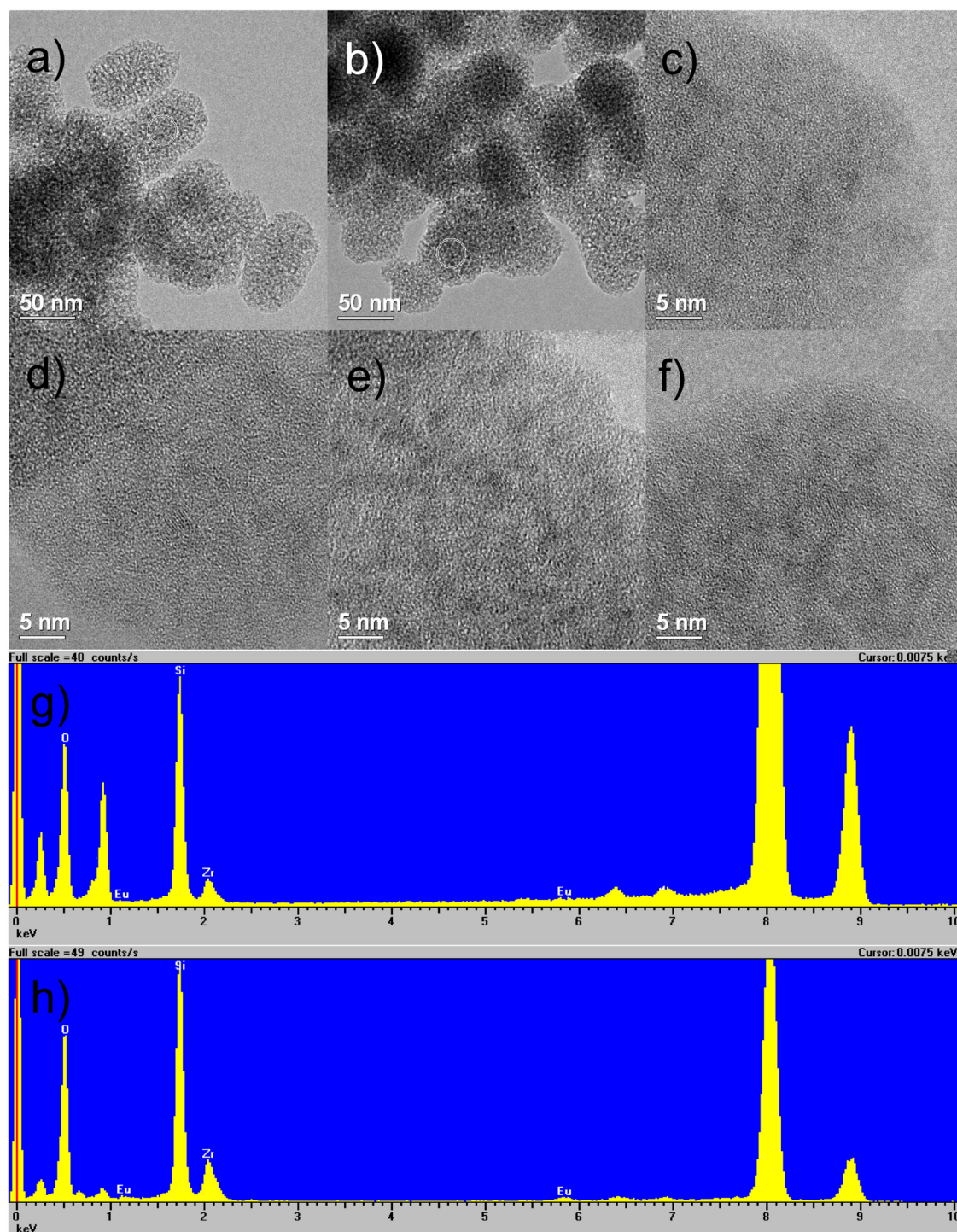


Figure 3.20 Representative TEM micrographs at different magnifications of samples EuA-D: (a,b) samples EuB and euD; (c-f) samples EuA-D respectively; (g,h) EDS analyses of circled areas (a,b) of samples EuB and euD.

N₂ adsorption/desorption measurements were performed for samples EuA-D (Fig. 3.21). All the curves display the typical shape of a mesoporous material (type IV isothermal), like the curve of the undoped ms-SiO₂ (see Fig 3.17), notwithstanding the impregnation and subsequent thermal treatment.

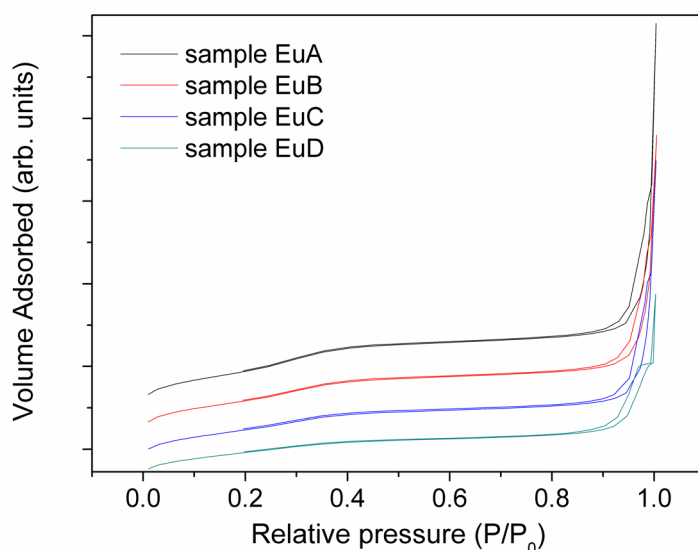
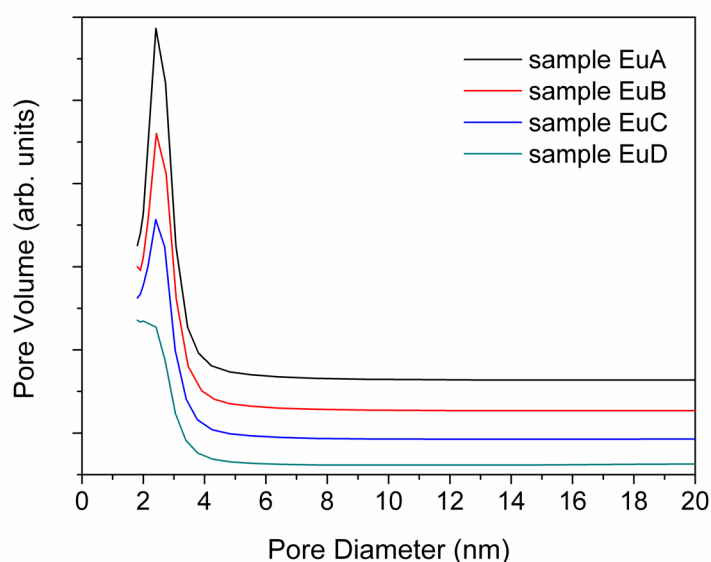


Figure 3.21 N₂ adsorption/desorption isothermal curves of ZrO₂:Eu³⁺@ms-SiO₂ series of samples.

The curves demonstrate that the four composites retained mesoporosity even with the presence of embedded ZrO₂:Eu³⁺ nanocrystals, though an expected decrease of the mesoporosity with the increasing fraction of loaded materials was measured. In particular, both the values for specific surface area and pore volume gradually decreased with the increasing loading (Tab. 3.3). For example, in sample EuD they are a 30-35% lower than the original mesoporous SiO₂. Contrastingly, the pore size distributions did not reveal any relevant changes throughout the series (Fig. 3.22), being the curves' shape and the average pore diameter (*ca.* 2.8 nm) unvaried. The only exception was represented by the different shape of the initial part of the curve in sample EuD (in the x range between 2 and 2.8 nm).

Table 3.3 Surface area and pore volume of $\text{ZrO}_2:\text{Eu}^{3+}@ms\text{-SiO}_2$ samples EuA-D.

sample	surface area (m^2/g)	pore volume (cm^3/g)
EuA	850 ± 10	1.1
EuB	770 ± 10	1.0
EuC	696 ± 7	1.0
EuD	613 ± 3	0.9

**Figure 3.22** Pore size distribution curves of $\text{ZrO}_2:\text{Eu}^{3+}@ms\text{-SiO}_2$ series of samples.

This anomalous behavior seems to indicate the formation of an additional microporosity in the sample, such as microfissures that could be attributed to a partial breaking of the silica network structure, possibly caused by the stresses due to the nanocrystals growth inside the pores. Nevertheless, this phenomenon, as will be shown later, did not occur in any other sample or any other series with identical or similar nominal loading levels, neither in the following series of terbium-doped samples $\text{ZrO}_2:\text{Tb}^{3+}@ms\text{-SiO}_2$, nor in the

$\text{FeO}_x@\text{ms-SiO}_2$ series of samples (see § 4.1.2). For this reason, the formation of additional microporosity in sample EuD seemed to be an isolated and accidental event. Anyway, it should be noticed that even in this sample the pore volume value associated to the pores with average diameter (i.e. the y value at 2.8 nm) decreased with respect to the previous samples, in accordance with the general trend along the series. Overall, the porosimetric results for the $\text{ZrO}_2:\text{Eu}^{3+}@\text{ms-SiO}_2$ series (EuA-D) proved valuable, since the retained mesoporosity in the loaded samples could potentially allow for further modification of the composites. For example, additional loading of magnetic materials, drugs or biomolecules would allow for the generation of multifunctional composite materials.

Besides the nanostructural and morphological characterization, the optical properties of the $\text{ZrO}_2:\text{Eu}^{3+}@\text{ms-SiO}_2$ series of samples were also investigated.

The photoluminescence (PL) emission spectra of samples EuA-D are reported in Fig. 3.23.

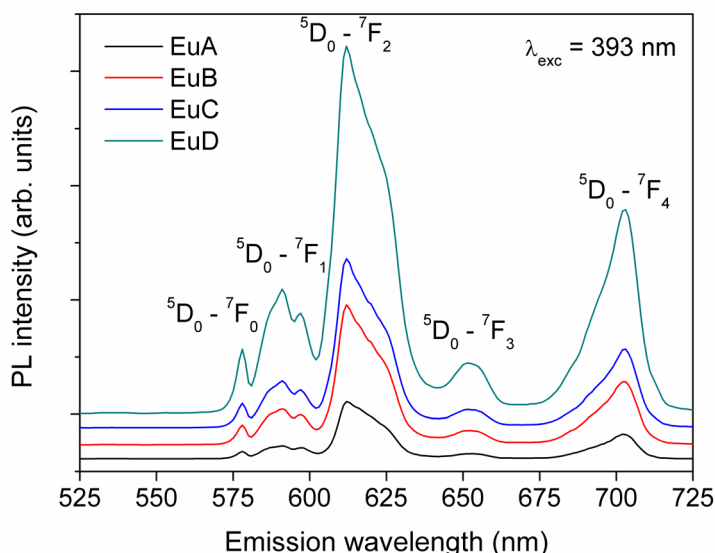


Figure 3.23 Luminescence emission spectra under 393 nm excitation for samples EuA-D of the $\text{ZrO}_2:\text{Eu}^{3+}@\text{ms-SiO}_2$ series.

All the four spectra presented the same profile that appeared in the previous study on the $\text{ZrO}_2:\text{Eu}^{3+}@\text{SiO}_2$ series (see Fig. 3.5), *i.e.* the five emission peaks that are related to the energy level structure of the Eu^{3+} ions. The shape of the peaks, as well as their relative intensities remained unvaried along the whole series of samples, while only the overall intensity of the emission resulted to change from sample to sample. As expected, also in this case the maximum of the emission was centered at 612 nm, as a confirmation that the Eu^{3+} luminescent centers are hosted by the zirconia crystalline structure and not directly embedded in a silica matrix, otherwise, as discussed before, the maximum should have appeared at 617 nm (see Fig. 3.7). Nevertheless, the small size (less than 3 nm) of the Eu(III) -doped zirconia nanocrystals in these composite materials caused a strong influence of the silica matrix on the optically active lanthanide ions. The result is an inhomogeneous line broadening with respect to bulk crystals and a consequent absence, in the examined spectra, of typical features of the zirconia structure (see Fig. 3.6), similarly to what was found for the majority of the samples belonging to the previously studied $\text{ZrO}_2:\text{Eu}^{3+}@\text{SiO}_2$ series. The relevant analogy between these two classes of composite materials is also depicted by Fig. 3.24, which shows the normalized emission spectra of sample EuC and sample E10S-700, *i.e.* two composites that were synthesized through different procedures but with the same nominal fraction of Eu(III) -doped zirconia (25%wt), same annealing temperature (700 °C) and very similar composition of the crystalline phase ($\text{Eu}_{0.08}\text{Zr}_{0.92}\text{O}_{1.96}$ and $\text{Eu}_{0.1}\text{Zr}_{0.9}\text{O}_{1.95}$ respectively). The two PL spectra are almost identical, as evidenced by their superposition. In particular, the index R (see § 3.1.2) values almost coincided, thus indicating a similar site symmetry of the Eu^{3+} ion in both the samples and in general in all the EuA-D series, since, as mentioned before, the shape of the spectra and the relative intensities (therefore the R values too) were quite constant along the series. On the basis of the consideration that was done while discussing the index R variation in the previous study, the constancy of the latter in this series of samples can be seen

as a further evidence of the unvarying size of the $\text{Eu}_2\text{O}_3\text{-ZrO}_2$ s. s. nanocrystals among the EuA-D samples, as corroborated by the XRD and TEM analyses.

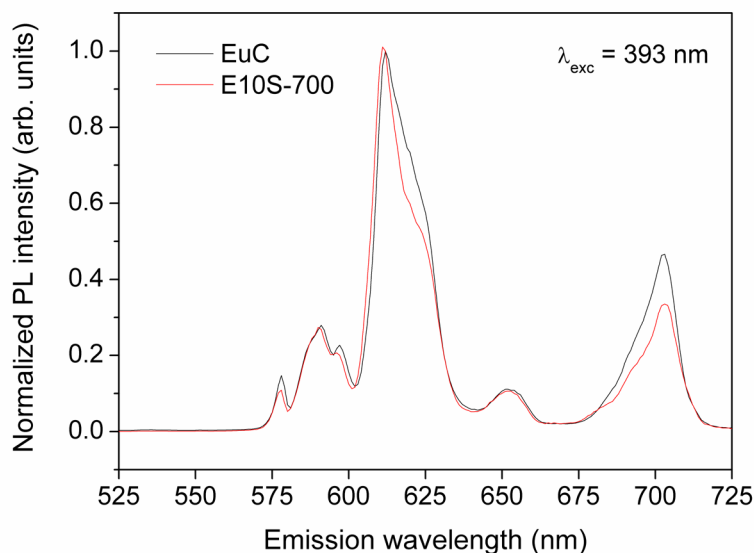


Figure 3.24 Luminescence emission spectra under 393 nm excitation for samples EuC of the $\text{ZrO}_2\text{:Eu}^{3+}\text{@ms-SiO}_2$ series and sample E10S-700 of the $\text{ZrO}_2\text{:Eu}^{3+}\text{@SiO}_2$ series. Both spectra are normalized at the maximum emission (612 nm).

The PL excitation spectra for the same four samples displayed the typical Eu^{3+} absorption peaks and hence confirmed the aforementioned findings for PL emission. Apart from the intensities, the spectra did not show any significant differences one another and with respect of those of the $\text{ZrO}_2\text{:Eu}^{3+}\text{@SiO}_2$ series; therefore, only the excitation spectrum of sample EuB is reported in Fig. 3.25 as an example.

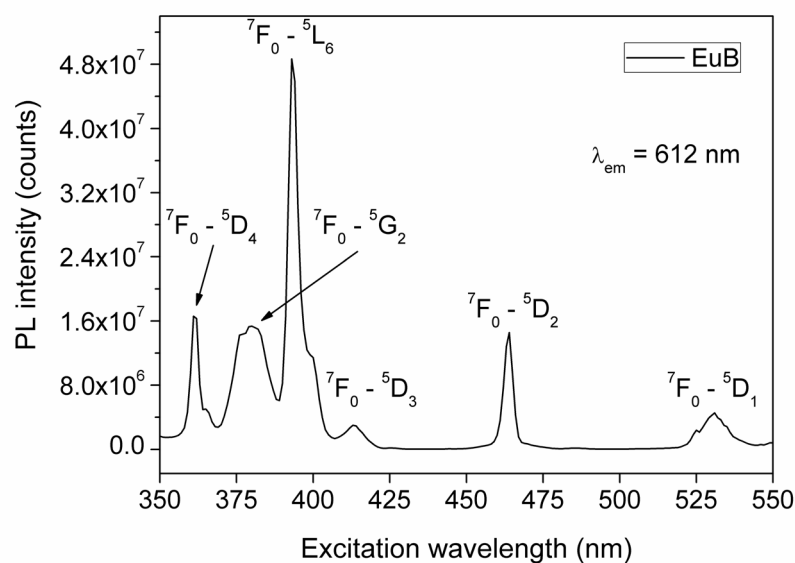


Figure 3.25 Luminescence excitation spectrum at 612 nm emission for the representative sample EuB.

An overall comparison of the relative PL emission intensities between the four samples of the series is demonstrated in Fig. 3.26. For each sample, the integral sum of the main emission peaks' area was calculated. As a general trend, the PL intensity increased with the increase in loaded fraction of $\text{ZrO}_2:\text{Eu}^{3+}$ from sample EuA to EuD, as expected since the intensity of the emitted signal in the sample is related to its general Eu^{3+} content. Anyway, all the four materials showed a satisfying luminescence emission that could make them suitable for labeling or imaging applications in the biological field.

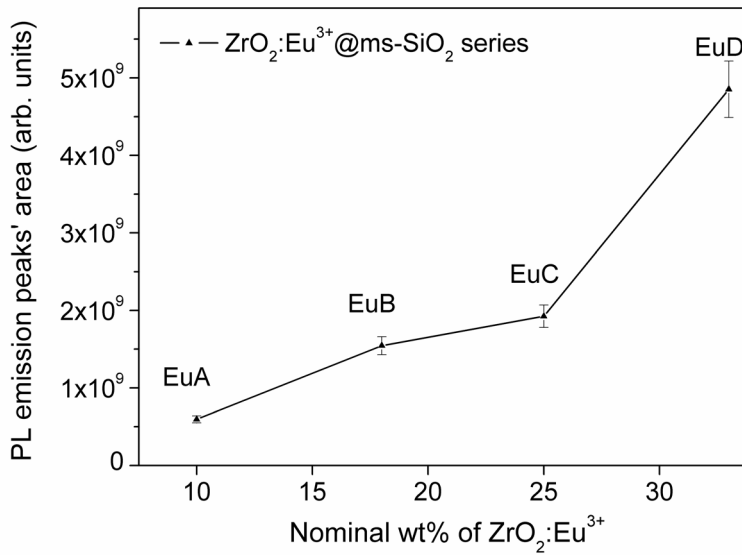


Figure 3.26 Comparison between the PL intensities (integral sum of the mean emission peaks' area under excitation at 393 nm) of the ZrO₂:Eu³⁺@ms-SiO₂ series of samples.

For all the EuA-D samples, the room temperature decay curves of the PL emission showed a non-exponential shape, similarly to what was found for the ZrO₂:Eu³⁺@SiO₂ series (see § 3.1.2). Therefore, also in this case the double exponential fitting equation:

$$I(t) = B + A_1 e^{-t/\tau_1} + A_2 e^{-t/\tau_2}$$

was applied for the calculation of a representative effective lifetime τ_{obs} for each sample. As discussed before, the non-exponential behavior of the luminescence decay curves could be reasonably attributed to the high degree of disorder affecting the sites in which the Eu³⁺ ions are accommodated and as a consequence, to the different local crystalline field to which each of them would be exposed, or to the presence of traps which act as quenching centers.

Fig. 3.27 presents the experimental decay curves and their fit, all shifted along the Y axis for a better visualization.

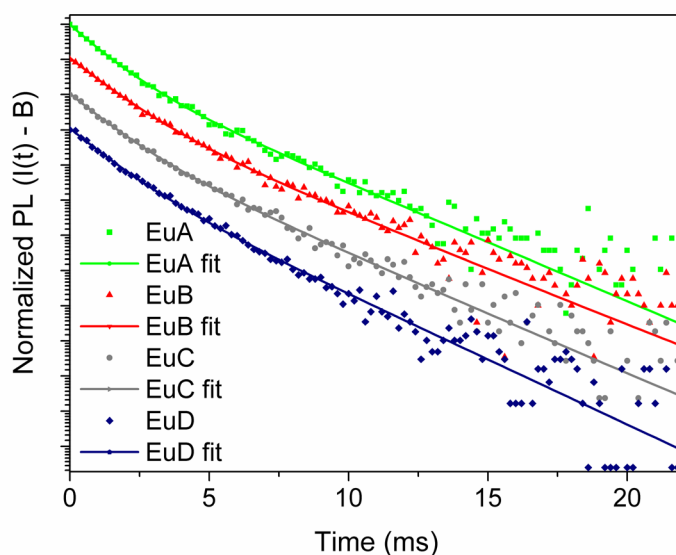


Figure 3.27 Time decay curves (MCSPC) and respective fits of the $\text{ZrO}_2:\text{Eu}^{3+}@\text{ms-SiO}_2$ series of samples. Intensity corrected using the background.

The observed effective lifetimes (τ_{obs}) are reported in Tab. 3.4.

Table 3.4 Luminescence lifetimes (emission 612 nm, excitation 377 nm) of the $\text{ZrO}_2:\text{Eu}^{3+}@\text{ms-SiO}_2$ series of samples EuA-D.

sample	lifetime (ms)
EuA	2.1 ± 0.2
EuB	2.2 ± 0.2
EuC	2.1 ± 0.2
EuD	2.0 ± 0.2

The results indicated that the EuA-D samples in general showed shorter lifetimes (around 2 – 2.2 ms) with respect to the E03S-x and E10S-x series that were discussed before (see § 3.1.2), while, considering the annealing

temperature of 700 °C and according to the concentration quenching effect, some intermediate values between those of sample E03S-700 (with 3% molar Eu content) and sample E10S-700 (with 10% molar Eu content) could be expected for samples EuA-D (all with 8% molar Eu content).

As a general behavior, the τ_{obs} value remained almost constant along the series and this was expected since, contrary to what happens for the emission intensity, the increasing fraction of loaded luminescent material in the composite does not provide an increase of the effective lifetime, whose value is usually strongly related to the s. s. composition (*i.e.* Eu^{3+} content in the crystalline structure). The latter therefore proved to remain effectively constant along the series. Nevertheless, the τ_{obs} values of the EuA-D samples resulted to be more similar to the usual lifetimes measured in silica, that are 2 – 2.5 ms,¹³ than to the higher values of 4 – 5 ms that appeared in the previous study and were close to the effective times measured for Eu-doped bulk tetragonal zirconia ($\text{Eu}_{0.01}\text{Zr}_{0.99}\text{O}_{1.995}$).¹² However, the hypothesis of the presence of europium ions that are directly hosted in the silica structure rather than in s. s. with the zirconia was excluded by the previously discussed evidences from the PL spectra (maxima at 612 nm rather than 617 nm in Fig. 3.23).

The lifetime values are therefore consistent with the presence of defects or traps, *i.e.* the –OH groups that can provide non-radiative recombination paths which are responsible for a decrease of the luminescent properties.

However, all the findings of the optical characterization not only evidenced the satisfying luminescent properties of the samples, but also confirmed that the nanostructure of the composite series was the desired one, *i.e.* a nanocrystalline structure consisting in a $\text{Eu}_2\text{O}_3\text{-ZrO}_2$ s. s. with an unvaried composition and embedded, with different loading levels, into a silica matrix.

$\text{ZrO}_2\text{:Tb}^{3+}\text{@ms-SiO}_2$ series: samples TbA-D

The $\text{ZrO}_2\text{:Tb}^{3+}\text{@ms-SiO}_2$ series of samples was prepared with the same nominal weight fractions of $\text{ZrO}_2\text{:Tb}^{3+}$ impregnated in mesoporous SiO_2 that were adopted in the correspondent samples of the $\text{ZrO}_2\text{:Eu}^{3+}\text{@ms-SiO}_2$ series

(see Tab. 3.2). Hence, the only difference between the two series of materials is represented by the employed trivalent lanthanide ions, since even the nominal composition of the crystalline phase ($\text{RE}_2\text{O}_3\text{-ZrO}_2$ s. s.) was not modified. As a consequence, no relevant changes in the nanostructural and morphological properties of the composites were expected with respect to the previous series, since the substitution of Eu^{+3} with Tb^{3+} does not imply any important effects on the nanostructure.

The results of the XRD, TEM and porosimetric analyses confirmed the aforementioned prediction, since the crystalline, morphological and porosimetric properties of the four samples TbA-D coincided with those of their correspondent samples EuA-D, both in terms of the variation along the series and with respect to the same undoped silica matrix ms-SiO₂. Therefore, the high nanostructural similarity of the two series of samples can be seen as a proof of the reproducibility that characterizes the impregnation process. To avoid repetitions, the XRD patterns, TEM micrographs, EDS spectra, N₂ adsorption/desorption and pore size distribution curves are not shown and discussed again here, since their aspect totally reminded the features that were depicted by Figs 3.19, 3.20, 3.21 and 3.22 respectively. Tab. 3.5 displays the values for specific surface area and pore volume, which both gradually decreased with the increasing level of loaded material also in this series of samples.

Table 3.5 Surface area and pore volume of $\text{ZrO}_2\text{:Tb}^{3+}\text{@ms-SiO}_2$ samples TbA-D.

sample	surface area (m ² /g)	pore volume (cm ³ /g)
TbA	815 ± 7	1.0
TbB	740 ± 10	0.9
TbC	680 ± 10	0.8
TbD	600 ± 7	0.7

Following the valuable results of the nanostructural and morphological characterization, the optical properties of the $\text{ZrO}_2:\text{Tb}^{3+}@m\text{s-SiO}_2$ series of samples were also investigated.

The photoluminescence (PL) emission spectra of samples TbA-D are reported in Fig. 3.28.

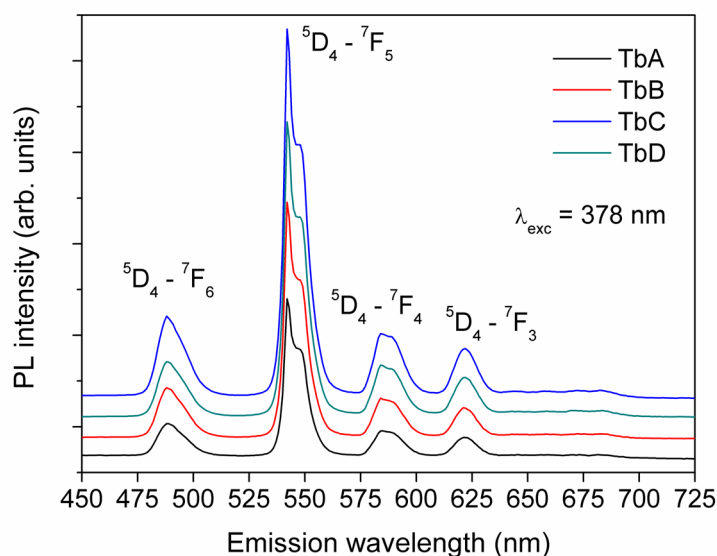


Figure 3.28 Luminescence emission spectra under 378 nm excitation for samples TbA-D of the $\text{ZrO}_2:\text{Tb}^{3+}@m\text{s-SiO}_2$ series.

All the four spectra presented the same characteristic profile of trivalent terbium, *i.e.* the four emission peaks observed at 488, 542 (maximum emission), 584 and 622 nm that are related to the energy level structure of the Tb^{3+} ions and correspond to the $^5\text{D}_4 \rightarrow ^7\text{F}_j$ ($j = 6, 5, 4, 3$) transitions. Also in this case, the shape of the peaks, as well as their relative intensities were maintained along the whole series of samples, while only the overall intensity of the emission resulted to change from sample to sample, as expected. Similarly to the previously discussed luminescent materials, the small size (less than 3 nm) of the Tb(III)-doped zirconia nanocrystals in these composites caused a strong influence of the silica matrix on the optically active lanthanide ions, which

were therefore accommodated in disordered sites. This structural disorder and the interactions with the surface and with the silica matrix beyond the particle boundaries resulted in a typical inhomogeneous line broadening with respect to bulk crystals and a consequent absence, in the examined spectra, of the narrow peaks of the trivalent terbium ions when hosted in bigger crystals or in a bulk structure made of zirconia.^{16,33}

An overall comparison of the relative PL emission intensities between the four samples of the series is depicted in Fig. 3.29.

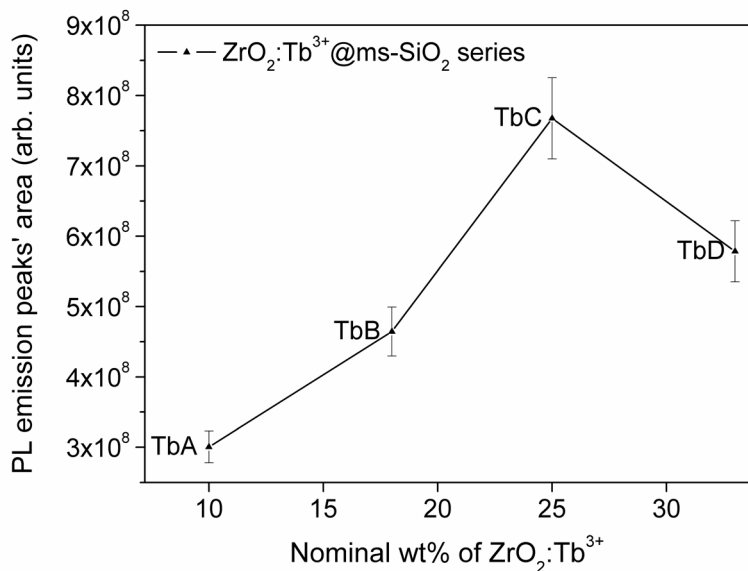


Figure 3.29 Comparison between the PL intensities (integral sum of the mean emission peaks' area under excitation at 378 nm) of the $ZrO_2:Tb^{3+}@ms-SiO_2$ series of samples.

As a general trend, also in this series the PL intensity increased with the increase in loaded fraction of $ZrO_2:Tb^{3+}$ from sample TbA to TbC, as expected since the intensity of the emitted signal in the sample is influenced by the overall Tb^{3+} content. Nevertheless, the nominally most loaded sample TbD did not follow the general trend of the series, since its emission resulted to be less intense than sample TbC, though the XRD and TEM characterization did not

show any relevant differences in the nanostructure of the sample with respect to the samples TbA-C. The decrease in the luminescence emission should not be attributed either to a reduction of the confinement effect introduced by an anomalous growth of the nanocrystals, or to a concentration quenching effect due to an unexpected higher fraction of terbium in the s. s., since both of them would also bring to a correspondent significant reduction in the effective lifetime of the sample, which on the contrary was not observed (Tab. 3.6).

Anyway, all the four samples showed satisfying luminescence emission that could make them suitable for labeling or imaging applications in the biological field.

For all the TbA-D samples, the room temperature decay curves of the PL emission showed a nearly mono-exponential shape. Anyway, also in this case the double exponential fitting equation:

$$I(t) = B + A_1 e^{-t/\tau_1} + A_2 e^{-t/\tau_2}$$

was applied for the calculation of a representative effective lifetime T_{obs} for each sample. With respect to the $\text{ZrO}_2:\text{Eu}^{3+}@\text{ms-SiO}_2$ series of samples, the greater closeness to mono-exponential shape of the decay curves is ascribed to the fact that terbium ions are less sensitive than europium ions to the $-\text{OH}$ groups which act as quenching centers.

Fig. 3.30 presents the experimental decay curves and their fit, all shifted along the Y axis for a better visualization.

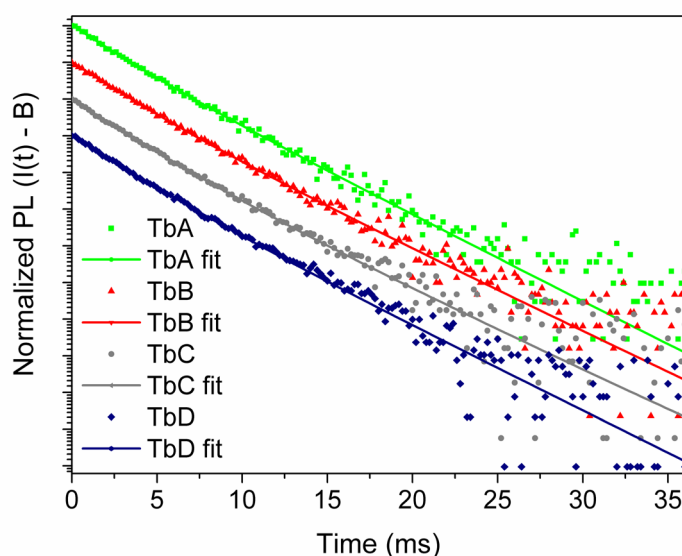


Figure 3.30 Time decay curves (MCSPC) and respective fits of the $\text{ZrO}_2:\text{Tb}^{3+}@\text{ms-SiO}_2$ series of samples. Intensity corrected using the background.

The observed effective lifetimes (τ_{obs}) are reported in Tab. 3.6.

Table 3.6 Luminescence lifetimes (emission 542 nm, excitation 377 nm) of the $\text{ZrO}_2:\text{Tb}^{3+}@\text{ms-SiO}_2$ series of samples TbA-D.

sample	lifetime (ms)
TbA	3.8 ± 0.3
TbB	3.8 ± 0.3
TbC	3.7 ± 0.3
TbD	3.7 ± 0.3

As a general behavior, the τ_{obs} value remained almost constant along the series (despite the decrease in the luminescence emission intensity of sample TbD) and this was expected since, contrary to what happens for the emission intensity, the increasing fraction of loaded luminescent material in the composite

does not provide an increase of the effective lifetime, whose value is usually strongly related to the s. s. composition (*i.e.* Tb³⁺ content in the crystalline structure). The latter therefore proved to remain effectively constant along the series. Moreover, as expected the τ_{obs} values of the TbA-D samples resulted to be more consistent with the lifetimes measured in previous study on similar composite materials made of Tb(III)-doped zirconia embedded in a silica matrix, (above 3 ms), than to the lower values (below 3 ms) that appeared in the same studies for both Tb³⁺-doped bulk zirconia and Tb³⁺-doped amorphous silica.^{16,33}

In conclusion, the aforementioned result and in general all the findings of the optical characterization not only evidenced the satisfying luminescent properties of the samples, but also confirmed the expectation about the nanostructure of the composite series.

ZrO₂:Er³⁺/Yb³⁺@ms-SiO₂: sample Er/Yb

A preliminary study was also performed on a third system of ZrO₂:RE³⁺@ms-SiO₂ composite material, in which the doping trivalent lanthanide cations were Er³⁺ and Yb³⁺, in order to obtain a luminescent material with up-converting properties. In this case, only a single sample was synthesized and investigated, with a definitely higher nominal level of loaded material into the silica host matrix, if compared to the other studied samples. Also the annealing temperature (1000 °C) was elevated in this case, because of the strong sensitivity of Er³⁺ ions to moisture and –OH groups. The high weight fraction (60%) of Er_{0.04}Yb_{0.1}Zr_{0.86}O_{1.93} crystalline phase was decided on the basis of previous studies about a similar composite material with the same crystalline phase that showed a weak luminescent emission²⁸ and therefore a strong increase in the amount of loaded luminescent phase in the composite was thought to be necessary to get a more intense luminescence. However, such a relevant fraction could be problematic for the nanostructural homogeneity of the sample. The usual nanostructural characterization was then performed on sample Er/Yb by means of XDR, TEM and porosimetric analyses.

The XRD pattern of sample Er/Yb is reported in Fig. 3.31 together with a reference pattern of cubic zirconia from the literature (PDF #781307).

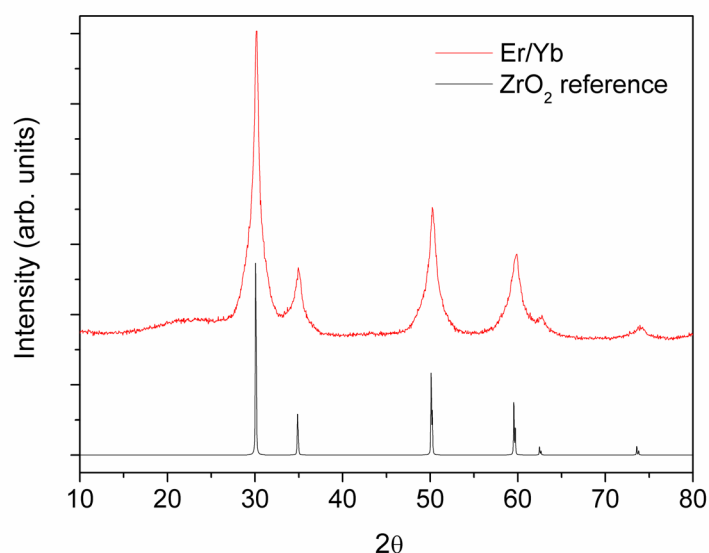


Figure 3.31 XRD patterns of sample Er/Yb and cubic ZrO₂ reference from the literature (PDF #781307).

As expected in consideration of the overall lanthanide content in the s. s., sample Er/Yb clearly showed the typical peaks of the cubic zirconia structure²⁸ and in this case their intensities were definitely higher than those of the Eu³⁺ and Tb³⁺ doped materials, due to the increased amount of crystalline phase in the composite. These intense crystalline peaks are predominant on the curve of amorphous silica, which is hardly visible in the figure while in the previous studies it could easily be distinguished from the signals of the loaded crystalline material. Moreover, not only the absolute intensity but also the broadness of the crystalline peaks seems to be changed this time, since their FWHM appears to be quite narrow, thus suggesting the presence of crystallites with bigger average size than the usual 2-3 nm and therefore this means that probably a fraction of crystalline phase has formed outside the pores of the silica matrix, at the expense of the nanostructural regularity of the composite. The occurrence

of this phenomenon could be expected with such a high level of loaded material, especially in consideration of the analogous results obtained from the investigation of the nanostructural properties in the highly doped samples of the $\text{FeO}_x@\text{ms-SiO}_2$ series (see § 4.1.2).

The results of the TEM analysis on sample Er/Yb (Fig. 3.32) confirmed the presence of strongly impregnated silica nanoparticles, as evidenced especially by the micrographs in Fig. 3.32b,c which show a high density of small (ca. 3 nm) nanocrystals embedded into the silica matrix.

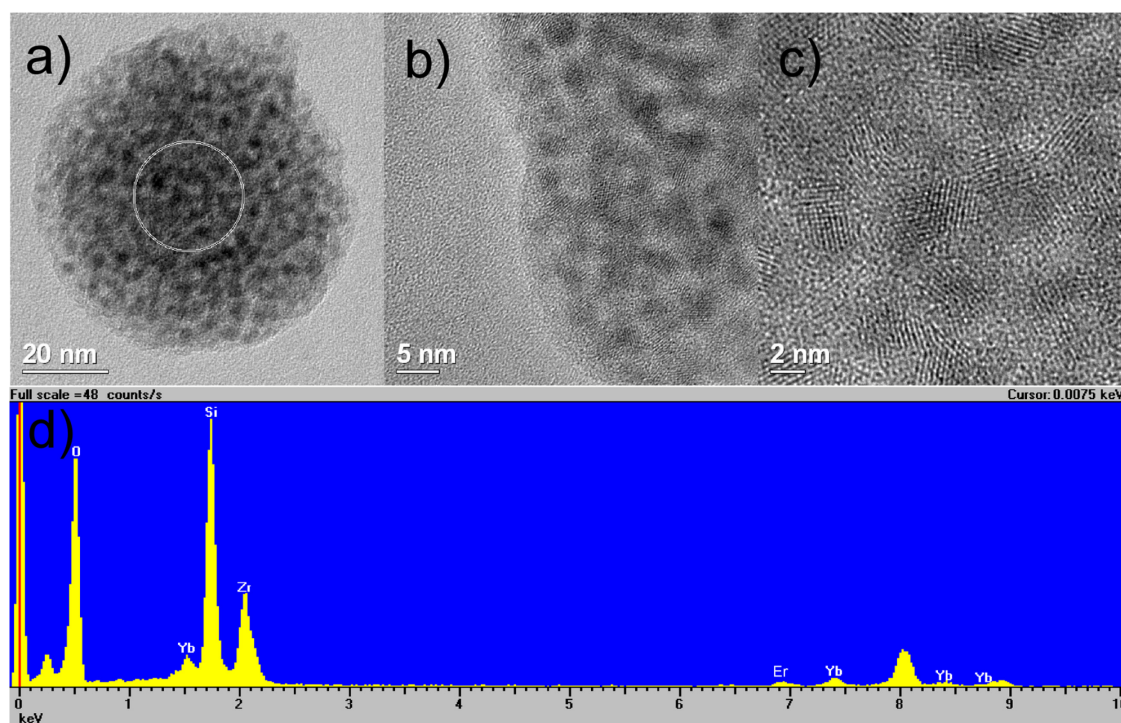


Figure 3.32 (a-c) TEM micrographs at different magnifications of sample Er/Yb and (d) EDS analysis of circled area (a).

The elemental EDS analysis (Fig. 3.32d) on an impregnated silica nanoparticle confirmed, as expected, the presence of Si, O, Zr, Er and Yb that are attributed to the $\text{Er}^{3+}/\text{Yb}^{3+}$ -co-doped zirconia and to the host silica matrix. Nevertheless, no additional material was observed externally to the silica nanoparticles during the analysis and therefore it was not possible to confirm nor to exclude the indication coming from the XRD characterization.

The N_2 adsorption/desorption isothermal curve of sample Er/Yb (Fig. 3.33) resulted to be very different from the previous ones. As shown by the comparison with the curve of the undoped mesoporous silica ms-SiO₂, the sample, following its impregnation and annealing at 1000 °C, lost the typical features of a mesoporous material and its curve (clearly visible in the inset of Fig. 3.33) displayed the typical shape of a non porous or macroporous material (type II isothermal according to IUPAC classification³⁰). The lack of the mesoporosity was further confirmed by the collapse of the surface area and pore volume values, if compared with the starting values of ms-SiO₂ (980 ± 10 m²/g and ca. 1.3 cm³/g respectively). In fact, the surface area of sample Er/Yb resulted to be 63 ± 4 m²/g, while its pore volume could not even be measured by the instrument and therefore its value is assumed to be near zero. As a consequence, the pore size distribution curve (Fig. 3.34) appeared almost flat if compared to that of ms-SiO₂.

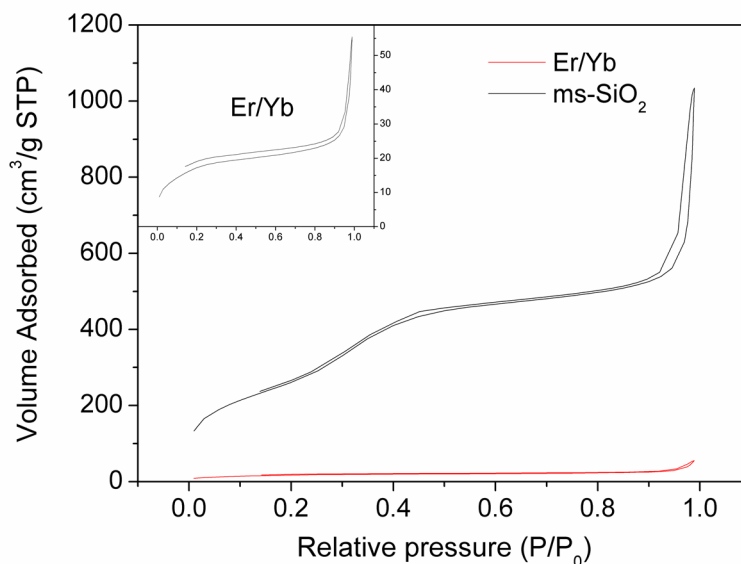


Figure 3.33 N_2 adsorption/desorption isothermal curves of sample Er/Yb and undoped mesoporous silica ms-SiO₂. Inset shows in a clearer way the shape of the red curve belonging to sample Er/Yb.

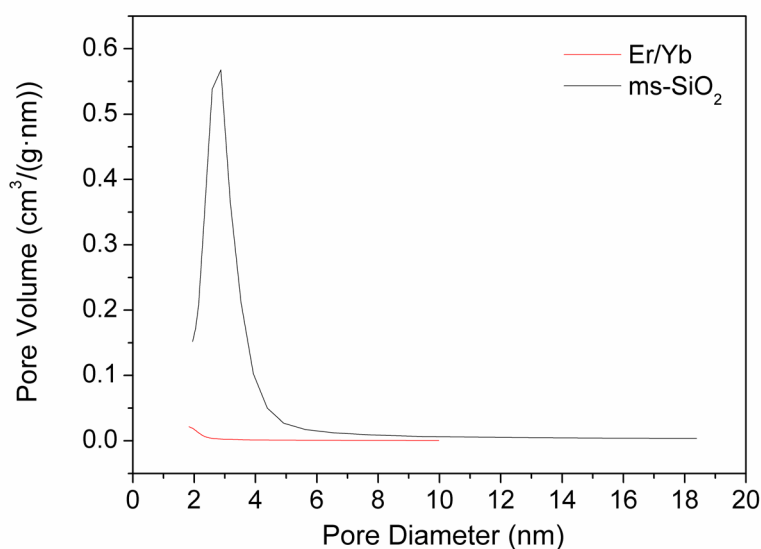


Figure 3.34 Pore size distribution curves of sample Er/Yb and undoped mesoporous silica ms-SiO₂.

The disappearing of the mesoporosity in sample Er/Yb can be attributed to the cooperation of two separate effects: one is the filling of a relevant fraction of the silica pores with the high amount of impregnated material, while the other is the sinterization process promoted by the high annealing temperature (1000 °C) that was demonstrated to cause pore shrinkage. Though it is not possible, with the available data, to quantify the effects of both these phenomena on the mesoporosity collapse, on the basis of the resulting lack of accessible pore volume, the hypothesis that the whole high amount of crystalline phase was totally embedded into the silica matrix without any residual left outside seems to be unlikely, since in other cases involving the same host matrix and with smaller or similar nominal fractions of loaded materials, the latter were proved to have partially formed outside the silica pores (see § 4.1.2 and 4.2.2).

In conclusion, the XRD, TEM and porosimetric analysis could not unanimously confirm but at least suggested a nanostructural heterogeneity of the composite, that was somewhat expected given the high quantity of precursors that were employed during the impregnation. Therefore, further

investigation is needed to study and probably improve the nanostructural regularity of the final composite material. Nevertheless, since the use of a massive amount of crystalline phase was meant to facilitate the study of the luminescent properties of the composite, a preliminary optical characterization of the sample was realized in any case, just in order to investigate the presence of up-converting properties in the material.

Fig. 3.35 shows the PL emission spectrum of sample Er/Yb under excitation at 980 nm (therefore in the IR region) by means of a diode laser.

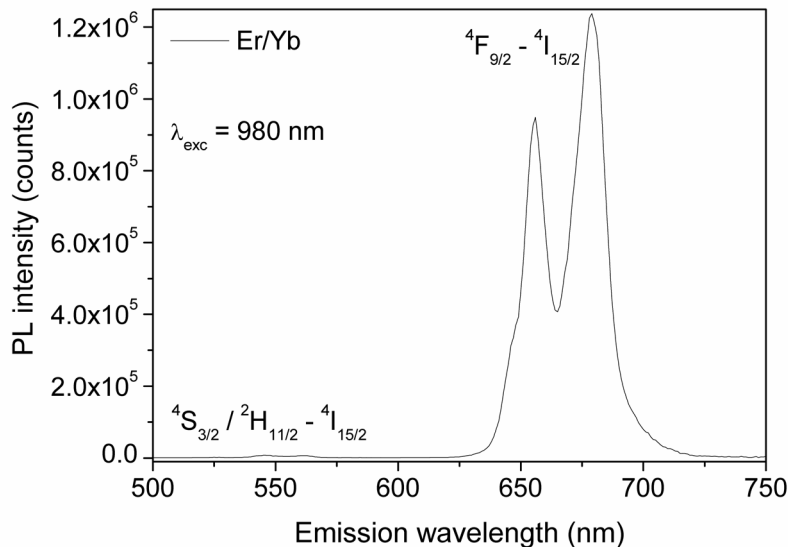


Figure 3.35 Luminescence emission spectrum (under 980 nm excitation) of sample Er/Yb.

The spectrum recalled the typical profile of the $\text{Er}_{0.04}\text{Yb}_{0.1}\text{Zr}_{0.86}\text{O}_{1.93}$ crystalline phase that has already been investigated by my research group²⁸, though with slightly broader peaks due to the presence of the silica matrix. But while in the aforementioned study the emission intensity was strongly decreased after the embedding of the luminescent phase into the silica, in this case, thanks to a higher fraction of loaded nanocrystals, the typical red emission in the 640 – 690 nm range that corresponds to the ${}^4\text{F}_{9/2} \rightarrow {}^4\text{I}_{15/2}$ transition between the Er^{3+} energy levels remained intense. On the contrary, the

green emission centered around 550 nm and related to the ${}^4S_{3/2} \rightarrow {}^4I_{15/2}$ and ${}^2H_{11/2} \rightarrow {}^4I_{15/2}$ transitions resulted to be very weak and almost invisible. Hence, these signals evidenced an intense up-conversion efficiency in the red region.

In this material, the use of trivalent erbium and ytterbium as activator and sensitizer, respectively, is justified by the fact that the latter has an energy level which, under 980 nm excitation, is available to promote energy transfer processes with the nearest erbium ions and the high absorption cross section of ytterbium enhances the quantity of exciting radiation absorbed by the material. Moreover, the introduction of Yb^{3+} as codoping ion brings to an intense red up-conversion emission, thanks to its capability to promote the ETU (Energy Transfer Up-conversion) process, which is more responsible for the red emission rather than the green one.^{34–36} The mechanism of the up-conversion processes is depicted in Fig 3.36. An initial population of the ${}^4S_{3/2}$ level, by means of energy transfer processes to the ${}^4F_{7/2}$ level followed by phonon relaxation, takes place. Then, being the energy gap between the ${}^4S_{3/2}$ and ${}^4F_{9/2}$ levels too elevated with respect to the typical phonon energies, the population of the ${}^4F_{9/2}$ level is made possible only by means of a EBT (Energy Back Transfer) process, which causes the repopulation of the $Yb^{3+} {}^2F_{5/2}$ level and the occupancy of the $Er^{3+} {}^4I_{13/2}$ level, while the energy gap is absorbed by a phonon; finally, via energy transfer (ET), the population of the ${}^4F_{9/2}$ level takes place and the consequent red emission occurs.³⁵ This process is so highly efficient to cause an almost complete quenching of the green emission, which only happens by means of ET processes among the closest ions and, above all, ESA (Excited State Adsorption) processes in isolated Er^{3+} ions.³⁵

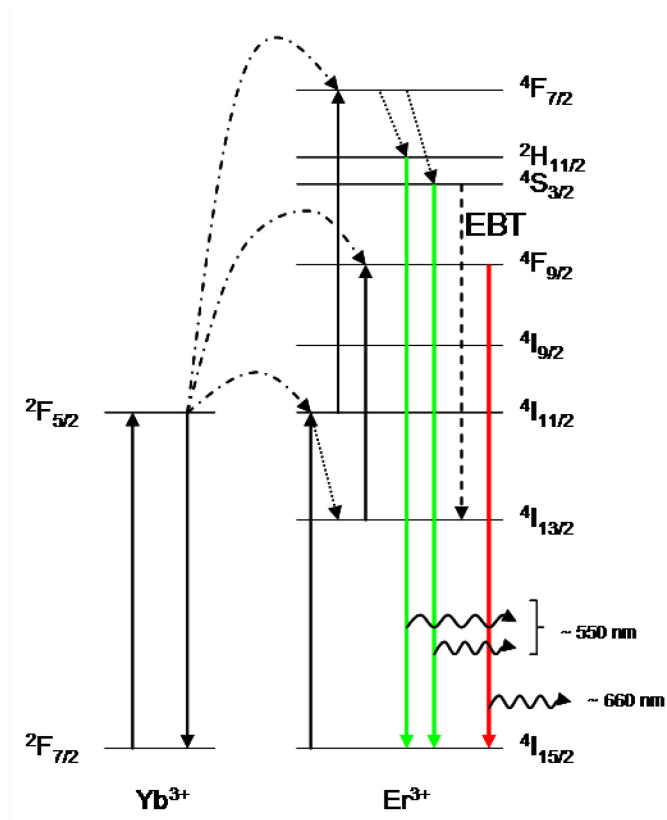


Figure 3.36 Scheme of the up-conversion processes in the $\text{Er}^{3+}/\text{Yb}^{3+}$ system.

In conclusion, this preliminary optical characterization confirmed the desired up-converting properties of the studied sample and therefore the possibility, by further investigation, to obtain a composite material with more structural order and quality and with satisfying up-conversion efficiency.

Surface functionalization of $\text{ZrO}_2:\text{RE}^{3+}@\text{ms-SiO}_2$ with APTES

At the same way than for the previously discussed $\text{ZrO}_2:\text{Eu}^{3+}@\text{SiO}_2$ nanophosphors²⁶ (see also § 3.1.2), the surface functionalizability of the studied samples was investigated by means of IR spectroscopy, since the functionalization of the silica surface with APTES allows the potential immobilization of biological molecules that can make these materials suitable for biolabeling applications (e.g. DNA microarray).

A representative sample, EuB, was chosen for both the $\text{ZrO}_2:\text{Eu}^{3+}@\text{ms-SiO}_2$ and $\text{ZrO}_2:\text{Tb}^{3+}@\text{ms-SiO}_2$ series of samples, since the different amounts

and type of loaded crystalline phase in the samples are not expected to influence the availability of silanol groups (active sites for functionalization) on the surface of silica, whose presence was demonstrated²⁶ (see also § 3.1.2) to be strongly related to the annealing temperature. The latter was set to the optimal value of 700 °C for all the samples of the two series EuA-D and TbA-D and therefore an easy functionalization with APTES could be performed for each of them. This is clearly shown in Fig. 3.37 by the comparison between the DRIFT spectra of sample EuB and EuBF (*i.e.* before and after the functionalization), that display, as expected, the same features of the previously discussed spectra of samples E10S-700 and E10S-700F (Fig. 3.14).

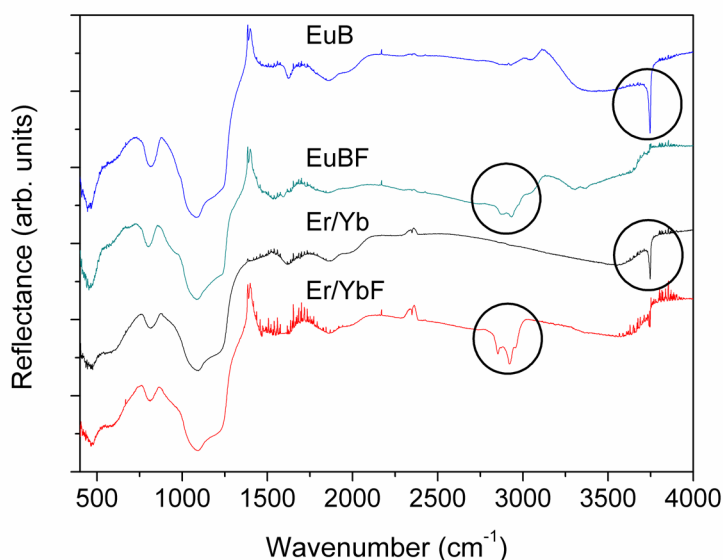


Figure 3.37 DRIFT spectra of sample EuB and sample Er/Yb before and after their functionalization with APTES (EuBF and Er/YbF respectively). Circled areas point out the sharp signal of active sites for functionalization (right) and the weak signals of aliphatic groups introduced with APTES (left).

Also in this case the presence of active sites for functionalization, *i.e.* free silanols, which include isolated and geminal groups, is evident from the sharp peak observed at 3750 cm^{-1} in the DRIFT spectrum of the non functionalized sample EuB. The attachment of APTES on the silica surface was qualitatively

confirmed, whereby the sharp peak at 3750 cm^{-1} was no longer present in the spectrum of sample EuBF, providing evidence for functionalization. Furthermore, the introduction of aliphatic groups attributed to APTES was evidenced by the appearance of weak signals just below 3000 cm^{-1} .

As depicted by Fig. 3.37, the same evidence was found also in the spectra of samples Er/Yb and Er/YbF, as a confirmation of a successful functionalization, which in this case was not so easily predictable. In fact, considering the previously mentioned observation about the importance of the annealing temperature for the availability of free silanols on the silica surface, the employed temperature ($1000\text{ }^{\circ}\text{C}$) for the synthesis of sample Er/Yb could have been problematic by causing a complete dehydroxylation of the surface silanols, similarly to what happened for sample E10S-1000 (see Fig. 3.13). On the contrary, this drawback was avoided and in the spectrum of sample Er/Yb the sharp peak at 3750 cm^{-1} could still be observed, though with less intensity than at $700\text{ }^{\circ}\text{C}$. Hence, if compared with the previously discussed unrealizable functionalization of sample E10S-1000, the successful functionalization of sample Er/Yb can be attributed to a double beneficial effect brought by a shorter duration of the thermal treatment at $1000\text{ }^{\circ}\text{C}$ (1 h rather than 12) and by an increased availability of surface silanols in the mesoporous silica ms-SiO₂ with respect to the non porous SiO₂, thanks to the huge value of available surface area that characterizes the former.

3.2.3 Conclusions

The presented luminescent nanocomposite materials ($\text{ZrO}_2\text{:RE}^{3+}\text{@ms-SiO}_2$) were obtained by embedding, via a wet impregnation route, RE^{3+} -doped ZrO_2 nanocrystals into an amorphous silica matrix made of previously synthesized mesoporous nanoparticles. Their characterizations provided a comparative study on the structural and luminescence properties of three different systems, containing trivalent europium, terbium and erbium/ytterbium (as activator/sensitizer respectively) cations as active species for the luminescence.

The obtained results were very satisfying, since all the investigated systems showed promise for potential application as biolabels in the biological and biomedical fields. The $\text{ZrO}_2:\text{Eu}^{3+}@m\text{-SiO}_2$ series of composites, as well as the $\text{ZrO}_2:\text{Tb}^{3+}@m\text{-SiO}_2$ one, proved to be characterized by nanostructural regularity and order (thanks to the efficiency and reliability of the impregnation process), which were reflected also in the resulting good luminescence properties coming from the small sized lanthanide-doped nanocrystals embedded in the protective silica matrix. The samples of both the aforementioned series showed an intense luminescence emission, which was related to the varying rare earth content in the composite along the series, together with quite long lifetimes (especially in the terbium-doped materials), whose values remained constant despite the different doping levels. Moreover, the retained mesoporosity in the loaded samples could potentially allow for further modification of the composites. For example, additional loading of magnetic materials, drugs or biomolecules would allow for the generation of multifunctional composite materials.

In the erbium/ytterbium-doped system, the up-conversion luminescence efficiency was favored in spite of the nanostructural order and regularity, since the density of embedded nanocrystals in the silica matrix was deliberately strongly enhanced and probably this aspect precluded to obtain a composite with the same homogeneity than the previous ones. However, the up-conversion efficiency was demonstrated and this system will be subjected to further investigation. In fact, after a necessary optimization of the overall quality of the composite, that should be based on the compromise between the necessity of an intense optical emission and a regular and homogeneous nanostructure, this kind of material, if appropriately functionalized, would show promise for its use in the biological and biomedical applications based on the luminescence. In fact, in the aforementioned applications the up-conversion represents an important way to overcome the drawback of the autofluorescence by the biological systems, as previously discussed (see § 1.3).

Finally, all three types of composite systems were successfully subjected to surface functionalization with APTES, for potential immobilization of biological molecules that can make these chemically stable materials suitable for biolabeling applications (e.g. DNA microarray).

3.3 $\text{Eu}(\text{DBM})_3\text{Phen}@m\text{-SiO}_2\text{F}$ nanocomposite

After showing promising features as a host matrix for inorganic luminescent species as the RE^{3+} -doped ZrO_2 nanocrystals, the mesoporous silica nanoparticles were also employed in the preparation of functionalized nanocomposite materials based on luminescent organic phosphors, such as the tris(dibenzoylmethane)mono(1,10-phenanthroline)europium(III) complex, also known as $\text{Eu}(\text{DBM})_3\text{Phen}$.

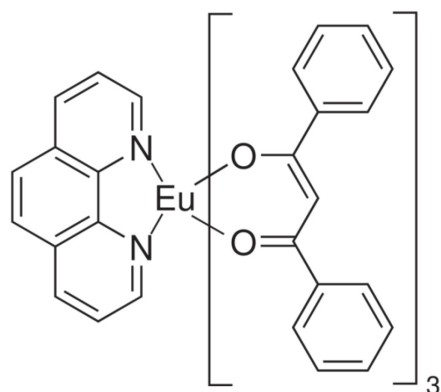


Figure 3.38 Chemical structure of a $\text{Eu}(\text{DBM})_3\text{Phen}$ molecule.

This complex (Fig. 3.38) was first synthesized and purified, and then it was embedded into the pores of the functionalized silica matrix, via a wet impregnation route in which dichloromethane (DCM) was used as solvent. The aim was to obtain a luminescent material with efficient optical properties and a very intense red emission, thanks to the beneficial effects produced by the complex on the active centers, e.g. the increment of the light absorption cross section by antenna effects, as discussed in the introductory chapter (see §

1.3.3). Such intense optical properties were mainly requested in order to prepare a multifunctional composite material with both luminescent and magnetic properties (which will be presented in the last study of this thesis), since the presence in the same material of a typically dark magnetic phase involves the drawback of its massive absorption of light that could weaken the luminescence from the optically active species.

Contrary to what was done for the previous classes of materials, in this case the surface functionalization of silica with APTES preceded, and did not follow, its impregnation with the luminescent material (*i.e.* the Eu(III) complex). This was possible since no thermal treatment following the impregnation was necessary. The nominal weight fraction of Eu(DBM)₃Phen was set to 7.5% on the total weight of the final composite material, on the basis of a previous study conducted by my research group on the optimal concentration of complex in silica in order to get the highest luminescence properties.

The morphological, structural and optical properties of the red emitting nanocomposite were investigated by means of XRD, TEM and porosimetric analyses, IR spectroscopy and photoluminescence measurements.

3.3.1 Samples preparation

Synthesis of mesoporous SiO₂ nanoparticles (ms-SiO₂)

The synthesis of mesoporous silica nanoparticles was adapted from the procedure by Qiao et al.²⁹ and has previously been reported in this thesis (see § 3.2.1).

Surface functionalization of ms-SiO₂ with APTES

The general procedure for surface functionalization with APTES,²⁶ which has already been described (see § 3.1.1), was here applied to 0.2 g of the undoped mesoporous silica nanoparticles (ms-SiO₂).

Synthesis and purification of $\text{Eu}(\text{DBM})_3\text{Phen}$ complex

The synthesis of $\text{Eu}(\text{DBM})_3\text{Phen}$ was adapted from the procedure by McGehee et al.³⁷

A solution of DBM (1.373 g, 6 mmol), 1,10-Phenanthroline (0.362 g, 2 mmol) and NaOH (0.241 g, 6 mmol) in ethanol (20 mL) was warmed with stirring. $\text{EuCl}_3 \cdot 6\text{H}_2\text{O}$ (0.733 g, 2 mmol) was first dissolved in 2 mL of distilled water and then added dropwise to the stirred ligand solution, inducing immediate precipitation of the complex. The luminescent precipitate was filtered (by means of a Büchner funnel equipped with filter paper) and washed several times with ethanol. Finally, a further purification of the complex was performed in order to remove the possible traces of NaCl formed as by-product: to this purpose, the recovered solid compound was suspended in DCM, in which the complex is soluble while NaCl is insoluble. By means of filtration, the NaCl was separated from the complex solution and the latter was recovered. The solvent was removed via rotavapor and a further drying was performed under reduced pressure (10^{-1} mbar for 1 h). The final amount of complex powder resulted to be ca. 1.3 g.

Synthesis of $\text{Eu}(\text{DBM})_3\text{Phen}@ms\text{-SiO}_2\text{F}$ sample

The Eu(III) complex-doped sample was prepared with a 7.5% nominal weight fraction of impregnated luminescent organic complex inside the silica pore network.

The sample was obtained by impregnating functionalized mesoporous SiO_2 nanoparticles (0.248 g) with a 8mM solution of $\text{Eu}(\text{DBM})_3\text{Phen}$ (0.020 g, 0.02 mmol) in DCM (2.48 mL), calculated according to the desired fraction of complex in the final nanocomposite. After stirring the mesoporous SiO_2 nanoparticles in DCM solution, the solvent was removed with the rotavapor and the dried impregnated powder was recovered and rinsed by repeated (2 times) DCM washing and centrifugation (30 min at 6 krpm), in order to remove the potential fraction of complex which could have remained outside the silica pores. Anyway, no relevant traces of complex were detected after each

centrifugation in the liquid supernatant, monitored by means of UV-VIS absorption spectroscopy. The obtained sample, $\text{Eu}(\text{DBM})_3\text{Phen}@ms\text{-SiO}_2\text{F}$ was dried under reduced pressure (10^{-1} mbar for 1 h).

3.3.2 Results and discussion

Functionalized mesoporous SiO_2 nanoparticles ($ms\text{-SiO}_2\text{F}$)

The mesoporous silica nanoparticles were synthesized, through the previously discussed process (see § 1.3.2) based on a templating surfactant, following the usual standard procedure that has already been described (§ 3.2.1); then they were functionalized with APTES and characterized, by means of IR spectroscopy, TEM and porosimetric analyses, at the same way as for precedent studies (e.g. § 3.2.2). The obtained results were, as expected, analogous to the previously studied undoped mesoporous silica sample (concerning the TEM and porosimetric analyses) and functionalized samples (concerning the IR spectroscopy) and therefore their detailed discussion is not repeated here. The main features of the functionalized mesoporous silica nanoparticles that were used in the present study are resumed in the following list:

- isolated and aggregated nanoparticles with spheroidal shape;
- nanoparticles' size: 60-70 nm;
- N_2 ads./des. isothermal curve: type IV (typical of a mesoporous material);
- surface area (B.E.T. method): $1090 \pm 10 \text{ m}^2/\text{g}$;
- pore volume: $1.4 \text{ cm}^3/\text{g}$;
- average pore diameter (B.J.H. method): ca. 2.8 nm;
- surface functionalization with APTES confirmed by IR spectroscopy.

$\text{Eu}(\text{DBM})_3\text{Phen}@ms\text{-SiO}_2\text{F}$ sample

The structural and morphological characterization of $\text{Eu}(\text{DBM})_3\text{Phen}@ms\text{-SiO}_2\text{F}$ sample was performed as usual by means of XRD, TEM and porosimetric analyses and IR spectroscopy.

The XRD pattern of $\text{Eu}(\text{DBM})_3\text{Phen}@ms\text{-SiO}_2\text{F}$ is reported together with that of the $\text{Eu}(\text{DBM})_3\text{Phen}$ complex in Fig. 3.39.

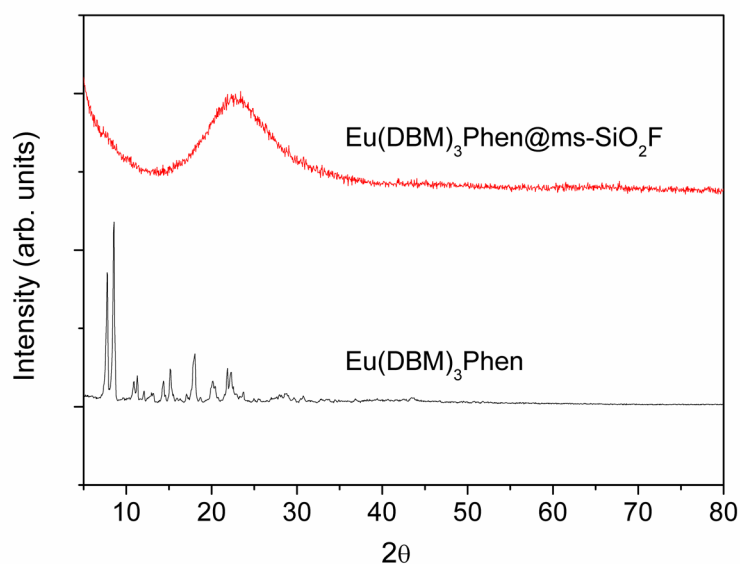


Figure 3.39 XRD patterns of sample $\text{Eu}(\text{DBM})_3\text{Phen}@ms\text{-SiO}_2\text{F}$ and $\text{Eu}(\text{DBM})_3\text{Phen}$ complex.

The impregnated material showed an XRD profile which is totally analogous to the amorphous curve of the undoped mesoporous silica $ms\text{-SiO}_2$ that has already been reported (see, for example, Fig. 3.19), while no additional signals that could be attributed to the narrow crystalline peaks of the complex appeared. This result can be due to several causes, among which some are definitely more probable than others. In fact, the total absence of complex in the sample should be a nonsense and will be excluded by the following characterization. The overall amount of complex in the material (nominal 7.5 %wt) could be too low for the detection of its XRD signals, but the most likely hypothesis, which will be further corroborated by the optical characterization, seems to be, as desired, the presence of complex inside the silica pores that, in cooperation with a loss of crystallinity after its dissolution in DCM solvent during the impregnation, account for the resulting amorphous pattern. The latter, therefore, is consistent with the hypothesis of the whole amount of complex

embedded into the silica matrix, without any external fraction, as preannounced by the DCM washings in the last part of the synthesis (see § 3.3.1). It should be noticed that, as expected, also the presence of APTES in the sample could not be detected by the diffraction measurement.

The same indications came from the TEM analysis. Micrographs of sample $\text{Eu}(\text{DBM})_3\text{Phen}@ms\text{-SiO}_2\text{F}$ (Fig. 3.40a,b) could not demonstrate the presence of complex inside the silica nanoparticles, nor the EDS analysis of a focused area on the silica matrix (Fig. 3.40c), since the low amount of complex in the sample brings to a fraction of elemental europium in the silica network which is below the detection limit (*ca.* 2%wt) of this technique. Only elemental Si and O could be detected as usual.

Anyway, the TEM analysis confirmed the absence of complex outside the silica matrix.

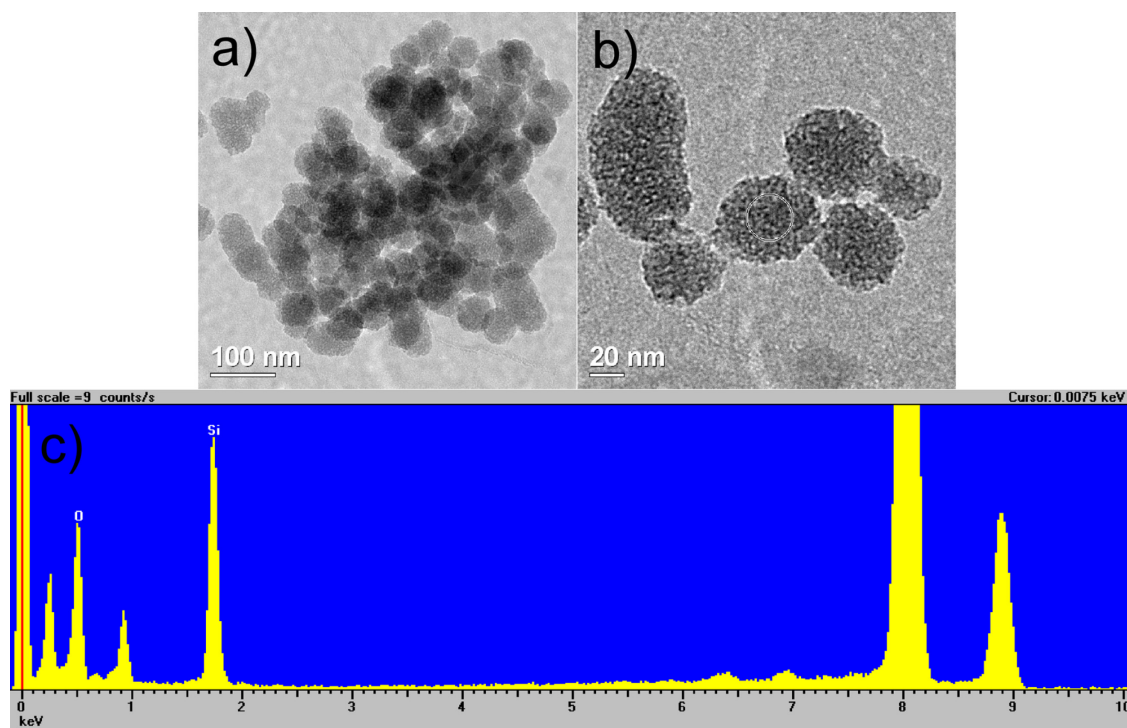


Figure 3.40 (a,b) TEM micrographs at different magnifications of sample $\text{Eu}(\text{DBM})_3\text{Phen}@ms\text{-SiO}_2\text{F}$ and (c) EDS analysis of circled area (b).

The N_2 adsorption/desorption isothermal curve of sample $Eu(DBM)_3Phen@ms-SiO_2F$ (Fig. 3.41) displays the typical shape of a mesoporous material (type IV isothermal), which corresponds to that of undoped mesoporous silica (see Fig. 3.17), notwithstanding the functionalization with APTES (which did not cause significant modification of the porosimetry) and the impregnation with the complex.

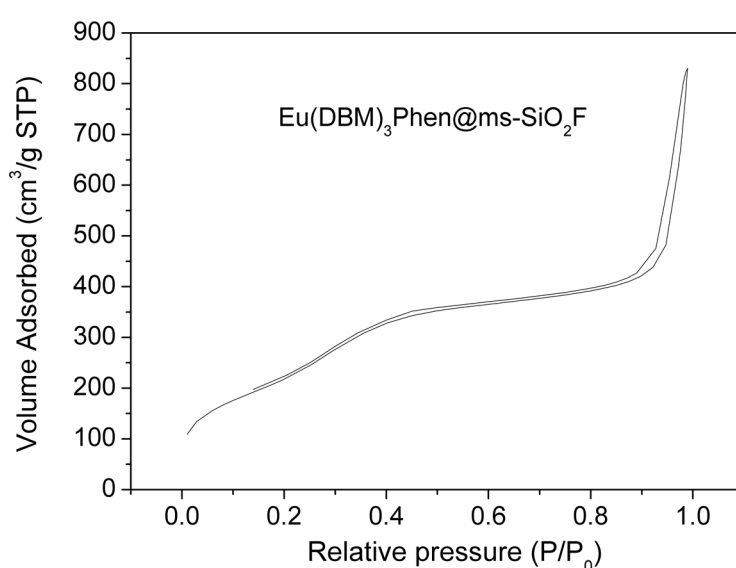


Figure 3.41 N_2 adsorption/desorption isothermal curve of $Eu(DBM)_3Phen@ms-SiO_2F$.

The aforementioned curve and the resulting modest decrease of the surface area and pore volume values ($820 \pm 10 \text{ m}^2/\text{g}$ and *ca.* $1.2 \text{ cm}^3/\text{g}$ respectively, to give correspondent decreases of 24 and 16% with respect to $ms-SiO_2F$) demonstrate that the composite retained a high degree of mesoporosity, as expected considering the low doping level. Also the pore size distribution curve (Fig. 3.42) featured a profile which is similar to the one that appeared for the undoped mesoporous silica (see Fig. 3.18), *i.e.* a narrow distribution that indicated an average pore size of *ca.* 2.7 nm.

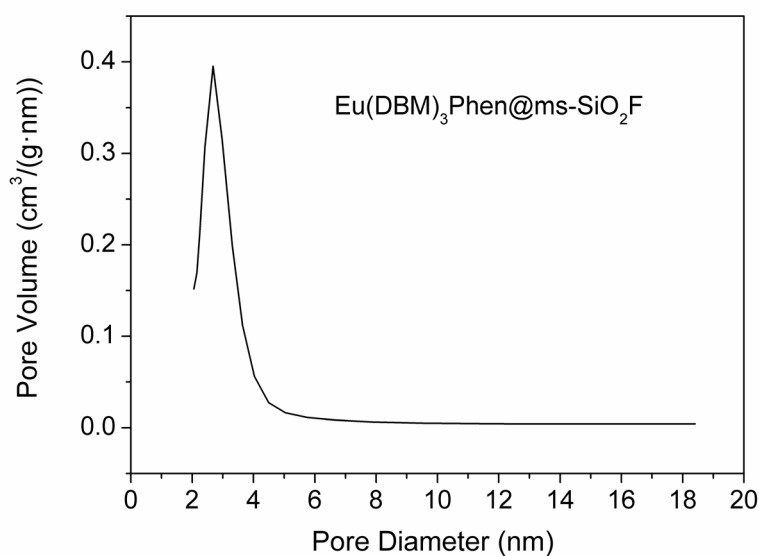


Figure 3.42 Pore size distribution curve of sample $\text{Eu}(\text{DBM})_3\text{Phen}@ms\text{-SiO}_2\text{F}$.

Overall, the porosimetric results for the $\text{Eu}(\text{DBM})_3\text{Phen}@ms\text{-SiO}_2\text{F}$ sample proved valuable, since the reduction of the pore volume and surface area values after the impregnation confirmed the presence of loaded complex in the sample, while at the same time the retained mesoporosity could potentially allow for further modification of the composite.

The IR spectroscopy (Fig. 3.43) could not prove the qualitative presence of complex in the $\text{Eu}(\text{DBM})_3\text{Phen}@ms\text{-SiO}_2\text{F}$ sample, since the IR spectrum of the impregnated sample (red curve) resulted to be almost identical to that of functionalized mesoporous silica $ms\text{-SiO}_2\text{F}$ (blue curve) prior to its impregnation, therefore without showing any signals that can be attributed to the complex.

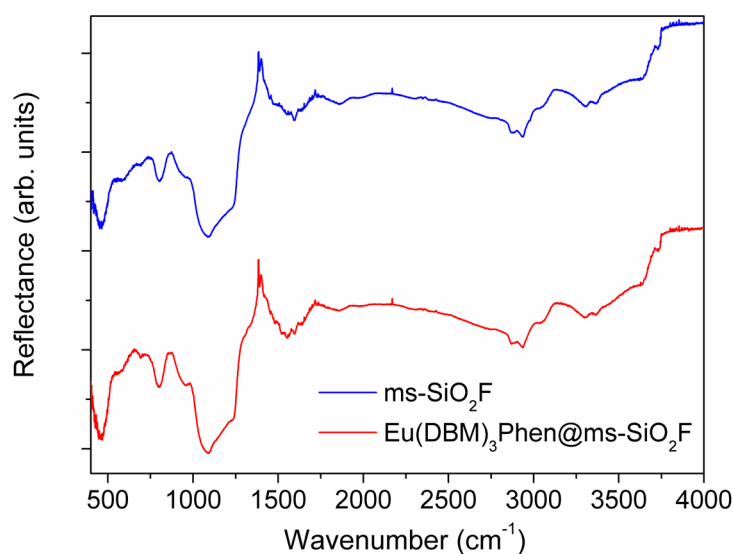


Figure 3.43 DRIFT spectra of sample $\text{Eu}(\text{DBM})_3\text{Phen}@ms\text{-SiO}_2\text{F}$ and undoped functionalized mesoporous silica $ms\text{-SiO}_2\text{F}$.

Anyway, the overall structural and morphological characterization of the composite pointed out the good regularity and homogeneity of the nanostructure and indicated the absence of residual traces of complex outside the silica nanoparticles, as expected in consideration of the DCM washings. Therefore, the whole amount of employed complex seemed to be incorporated into the silica host matrix. This indication was confirmed by the optical characterization of sample $\text{Eu}(\text{DBM})_3\text{Phen}@ms\text{-SiO}_2\text{F}$.

Thanks to the relevant intensity of the emitted luminescence under UV excitation, some optical microscopy photographs of the $\text{Eu}(\text{DBM})_3\text{Phen}@ms\text{-SiO}_2\text{F}$ sample, with and without UV light as exciting source (see § 2.2) could be realized. In Fig. 3.44, four images of two powder fractions at different magnifications are shown and the strong red emission of the UV excited powders is clearly visible.

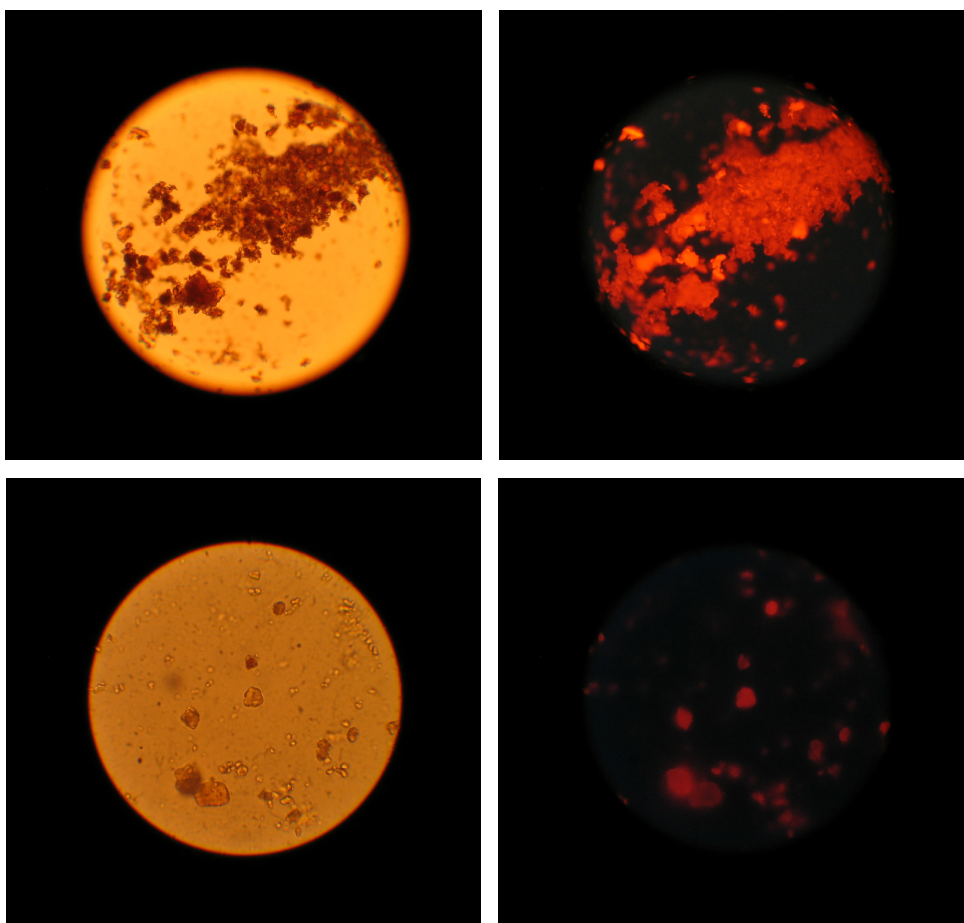


Figure 3.44 Optical microscopy photographs of sample $\text{Eu}(\text{DBM})_3\text{Phen}@ms\text{-SiO}_2\text{F}$ at different magnifications; two different powder fractions (top and bottom, respectively) in absence (left) and in presence (right) of the UV excitation.

The photoluminescence excitation spectra of $\text{Eu}(\text{DBM})_3\text{Phen}$ complex and of sample $\text{Eu}(\text{DBM})_3\text{Phen}@ms\text{-SiO}_2\text{F}$ are reported (normalized at their maximum value and shifted along the Y axis for a better visualization) in Fig. 3.45.

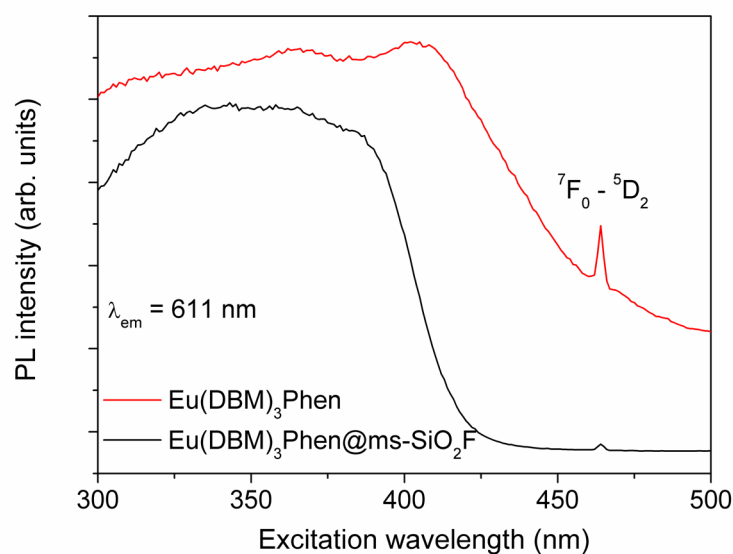


Figure 3.45 Luminescence excitation spectra at 611 nm emission for $\text{Eu}(\text{DBM})_3\text{Phen}$ complex and for sample $\text{Eu}(\text{DBM})_3\text{Phen}@ms\text{-SiO}_2\text{F}$.

The spectrum of complex showed a broad absorption band, with a maximum intensity around 400 nm, which is attributed to the organic ligands ($\pi \rightarrow \pi^*$ transitions³⁸) of the complex and to their antenna effect, while the sharp peak at 464 nm is ascribed to the ${}^7\text{F}_0 \rightarrow {}^5\text{D}_2$ transition of the Eu^{3+} ion. The other $f \rightarrow f$ transitions of the Eu^{3+} ion are weak and covered by the strong absorption band of the organic ligands. The latter resulted to be shifted towards higher frequencies (maximum intensity around 350 nm ca.) in the excitation spectrum of sample $\text{Eu}(\text{DBM})_3\text{Phen}@ms\text{-SiO}_2\text{F}$; this blue shift of the excitation band can be attributed to the interaction of the complex with the inorganic matrix, in particular to the change in the polarity of the environment surrounding the europium complex due to its introduction in the mesoporous silica matrix.³⁹

It should be noticed that the relative intensity of the organic ligands broad absorption band with respect to the Eu^{3+} sharp peak at 464 nm is definitely higher in the composite than in the complex. This phenomenon can be ascribed to the self-quenching effect of the organic ligands in the complex in a solid state, that brings to a lower emission of the complex itself, while when the latter

is well dispersed in a host matrix as SiO_2 , the self-quenching effect is significantly reduced.

In Fig. 3.46 the PL emission spectra under 393 nm excitation of the complex and the composite samples are shown (normalized at their maximum value and shifted along the Y axis for a better visualization).

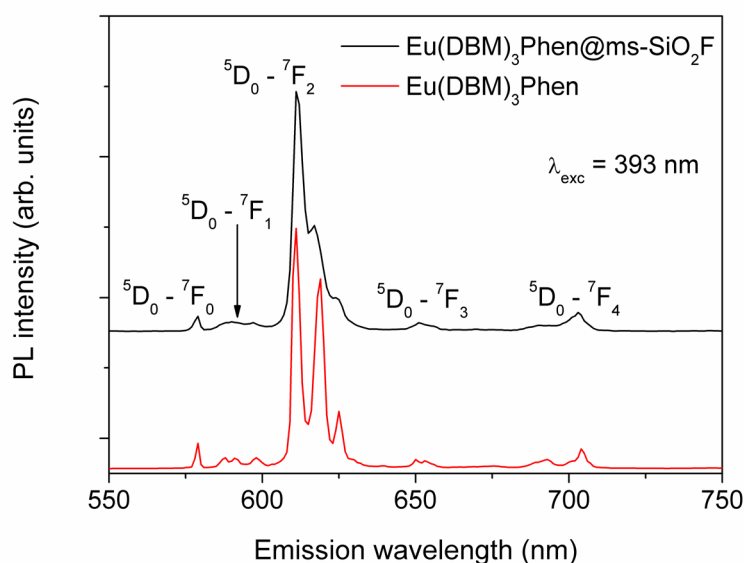


Figure 3.46 Luminescence emission spectra under 393 nm excitation for $\text{Eu}(\text{DBM})_3\text{Phen}$ complex and for sample $\text{Eu}(\text{DBM})_3\text{Phen}@ms\text{-SiO}_2\text{F}$.

The spectrum of complex displayed five signal at 579 nm, 591 nm, 611 nm, 652 nm and 703 nm that are associated to the typical ${}^5\text{D}_0 \rightarrow {}^7\text{F}_j$ ($j = 0, \dots, 4$) transitions of Eu^{3+} . The main emission band that gives the typical intense red emission of the complex is splitted in three sharp peaks and the associated ${}^5\text{D}_0 \rightarrow {}^7\text{F}_2$ transition, as previously discussed, is strongly dependent on the chemical environment around the metallic ion (hypersensitive transition), being a forced electric dipole transition only allowed at low symmetries.

The spectrum of $\text{Eu}(\text{DBM})_3\text{Phen}@ms\text{-SiO}_2\text{F}$ sample showed a similar emission profile but with an expected general broadening of the peaks that is

ascribed to the enhanced disorder brought by the interactions with the silica host matrix, into which the complex is incorporated.

As desired, the overall emission intensity of the composite resulted to be relevant if compared to the previously studied inorganic luminescent materials measured under the same conditions, thanks to the intrinsic luminescent properties of the Eu(III) complex.

The same PL emission measurements for sample $\text{Eu}(\text{DBM})_3\text{Phen}@ms\text{-SiO}_2\text{F}$ were also performed under 350 and 464 nm excitation wavelengths. Apart from an obvious difference in the overall emission intensity with respect to 393 nm excitation (quite similar for 350 nm, definitely lower for 464 nm excitation), the aforementioned measurements gave spectra with identical profiles in terms of shape, position and relative intensities of the peaks with respect to the previous and therefore they are not reported. In particular, since the emission under excitation at 464 nm gives signal that are attributable to the direct excitation of the Eu^{3+} ion, this result confirmed, as expected, the existence of only one Eu(III) ion site (that is the site of the metallic ion in the complex) in the composite sample. The same indication came also from the fact that the ${}^5\text{D}_0 \rightarrow {}^7\text{F}_0$ transition (579 nm) consists of one peak only (Fig 3.46), which means that all the Eu^{3+} ions occupy a site of the same symmetry and/or crystal-field strength.

From the decay curves of the PL emission (under 377 nm excitation) of the complex and the composite samples, their observed lifetimes (τ_{obs}) could be calculated, at the same way as for the previously studied samples (see, for example, § 3.1.2). Fig. 3.47 reports the experimental decay curves of $\text{Eu}(\text{DBM})_3\text{Phen}$ and $\text{Eu}(\text{DBM})_3\text{Phen}@ms\text{-SiO}_2\text{F}$ and their fits.

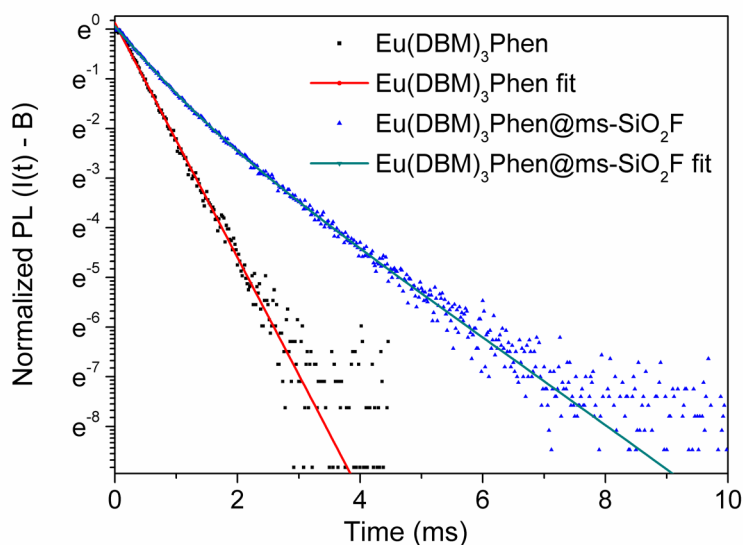


Figure 3.47 Time decay curves (MCSPC) and respective fits of $\text{Eu}(\text{DBM})_3\text{Phen}$ complex and of sample $\text{Eu}(\text{DBM})_3\text{Phen}@ms\text{-SiO}_2\text{F}$. Intensity corrected using the background.

The mono-exponential shape of the decay curve is evident for the complex. Also the decay curve of sample $\text{Eu}(\text{DBM})_3\text{Phen}@ms\text{-SiO}_2\text{F}$ showed a shape which is close to mono-exponential, therefore accounting for a low degree of disorder affecting the sites in which the Eu^{3+} ions are accommodated in the material.

Moreover, the calculated effective lifetime τ_{Obs} for sample $\text{Eu}(\text{DBM})_3\text{Phen}@ms\text{-SiO}_2\text{F}$ was 0.87 ± 0.07 ms, a value that resulted to be higher if compared with other values coming from $\text{Eu}(\text{III})$ β -diketonate complexes when incorporated in silica.^{40,41} An enhancement of the lifetime could be ascribed to the presence of APTES⁴² but more investigation would be needed to study the effect of silica functionalization on the luminescent properties in such composite materials. On the other hand, the calculated value for the $\text{Eu}(\text{DBM})_3\text{Phen}$ complex (0.42 ± 0.03 ms) was in agreement with the available data on this complex in solid state.⁴¹ The higher lifetime value of the

composite suggests that the luminescence stability of the complex was enhanced after its incorporation into the mesoporous matrix.

Overall, the optical characterization, in agreement with the nanostructural investigation, confirmed the presence of the $\text{Eu}(\text{DBM})_3\text{Phen}$ complex embedded into the silica matrix and demonstrated the high luminescence emission intensity of the material, which represents the main reason for which the composite was prepared and studied.

3.3.3 Conclusions

The present study was performed to investigate the possibility to load, via impregnation, the APTES functionalized mesoporous silica nanoparticles with a lanthanide complex, in order to obtain a composite material with efficient, and especially very intense, luminescence and nanostructural homogeneity. The nominal loaded fraction of complex was determined on the basis of previous investigation about the dependence of the emission intensity on the loading level and the latter was set to a nominal 7.5% on the total weight of the final material, therefore a moderate value which could even allow the introduction of different materials in the same host matrix. In fact, the final purpose for which this material was studied is the realization of a multifunctional nanocomposite with both luminescent and magnetic properties, whose synthesis and characterization will be presented in § 5.1.

The characterization of sample $\text{Eu}(\text{DBM})_3\text{Phen}@ms\text{-SiO}_2\text{F}$ proved a good outcome of the study, since the composite material resulted to have regular morphology and nanostructure coming from an efficient impregnation of the silica nanoparticles with the complex. The latter was totally embedded into the host matrix but relevant available room was left inside the pores for possible further loading of material. Most of all, the composite showed a remarkable luminescent emission in the red range under UV excitation, as desired.

Further investigation would be needed to deepen the role of APTES in terms of its interaction with the complex and subsequent effect on the optical properties and chemical stability of the composite.

3.4 $\text{Sr}_2\text{MgSi}_2\text{O}_7:\text{Eu}^{2+},\text{Dy}^{3+}$ persistent luminescence materials

The $\text{Sr}_2\text{MgSi}_2\text{O}_7:\text{Eu}^{2+},\text{Dy}^{3+}$ material has been synthesized with the simple solid state reaction and then characterized in order to study the effects of the concentration of Eu^{2+} and Dy^{3+} on its performance as a persistent luminescence material. The strontium magnesium disilicate materials were co-doped with a constant level of divalent europium Eu^{2+} and a varying level of trivalent dysprosium Dy^{3+} . Moreover, a $(\text{Sr}_{1-x}\text{Eu}_x)_2\text{MgSi}_2\text{O}_7$ solid solution series with several different europium fractions has been prepared to investigate the formation of the $\text{Eu}_2\text{MgSi}_2\text{O}_7$ phase.

3.4.1 Samples preparation

Two different series of samples were studied. First, the solid solutions $(\text{Sr}_{1-x}\text{Eu}_x)_2\text{MgSi}_2\text{O}_7$ with x : 0, 0.01, 0.05, 0.1, 0.2, 0.4, 0.6, 0.8 and 1.0 were synthesized. Finally, the $\text{Sr}_2\text{MgSi}_2\text{O}_7:\text{Eu}^{2+},\text{Dy}^{3+}$ materials with constant x_{Eu} : 0.01 and x_{Dy} : 0.001, 0.01, 0.02, 0.04, 0.06 and 0.08 were prepared.

As shown in Tab. 3.7, samples were named according to the nominal concentrations of the (co-)doping ions (in molar % of the strontium amount). All samples were prepared with solid state reactions. The starting materials were strontium carbonate (SrCO_3), magnesium nitrate hexahydrate ($\text{Mg}(\text{NO}_3)_2 \cdot 6\text{H}_2\text{O}$), rare earth oxides (Eu_2O_3 , Dy_2O_3) and fumed silica (SiO_2).

The stoichiometric amounts of the starting materials were intimately ground by a ball mill (10 minutes at 1800 rpm) to form a homogeneous mixture, which was then annealed in an alumina crucible for 1 h at 700 °C and for 10 h at 1350

°C in a reducing $N_2 + 10\% H_2$ atmosphere in an Elite TSH 15/50/450-2416CG tube furnace.

Table 3.7 The nominal compositions of the Eu^{3+} -doped (left) and co-doped (right) series of samples.

sample	nominal composition	sample	nominal composition
0% Eu	$Sr_2MgSi_2O_7$	1% Eu_0.1% Dy	$(Sr_{0.989}Eu_{0.01}Dy_{0.001})_2MgSi_2O_7$
1% Eu	$(Sr_{0.99}Eu_{0.01})_2MgSi_2O_7$	1% Eu_1% Dy	$(Sr_{0.98}Eu_{0.01}Dy_{0.01})_2MgSi_2O_7$
5% Eu	$(Sr_{0.95}Eu_{0.05})_2MgSi_2O_7$	1% Eu_2% Dy	$(Sr_{0.97}Eu_{0.01}Dy_{0.02})_2MgSi_2O_7$
10% Eu	$(Sr_{0.9}Eu_{0.1})_2MgSi_2O_7$	1% Eu_4% Dy	$(Sr_{0.95}Eu_{0.01}Dy_{0.04})_2MgSi_2O_7$
20% Eu	$(Sr_{0.8}Eu_{0.2})_2MgSi_2O_7$	1% Eu_6% Dy	$(Sr_{0.93}Eu_{0.01}Dy_{0.06})_2MgSi_2O_7$
40% Eu	$(Sr_{0.6}Eu_{0.4})_2MgSi_2O_7$	1% Eu_8% Dy	$(Sr_{0.91}Eu_{0.01}Dy_{0.08})_2MgSi_2O_7$
60% Eu	$(Sr_{0.4}Eu_{0.6})_2MgSi_2O_7$		
80% Eu	$(Sr_{0.2}Eu_{0.8})_2MgSi_2O_7$		
100% Eu	$Eu_2MgSi_2O_7$		

3.4.2 Results and discussion

Formation and structure of disilicates

In order to study the solid state reaction and to investigate the formation of disilicates, some thermogravimetric measurements (TG) were carried out. Fig. 3.48 shows the TG curves of two different starting powder mixtures which, after thermal treatment, should form two significant samples of the first series ($Sr_2MgSi_2O_7:Eu^{2+}$ material), *i.e.* the undoped (0% Eu) and the most doped one (100% Eu). Considering that low (co-)doping levels should not have any noticeable influence on the solid state reaction and on the formation of the expected disilicate, the remaining samples of the series, as well as the co-doped ones, were not measured. Both measurements were carried out in a $N_2 + 10\% H_2$ atmosphere, from room temperature to 1350 °C (5 °C min^{-1} of heating rate), in order to simulate the experimental conditions of the thermal treatment that was used to prepare all the samples.

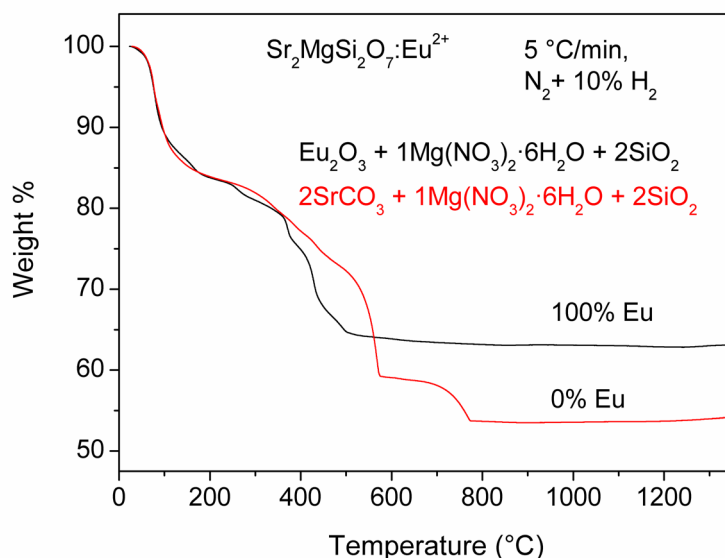
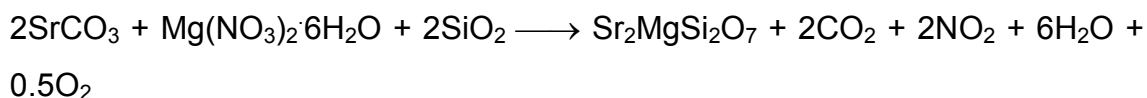


Figure 3.48 TG curves of the starting powder mixtures for the preparation of samples 0% Eu ($\text{Sr}_2\text{MgSi}_2\text{O}_7$) and 100% Eu ($\text{Eu}_2\text{MgSi}_2\text{O}_7$).

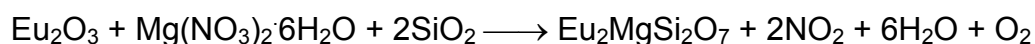
These two measurements gave really different results. The undoped sample curve was, as expected, in total agreement with previous measurements done in the past on the same material. On the contrary, no previous thermogravimetry data about the 100% Eu^{2+} -doped material were available for a comparison.

The theoretical remaining weight % of sample 0% Eu, calculated according to the following reaction



was then compared to the observed one and the two values resulted to be very similar (54.7% and 53.9% respectively), thus indicating that the solid state reaction of the starting mixture should lead to the formation of the expected $\text{Sr}_2\text{MgSi}_2\text{O}_7$, as it was successively confirmed by X-ray powder diffraction (XRPD) measurements.

The same calculation was made on sample 100% Eu, according to the following reaction:



but in this case the theoretical and observed remaining weight % did not correspond (68.1% and 63.1% respectively), thus indicating that probably, under these experimental conditions, the solid state reaction above could not occur in the expected way and a different final compound could form.

This suggestion was then investigated by means of XRD measurements. X-ray powder diffraction was used to confirm the structure and phase purity of the materials. Fig. 3.49 shows the experimental X-ray diffraction patterns of the $\text{Sr}_2\text{MgSi}_2\text{O}_7 \cdot \text{Eu}^{2+}$ series, which resulted to be quite surprising. In fact, while for the samples with low doping levels the formed phase was the expected one (tetragonal $\text{Sr}_2\text{MgSi}_2\text{O}_7$, as it can be easily verified through comparison with a reference calculated pattern of this material), for the samples with high doping levels a different phase appeared, gradually replacing the previous one with increasing doping levels (starting from 10% Eu sample). This different diffraction pattern totally characterizes the measurement of 100% Eu sample and was not supposed to appear. In fact, the crystalline structure of the $\text{Eu}_2\text{MgSi}_2\text{O}_7$ material should be very similar to the $\text{Sr}_2\text{MgSi}_2\text{O}_7$ one, since the Eu^{2+} ion is expected to replace Sr^{2+} and the ionic radii of both species are close to a perfect match (1.25 and 1.26 Å respectively).⁴³

On the contrary, the formation of a different compound occurred and the fact that its presence seemed to be strongly correlated to the europium content suggested that the unexpected compound could have been formed due to the presence of Eu^{3+} in addition to Eu^{2+} , probably because the thermal treatment was not effective enough to reduce the whole europium amount.

In consequence, the hypothesis of a relevant presence of trivalent europium was subsequently investigated by UV excited luminescence and XANES measurements (that are discussed hereinafter).

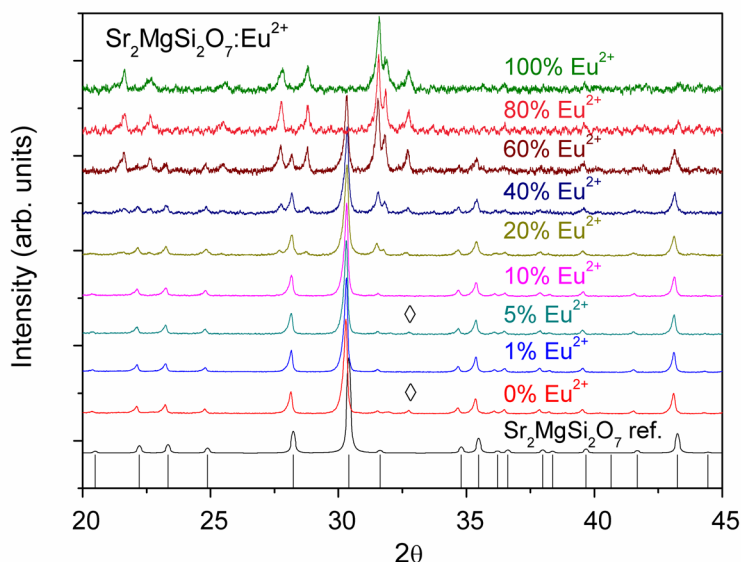


Figure 3.49 Experimental X-ray powder diffraction patterns of the $\text{Sr}_2\text{MgSi}_2\text{O}_7:\text{Eu}^{2+}$ series at room temperature. The calculated pattern of the $\text{Sr}_2\text{MgSi}_2\text{O}_7$ compound (black curve + bars) was used as reference.⁴⁴ Impurity reflections: \diamond $\text{Sr}_3\text{MgSi}_2\text{O}_8$.⁴⁵

The phase purity of the low doped samples (0% Eu to 10% Eu) was good, since only in a couple of samples (0% and 5% Eu^{2+} -doped) a little presence of $\text{Sr}_3\text{MgSi}_2\text{O}_8$ (that sometimes appears as an impurity in such materials⁴⁶) was found, while no other impurities appeared.

The high background noise (*i.e.* the low intensity of the signal) in high doped samples was due to the strong absorption of the $\text{CuK}\alpha_1$ radiation by europium and could not be avoided with the instrumental set up used for these measurements.

The structure and phase purity were investigated also on the co-doped materials. Fig. 3.50 shows the experimental X-ray diffraction patterns of the $\text{Sr}_2\text{MgSi}_2\text{O}_7:\text{Eu}^{2+}, \text{Dy}^{3+}$ series.

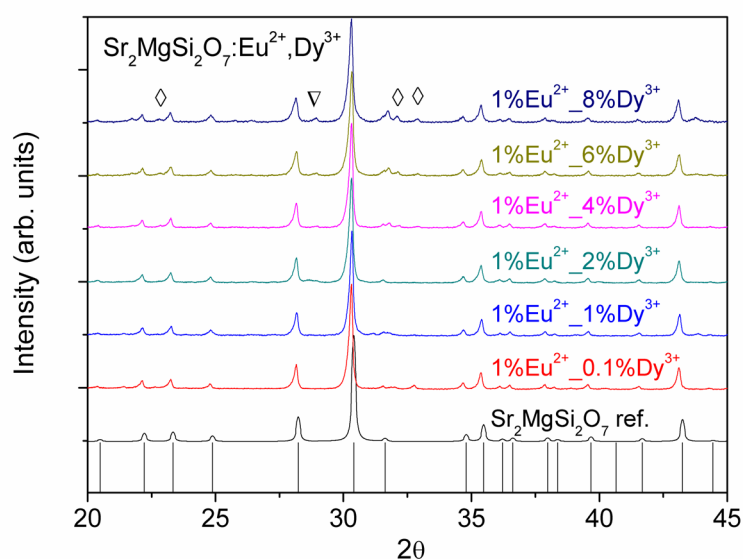


Figure 3.50 Experimental X-ray powder diffraction patterns of the $\text{Sr}_2\text{MgSi}_2\text{O}_7:\text{Eu}^{2+},\text{Dy}^{3+}$ series at room temperature. The calculated pattern of the $\text{Sr}_2\text{MgSi}_2\text{O}_7$ compound (black curve + bars) was used as reference.⁴⁴ Impurity reflections: ∇ Dy_2O_3 , \diamond $\text{Sr}_3\text{MgSi}_2\text{O}_8$.⁴⁵

All the curves were characterized by the typical reflections of tetragonal $\text{Sr}_2\text{MgSi}_2\text{O}_7$. In this case the resulting diffraction patterns were consistent with the expected ones, since in all the series of samples the quite low co-doping levels should not have a noticeable effect on the crystalline structure, which therefore is the same of the undoped material.

The purity grade of the samples was quite good, though a little bit lower compared to the low doped samples of the $\text{Sr}_2\text{MgSi}_2\text{O}_7:\text{Eu}^{2+}$ series, since this time some impurities were present in most of samples. In particular, not only the typical $\text{Sr}_3\text{MgSi}_2\text{O}_8$ phase was present in small amounts as impurity (0.1%, 4%, 6% and 8% Dy^{3+} -doped samples), but also small amounts of Dy_2O_3 seemed to be present as impurities in high Dy^{3+} -doped samples (4%, 6% and 8% Dy^{3+} -doped samples), thus suggesting that, during the solid state reaction, the amount of the starting Dy_2O_3 was not entirely involved in the formation of the $\text{Sr}_2\text{MgSi}_2\text{O}_7:\text{Eu}^{2+},\text{Dy}^{3+}$ compound and a little fraction of the oxide remained in the final product.

UV excited luminescence

In order to investigate the optical properties of the materials, UV excited luminescence measurements were carried out for both the series of samples ($\text{Sr}_2\text{MgSi}_2\text{O}_7:\text{Eu}^{2+}$ and $\text{Sr}_2\text{MgSi}_2\text{O}_7:\text{Eu}^{2+},\text{Dy}^{3+}$).

Fig. 3.51 shows the UV excited ($\lambda_{\text{exc}} = 300 \text{ nm}$) PL emission spectra of the $\text{Sr}_2\text{MgSi}_2\text{O}_7:\text{Eu}^{2+}$ series at room temperature (RT).

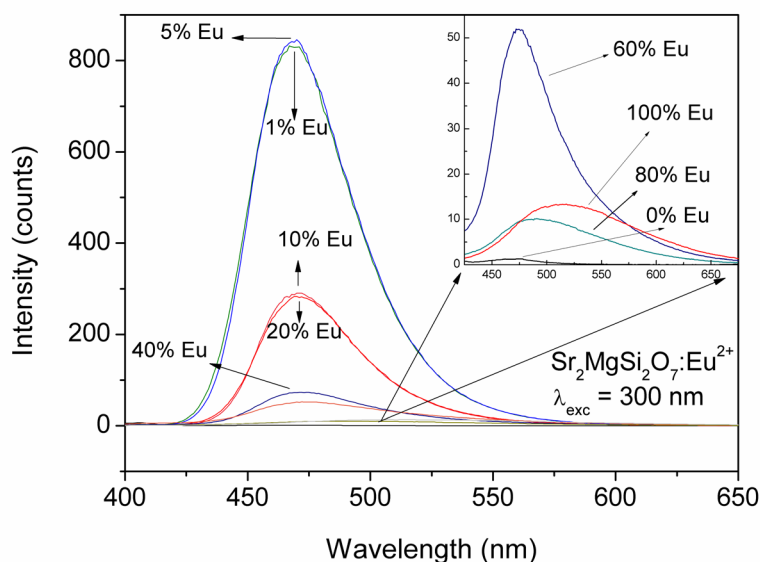


Figure 3.51 UV excited emission spectra of the $\text{Sr}_2\text{MgSi}_2\text{O}_7:\text{Eu}^{2+}$ series ($\lambda_{\text{exc}} = 300 \text{ nm}$) at RT. Inset: spectra with weak intensities.

All samples except 0, 80 and 100% Eu^{2+} -doped showed a typical wide band centered in the blue range at about 470 nm which is due to the $4f^65d^1(^2D) \rightarrow 4f^7(^8S_{7/2})$ transition of Eu^{2+} .⁴⁷ Since the $4f^65d^1$ configuration strongly interacts with the lattice phonons, the emission is shown as a broad band. The resulting spectra were in good agreement with the previous studies on $\text{Sr}_2\text{MgSi}_2\text{O}_7:\text{Eu}^{2+}$ materials, confirming that the Eu^{2+} ions in these samples occupy the Sr site. No changes in the band shape and position with the varying Eu^{2+} doping level were observed among these six samples (1, 5, 10, 20, 40 and 60% Eu).

Of course the absence of the emission wide band in sample 0% Eu was expected since no rare earth doping was present in the material. On the other hand, the most doped samples, *i.e.* 80% Eu and 100% Eu, were characterized by a noticeable shifting of the emission wide band towards higher wavelengths (*ca.* 490 and 520 nm respectively, *i.e.* *ca.* 20408 and 19231 cm^{-1}). Such a phenomenon seemed to confirm that in these materials a different structure in the host lattice is present, as shown by XRD patterns too. In fact, a different host lattice means a different chemical environment around the Eu^{2+} ions which can of course modify the energy of Eu^{2+} 5d levels of the excited state configuration and therefore the energy and wavelength associated to the transition. A possible lowering of the 5d energy levels could explain the observed redshift of the emission wide band in 80% and 100% Eu^{2+} -doped samples.

In theory, no reliable information regarding the comparison of the emission intensities could be achieved from these and from all the following luminescence measurements that are presented in this study, since the intensity of the emitted signal strongly depends on the amount of the powder which is exposed to the excitation source and, therefore, this amount should be exactly the same for each measured sample. But the setup which was employed for all the luminescence measurements carried out during this study did not allow to check in a scientific way the use of an exactly constant amount of material for each sample. Hence, the comparison of the luminescence intensities could be affected by uncertainty due to the human error. In spite of this observation, a general trend in the intensity variation can be noticed through the comparison among the whole series of samples and this trend definitely seems to be real and not accidental. In fact, as it evidently appears by observing Fig. 3.51, the emission band intensity generally lowers with the increasing Eu^{2+} concentration. Therefore, the best samples in terms of UV excited luminescence emission resulted to be the low doped ones (*i.e.* 1% Eu and 5% Eu).

The excitation spectrum ($\lambda_{em} = 465 \text{ nm}$) of a representative sample (1% Eu) of the $\text{Sr}_2\text{MgSi}_2\text{O}_7:\text{Eu}^{2+}$ series is reported in Fig. 3.52. The excitation spectra were similar for the whole series of samples and resulted to be quite complicated and probably disturbed by the presence of persistent luminescence that causes a continue emission even if no excitation occurs. Anyway, the measurements were carried out mainly to confirm that the 300 nm excitation wavelength selected for the previous measurements was able to produce an efficient intensity of the emission band.

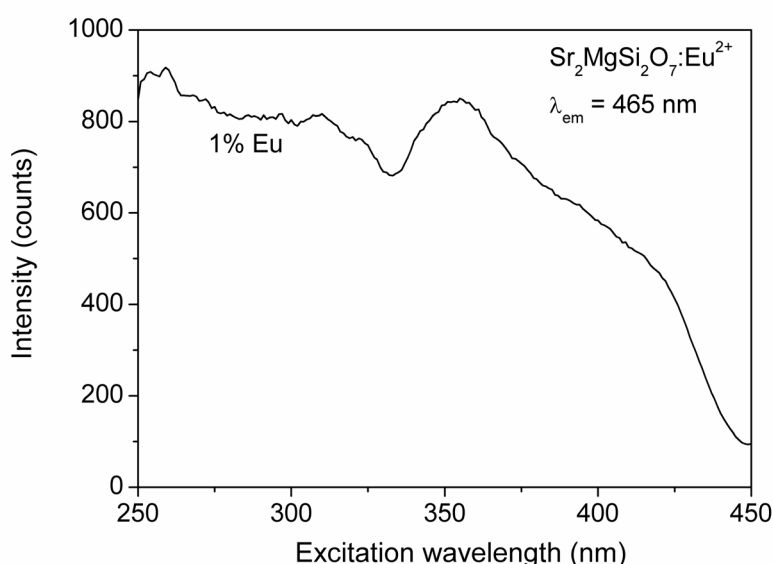


Figure 3.52 Excitation spectrum of a representative sample (1% Eu) of the $\text{Sr}_2\text{MgSi}_2\text{O}_7:\text{Eu}^{2+}$ series ($\lambda_{em} = 465 \text{ nm}$) at RT.

The UV excited luminescence of the $\text{Sr}_2\text{MgSi}_2\text{O}_7:\text{Eu}^{2+}$ material was also measured at 77 K (liquid nitrogen temperature) for some samples of the series. These measurements were carried out by merging a quartz tube containing the sample powder into a liquid nitrogen bath placed inside the spectrophotometer camera. Fig. 3.53 shows a comparison of the emission spectra at RT and at 77 K for a representative sample of the series (1% Eu). The emission peak position is the same at both temperatures, while its width (Full Width at Half Maximum,

i.e. FWHM) changes at 77 K and the emission band becomes narrower. The increase in FWHM of the emission band with increasing temperature can be explained by considering the strong interaction between the excited $4f^65d^1$ configuration of Eu^{2+} ions and the lattice phonons. With respect to the lower temperature, at RT the population density of phonons is increased and the electron–phonon interaction is dominant; this phenomenon causes a broadening of the emission band. For the reasons mentioned before and also for the different setup used in RT and 77 K measurements, no reliable observation about the comparison of the emission intensities can be done.

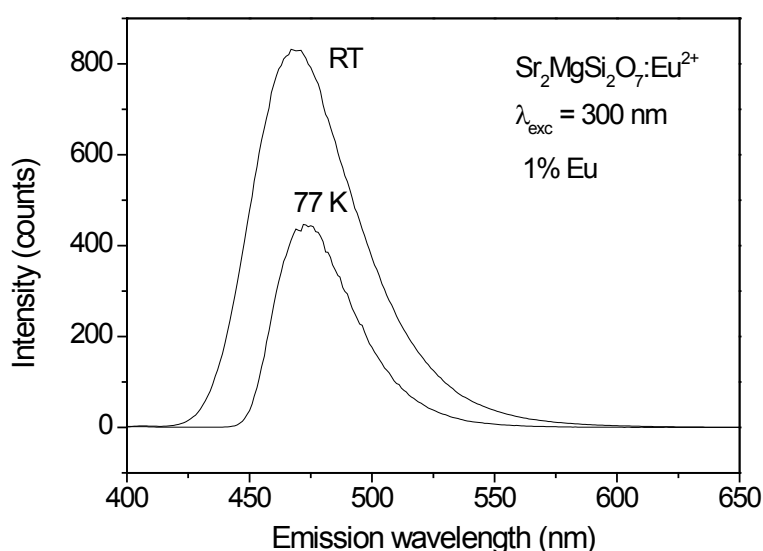


Figure 3.53 UV excited emission spectra of a representative sample (1% Eu) of the $\text{Sr}_2\text{MgSi}_2\text{O}_7:\text{Eu}^{2+}$ series ($\lambda_{\text{exc}} = 300 \text{ nm}$) measured at RT and at 77 K.

In order to investigate the presence of Eu^{3+} suggested by the XRD measurements, the samples of the $\text{Sr}_2\text{MgSi}_2\text{O}_7:\text{Eu}^{2+}$ series were also excited at a different wavelength from 300 nm. As confirmed in Fig. 3.54 by the excitation spectrum ($\lambda_{\text{em}} = 615 \text{ nm}$) of 100% Eu sample, a good excitation wavelength for detecting the typical Eu^{3+} main emission at ca. 615 nm resulted to be 395 nm.

As already discussed in this thesis, this wavelength is associated to the transition between the ${}^7F_0 \rightarrow {}^5L_6$ levels of the $\text{Eu}^{3+} 4f^6$ configuration.

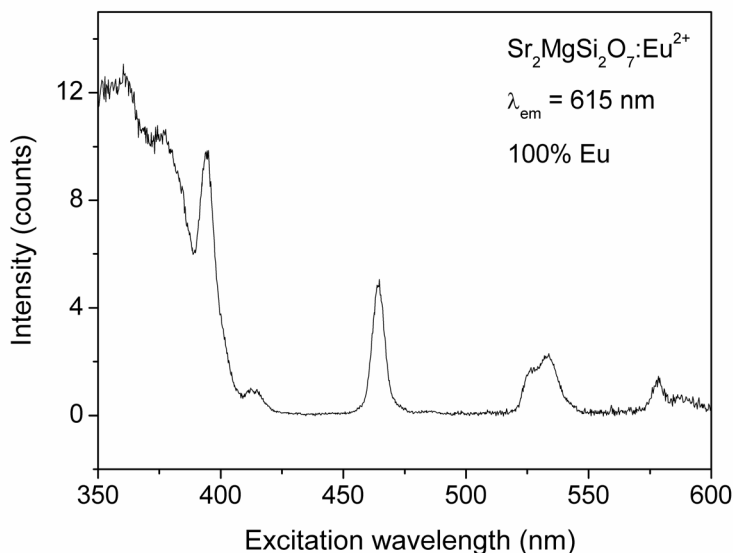


Figure 3.54 Excitation spectrum of a sample (100% Eu) of the $\text{Sr}_2\text{MgSi}_2\text{O}_7:\text{Eu}^{2+}$ series ($\lambda_{\text{em}} = 615 \text{ nm}$) at RT.

Only the emission spectra of high doped samples (100% Eu and 80% Eu) showed, at RT, the typical narrow emission bands of trivalent europium with the main peak at ca. 615 nm, which is associated to the ${}^5D_0 \rightarrow {}^7F_2$ transition of the $4f^6$ configuration (Fig. 3.55). Moreover, also the broad band of the Eu^{2+} emission was visible with this excitation wavelength. The peaks of the Eu^{3+} emission, however, were weaker in the 80% Eu sample and did not appear in the spectra of the remaining samples of the series (which for this reason are not reported). This fact indicates that the trivalent europium, which could be responsible for the different crystalline structure that appeared in the XRD patterns of high doped samples (from 20-40 to 100% Eu), is not present or cannot be detected with these optical measurements in all the samples but only for nominal Eu^{2+} concentrations at least higher than 60%. Therefore, a further investigation on the $\text{Sr}_2\text{MgSi}_2\text{O}_7:\text{Eu}^{2+}$ series was necessary to confirm the

presence of trivalent europium not only in 80 and 100% Eu but also in the less doped samples and this goal was achieved by means of XANES measurements (see the final part of the present study).

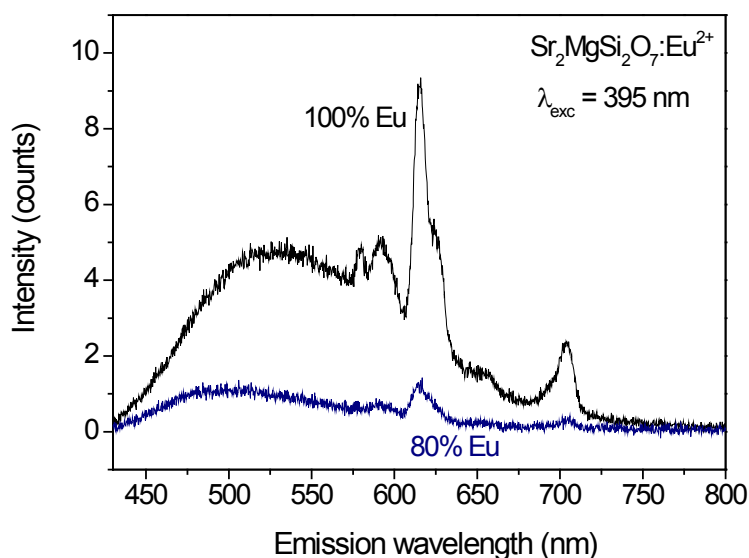


Figure 3.55 UV excited emission spectra ($\lambda_{\text{exc}} = 395 \text{ nm}$) of some representative samples of the $\text{Sr}_2\text{MgSi}_2\text{O}_7:\text{Eu}^{2+}$ series (100% Eu and 80% Eu) measured at RT.

The UV excited luminescence properties were also studied for the $\text{Sr}_2\text{MgSi}_2\text{O}_7:\text{Eu}^{2+},\text{Dy}^{3+}$ series of samples.

In Fig. 3.56 the emission spectra ($\lambda_{\text{exc}} = 300 \text{ nm}$) at RT of the six co-doped samples with nominal constant Eu^{2+} and varying Dy^{3+} fractions are reported. The shape and position of the wide emission band were the same of the $\text{Sr}_2\text{MgSi}_2\text{O}_7:\text{Eu}^{2+}$ series and they resulted to be independent of the different Dy^{3+} co-doping level. The emission is therefore totally associated to the divalent europium (which acts as the luminescent center in the host lattice), and no additional peaks which could concern the Dy^{3+} presence appeared in any of the samples, in good agreement with the literature.⁴⁸

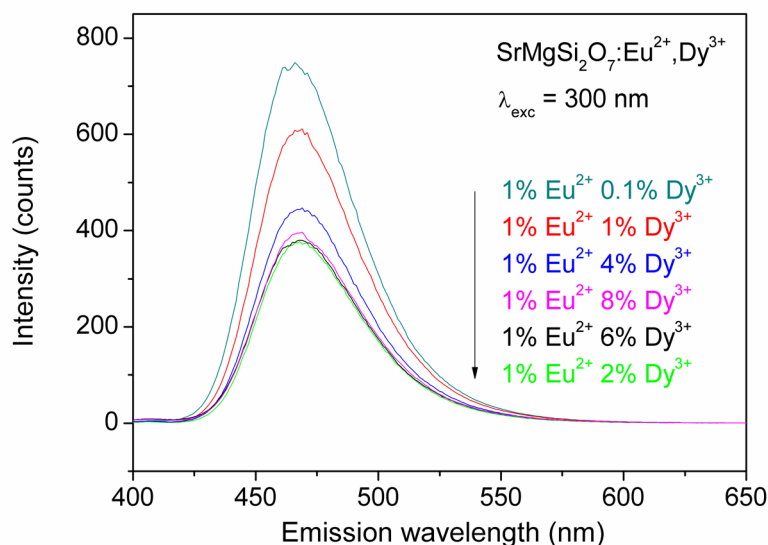


Figure 3.56 UV excited emission spectra of the Sr₂MgSi₂O₇:Eu²⁺,Dy³⁺ series (λ_{exc} = 300 nm) at RT.

For the previously explained reason no reliable comparison of the emission intensities between the samples can be made; in general, however, the Sr₂MgSi₂O₇:Eu²⁺,Dy³⁺ samples showed an efficient intensity of the UV excited luminescence emission.

Even the excitation spectra were very similar to the ones that were previously shown for the Sr₂MgSi₂O₇:Eu²⁺ series and they confirmed the good choice for the selected 300 nm excitation wavelength. The same observation can be made for the 77 K excitation spectra. Examples of an excitation spectrum of a representative sample (1% Eu_8% Dy) at RT together with one at 77 K are reported in Fig. 3.57.

The emission spectra of the co-doped series of samples were also measured at 77 K, with the same procedure described for the Sr₂MgSi₂O₇:Eu²⁺ series. Fig. 3.58 shows the comparison between the UV excited luminescence spectra at the liquid nitrogen temperature and at RT for a couple of representative samples (1% Eu_2% Dy and 1% Eu_8% Dy).

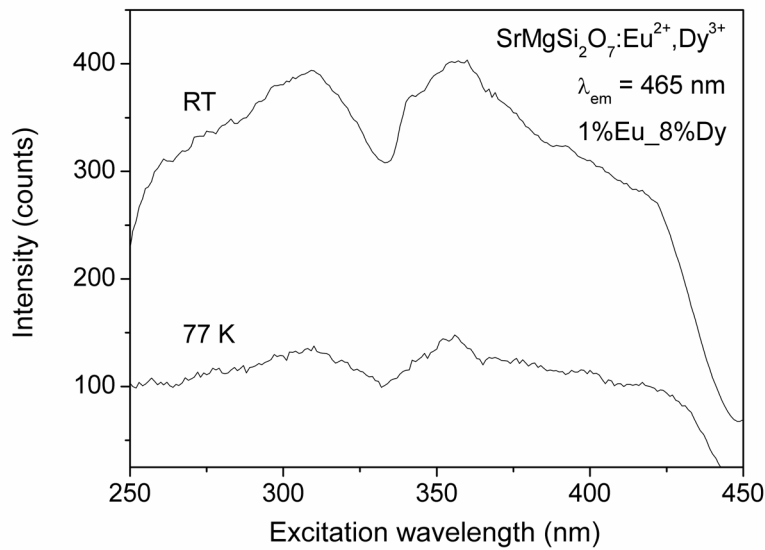


Figure 3.57 Excitation spectra of a representative sample (1% Eu_8% Dy) of the $\text{Sr}_2\text{MgSi}_2\text{O}_7:\text{Eu}^{2+},\text{Dy}^{3+}$ series ($\lambda_{\text{em}} = 465 \text{ nm}$) at RT and at 77 K.

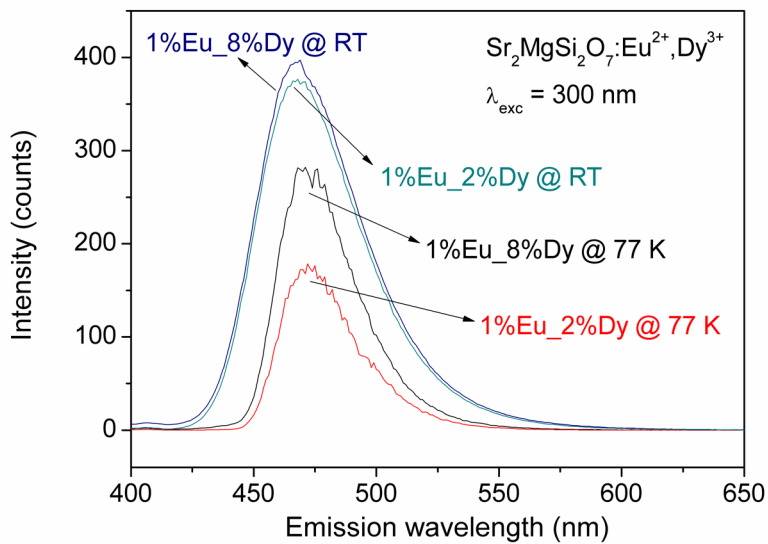


Figure 3.58 UV excited emission spectra of two representative samples (1% Eu_2%Dy and 1% Eu_8% Dy) of the $\text{Sr}_2\text{MgSi}_2\text{O}_7:\text{Eu}^{2+},\text{Dy}^{3+}$ series ($\lambda_{\text{exc}} = 300 \text{ nm}$) measured at RT and at 77 K.

Except for a noisier signal and some oscillations at the top of the 1%Eu_8%Dy peak, the 77 K spectra showed exactly the same features of the ones measured for the $\text{Sr}_2\text{MgSi}_2\text{O}_7:\text{Eu}^{2+}$ series: in comparison with the RT spectra the position of the emission band remains unvaried while its width decreases, for the same reason explained before for the Eu^{2+} -doped series. In fact, the behavior of 1% Eu_2% Dy and 1% Eu_8% Dy samples is equal to the one shown in Fig. 3.53 by 1% Eu sample and this was expected since the nominal Eu^{2+} (*i.e.* the ion acting as the luminescent center) content is the same in all three samples.

Finally, the presence of trivalent europium was investigated also in the co-doped series at the same way that was previously described for $\text{Sr}_2\text{MgSi}_2\text{O}_7:\text{Eu}^{2+}$ samples. But in this case no Eu^{3+} signals were found in any of the six co-doped samples. Following the results of the Eu^{3+} investigation in the previous series, this was not surprising at all in consideration of the low nominal europium content which characterizes the whole $\text{Sr}_2\text{MgSi}_2\text{O}_7:\text{Eu}^{2+},\text{Dy}^{3+}$ series.

Persistent luminescence

Persistent luminescence measurements were carried out on some samples (those with the best UV excited luminescence properties) of the $\text{Sr}_2\text{MgSi}_2\text{O}_7:\text{Eu}^{2+}$ series, but none of them showed relevant strength and duration of the emission.

The persistent luminescence was measured for each sample by exciting the powder with a UV lamp ($\lambda_{\text{exc}} = 254 \text{ nm}$) for 5 minutes and then acquiring the emission spectra (in bio-chemiluminescence mode) after some defined time intervals (delays).

In Fig. 3.59 the persistent luminescence spectra of sample 1% Eu (the best of the series) measured after 1, 2 and 3 minutes from the ending of the exposure to the excitation source are reported. All spectra were characterized by a noisy and weak emission and already after a 3 minutes delay the intensity was very low, thus indicating a very small duration of the persistent luminescence. Anyway, the persistent luminescence band was observed to be

centered at the same wavelength (*ca.* 470 nm) as the UV excited emission band of the material (see Fig. 3.51). Hence, the luminescent centers which are responsible for the persistent luminescence are the same that are responsible for the conventional UV excited emission.

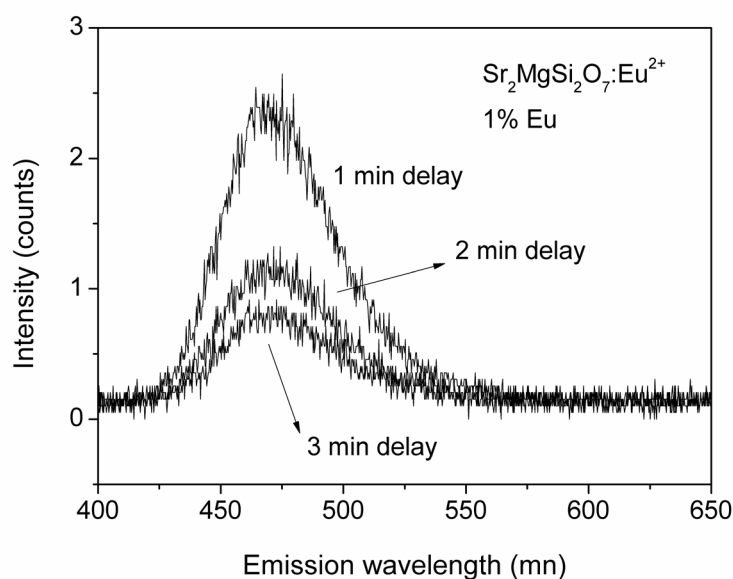


Figure 3.59 Persistent luminescence spectra of a representative sample (1% Eu) of the $\text{Sr}_2\text{MgSi}_2\text{O}_7:\text{Eu}^{2+}$ series after exposure to radiation from a UV lamp ($\lambda_{\text{exc}} = 254$ nm) at RT. Gate time = 1 ms. Delays: 60, 120 and 180 s.

In order to study the effect of the co-doping trivalent rare earth ion, the persistent luminescence properties of the $\text{Sr}_2\text{MgSi}_2\text{O}_7:\text{Eu}^{2+},\text{Dy}^{3+}$ series of samples were investigated, with the same procedure just described for the previous series.

Fig. 3.60 shows the persistent luminescence spectra of the six co-doped samples at the starting maximum value of intensity (1 minute delay), which of course decreased for bigger delays. As for the previous series, the shape and position of the band were exactly the same of UV excited emission band, thus confirming that in co-doped materials the Eu^{2+} ions are the only that act as luminescent centers in the persistent luminescence mechanism. But it is evident

that the emission appeared much stronger in each sample of the co-doped series, in comparison with the 1% Eu^{2+} -doped sample. Even the lowest co-doped sample 1% Eu _0.1% Dy showed enhanced persistent luminescence intensity with respect to 1% Eu sample, though its value resulted very low when compared to the other co-doped samples. This means that Dy^{3+} ions enhanced the persistent luminescence intensity, without causing any change in the position and in the shape of the spectrum, in agreement with the previous studies.⁴⁹

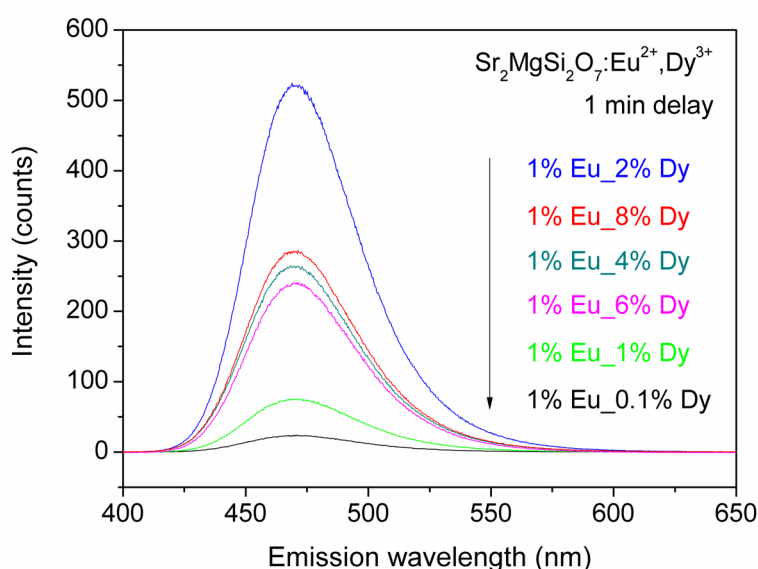


Figure 3.60 Persistent luminescence spectra of the $\text{Sr}_2\text{MgSi}_2\text{O}_7:\text{Eu}^{2+},\text{Dy}^{3+}$ series after exposure to radiation from a UV lamp ($\lambda_{\text{exc}} = 254 \text{ nm}$) at RT. Gate time = 1 ms. Delay: 60 s.

Taking into account the usual observation about the uncertainty in a quantitative comparison of the intensities between different samples, it seems quite evident that the strongest persistent luminescence occurred in sample 1% Eu _2% Dy , while for lower (0.1 and 1%) and also for higher (4, 6 and 8%) Dy^{3+} molar concentrations the intensity was weaker.

Similar results were observed about the duration of the persistent luminescence, which, in general, was very satisfying for the whole $\text{Sr}_2\text{MgSi}_2\text{O}_7:\text{Eu}^{2+},\text{Dy}^{3+}$ series. It is worth noting that the persistent luminescence observed by human eye was much longer than the one that could be measured by the instrument. For most of co-doped samples the persistent luminescence was observed for at least 24 h by human eye, a very long duration which was in agreement with the literature data.⁵⁰ With the spectrophotometer it was possible to measure the persistent luminescence decay of all samples for a period of 3 h (4 h for sample 1% Eu_2% Dy). In Fig. 3.61 the decay is reported, for each sample, as the variation with time of the persistent luminescence emission peak area.

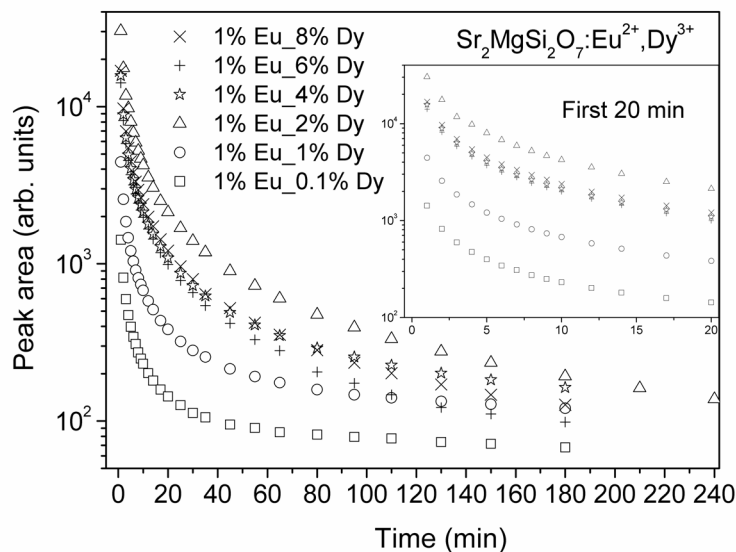


Figure 3.61 Persistent luminescence decay curves (peak area VS time) of the $\text{Sr}_2\text{MgSi}_2\text{O}_7:\text{Eu}^{2+},\text{Dy}^{3+}$ series. Inset: first 20 minutes.

According to the variation of the curve slopes, several different processes seem to describe the persistent luminescence decay of all the samples. Most of the processes are rapid and occur more or less in the early 20 minutes, while the slow final one extends up to hours. However, more elaborated studies and

additional work are needed to analyze and describe in a complete way the persistent luminescence decay of these materials.

Anyway, the most relevant aspect concerns the resulting enhanced duration and intensity of the persistent luminescence by means of the trivalent rare earth ions (Dy^{3+}) co-doping. This was confirmed to occur not only for intermediate values of the co-doping level, but also for low and high values. However, both for the intensity and the duration of the persistent luminescence, the best sample of the series resulted to be 1% Eu_2% Dy, *i.e.* the one with a $\text{Eu}^{2+}:\text{Dy}^{3+}$ molar concentration ratio of 1:2. Fig. 3.62 shows the 3D wavelength resolved persistent luminescence decay of the sample, from which the trend of the main peak with the increasing time can easily be observed.

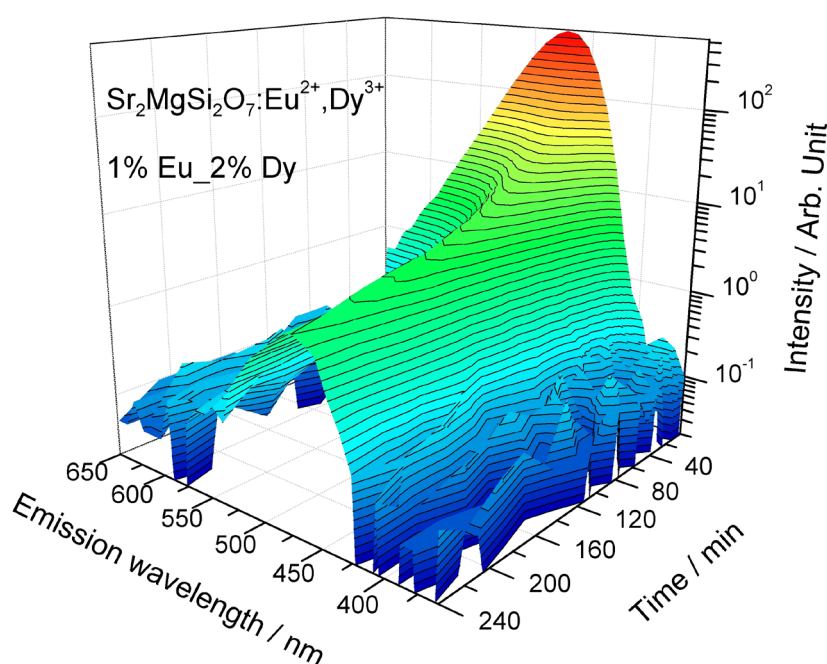


Figure 3.62 Wavelength resolved persistent luminescence decay curve of a representative sample (1% Eu_2%Dy) of the $\text{Sr}_2\text{MgSi}_2\text{O}_7:\text{Eu}^{2+},\text{Dy}^{3+}$ series.

The observed 1:2 optimal value of the $\text{Eu}^{2+}:\text{Dy}^{3+}$ molar concentration ratio is in good agreement with previous studies^{48,51} and can be explained considering

the role of Dy^{3+} ions in the persistent luminescence mechanism. As mentioned before in the introduction (see § 1.3.4), Dy^{3+} ions mostly act as the traps in the host or create them through charge compensation effects which cause lattice defects. Therefore, the Dy^{3+} ions concentration regulates the traps density and maybe also depth. The latter strongly influences the duration of the afterglow, since deeper traps release the carriers slowly (producing a longer duration of the emission), while too deep traps may not be emptied at all at room temperature. As a consequence, for an optimal duration of the persistent luminescence, the Dy^{3+} ions concentration must be neither too low nor too high. Such considerations can explain why in this work both the samples with lower and those with higher Dy^{3+} concentration than 2% did not showed the same optimal duration of persistent luminescence of the 2% Dy^{3+} co-doped sample.

Synchrotron radiation measurements

In order to get further information about the unclear nature of the $\text{Sr}_2\text{MgSi}_2\text{O}_7:\text{Eu}^{2+}$ series of samples some synchrotron radiation measurements were programmed. In particular, excitation and emission spectra with the synchrotron radiation at selected temperatures as well as XANES measurements were performed.

Excitation and emission spectra have been measured for sample 100% Eu, the one that was considered as the most interesting to investigate, and so only preliminary investigation has been accomplished. Figs. 3.63 and 3.64 show, respectively, the synchrotron radiation excitation spectra (UV-VUV range) and the emission spectra (visible range) of sample 100% Eu, which were measured at 9 and 300 K with different emission and excitation wavelengths.

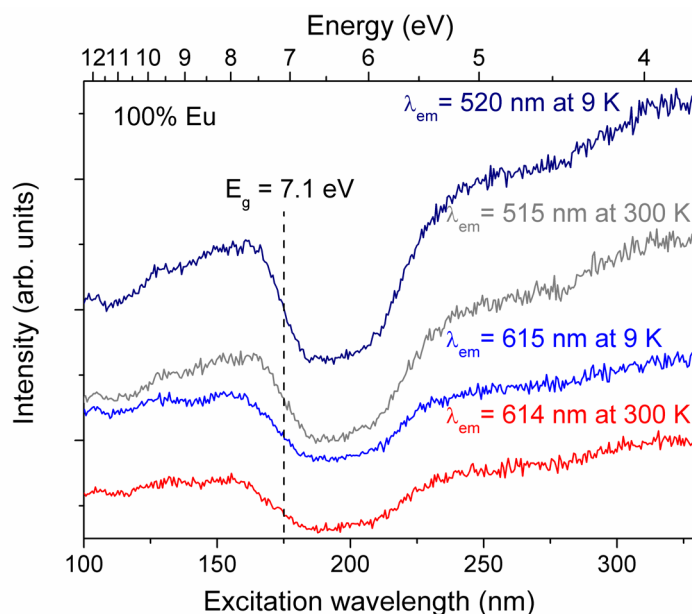


Figure 3.63 The UV-VUV synchrotron radiation excitation spectra of a sample (100% Eu) of the $\text{Sr}_2\text{MgSi}_2\text{O}_7:\text{Eu}^{2+}$ series at 9 and 300 K and with selected emission wavelengths.

The excitation spectra resulted to be quite weak and therefore noisy. Anyway, no significant differences appeared between the spectra collected at 9 K and at 300 K, except for a little decrease of the intensity at the higher temperature. The selected emission wavelengths were those that are associated to the maxima of Eu^{2+} and Eu^{3+} main emission bands (respectively, 515-520 nm and 614-615 nm). Moreover, the most pronounced feature at ca. 175 nm, which is clearer in the excitation spectrum at 9 K with $\lambda_{\text{em}} = 520$ nm, can be interpreted as the host excitation. The position of this feature made possible to estimate the band gap energy E_g , *i.e.* the energy difference between the top of the valence band and the bottom of the conduction band, of the material at 9 K. The estimated E_g value was 7.1 ± 0.1 eV, which corresponds very well to the value (ca. 7.1 eV) that resulted in some previous studies on the $\text{Sr}_2\text{MgSi}_2\text{O}_7:\text{Eu}^{2+}$ material.⁵²

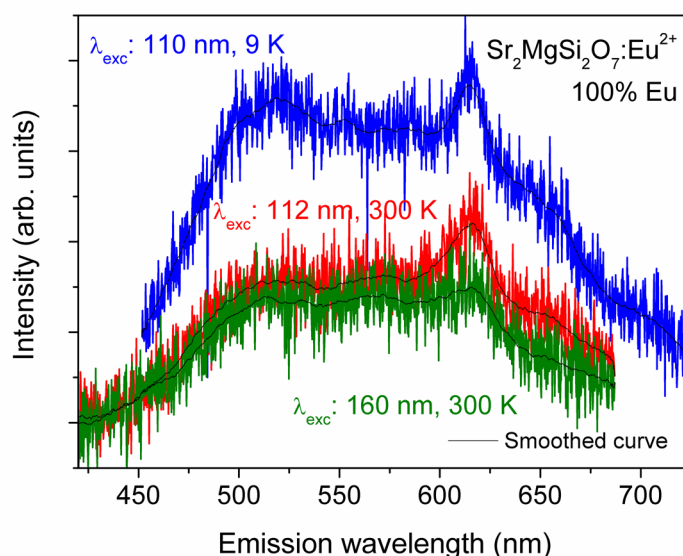


Figure 3.64 The emission spectra (in the visible range) of a sample (100% Eu) of the $\text{Sr}_2\text{MgSi}_2\text{O}_7:\text{Eu}^{2+}$ series at 9 and 300 K and with selected excitation wavelengths. Black lines: smoothed data (smoothing: Adjacent-Averaging, 50 pts).

The emission spectra were characterized by a very weak and noisy signal and therefore the quality of the measurements was not good. In order to improve the visualization of the curves shape, a smoothing of the data was carried out. The most interesting indication was given by the emission spectrum at 9 K with $\lambda_{\text{exc}} = 110$ nm, which showed both the Eu^{2+} (centered at ca. 520 nm) and the Eu^{3+} (ca. 615 nm) emission bands, with the same peak positions as those measured in the UV excited luminescence spectra, despite of the different excitation wavelength. Since at such a low temperature there is no persistent luminescence which could have influenced the investigation on the trivalent europium presence, the hypothesis that the latter should be caused by an insufficient reduction of the starting trivalent europium during thermal treatment seems to be enforced and a further confirmation came out from X-ray absorption (XANES) measurements.

In fact, in order to investigate the valence of the europium ions in the materials, XANES measurements were performed on most of the $\text{Sr}_2\text{MgSi}_2\text{O}_7:\text{Eu}^{2+}$ series of samples.

Fig. 3.65 shows the Eu(L_{III}) edge XANES spectra of the Sr₂MgSi₂O₇:Eu²⁺ complete series (with the exception of 5% Eu and 10% Eu samples) measured at 300 K and at 10 K. From them the Eu²⁺:Eu³⁺ ratio in the materials can be investigated, since each valence is associated to a well defined absorbance peak on the absorption edge.

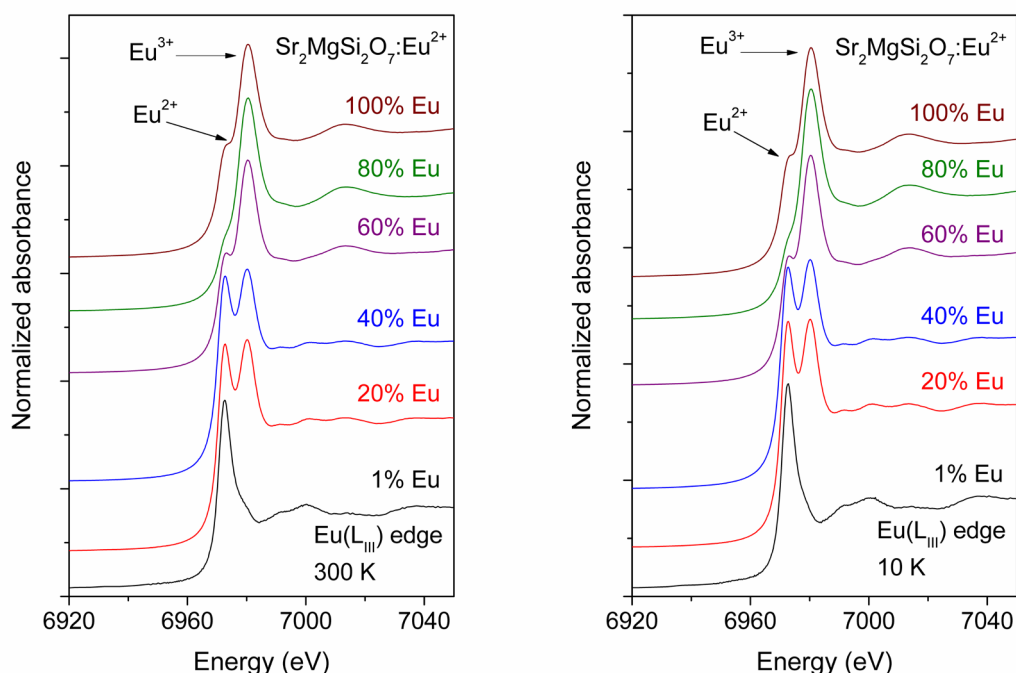


Figure 3.65 Eu(L_{III}) edge XANES spectra of the Sr₂MgSi₂O₇:Eu²⁺ series (with the exception of 5% Eu and 10% Eu samples) at 300 K (left) and at 10 K (right).

The observed results were quite clear: both at 300 K and at 10 K, all the examined samples except the low doped 1% Eu showed a relevant presence of trivalent europium which became more and more dominant with the increasing doping level. This fact confirmed that the growing molar concentration (at least starting from the nominal 20% but even lower values could be problematic) of europium as a dopant in the host lattice caused an increasing presence of trivalent europium, while typically for Sr₂MgSi₂O₇:Eu²⁺ material the divalent form

dominates.⁵³ This fact confirms that a different structure than $\text{Sr}_2\text{MgSi}_2\text{O}_7:\text{Eu}^{2+}$ characterizes most of the investigated samples. Moreover, the spectra resulted to be almost identical at both temperatures and the behavior of the $\text{Eu}^{2+}:\text{Eu}^{3+}$ ratio did not change at all at 10 K. Since the creation of Eu^{3+} species, or Eu^{2+} -hole pair, is essential in the mechanism of persistent luminescence, the 10 K measurements were performed to verify that the investigation on the Eu^{3+} presence were not affected by the persistent luminescence, which is not present at 10 K.

In conclusion, the XANES measurements confirmed that the unknown crystalline structure which arose out of the XRD pattern of most of the $\text{Sr}_2\text{MgSi}_2\text{O}_7:\text{Eu}^{2+}$ series of samples is due to the relevant presence of trivalent europium in the material, caused by an insufficient reduction of the europium from trivalent to divalent form during the solid state reaction.

3.4.3 Conclusions

Two different series of distrontium magnesium disilicate materials with varying (co)-doping levels were synthesized and characterized.

The $\text{Sr}_2\text{MgSi}_2\text{O}_7:\text{Eu}^{2+}$ series gave heterogeneous and unfulfilling results, since the high doped samples, apart from showing poor luminescence properties, did not consist of the expected final composition. Their characterization (XRD and XANES measurements above all) proved that this was caused by an incomplete reduction of trivalent europium to divalent form during the solid state reaction, despite of the reducing $\text{N}_2 + 10\% \text{H}_2$ atmosphere which was applied during the thermal treatment. Probably the annealed Eu_2O_3 that was employed as a starting reagent was too strongly passivated to be sufficiently reactive for its reduction. Hence the purposes to replace trivalent with divalent europium oxide as a starting reagent, or alternatively to facilitate the Eu^{3+} reduction by using a freshly prepared Eu_2O_3 seem to be a promising way to solve the problem. Anyway, some preliminary tries to get the EuO compound from Eu_2O_3 (by means of its annealing at 700 °C in a strongly

reducing ammonia atmosphere) or from europium oxalate (with a first annealing in air in order to get the fresh Eu_2O_3 and then a strongly reducing thermal treatment in ammonia atmosphere) were not successful, as well as the employment of fresh Eu_2O_3 (obtained from europium oxalate) in the solid state reaction. Therefore, further activity and study would be needed in order to optimize the preparation procedure and get the expected final material.

On the contrary, the low doped samples of the $\text{Sr}_2\text{MgSi}_2\text{O}_7:\text{Eu}^{2+}$ series showed a good quality of the disilicates, in terms of formation and purity of the crystalline structure. Also their UV excited luminescence properties were very good, showing a strong emission typical of Eu^{2+} , but the persistent luminescence resulted to have very weak intensity and duration. The comparison of the 1% Eu^{2+} -doped sample with the Dy^{3+} co-doped ones containing the same Eu^{2+} fraction definitely indicated that the lack of trivalent rare earth ions in the $\text{Sr}_2\text{MgSi}_2\text{O}_7:\text{Eu}^{2+}$ materials should be the main reason for their poor persistent luminescence. Anyway, further studies on these materials are needed; in particular, thermoluminescence analysis certainly can add important information on the samples and hence be helpful in the interpretation of the persistent luminescence mechanism and properties of the materials.

Definitely better results came out from the $\text{Sr}_2\text{MgSi}_2\text{O}_7:\text{Eu}^{2+},\text{Dy}^{3+}$ series. The samples showed an appreciable quality of the crystalline structure, though some small amounts of impurities were present but without affecting the remarkable luminescence properties of the materials. The UV excited luminescence was characterized by a good emission and did not show any relevant differences from the low doped samples of the $\text{Sr}_2\text{MgSi}_2\text{O}_7:\text{Eu}^{2+}$ series, as a confirmation that the Dy^{3+} co-doping has no influence on the UV excited luminescence properties of the material. On the contrary, its beneficial role was totally pointed out by the persistent luminescence properties, which were really satisfying for the whole series of samples. In fact, as mentioned before, the comparison between the co-doped $\text{Sr}_2\text{MgSi}_2\text{O}_7:\text{Eu}^{2+},\text{Dy}^{3+}$ series of samples and the 1% Eu^{2+} -doped one showed a huge enhancement in terms of the strength and duration of the emission in the co-doped materials, in agreement with the

theory. The literature⁵⁰ value of a 25 h (or more) duration of the afterglow was confirmed for the $\text{Sr}_2\text{MgSi}_2\text{O}_7:\text{Eu}^{2+},\text{Dy}^{3+}$ series and the best sample, both for the strength and for the duration of the persistent luminescence, resulted to be the 2% Dy^{3+} -co-doped one, *i.e.* the one with a 1:2 $\text{Eu}^{2+}:\text{Dy}^{3+}$ ratio, which was in concordance with some previous studies.^{48,51} Moreover, in terms of the co-doping fraction, this sample was intermediate within the $\text{Sr}_2\text{MgSi}_2\text{O}_7:\text{Eu}^{2+},\text{Dy}^{3+}$ series, as a confirmation that for an optimal regulation of the traps depth, which leads to the best persistent luminescence duration, the trivalent rare earth content cannot be either too high or too low. However, an even more complete description of the $\text{Sr}_2\text{MgSi}_2\text{O}_7:\text{Eu}^{2+},\text{Dy}^{3+}$ series could be achieved by means of thermoluminescence and synchrotron radiation characterizations, which make possible the investigation of the electronic and defect energy level structure of the materials.

List of references:

- (1) Bazzi, R.; Flores-Gonzalez, M. A.; Louis, C.; Lebbou, K.; Dujardin, C.; Brenier, A.; Zhang, W.; Tillement, O.; Bernstein, E.; Perriat, P. *J. Lumin.* **2003**, *102*, 445-450.
- (2) Stöber, W.; Fink, A.; Bohn, E. *J. Colloid Interface Sci.* **1968**, *26*, 62-69.
- (3) Chen, T. M.; Brauer, G. M. *J. Dent. Res.* **1982**, *61*, 1439-1443.
- (4) Freris, I.; Riello, P.; Enrichi, F.; Cristofori, D.; Benedetti, A. *Optical Materials* **2011**, *33*, 1745-1752.
- (5) Reisfeld, R.; Jorgensen, C. K. *Lasers and excited states of rare earths*; Springer-Verlag: Berlin; New York, 1977.
- (6) Reisfeld, R.; Jorgensen, C. K. In *Handbook on the Physics and Chemistry of Rare earths*; Gschneider Jr., K. A.; Eyring, L.; Hüfner, S., Eds.; Elsevier: Amsterdam, 1987.
- (7) Lezhnina, M. M.; Jüstel, T.; Kätker, H.; Wiechert, D. U.; Kynast, U. H. *Adv. Funct. Mater.* **2006**, *16*, 935-942.
- (8) Solarz, P.; Ryba-Romanowski, W. *Phys. Rev. B* **2005**, *72*, 075105.
- (9) Ryba-Romanowski, W.; Solarz, P.; Dominiak-Dzik, G.; Gusowski, M. *Opt. Mater.* **2006**, *28*, 77-84.
- (10) Zhorin, V. V.; Liu, G. K. *J. Alloys Compd.* **1998**, *275-277*, 137-141.
- (11) Liu, G.; Chen, X. *Handbook on the Physics and Chemistry of Rare Earths* **2007**, *37*, 99-169.
- (12) Speghini, A.; Bettinelli, M.; Riello, P.; Bucella, S.; Benedetti, A. *J. Mater. Res.* **2005**, *20*, 2780-2791.
- (13) Enrichi, F.; Riccò, R.; Scopece, P.; Parma, A.; Mazaheri, A. R.; Riello, P.; Benedetti, A. *J. Nanopart. Res.* **2009**, *12*, 1925-1931.
- (14) Riello, P.; Bucella, S.; Brunelli, D.; Fossa, F.; Benedetti, A.; Trave, E.; Mazzoldi, P. *Opt. Mater.* **2006**, *28*, 1261-1265.
- (15) Wakefield, G.; Keron, H. A.; Dobson, P. J.; Hutchison, J. L. *J. Colloid Interface Sci.* **1999**, *215*, 179-182.

- (16) Riello, P.; Bucella, S.; Cristofori, D.; Benedetti, A.; Polloni, R.; Trave, E.; Mazzoldi, P. *Chem. Phys. Lett.* **2006**, *431*, 326-331.
- (17) Wovchko, E. A.; Camp, J. C.; Glass Jr., J. A.; Yates Jr., J. T. *Langmuir* **1995**, *11*, 2592-2599.
- (18) Hench, L. L.; West, J. K. *Chem. Rev.* **1990**, *90*, 33-72.
- (19) Pelmeshnikov, A. G.; Morosi, G.; Gamba, A. *J. Phys. Chem.* **1991**, *95*, 10037-10041.
- (20) Dhas, N. A.; Gedanken, A. *J. Phys. Chem. B* **1997**, *101*, 9495-9503.
- (21) *Immobilized Biomolecules in Analysis—A Practical Approach*; Cass, T.; Ligler, F. S., Eds.; Oxford University Press: New York, 1998.
- (22) *Immobilized Cells & Enzymes: A Practical Approach*; Woodward, J., Ed.; IRL Press: Oxford, U.K., 1985.
- (23) Subramanian A.; Kennel S. J.; Oden P. I.; Jacobson K. B.; Woodward J.; Doktycz M. J. *Enzyme Microb. Technol.* **1999**, *24*, 26-34.
- (24) *Protein Immobilization: Fundamentals and Applications*; Taylor, R. F., Ed.; Marcel Dekker: New York, 1991.
- (25) Tisher, W.; Wedekind, F. *Topics in Current Chemistry—Immobilized Enzymes: Method and Applications*; Springer-Verlag: Berlin, 1999.
- (26) Parma, A.; Freris, I.; Riello, P.; Enrichi, F.; Cristofori, D.; Benedetti, A. *J. Lumin.* **2010**, *130*, 2429-2436.
- (27) Parma, A.; Freris, I.; Riello, P.; Cristofori, D.; de Julián Fernández, C.; Amendola, V.; Meneghetti, M.; Benedetti, A. submitted to *J. Mater. Chem.*
- (28) Marin, R. Preparazione di biolabels a base di erbio con eccitazione nell'infrarosso, Ca' Foscari Venezia, Bachelor's degree in Scienze e Tecnologie dei Materiali, 2009.
- (29) Qiao, Z.-A.; Zhang, L.; Guo, M.; Liu, Y.; Huo, Q. *Chem. Mater.* **2009**, *21*, 3823-3829.
- (30) Rouquerol, F.; Rouquerol, J.; Sing, K. *Adsorption by powders & porous solids. Principles, methodology and applications*; Academic Press: London, 1999.

- (31) Brunauer, S.; Emmett, P. H.; Teller, E. *J. Am. Chem. Soc.* **1938**, *60*, 309-319.
- (32) Barrett, E. P.; Joyner, L. G.; Halenda, P. P. *J. Am. Chem. Soc.* **1951**, *73*, 373-380.
- (33) Parma, A. Sintesi e caratterizzazione di compositi luminescenti di ossido di zirconio drogato con terbio in silice, Ca' Foscari Venezia, Bachelor's degree in Scienze e Tecnologie dei Materiali, 2005.
- (34) Jia, R.; Yang, W.; Bai, Y.; Li, T. *Opt. Mater.* **2006**, *28*, 246-249.
- (35) Chen, G.; Somesfalean, G.; Liu, Y.; Zhang, Z.; Sun, Q.; Wang, F. *Phys. Rev. B* **2007**, *75*, 195204.
- (36) Salas, P.; Angeles-Chávez, C.; Montoya, J. A.; De la Rosa, E.; Diaz-Torres, L. A.; Desirena, H.; Martínez, A.; Romero-Romo, M. A.; Morales, J. *Opt. Mater.* **2005**, *27*, 1295-1300.
- (37) McGehee, M. D.; Bergstedt, T.; Zhang, C.; Saab, A. P.; O'Regan, M. B.; Bazan, G. C.; Srdanov, V. I.; Heeger, A. J. *Adv. Mater.* **1999**, *11*, 1349-1354.
- (38) Li, H.; Inoue, S.; Machida, K.-i.; Adachi, G.-y. *Chem. Mater.* **1999**, *11*, 3171-3176.
- (39) Yan, B.; Zhou, B. *J. Photochem. Photobiol. A Chem.* **2008**, *195*, 314-322.
- (40) Binnemans, K.; Lenaerts, P.; Driesen, K.; Görrler-Walrand, C. *J. Mater. Chem.* **2004**, *14*, 191-195.
- (41) Zhao, D.; Qin, W.; Wu, C.; Qin, G.; Zhang, J.; Lü, S. *Chem. Phys. Lett.* **2004**, *388*, 400-405.
- (42) Xu, Q.; Li, L.; Liu, X.; Xu, R. *Chem. Mater.* **2002**, *14*, 549-555.
- (43) Shannon, R. D. *Acta Cryst. A* **1976**, *32*, 751-767.
- (44) Kimata, M. *Z. Kristallogr.* **1983**, *163*, 295-304.
- (45) Hölsä, J.; Isotahdon, M.; Laamanen, T.; Lastusaari, M.; Malkamäki, M.; Myllykoski, M.; Niittykoski, J. In *Proc. 11th Eur. Powder Diffr. Conf. (EPDIC 11)*; Warsaw, Poland, 2008; pp. 16-17.
- (46) Furusho, H.; Hölsä, J.; Laamanen, T.; Lastusaari, M.; Niittykoski, J.; Okajima, Y.; Yamamoto, A. *J. Lumin.* **2008**, *128*, 881-884.

- (47) Blasse, G.; Wanmaker, W. L.; ter Vrugt, J. W.; Brill, A. *Philips Res. Repts.* **1968**, *23*, 189.
- (48) Wu, H.; Hu, Y.; Wang, Y.; Zeng, B.; Mou, Z.; Deng, L.; Xie, W. *J. Alloy Compd.* **2009**, *486*, 549-553.
- (49) Aitasalo, T.; Dereń, P.; Hölsä, J.; Jungner, H.; Krupa, J.-C.; Lastusaari, M.; Legendziewicz, J.; Niittykoski, J.; Stręk, W. *J. Solid State Chem.* **2003**, *171*, 114-122.
- (50) Hölsä, J. *ECS Interface* **2009**, *18*, 42-45.
- (51) Lin, Y.; Tang, Z.; Zhang, Z.; Wang, X.; Zhang, J. *J. Mater. Sci. Lett.* **2001**, *20*, 1505-1506.
- (52) Aitasalo, T.; Hassinen, J.; Hölsä, J.; Laamanen, T.; Lastusaari, M.; Malkamäki, M.; Niittykoski, J.; Novák, P. *J. Rare Earth* **2009**, *27*, 529-538.
- (53) Carlson, S.; Hölsä, J.; Laamanen, T.; Lastusaari, M.; Malkamäki, M.; Niittykoski, J.; Valtonen, R. *Opt. Mat.* **2009**, *31*, 1877-1879.

CHAPTER 4

MAGNETIC MATERIALS

4.1 $\text{FeO}_x@ms\text{-SiO}_2$, $\text{CoFe}_2\text{O}_4@ms\text{-SiO}_2$ magnetic nanocomposites

The preparation and characterization of two nanocomposites comprising iron oxide and cobalt-iron oxide nanocrystals embedded within the pores of an amorphous SiO_2 matrix are herein reported. The mesoporous SiO_2 nanoparticles, with their high surface area and spheroidal shape of 60-70 nm, were loaded as required with aqueous solutions of $\text{Fe}(\text{NO}_3)_3 \cdot 9\text{H}_2\text{O}$ and $\text{Co}(\text{NO}_3)_2 \cdot 6\text{H}_2\text{O}$ via a wet impregnation route. The iron oxide@ms- SiO_2 nanocomposite was obtained following two consecutive thermal treatments, in air and 5% H_2 in N_2 , respectively. Four different materials with varying wt% composition of SiO_2 and iron oxide were prepared. Variation of the composition gave increasing fractions of iron oxide inside the silica pores (the nominal fractions of Fe_3O_4 with respect to the total weight of the material were 0.06, 0.17, 0.24 and 0.29, respectively). Then X-ray diffractograms (XRD), transmission electron microscopy (TEM), Raman spectroscopy, thermogravimetric (TGA) and porosimetric analyses were observed to investigate the crystallographic phase, structure and morphology of the samples. On the basis of results obtained for the iron oxide system, an additional nanocomposite containing magnetic CoFe_2O_4 nanocrystals embedded in SiO_2 nanoparticles was synthesized. The cobalt-iron oxide@ms- SiO_2 nanocomposite was obtained following a single thermal treatment in air, and characterized as for the previous materials. Herein, the aim of the study was to elucidate the magnetic properties of the nanocomposite materials. The CoFe_2O_4 oxide exhibits larger anisotropy than ferrites^{1,2} which is dependent on the Co content.^{3,4} Hence, the magnetic properties of nanoparticles based on this oxide can be tailored by controlling size and composition.⁴⁻⁶ Therefore, magnetic measurements by SQUID magnetometer were performed on both the magnetic systems and the magnetic data were analyzed, in order to extract important information such as the degree and type of magnetization with

respect to nanocrystalline/nanocomposite system, particle sizes and their distributions, as well as the blocking temperatures.

The post synthetic grafting of the composites with silane coupling agent, (3-aminopropyl)triethoxysilane (APTES), was investigated by monitoring the availability of surface silanols after the thermal treatments. As previously mentioned, surface functionalization is necessary in applications such as bio-labeling, in which further immobilization of biological molecules is required.

4.1.1 Samples preparation

Synthesis of mesoporous SiO_2 nanoparticles (*ms-SiO₂*)

The synthesis of mesoporous silica nanoparticles was adapted from the procedure by Qiao et al.⁷ and has previously been reported in this thesis (see § 3.2.1).

Synthesis of FeO_x @*ms-SiO₂* series: samples A-D

Four different samples were prepared with varying nominal fractions of impregnated iron oxide inside the silica pore network. These fractions (respectively, 6, 17, 24 and 29% for samples A, B, C, D) correspond to the calculated nominal weight % (on the total weight of composite material) of Fe_3O_4 (magnetite) which should have formed after the two consecutive thermal treatments. These values are therefore indicative and considered herein as reference values.

Each sample was obtained by impregnating mesoporous SiO_2 nanoparticles (0.3 g) with an aqueous solution (4 mL) of $\text{Fe}(\text{NO}_3)_3 \cdot 9\text{H}_2\text{O}$ salt, calculated according to the desired nominal fraction. After stirring the mesoporous SiO_2 nanoparticles in iron nitrate solutions overnight, the samples were dried by removing the solvent under reduced pressure. The impregnated silica powders were then annealed at 700 °C for 12 hours in air (first oxidating thermal treatment) and at the same temperature for 12 hours in $\text{N}_2 + 5\% \text{H}_2$ gas atmosphere (second reducing thermal treatment).

The respective quantities of $\text{Fe}(\text{NO}_3)_3 \cdot 9\text{H}_2\text{O}$ salt used for the impregnation of SiO_2 to produce samples A-D are reported in Tab. 4.1.

Table 4.1 Total amount of $\text{Fe}(\text{NO}_3)_3 \cdot 9\text{H}_2\text{O}$ used during impregnation for each sample of $\text{FeO}_x@ms\text{-SiO}_2$ series.

sample	nominal %wt of Fe_3O_4	total amount of $\text{Fe}(\text{NO}_3)_3 \cdot 9\text{H}_2\text{O}$
A	6%	0.101 g, 0.25 mmol
B	17%	0.328 g, 0.81 mmol
C	24%	0.491 g, 1.21 mmol
D	29%	0.655 g, 1.62 mmol

Synthesis of $\text{CoFe}_2\text{O}_4@ms\text{-SiO}_2$ sample

Mesoporous SiO_2 nanoparticles (0.3 g) were impregnated with an aqueous solution (4 mL) of $\text{Co}(\text{NO}_3)_2 \cdot 6\text{H}_2\text{O}$ (0.061 g, 0.21 mmol) and of $\text{Fe}(\text{NO}_3)_3 \cdot 9\text{H}_2\text{O}$ (0.168 g, 0.42 mmol) salts in accord with the required stoichiometric ratio of Co and Fe to give the desired nominal fraction of cobalt-iron oxide (CoFe_2O_4). This weight fraction of CoFe_2O_4 was fixed to 14% of the total composite weight ($\text{CoFe}_2\text{O}_4@ms\text{-SiO}_2$). After stirring the suspension overnight, the sample was dried by removing the solvent under reduced pressure. The impregnated material was annealed at 700 °C for 12 h in air.

Surface functionalization of magnetic nanocomposites with APTES

The general procedure for surface functionalization with APTES,⁸ which has already been described (see § 3.1.1), was here applied to samples B (of $\text{FeO}_x@ms\text{-SiO}_2$ series) and $\text{CoFe}_2\text{O}_4@ms\text{-SiO}_2$.

4.1.2 Results and discussion

Mesoporous SiO₂ nanoparticles (ms-SiO₂)

The mesoporous silica nanoparticles were synthesized, through the previously discussed process (see § 1.3.2) based on a templating surfactant, following the usual standard procedure that has already been described (§ 3.2.1); then they were characterized, by means of TEM and porosimetric analyses, at the same way as for precedent studies (e.g. § 3.2.2). The obtained results were, as expected, very similar to the previous and therefore their detailed discussion is not repeated here. The main features of the mesoporous silica nanoparticles that were used in the present study are resumed in the following list:

- isolated and aggregated nanoparticles with spheroidal shape;
- nanoparticles' size: 60-70 nm;
- N₂ ads./des. isothermal curve: type IV (typical of a mesoporous material);
- surface area (B.E.T. method): 1040 ± 30 m²/g;
- pore volume: 1.3 cm³/g;
- average pore diameter (B.J.H. method): ca. 2.8 nm.

Samples A-D of the FeO_x@ms-SiO₂ series

The FeO_x@ms-SiO₂ series of samples was prepared with varying nominal fractions of FeO_x impregnated in mesoporous SiO₂. On the basis of pore volume availability, four samples were obtained by varying the amount of iron salt in the impregnating solutions, thereby filling the pores to varying degrees. Accordingly, the respective nominal weight fractions of Fe₃O₄ in the samples A-D were calculated (Tab. 4.2).

Two sequential thermal treatments, in air and 5% H₂ in N₂, were conducted at 700 °C. This temperature was chosen by careful consideration, taking into account the following physical properties: the integrity of the magnetic crystals obtained at 700 °C and the subsequent availability of SiO₂ surface silanols for post functionalization.

Table 4.2 Different nominal fractions of impregnated material in the $\text{FeO}_x@\text{ms-SiO}_2$ series of samples.

sample	% v/v iron salt / pores	nominal %wt of Fe_3O_4
A	15%	6%
B	50%	17%
C	75%	24%
D	100%	29%

XRD analysis was performed on the samples A-D after the initial oxidative thermal treatment at 700 °C (Fig. 4.1). Hereby, the efficiency of the impregnation method was evaluated through the structural investigation of the resulting composite material, comprising amorphous SiO_2 and a crystalline iron oxide phase.

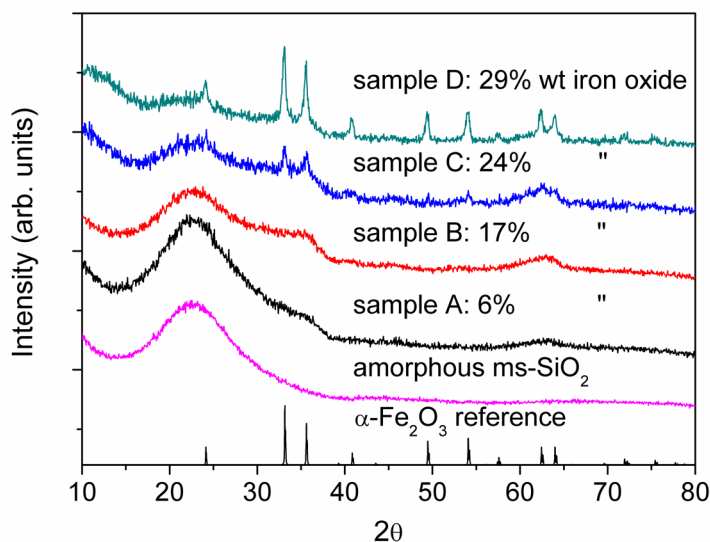


Figure 4.1 XRD patterns of: $\text{FeO}_x@\text{ms-SiO}_2$ series of samples after the first thermal treatment (air atmosphere), calcined mesoporous SiO_2 , $\alpha\text{-Fe}_2\text{O}_3$ (hematite) reference from the literature (PDF #33664).

A crystalline phase evidenced in the diffraction patterns of all composite materials, albeit with relatively weak signals in samples A and B, was determined to be α -Fe₂O₃ hematite. The sharp and intense peaks typical of pure α -Fe₂O₃ hematite (PDF #33664) are clearly visible in the diffraction patterns of C and D (Fig. 4.1). Hence, as would be expected from the oxidative treatment, a single crystalline phase of α -Fe₂O₃ hematite was found in samples C and D. Alternatively, in the samples of lowest FeO_x nominal fractions (A and B), the visible peaks are weak and broad, whereby their identification in the presence of the amorphous SiO₂ pattern is rendered difficult. Since all samples were thermally treated under identical conditions, it is expected that samples A and B would also contain crystalline α -Fe₂O₃ hematite. However, the presence of a single crystalline phase in samples A and B cannot be deduced unequivocally from their XRD analysis. The width of the diffraction peaks was qualitatively used as an indication of the crystalline phase location with respect to the mesoporous SiO₂ network. The broad peaks observed in samples A and B suggest that the crystallites are relatively small. The small dimensions of the crystallites would also be consistent with the presence of crystalline iron oxide inside the silica pores. The average pore size determined by B.E.T. was 2.8 nm. Therefore, assuming adequate impregnation of the salt precursor solutions, the small pores can potentially limit the growth of the crystals within to give a regularly structured nanocomposite material. Contrastingly, in samples C and D the hematite peaks are sharper, supporting the formation of larger crystallites which are likely to exceed the dimensions of the pores. This suggests that at least a fraction of iron oxide has formed outside the pores, yielding composite materials with reduced regularity. It was deduced from XRD analysis that effective impregnation of the mesoporous SiO₂ used in this study could be achieved with a loading amount equal to or below a nominal 50% v/v fraction of iron salt for the total pore volume (corresponding to a nominal 17% weight fraction of iron oxide with respect to the total weight). In this study, exceeding

this value proved inefficient on the basis that a fraction of the loaded material was not contained in the pore network.

The aforementioned results derived from XRD analysis of the $\text{FeO}_x@\text{ms-SiO}_2$ series were further corroborated by TEM and EDS analyses. Representative TEM micrographs of sample B demonstrate the presence of dark nanocrystals (ca. 3 nm size) embedded within the porous SiO_2 nanoparticles (Fig. 4.2).

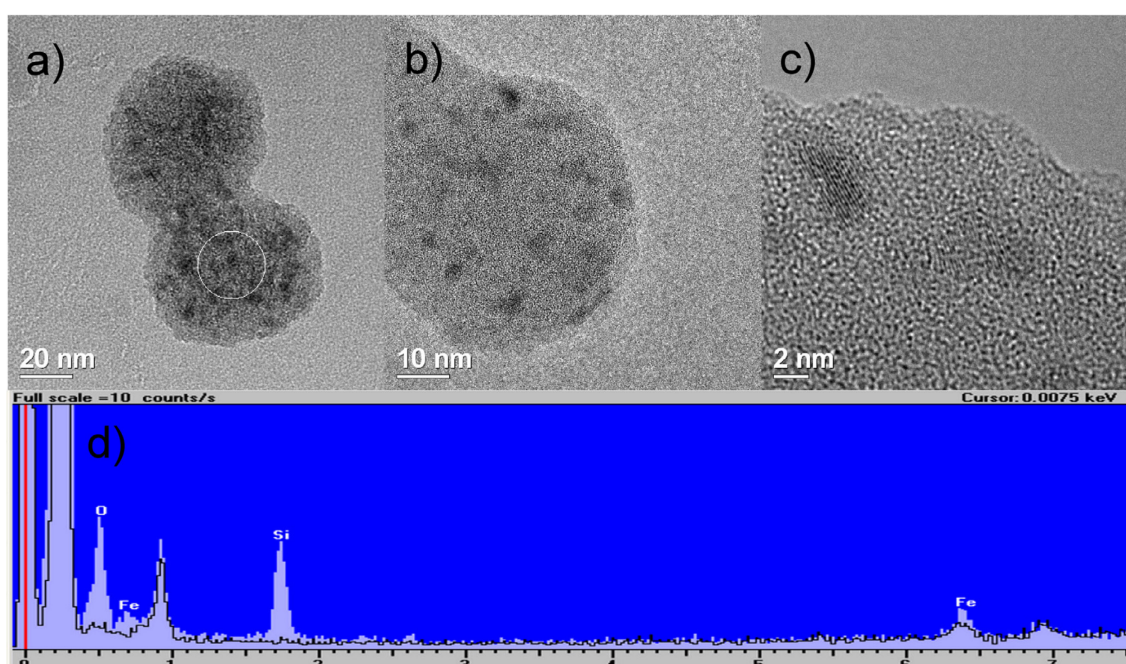


Figure 4.2 TEM micrographs at different magnifications (a-c) and EDS analysis (d) of circled area (a) of sample B.

Small domains of a crystalline phase are clearly visible in Fig. 4.2c, and agree with the presence of crystal planes for iron oxide. An EDS spectrum of the circled area in Fig. 4.2a is shown (Fig. 4.2d). The elemental analysis identified the presence of Si, O and Fe, which is attributed to the amorphous SiO_2 matrix and iron oxide nanocrystals.

In comparison to sample B, TEM micrographs of sample D showed a higher density of nanocrystals embedded in the SiO_2 matrix and the presence of larger nanocrystals outside the SiO_2 pore network (Fig. 4.3a), in concordance with

XRD findings. EDS elemental analysis (Fig. 4.3c) was in agreement with the hypothesis that the larger nanocrystals were also iron oxide.

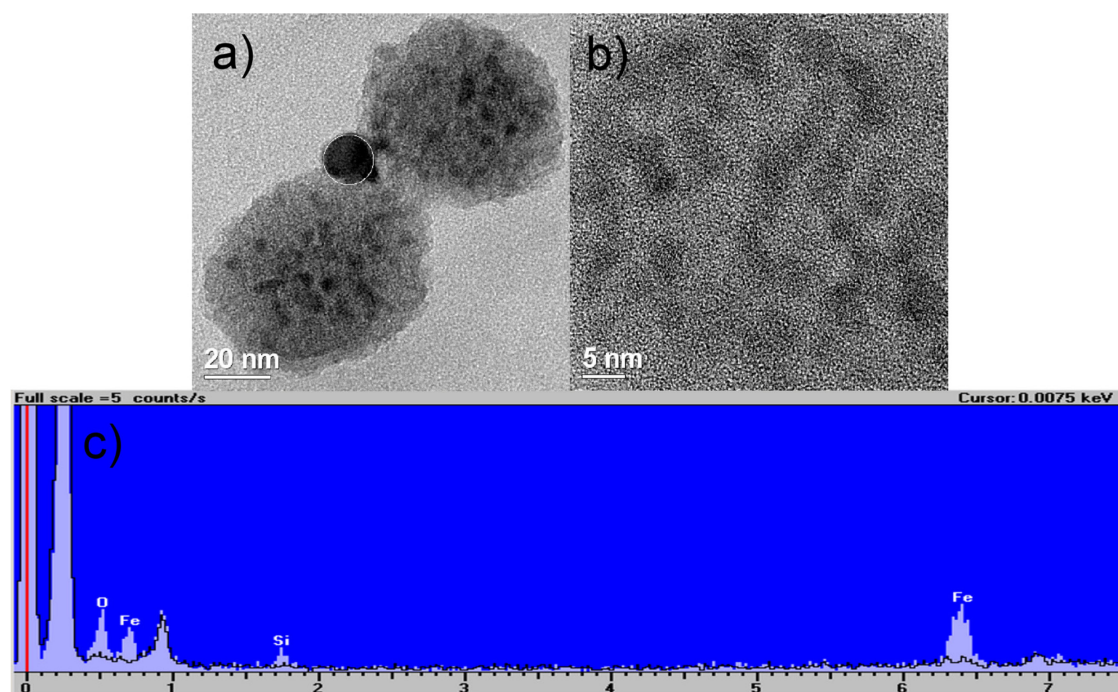


Figure 4.3 TEM micrographs at different magnifications (a,b) and EDS analysis (c) of circled area (a) of sample D.

N_2 adsorption/desorption measurements were performed for samples A-D (Fig. 4.4). They all display the typical shape of a mesoporous material (type IV isothermal), notwithstanding their impregnation and subsequent thermal treatments. The curves demonstrate that the composite retained mesoporosity even with the presence of embedded iron oxide nanocrystals.

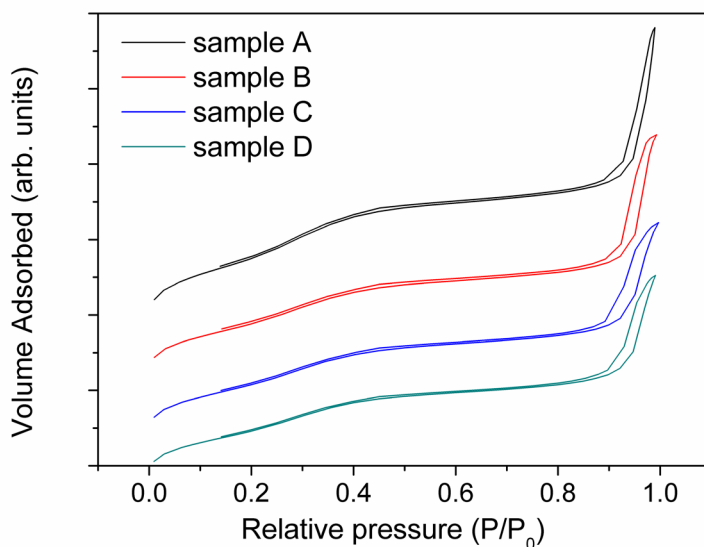


Figure 4.4 N_2 adsorption/desorption isothermal curves of $FeO_x@ms-SiO_2$ series of samples.

The values for specific surface area and pore volume both decreased with the increasing iron oxide loading (Tab. 4.3).

Table 4.3 Surface area and pore volume of $FeO_x@ms-SiO_2$ samples A-D.

sample	surface area (m^2/g)	pore volume (cm^3/g)
A	900 ± 20	1.2
B	720 ± 10	1.0
C	690 ± 10	0.9
D	650 ± 10	0.8

For example, in sample D they are almost 40% lower than the original mesoporous SiO_2 . Contrastingly, the pore size distributions did not reveal any relevant changes throughout the series (Fig. 4.5). Overall, the porosimetric results for the $FeO_x@ms-SiO_2$ series (A-D) proved valuable, since the retained

mesoporosity in the loaded samples could potentially allow for further modification of the composites.

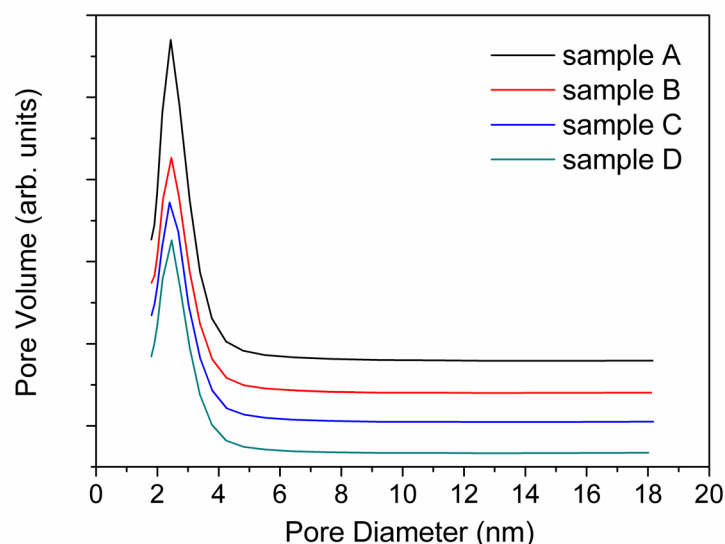


Figure 4.5 Pore size distribution curves of $\text{FeO}_x@ms\text{-SiO}_2$ series of samples.

On the basis of XRD, TEM, EDS and porosimetric analyses of the $\text{FeO}_x@ms\text{-SiO}_2$ series, sample B was selected as optimum in terms of the regularity and quality of its composite nanostructure. Therefore, further experimental investigation and characterization was performed for sample B.

Sample B was further calcined in a reducing atmosphere (700 °C), in order to promote the embedded hematite phase to magnetite. This transformation was expected following an experimental confirmation of the hematite to magnetite transition that was obtained by means of synchrotron radiation XRD. In this latter case, an innovative apparatus was used, allowing for the incorporation of gas flow, temperature variation and control during the measurement. Hence, the structural behavior of a pure hematite bulk sample was examined while heating from RT to 800 °C in a reducing gas flow ($\text{N}_2 + 4\% \text{H}_2$). The diffraction patterns were acquired at 12 keV ($\lambda = 1.034$ Å). The background arises from quartz capillary.

The transformation of pure hematite into magnetite is clearly shown in Fig. 4.6, in which the first acquired pattern (25 °C) is reported with the final pattern (obtained after cooling to RT from 800 °C) and the simulated patterns of hematite and magnetite. Fig. 4.7 shows the acquisitions at 400 °C, 500 °C and 600 °C, which demonstrate where the phase transition occurred.

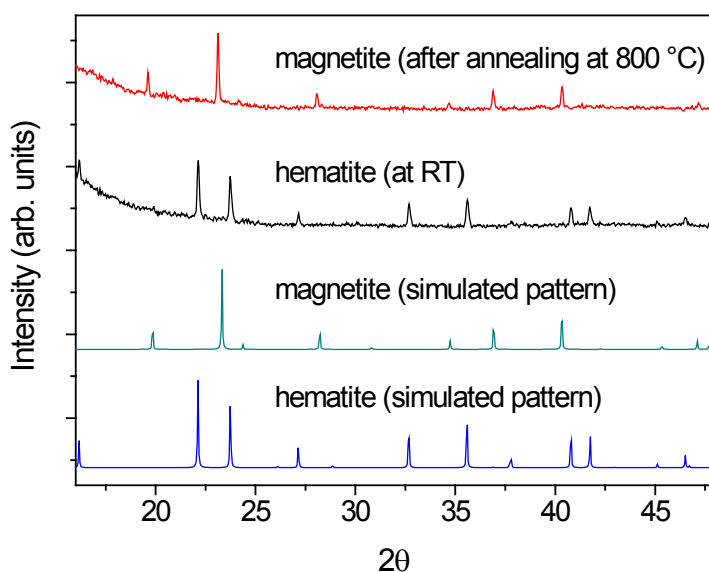


Figure 4.6 Hematite and magnetite synchrotron radiation XRD patterns, acquired (at 25 °C and after cooling to RT from a 800 °C annealing in $N_2 + 4\% H_2$ atmosphere, respectively) and simulated (PDF #33664, #19629 respectively) at room temperature.

The transformation of hematite into magnetite with a reductive thermal treatment was further examined by TG analysis. TG analysis of the pure hematite bulk sample in a reducing $N_2 + 5\% H_2$ atmosphere is shown in Fig. 4.8.

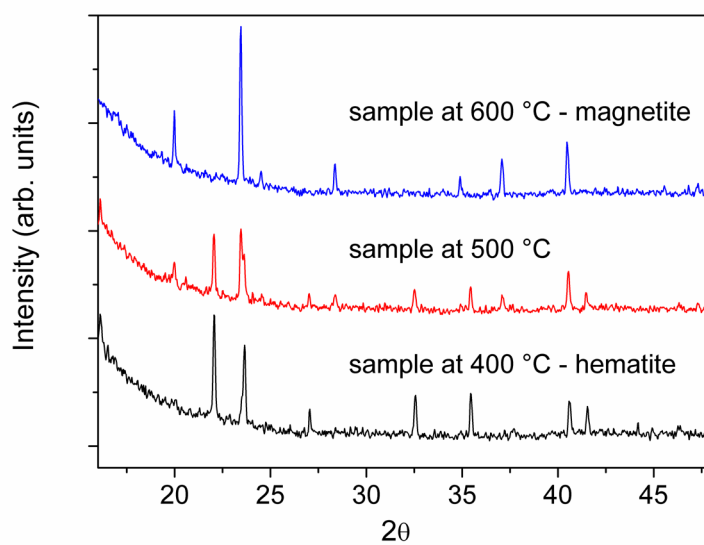


Figure 4.7 Synchrotron radiation XRD patterns of a pure crystalline hematite sample. Transformation to magnetite between 400-600 °C by annealing in $N_2 + 4\% H_2$ atmosphere.

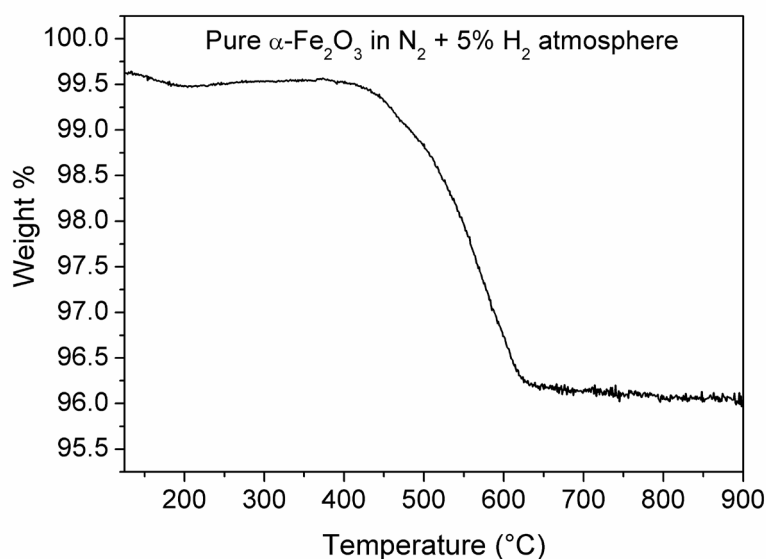


Figure 4.8 TG analysis of bulk pure hematite ($\alpha\text{-Fe}_2\text{O}_3$) in a reducing $N_2 + 5\% H_2$ atmosphere.

The TG results agree with the findings obtained by synchrotron radiation XRD. In Fig. 4.8, the transformation of hematite into magnetite is evident from the slope centered around 500 °C, which indicates complete transformation prior to reaching 700 °C. The mass loss of approximately 3.3% observed during transformation agrees with the theoretical loss of an oxygen atom for every six iron atoms, that would occur during the transition between hematite (Fe_6O_9) and magnetite (Fe_6O_8).

On the basis of the aforementioned results for pristine hematite, a complete transformation of hematite into magnetite was similarly expected for the systems comprising iron oxide nanocrystals embedded within the SiO_2 matrix. Hence, XRD analysis (measured with the Philips X'Pert vertical goniometer hereforth) was performed for sample B after the first (oxidizing) and after the second (reducing) thermal treatment and compared with the patterns of three pure iron oxide phases from the literature (Fig. 4.9).

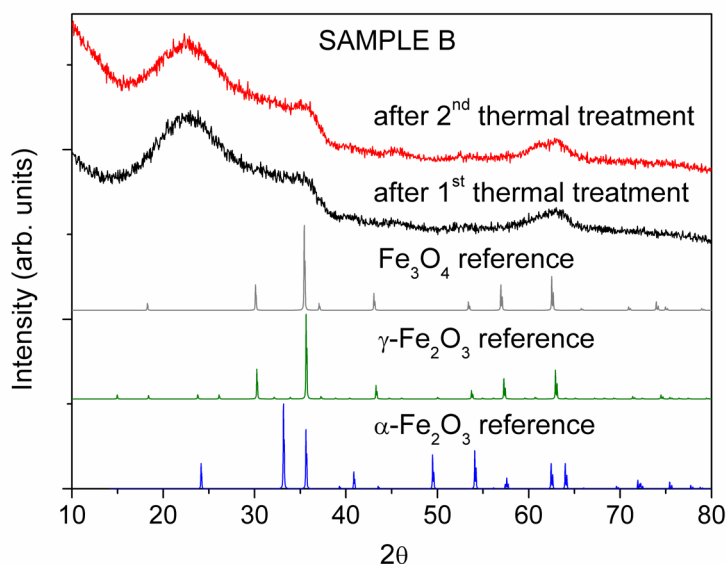


Figure 4.9 XRD patterns of: sample B after the first (oxidizing) and the second (reducing) thermal treatment, Fe_3O_4 (magnetite), $\gamma\text{-Fe}_2\text{O}_3$ (maghemite) and $\alpha\text{-Fe}_2\text{O}_3$ (hematite) references from the literature (PDF #19629, #391346, #33664 respectively).

It is evident from the diffraction patterns of sample B, that the anticipated phase transition for SiO₂ embedded hematite into magnetite did not occur (Fig. 4.9). Furthermore, the peaks corresponding to the iron oxide phase are broad, thus increasing the difficulty in their identification. A comparison of the patterns for sample B following its respective oxidative and reductive treatments shows that both patterns are consistent with the presence of either magnetite Fe₃O₄ or maghemite γ -Fe₂O₃ (Fig. 4.9). Distinction between magnetite and maghemite is often difficult since their diffraction patterns are extremely similar. Furthermore, when the diffraction peaks are broad and the material is embedded in SiO₂, as in this composite, it is difficult to distinguish them from the diffraction pattern of hematite. Therefore, the presence of hematite in both instances cannot be excluded nor affirmed. However, it is possible to suggest that magnetite and/or maghemite were present prior to the reductive treatment, contrary to the initial deduction made for samples A and B, in which the presence of hematite was assumed on the basis of its predominance in samples C and D (Fig. 4.1). The consolidated XRD findings indicate that formation of magnetite and/or maghemite is favored inside the SiO₂ pores during the oxidizing thermal treatment, while the opposite occurs for the iron oxide phase outside the pores in samples C and D, which maintained the prevalent hematite even after the subsequent reducing thermal treatment. The formation of magnetite/maghemite inside the host matrix during the first annealing in air could be due to the presence of some organic impurities contained in the SiO₂ (and not totally eliminated at 700 °C) which produced a reduction-oxidation reaction. The reduction of the initial Fe³⁺ ions to magnetite, due to the carbonaceous species coming from the organic fraction, is followed by the formation of maghemite by oxidation. This behavior has already been manifested in the literature.⁹

In sample B the observed results allow to hypothesize the presence of both magnetite and maghemite being embedded in SiO₂ following sequential oxidizing and reducing thermal treatments, and that the reducing treatment was less effective on the crystalline phase embedded in the composite, compared with the transformation seen for pure hematite samples (as already described

with TG analysis and synchrotron radiation XRD). However, qualitative Raman spectroscopy performed for sample B following the respective oxidizing and reducing treatments did not unequivocally confirm the hypothesis (Fig. 4.10).

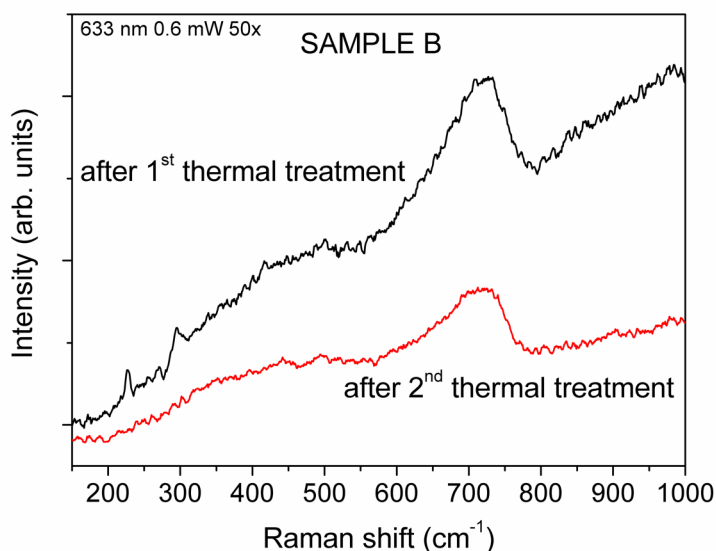


Figure 4.10 Raman spectra of sample B after the first (oxidizing) and the second (reducing) thermal treatment.

The Raman spectrum of sample B (Fig. 4.10), recorded after the first oxidizing treatment, shows a prominent band with a large width at about 720 cm⁻¹ and two weak bands of small intensity at 227 and 295 cm⁻¹. The band at 720 cm⁻¹ is also visible in the spectrum recorded after the second reducing thermal treatment, while the two weaker bands disappeared. A very broad band visible between 300 and 500 cm⁻¹ in both spectra can be assigned to the SiO₂. The weak bands at 227 and 295 cm⁻¹ can be attributed to the hematite phase, while their disappearance in the second spectrum may be promoted by the reducing thermal treatment. The origin of the band around 720 cm⁻¹ is not unequivocally assigned. It is known that magnetite shows a prominent broad band at 660 cm⁻¹, whereas maghemite shows a broad band at 700 cm⁻¹ together with two other broad bands at 350 and 500 cm⁻¹.¹⁰ On the basis of literature data, the attribution of the band at 720 cm⁻¹ to maghemite is unlikely.

However, in this study it must be taken into account that the iron oxide nanoparticles are very small and embedded in a confined environment. Such confinement can create strains in the nanocrystals and consequently the vibrational modes can show differences with respect to a bulk sample. Since an increase in their vibrational frequencies is reasonable, it is possible to assign the band to maghemite, while a minor contribution of magnetite could also be present under the large band between 600 to 700 cm^{-1} . In terms of crystallinity and structure, the two respectively oxidized and reduced samples of B appear similar. The most notable difference is the minor presence of hematite after the oxidative annealing, which disappears following the reductive treatment. Raman analysis confirmed that the reducing thermal treatment readily transformed the minute hematite fraction into maghemite and/or magnetite.

The magnetic properties of sample B following the sequential oxidative and reductive treatments were investigated. A preliminary check by visual means was performed by suspending the powders in ethanol and placing them in the proximity of a strong magnet for several minutes (Fig. 4.11). The samples showed comparable magnetic behavior, as in both cases almost the total visible amount of powder migrated towards the magnet within one hour.

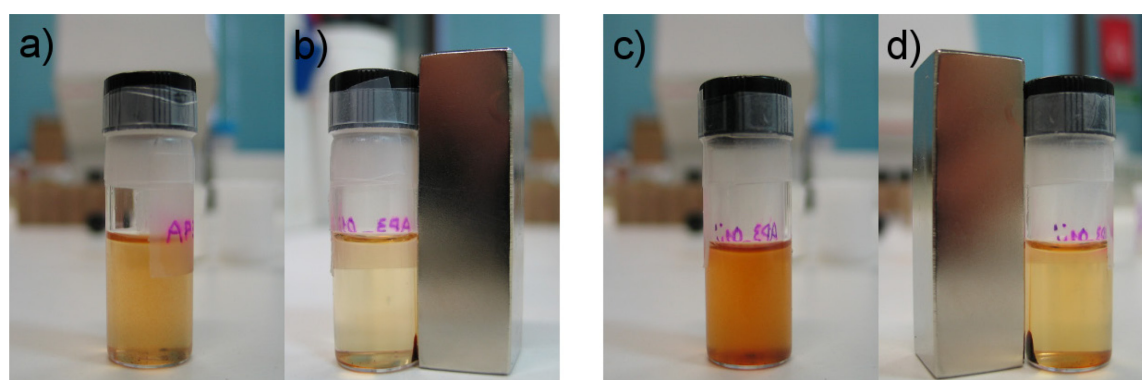


Figure 4.11 Left side photos: images of sample B after the first thermal treatment (in air atmosphere) , with powders dispersed in EtOH (a) and in presence of a magnet (b); right side photos: images of sample B after the second thermal treatment (in N_2/H_2 atmosphere), with powders dispersed in EtOH (c) and in presence of a magnet (d).

The magnetic properties of the two samples, measured after oxidizing and after oxidizing plus reducing thermal treatments respectively, were assessed by measuring their hysteresis loops. The loops measured at 3 K and 300 K are respectively shown in Figs. 4.12 (a) and (b).

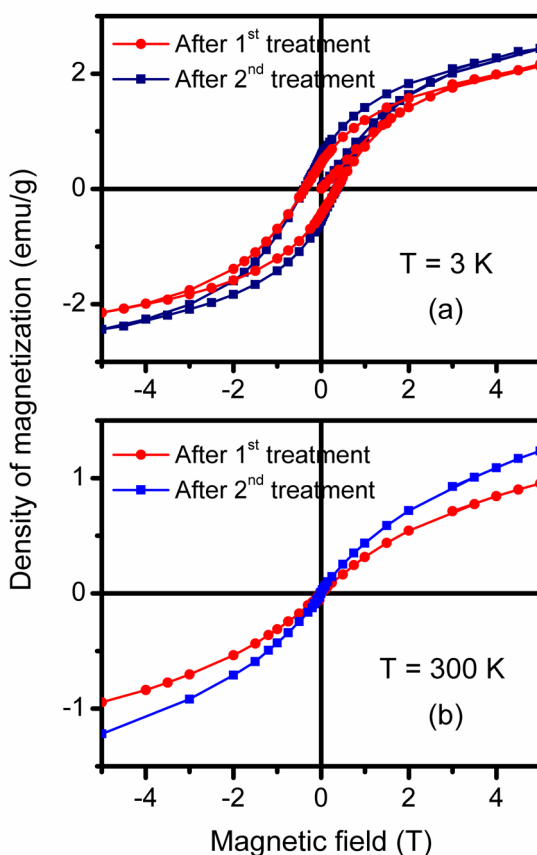


Figure 4.12 Hysteresis loops of the sample B after the 1st and 2nd thermal treatment measured at 3 K (a) and 300 K (b).

The magnetic properties of the two samples are quite similar, demonstrating open hysteresis loops at 3 K that do not close up to magnetic fields as high as 3 T, and that the density of the magnetization does not reach saturation even at magnetic fields of 5 T. The magnetic moments at 5 T for the two sample B composites are several emu/g, increasing from 2.0 emu/g to 2.4 emu/g from the

first to the second thermal treatment. Considering that the composites contain a nominal 17%wt of Fe_3O_4 , it implies that the densities of magnetization at 5 T for the iron oxide embedded in sample B after the first and the second treatment are 11.7 and 14.0 emu/g, respectively. Hence, the increase in magnetization after the reducing thermal treatment is equivalent to 20%. Comparing these values with those of bulk magnetite (92 emu/g) or maghemite (82 emu/g),¹¹ one can deduce that the amount of ferrimagnetic iron oxides at 3 K is between 13% and 17%, in accordance with the iron oxide or the chosen reference values used for the estimation. The inferiority of these magnetization values with respect to the bulk may be attributed to the presence of paramagnetic free Fe ions or very small clusters. This contribution, since it follows the Curie law temperature dependence, should exhibit a negligible magnetic behavior at room temperature. At this temperature, the densities of the magnetization showed a 50% decrease giving 0.9 emu/g and 1.2 emu/g for the samples obtained after the first and the second thermal treatment, respectively. Despite the low magnetization values, they do not reach saturation at high fields in the hysteresis loops measured at 3 K and high magnetic fields are required to close the loops. Additionally, the coercive fields are very large, 330 mT, in comparison to the classical values obtained in iron oxide nanoparticles, typically smaller than 50 mT. These observations indicate that the nanoparticles exhibit a spin glass magnetic behavior instead of a proper single domain ferrimagnetic behavior. Such spin glass magnetic behavior is due to spin frustration of the antiferromagnetic structure of these oxides arising from structural defects and from the surface of small nanoparticles.¹²⁻¹⁴ This behavior would also give rise to a further decrease in the magnetization.

In both loops, measured at 3 K and 300 K, the density of magnetization was about 20-30% larger in sample B after the second thermal treatment (Fig. 4.12). This increase in magnetization may be due to one of the following: (i) a further increase in the amount of magnetic material formed; (ii) a modification of the nanoparticles' magnetic properties by chemical change induced by the reduction (transformation of hematite fraction into maghemite and/or magnetite,

as indicated by the Raman spectroscopy data); (iii) an increase of the particles' size or an improvement of the crystalline structure. The aforementioned hypotheses were investigated by analyzing the superparamagnetic behavior of the nanoparticles.

Superparamagnetism is the magnetic behavior that small single domain magnetic nanoparticles can exhibit.^{15,16} It is characterized by a lack of irreversible processes, in particular open loops, whereby the magnetic behavior resembles that of a paramagnetic material. This occurs because the thermal activation processes produce a faster relaxation of the magnetization. Consequently, it is observed only above a certain temperature known as the blocking temperature (T_B). Below this temperature the loops exhibit hysteresis, which disappears above T_B . This behavior was evident in the two samples (Fig. 4.12). The hysteresis loops at 3 K are clearly open and with coercive fields of 0.33 T, while at room temperature (Fig. 4.12 (b)) no hysteresis is observed. The T_B depends on the particle size and on the magnetic properties of the nanoparticles according to the expression:^{16–18}

$$T_B = K_{ef} V / \ln(\tau_0 / \tau_i) k_B \quad (1)$$

where K_{ef} is the effective magnetic anisotropy of the nanoparticles, V corresponds to the particle volume, τ_0 is the attempt time of the nanoparticles, τ_i is measurement time and k_B is the Boltzmann constant. The T_B can be determined from the measurement of the temperature dependence of the ZFC and FC magnetizations that is represented in Fig. 4.13.

The maximum in the ZFC curve is characteristic of the average T_B of the nanoparticles while the temperature at which the ZFC and FC curves join, T_{max} , corresponds to the temperature above which all the nanoparticles are superparamagnetic.

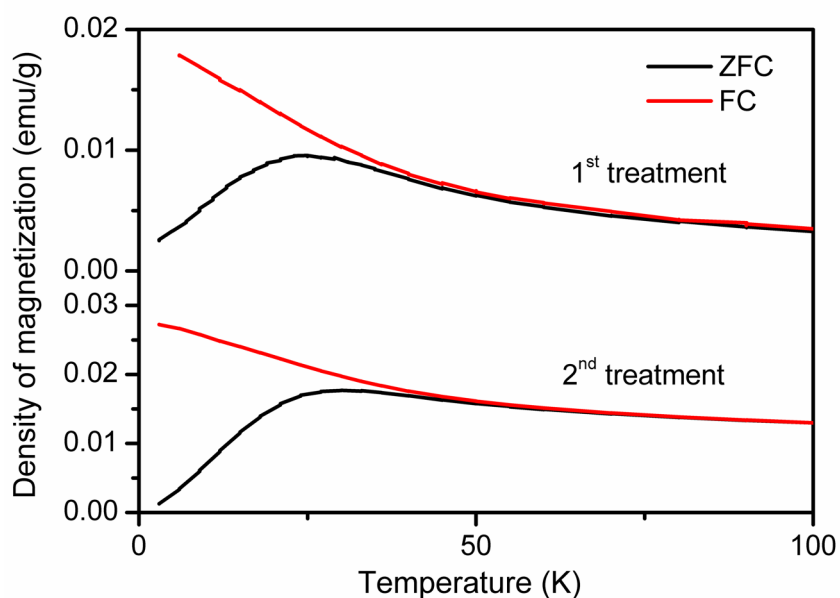


Figure 4.13 Temperature dependence of the ZFC and FC magnetization of the sample B after the 1st and 2nd thermal treatment.

In sample B, after the first thermal treatment $T_B = 25$ K and $T_{max} = 40$ K, while the respective temperatures are larger after the second thermal treatment for which $T_B = 30$ K and $T_{max} = 80$ K. Hence, from the T_B values one can deduce that the nanoparticles' size increased (presumably by 20%) following the second treatment, or that their magnetic properties changed (whereby the anisotropy increased). Since the difference between T_B and T_{max} corresponds to the broadening of the T_B distribution, the larger value of $T_{max}-T_B$ in sample B after the second thermal treatment indicates a change in the particle size or the anisotropy distribution. On the other hand, when the nanoparticles are superparamagnetic the magnetic field of the magnetization follows the Langevin function:

$$M(H,T) = M_{Sat} (\coth(CH/T) - 1/(CH/T))$$

where M_{sat} is the magnetization or moment at the saturation, H is the magnetic field, T is the temperature and $C = \mu/k_B$, being μ the magnetic moment of the nanoparticles. Fitting the loops measured at 300 K to this function gave an excellent agreement ($R = 0.998$) to C (μ) values equal to 220 ($330 \mu_B$) and 250 ($370 \mu_B$) for sample B after the first and the second thermal treatment, respectively. The constant C is proportional to the average magnetic moment of the nanoparticles, that is proportional to the volume and the magnetization ($\mu = M_S V$). The change of the particles' moment can be related to the increase in the magnetization (due to an improvement of the magnetic order or structure) and/or in the volume (growth of the grains or improvement of the surface structure crystallinity). It is difficult to unequivocally ascertain the origin of this increase in magnetization. For example, if one considers the simple hypothesis that the magnetization of the nanoparticles does not change after the second treatment, that the magnetization is that of the bulk magnetite ($4 \mu_B/\text{unit cell}$), and that the nanoparticles are spherical, the calculated particle diameters of 4.5 nm and 4.7 nm (for sample B after the first and the second thermal treatment, respectively) are very similar. The minute difference between the two average sizes is difficult to ascertain by TEM or XRD analysis. However, in view of the nanoparticles' small size, any change in their dimensions or crystalline structure would be directly linked to changes in the magnetization arising from modification of the surface and bulk magnetic order. The calculated particle sizes are larger than those estimated from the TEM micrographs. This difference between the calculated (*ca.* 4.5 nm) and observed particle size (*ca.* 3 nm size) may be due to an underestimation of the magnetization value per unit cell, or alternatively because the particle diameter is calculated from the particles' average magnetic volume which is larger than the medium volume that results from the average diameter ($V_m = \pi/6 \langle D \rangle^3$) determined by TEM analysis.

Following the first and second thermal treatment for sample B, the magnetic moment of the nanoparticles (and presumably also their volume) increased by 12%. This increase in magnetic moment is smaller than the 20% increase

observed for T_B (that is dependent on the particle volume), and also smaller than the 20% increase seen for the density of magnetization. Overall, these observations bring to the conclusion that the second thermal treatment produced a small improvement in the nanoparticles' magnetic anisotropy and an increase in the amount of magnetic iron oxide nanoparticles present by hematite transformation into magnetite/maghemite. These conclusions support the observed increase for T_B distribution.

The coercive field of 0.33 T that was seen for sample B after the two treatments is significantly high in comparison to the typical literature values given for iron oxide nanoparticles, typically below 50 mT. Considering the classical reversal process of single domain nanoparticles,^{16,18,19} the coercive field is proportional to the effective anisotropy, K_{ef} , and inversely proportional to the magnetization. As discussed previously, a decrease in the average magnetization was observed. The magnetic anisotropy of these nanoparticles can be investigated from the analysis of the superparamagnetic behavior and in particular from the values of T_B and particle volume according to the expression (1). If a diameter of 4.5 nm, as a representative value for the calculation of the nanoparticle volume, and the typical value of $\ln(T_0/T_i) = 25$,^{16,18} are inserted into the expression, the resulting K_{ef} values are 1.8×10^5 and $2.1 \times 10^5 \text{ Jm}^{-3}$ after the first and the second thermal treatment, respectively. These values are one order of magnitude larger of those of the bulk,¹¹ indicating that enhancement of the magnetic anisotropy occurs in these nanoparticles which may be the origin of the large coercive fields.

Going back to the magnetic separation of the powders in suspension (Fig. 4.11), in which not all of the suspended nanoparticles were attracted to the external magnet, some additional observations can be done. Since the magnetic forces depend on the susceptibility of the magnetic material,^{20,21} which in turn depends on the total magnetic moment and magnetic response to a magnetic field, the lack of complete separation is reasonably attributed to a low density of magnetization in the composite material and low magnetic response because the nanoparticles are superparamagnetic. On the other hand, due to

the nanoparticles' small size (3-4 nm) it is reasonable to assume that the gradient of the external magnetic field in such a small distance would be negligible.

Sample $\text{CoFe}_2\text{O}_4@\text{ms-SiO}_2$

An additional nanostructured composite containing embedded CoFe_2O_4 nanocrystals in SiO_2 was prepared. The nominal fraction was based on that of sample B and adapted accordingly for the mixed oxide. Specifically, a nominal 30% v/v fraction of salts with respect to the total pore volume was used to obtain a nominal 14% weight fraction of cobalt-iron oxide on the total weight.

The XRD pattern of the $\text{CoFe}_2\text{O}_4@\text{ms-SiO}_2$ sample (black line) clearly shows the amorphous silica profile and the typical peaks of the CoFe_2O_4 crystalline phase (Fig. 4.14).

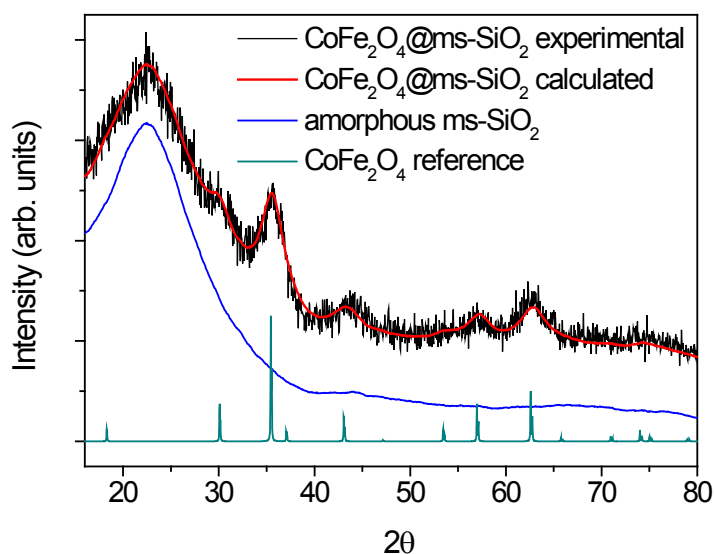


Figure 4.14 XRD patterns of: $\text{CoFe}_2\text{O}_4@\text{ms-SiO}_2$ sample (experimental and refined with Rietveld method), mesoporous undoped SiO_2 , CoFe_2O_4 reference from the literature (PDF #221086).

Unlike the previous sample series, well defined peaks were visible thus allowing a thorough analysis of the crystalline properties. The calculated XRD

pattern (red curve) was obtained by Rietveld refinement²² using the structure reported by ICSD 160059. Quantification of the crystalline phase content was made from the calculated pattern to give $15 \pm 1\%$ weight fraction of cobalt-iron oxide, which is consistent with the nominal value (14%wt). The dimension of the crystallites was determined using the Line Broadening Analysis (LBA). The average volumetric diameter of crystallites ($\langle D \rangle_{\text{vol}}$) was found to be 2.6 nm, in agreement with the SiO_2 pore size. On this basis, similarly with the findings for the FeO_x embedded phases in sample B, it is reasonable to suggest that the nanocrystals are located inside the silica matrix.

The successful embedding of CoFe_2O_4 in the SiO_2 matrix was supported by TEM and EDS analyses (Fig 4.15).

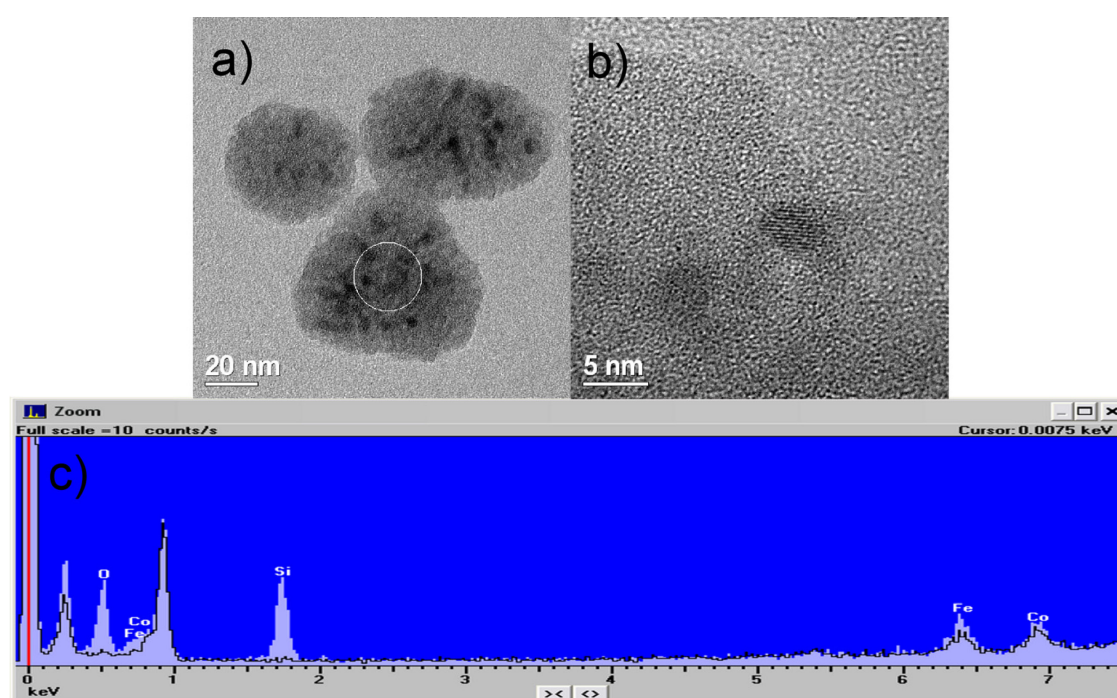


Figure 4.15 TEM micrographs at different magnifications (a,b) and EDS analysis (c) of circled area (a) of CoFe_2O_4 @ms- SiO_2 sample.

The TEM micrographs (Fig. 4.15a-b) evidence the presence of dark nanocrystals with an approximate 3 nm size embedded in the porous SiO_2 matrix, and the absence of crystalline material outside the SiO_2 nanoparticles.

The crystalline planes of the CoFe_2O_4 domains are clearly visible in Fig. 4.15b. In Fig. 4.15c, an EDS spectrum of the circled area in the first micrograph is reported. The elemental analysis confirmed the presence of Si, O, Fe and Co attributed to the SiO_2 matrix and the CoFe_2O_4 nanocrystals.

The porosimetric analysis of $\text{CoFe}_2\text{O}_4@\text{ms-SiO}_2$ gave comparable results with those of the previous series. The surface area of sample $\text{CoFe}_2\text{O}_4@\text{ms-SiO}_2$ was $768 \text{ m}^2/\text{g}$ and the pore volume $1.14 \text{ cm}^3/\text{g}$. These values are positioned between the corresponding values for samples A and B of the $\text{FeO}_x@\text{ms-SiO}_2$ series (see Tab. 4.3). By relating the surface area and pore volume to the %wt of crystalline material in the composite, a nominal 14% of CoFe_2O_4 in this composite is in reasonable agreement with samples A and B of the $\text{FeO}_x@\text{ms-SiO}_2$ series, which have nominal FeO_x %wt fractions of 6% and 17%, respectively.

The identification of $\text{CoFe}_2\text{O}_4@\text{ms-SiO}_2$ by XRD analysis was further corroborated by Raman spectroscopy, which evidenced the typical features of the CoFe_2O_4 tetragonal phase (Fig. 4.16).²³

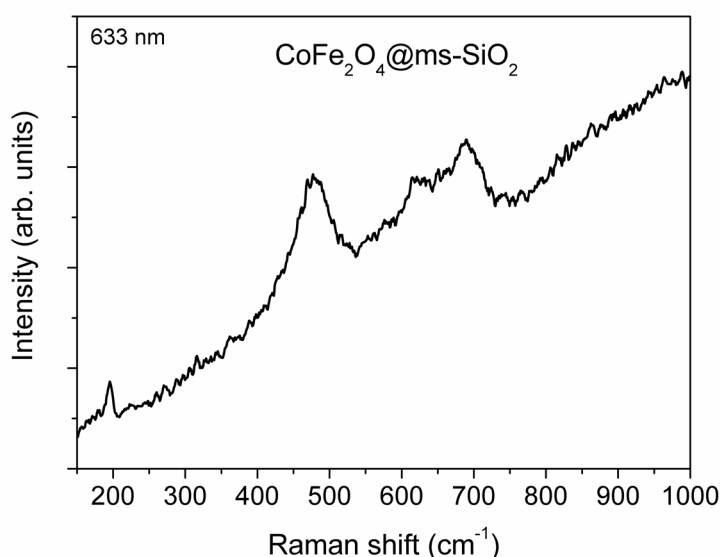


Figure 4.16 Raman spectrum of $\text{CoFe}_2\text{O}_4@\text{ms-SiO}_2$ sample.

As for sample B of the $\text{FeO}_x@\text{ms-SiO}_2$ series, the magnetic properties of $\text{CoFe}_2\text{O}_4@\text{ms-SiO}_2$ were examined. A preliminary check by visual means was performed by suspending the powder in ethanol and placing a strong magnet in close proximity for several minutes (Fig. 4.17).

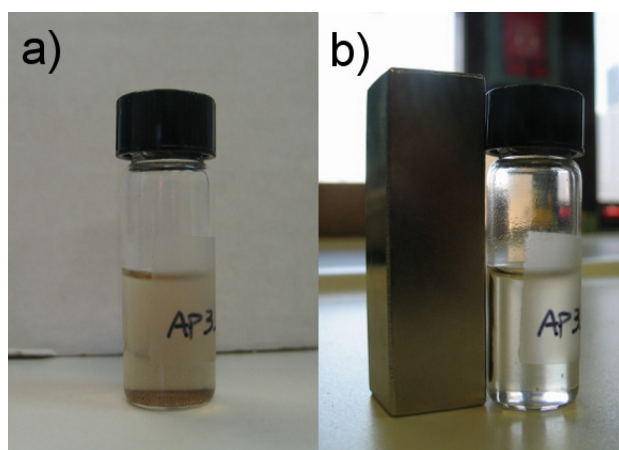


Figure 4.17 Images of $\text{CoFe}_2\text{O}_4@\text{ms-SiO}_2$ sample with powder dispersed in EtOH (a) and in presence of a magnet (b).

The magnetic properties of $\text{CoFe}_2\text{O}_4@\text{ms-SiO}_2$ appeared superior with respect to sample B, since the total content of visible powder migrated towards the magnet within several minutes.

The hysteresis loops of the $\text{CoFe}_2\text{O}_4@\text{ms-SiO}_2$ composite material were measured at 3 K and 300 K (Fig. 4.18).

The first measurement (3 K) shows that the density of magnetization at 5 T is 8 emu/g. In comparison with the respective curves of sample B (Fig. 4.12), the density of magnetization for $\text{CoFe}_2\text{O}_4@\text{ms-SiO}_2$ is larger and the shape of the loop is completely different. The loop of the latter exhibits a large coercive field of 1.16 T, and rather than being fully closed at 5 T, it demonstrates a minor loop suggesting that a percentage of nanoparticles exhibit anisotropy fields larger than 5 T (Fig. 4.18).

Alternatively, the temperature dependence of the ZFC and FC magnetizations (Fig. 4.19) indicates that the blocking temperatures of these nanoparticles are much larger than those of the FeO_x nanoparticles.

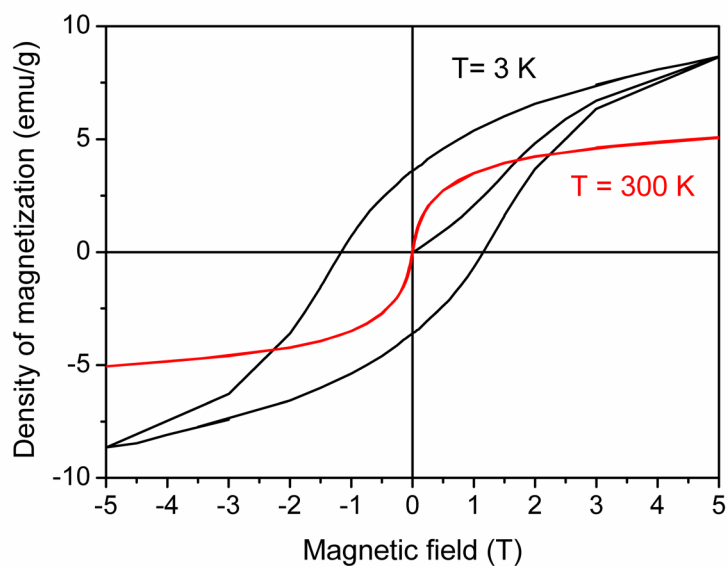


Figure 4.18 Hysteresis loops of the $\text{CoFe}_2\text{O}_4@\text{ms-SiO}_2$ composite measured at 3 K and 300 K.

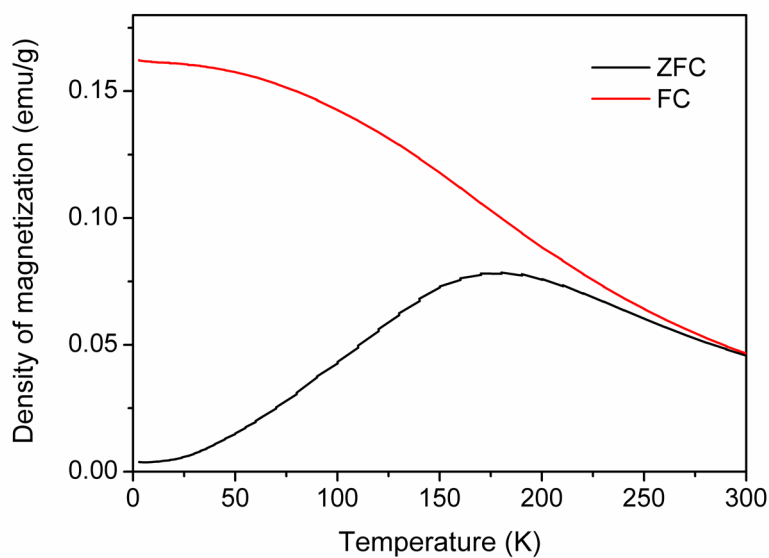


Figure 4.19 Temperature dependence of the ZFC and FC magnetization of the $\text{CoFe}_2\text{O}_4@\text{ms-SiO}_2$ composite material.

The maximum in the ZFC, T_B , is at 177 K, while the ZFC and FC curves separate at room temperature indicating that a percentage of nanoparticles are blocked. In fact, the hysteresis loop exhibits a coercive field of 5 mT. Both the ZFC-FC curves and the hysteresis loop show that the 3 nm nanoparticles have a large effective anisotropy, at least 7 times larger than that of the FeO_x nanoparticles. This high anisotropy is a fingerprint for the presence of high anisotropic Co^{2+} ions in the octahedral sites of the ferrite spinel structure,^{1,3,24} being the ferrite with the largest anisotropy.^{2,3,5} The anisotropy values can depend on many correlated factors,^{2-5,25,26} such as the cobalt content, the inversion degree of the cobalt, the chemical state of iron, the order and disorder of the magnetic structure, the particle size. Notwithstanding the varying influences, it is always very large.

The density of magnetization at 3 K was accordingly corrected by considering the mass contribution of SiO_2 . Hence, the density of the magnetization for the CoFe_2O_4 nanoparticles at 5 T is 57 emu/g, which is smaller than that of the bulk (92 emu/g)^{b,4}. At room temperature the density of magnetization for the composite is 4.9 emu/g, and the density of magnetization for the magnetic fraction is equivalent to 35 emu/g. Hence, the density of magnetization decreases by 38% when increasing the temperature from 3 K to 300 K. Such lowering of the magnetization density with increasing temperature was also observed in the FeO_x nanoparticles, and was attributed to free ions, clusters and the spin-glass behavior in the nanoparticles. However, at room temperature the magnetic content for the FeO_x nanoparticles was a low 6-8%, while that of the CoFe_2O_4 nanoparticles is close to 40%. This further confirms the smaller content of non ferrimagnetic species observed in the CoFe_2O_4 composite, while the larger density of magnetization can explain the greater efficiency observed in the magnetic separation of this material (Fig. 4.17).

^b The bulk density of magnetization depends on the Co/Fe ratio and site occupancy, but typically the values are larger.

Surface functionalization with APTES

As similarly discussed in a previous study on luminescent nanocomposites⁸ (see also § 3.1.2), embedding the iron oxide nanocrystals within an amorphous SiO₂ matrix not only creates a protective coating for the magnetic particles, it also provides a layer of superficial hydroxyl groups (isolated and geminal silanols) which may be further functionalized via a suitable post-grafting method. Treating silica at extremely high temperatures promotes complete dehydroxylation of the surface silanols and produces siloxane groups. Complete dehydroxylation would be undesirable for the following reasons: (1) the silica surface would lose its ability to undergo further modification in the absence of superficial silanols; and (2) the mesoporosity would be compromised if thermal treatment were to exceed 800 °C due to sinterization, as discussed before. Therefore, annealing the studied magnetic samples at 700 °C for 12 h was suitable to maintain the integrity of the structural and magnetic properties without causing complete surface dehydroxylation.

In order to functionalize with APTES the silica surface for potential immobilization of biological molecules, the presence of silanol groups on the surface of silica in sample B (FeO_x@ms-SiO₂ series) was monitored by performing DRIFT IR spectroscopy before and after the functionalization reaction with APTES (Fig. 4.20).

The presence of active sites for functionalization, *i.e.* free silanols, which includes isolated and geminal groups, is evident from the sharp peak observed at 3750 cm⁻¹ in the DRIFT spectrum of the non functionalized composite material (curve in the middle), which is similar to that of non impregnated mesoporous silica (curve at the top). The additional signals observed for non impregnated mesoporous silica and for non functionalized sample B treated at 700 °C are in accordance with the expected spectral features of a calcined silica⁸ (see also § 3.1.2).

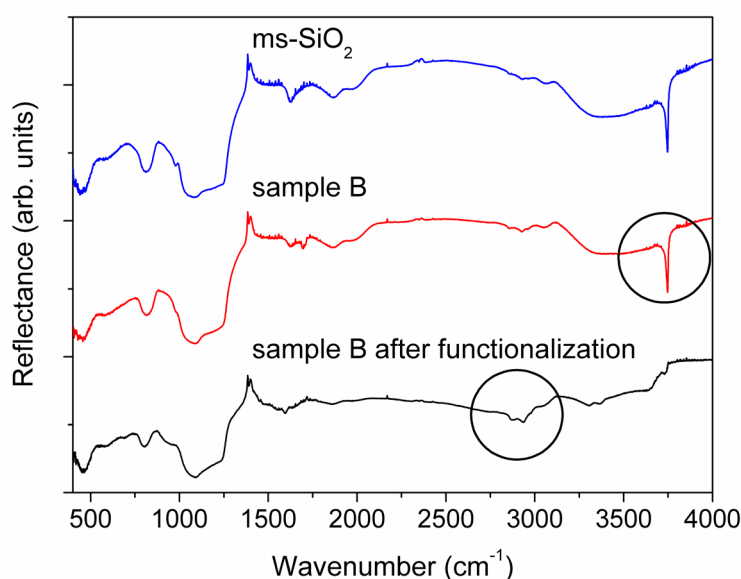


Figure 4.20 DRIFT spectra of calcined mesoporous SiO₂ and of sample B before and after functionalization with APTES. Circled areas point out the sharp signal of active sites for functionalization (right) and the weak signals of aliphatic groups introduced with APTES (left).

The attachment of APTES on the silica surface in sample B was qualitatively confirmed by IR, whereby the sharp peak at 3750 cm⁻¹ was no longer present providing evidence for functionalization (curve at the bottom). Furthermore, the introduction of aliphatic groups attributed to APTES was evidenced by the appearance of weak signals just below 3000 cm⁻¹. The samples were thoroughly washed via repeated centrifugation and redispersion in organic solvent in order to remove any residual or unbound APTES, and subsequently dried *in vacuo* prior to IR measurements being recorded.

As for sample B of the FeO_x@ms-SiO₂ series, the surface functionalization of sample CoFe₂O₄@ms-SiO₂ also was investigated through DRIFT IR spectroscopy. Similarly, the attachment of APTES on the SiO₂ surface was qualitatively confirmed by IR (not shown). It should be noted that the presence of iron oxide or cobalt-iron oxide in the composite nanostructured systems cannot be detected through IR spectroscopy. Therefore, the DRIFT IR spectra

of the $\text{CoFe}_2\text{O}_4@\text{ms-SiO}_2$ sample before and after its functionalization are comparable to the corresponding spectra of sample B reported in Fig. 4.20.

4.1.3 Conclusions

The structural and magnetic properties of mesoporous silica nanoparticles embedded with iron oxide and cobalt-iron oxide nanocrystals were examined. A series of $\text{FeO}_x@\text{ms-SiO}_2$ composite materials with increasing nominal fractions of iron oxide were prepared via a wet impregnation procedure. The composites were thermally treated sequentially, under oxidizing and reducing conditions. Elucidation of their phase composition, structural and morphological homogeneity was achieved by XRD, TEM, IR and Raman spectroscopy. The composite with a nominal 17%wt of iron oxide was considered optimal, since the obtained mixture of crystalline and magnetic Fe_3O_4 (magnetite) and $\gamma\text{-Fe}_2\text{O}_3$ (maghemite) was completely embedded in the silica matrix. The magnetic properties of the composite were examined, before and after the reducing treatment. An enhancement in the density of magnetization was observed following the reducing treatment, and attributed to an increase in the magnetic material content. Similarly, a $\text{CoFe}_2\text{O}_4@\text{ms-SiO}_2$ composite containing a nominal 14%wt mixed oxide was prepared. The composite showed comparable structural and morphological homogeneity with the optimal sample from the $\text{FeO}_x@\text{ms-SiO}_2$ series. Rietveld analysis of the XRD pattern supported that crystallite dimensions were in close agreement with the pore size, while quantification of the CoFe_2O_4 phase agreed with the nominal value. The magnetic properties of the $\text{CoFe}_2\text{O}_4@\text{ms-SiO}_2$ composite were found to be superior to those of the $\text{FeO}_x@\text{ms-SiO}_2$ material. The higher density of magnetization in the former was attributed to a higher content of magnetic material in the crystalline phase. The facile surface functionalization of the $\text{FeO}_x@\text{ms-SiO}_2$ and $\text{CoFe}_2\text{O}_4@\text{ms-SiO}_2$ composites was demonstrated using APTES.

4.2 Investigation on Fe(0)@ms-SiO₂ magnetic nanocomposites

The possibility to load in readiness a variety of different types and amounts of materials into the mesoporous silica nanoparticles and to preserve their chemical stability was exploited to investigate the feasibility of embedding also metallic iron nanocrystals inside the silica matrix. In fact, as mentioned in the introduction, magnetic nanocomposite materials have gained an increasing interest in several biological applications in recent years. In particular, the strong magnetic properties of zero-valent iron nanoparticles are also well known and used in the biomedical field.^{27,28}

To this purpose, the study was focused on the impregnation of the mesoporous silica nanoparticles with iron pentacarbonyl (Fe(CO)₅), a liquid precursor that was found in the literature^{29–31} to be suitable for the production of metallic iron with different synthetic approaches. In this compound, the iron oxidation state is 0. Hence, in order to avoid its oxidation during the preparation of the nanocomposite material, an inert atmosphere was supposed to be necessarily applied.

Three different procedures were employed in order to obtain the desired final magnetic nanocomposite; a first try (sample A) was based on the impregnation in air of the presynthesized mesoporous silica nanoparticles with a solution of Fe(CO)₅ in an appropriate solvent (tetrahydrofuran, *i.e.* THF, since the precursor is not soluble in water while it is soluble in organic solvents), followed by a thermal treatment of the dried impregnated powder in nitrogen gas under controlled pressure (by means of an autoclave). The amount of used iron pentacarbonyl was calculated on the basis of a desired nominal fraction (22%wt) of metallic iron (which should have formed after the thermal treatment) on the total weight of the final nanocomposite. This value is related to a nominal 50% fraction of silica pore volume occupied by the starting precursor, since in previous studies on the same mesoporous host matrix this volume fraction

resulted to allow an optimal impregnation and hence a good nanostructural quality of the final product³² (see § 4.1.2).

A second attempt (sample B) consisted in following the same aforementioned procedure but with a modification on the mesoporous silica host matrix, which, prior to its impregnation, was functionalized with trimethyl ethoxysilane (TMES), in order to make the silica surface hydrophobic, since in the literature some cases in which iron pentacarbonyl was easily incorporated in an hydrophobic chemical environment are reported.^{30,33}

The last synthetic approach (sample C), which is reported next in details, involved the use of hydrophobic functionalized mesoporous silica nanoparticles, a higher amount of iron precursor, a different solvent (*n*-hexane) and a more sophisticated impregnation process, which was entirely performed under inert atmosphere.

The morphology and nanostructure of the obtained materials were studied and characterized by means of XRD, TEM and porosimetric analyses, IR and Raman spectroscopy, while only for the sample that gave the most interesting results (sample C) a magnetic characterization was performed.

4.2.1 Samples preparation

Synthesis of mesoporous SiO₂ nanoparticles (ms-SiO₂)

The synthesis of mesoporous silica nanoparticles was adapted from the procedure by Qiao et al.⁷ and has previously been reported in this thesis (see § 3.2.1).

Hydrophobic functionalization of ms-SiO₂ with TMES (ms-SiO₂F)

The general procedure for surface functionalization with APTES,⁸ which has already been described (see § 3.1.1), was here applied to 1 g of undoped silica nanoparticles (ms-SiO₂), after being adapted by replacing APTES with a different silane, TMES, in order to obtain an hydrophobic surface functionalization of the mesoporous silica nanoparticles (ms-SiO₂F).

Synthesis of Fe(0)@ms-SiO₂ samples

Sample A was prepared by impregnating the mesoporous silica nanoparticles (0.3 g) with a solution (2 mL) of Fe(CO)₅ (0.19 mL, 1.42 mmol) in THF (1.81 mL), according to the desired nominal values of silica pore volume fraction occupied by the starting precursor (ca. 50%, calculated on the basis of the porosimetric characterization of ms-SiO₂) and of weight fraction of metallic iron on the final composite (22%). After stirring the mesoporous SiO₂ nanoparticles in Fe(CO)₅ solution for a few hours in air, the solvent was evaporated and the impregnated powder was recovered and transferred to the autoclave for the thermal treatment. A N₂ gas atmosphere with ca. 2 atm. of pressure was created inside the autoclave at room temperature, in order to avoid the presence of oxygen before and during the thermal treatment. Then the small autoclave was introduced into a tubular oven and the inner temperature of the autoclave, which was monitored by means of a thermocouple, was gradually raised to 250 °C and maintained for 1 h, after which the system was cooled to room temperature.

Sample B was prepared following exactly the same aforementioned procedure, with an identical impregnating solution and the same thermal treatment, but this time the silica nanoparticles (ms-SiO₂F, 0.34 g which corresponds to the usual 0.3 g of ms-SiO₂) were previously functionalized with TMES prior to their impregnation.

Finally, sample C was synthesized in a different and more controlled way, in order to promote the formation of the desired magnetic nanostructure. In this case the aim was to avoid or reduce the presence of oxygen for the entire process of preparation and not only during the thermal treatment. Moreover, compared to samples A and B, a different solvent and a definitely higher amount of iron precursor were utilized here.

The starting amount of functionalized mesoporous silica nanoparticles ms-SiO₂F (0.34 g) were kept inside a double-necked flask under N₂ atmosphere prior to their impregnation. Also the impregnating solution (2 mL), made of

Fe(CO)₅ (1 mL) and *n*-hexane solvent (1 mL) was prepared in a Schlenk flask under N₂ atmosphere and kept inside the flask, from which it was poured dropwise into the flask containing the silica powder by means of the *cannula transfer* method. A long double-ended syringe needle and two rubber septa were used to transfer the liquid solution from the Schlenk flask to the double-necked flask while maintaining a N₂ atmosphere inside the overall system. After stirring the mesoporous SiO₂ nanoparticles in Fe(CO)₅ solution for a few hours, the solvent was evaporated and the impregnated powder was recovered and transferred to the autoclave for the thermal treatment, which was exactly the same of samples A and B. With this strategy, the material was constantly kept under inert atmosphere for the whole duration of its preparation process, with the exception of the very short time needed to move the impregnated sample from the double-necked flask to the autoclave.

4.2.2 Results and discussion

Mesoporous SiO₂ nanoparticles (*ms-SiO₂*)

The mesoporous silica nanoparticles were synthesized, through the previously discussed process (see § 1.3.2) based on a templating surfactant, following the usual standard procedure that has already been described (§ 3.2.1); then they were characterized, by means of TEM and porosimetric analyses, at the same way as for precedent studies (e.g. § 3.2.2). The obtained results were, as expected, very similar to the previous and therefore their detailed discussion is not repeated here. The main features of the mesoporous silica nanoparticles that were used in the present study are resumed in the following list:

- isolated and aggregated nanoparticles with spheroidal shape;
- nanoparticles' size: 60-70 nm;
- N₂ ads./des. isothermal curve: type IV (typical of a mesoporous material);
- surface area (B.E.T. method): 980 ± 10 m²/g;
- pore volume: 1.3 cm³/g;
- average pore diameter (B.J.H. method): ca. 2.8 nm.

Hydrophobic functionalization of $ms\text{-SiO}_2$ with TMES ($ms\text{-SiO}_2F$)

In order to investigate on the possibility to improve the silica matrix impregnation with $\text{Fe}(\text{CO})_5$, the surface of the mesoporous silica nanoparticles was functionalized with an appropriate organic compound, TMES, a silane which contains an ethoxy group that can easily form covalent linkages with the isolated and germinal silanols of the silica surface, thus rendering the surface hydrophobic thanks to the presence of three terminal methyl groups (Fig. 4.21).

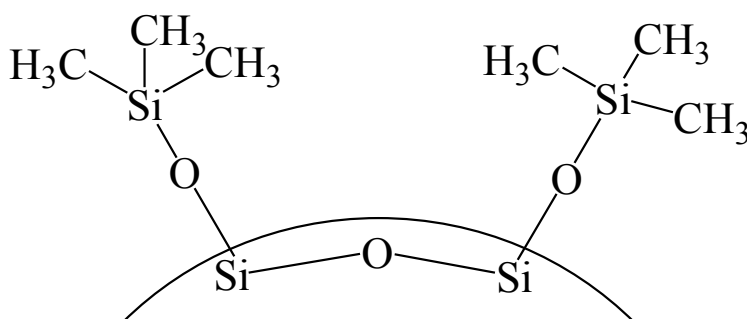


Figure 4.21 Representation of the hydrophobic surface functionalization of silica with TMES.

In theory, this modification of the silica surface should facilitate the impregnation process of iron pentacarbonyl, since the latter is a nonpolar compound and therefore has an hydrophobic nature, while the silanols on the silica surface make it hydrophilic and so the aforementioned modification is meant to create a more affine surface for the iron precursor.

The chemistry which is involved in this hydrophobic functionalization is analogous to that of the silica functionalization with APTES, that was time and time again presented in this thesis; hence, the usual procedure for silica functionalization with APTES was readily adapted to this case, simply by substituting the silane (APTES with TMES). Also the followed characterization was the same, since the availability of hydroxyl groups (free silanols, *i.e.* active sites for functionalization) on the silica surface as well as the qualitative confirmation of its hydrophobic functionalization were monitored by performing

DRIFT IR spectroscopy before and after the functionalization reaction with TMES (Fig. 4.22).

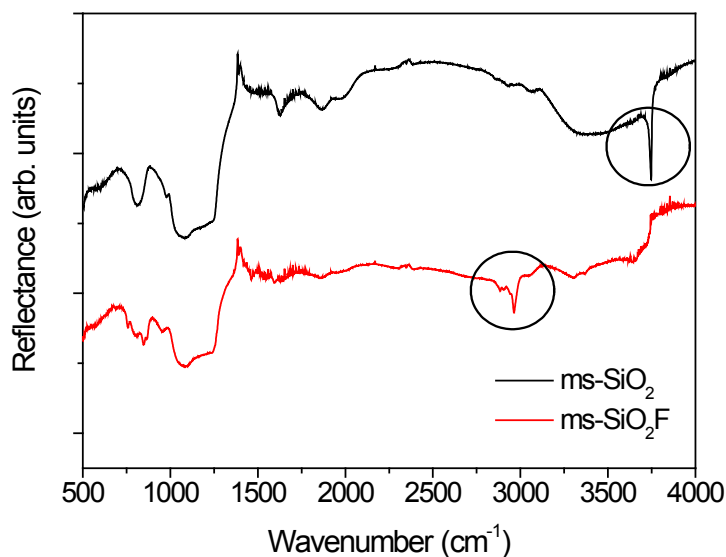


Figure 4.22 DRIFT spectra of mesoporous SiO₂ before (ms-SiO₂) and after (ms-SiO₂F) functionalization with TMES. Circled areas point out the sharp signal of active sites for functionalization (right) and the weak signals of aliphatic groups introduced with TMES (left).

Similarly to the discussed results of the functionalization with APTES (see, for example, § 4.1.2), also in this case the presence of free silanols, which includes isolated and geminal groups, is evident from the sharp peak observed at 3750 cm⁻¹ in the DRIFT spectrum of the non functionalized calcined silica (curve at the top). The additional signals observed for non functionalized mesoporous silica are in accordance with the expected spectral features of a calcined silica⁸ (see also § 3.1.2).

The attachment of TMES on the silica surface was qualitatively confirmed by IR, whereby the sharp peak at 3750 cm⁻¹ was no longer present in the spectrum of ms-SiO₂F providing evidence for functionalization (curve at the bottom). Furthermore, the introduction of aliphatic groups attributed to TMES was evidenced by the appearance of weak signals just below 3000 cm⁻¹.

Sample A

Sample A was prepared via the impregnation in air of the mesoporous silica nanoparticles $ms\text{-SiO}_2$ with a solution of $\text{Fe}(\text{CO})_5$ in THF, followed by a thermal treatment at 250 °C of the dried impregnated powder in nitrogen gas under controlled pressure.

A preliminary check of the magnetic properties by visual means was performed by suspending the obtained brick red – brown powder in ethanol and placing a strong magnet in close proximity for several minutes (Fig. 4.23).

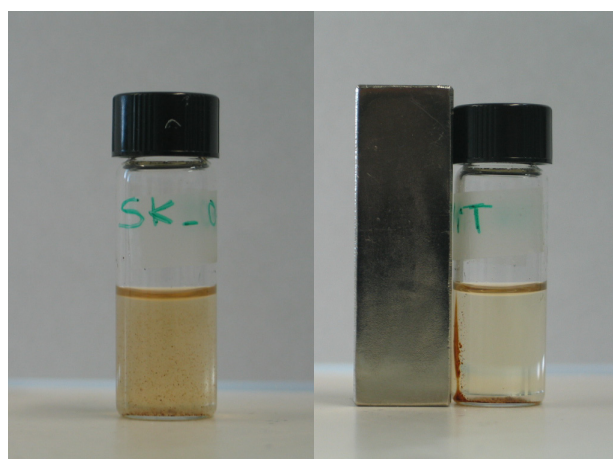


Figure 4.23 Images of sample A with powder dispersed in EtOH (left) and in presence of a magnet (right).

The sample showed an appreciable even though not very quick magnetic response, since almost the total visible amount of powder migrated towards the magnet within one hour. Hence, this behavior just proved the presence of a certain magnetic phase in the examined material.

TEM analysis was performed in order to investigate the structural quality of the nanocomposite as well as the efficiency of the impregnation process. As shown by the micrographs in Fig. 4.24a and b, some dark nanocrystals embedded into the silica nanoparticles were observed and their dimension appeared to be consistent with the silica pores' size. No additional material

external to the silica nanoparticles was observed. However, some unloaded silica nanoparticles were also observed during the analysis of the sample.

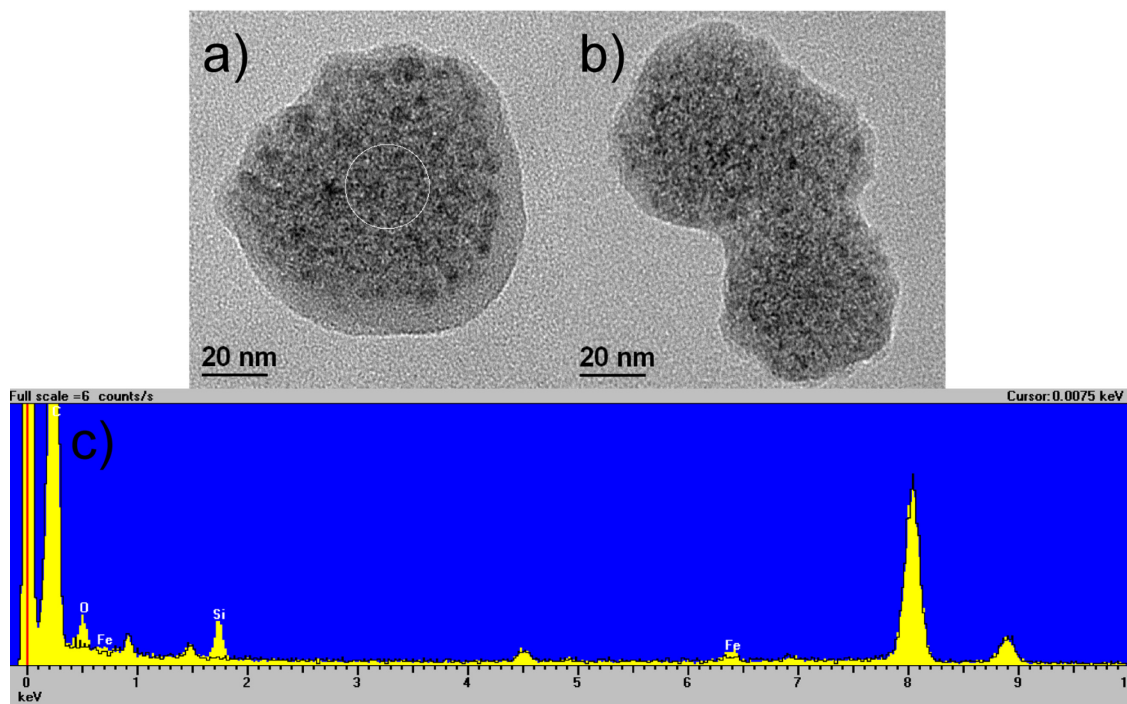


Figure 4.24 TEM micrographs (a,b) and EDS analysis (c) of circled area (a) of sample A.

An EDS analysis of the circled area in the first micrograph is also reported in Fig. 4.24c. The elemental analysis confirmed the presence of Si and O, attributed to the SiO_2 matrix, while the presence of Fe, which should be attributed to the embedded nanocrystals, was hardly detected (the intensity of its related peak in the spectrum is close to the background level), thus suggesting a small content of this element in the examined material. TEM analysis therefore indicates that an impregnation of the silica matrix occurred but probably with a low efficiency from a quantitative point of view.

This indication was also confirmed by the porosimetric analysis of sample A. The N_2 adsorption/desorption measurement (Fig. 4.25) displays the typical shape of a mesoporous material (type IV isothermal), notwithstanding the

impregnation. Also the shape of the pore size distribution curve (Fig. 4.26) did not reveal any relevant changes with respect to the undoped mesoporous silica.

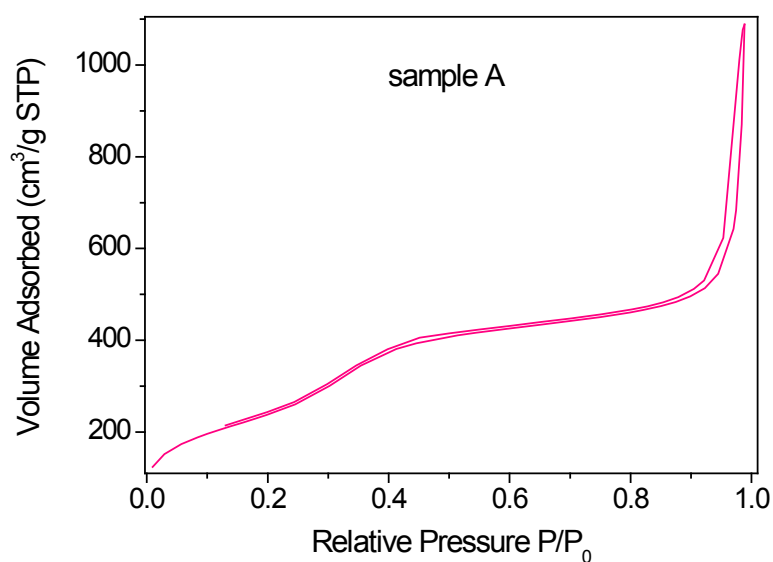


Figure 4.25 N₂ adsorption/desorption isothermal curve of sample A.

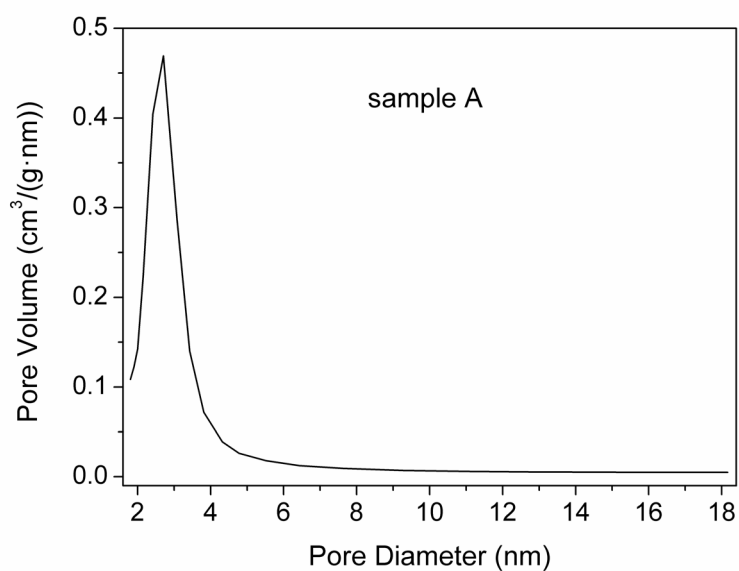


Figure 4.26 Pore size distribution curve of sample A.

Moreover, the resulting values of surface area ($850 \pm 10 \text{ m}^2/\text{g}$) and pore volume (ca. $1.1 \text{ cm}^3/\text{g}$) were higher than expected, since, if compared with the respective values of the non impregnated ms-SiO₂, their decrease (ca. 13% and 10% respectively) after the impregnation is quite small, as a confirmation that in the present sample the efficiency of the impregnation seems to be unsatisfactory.

Nevertheless, XRD analysis was performed on the sample in order to investigate the crystalline structure of the nanocomposite (Fig 4.27).

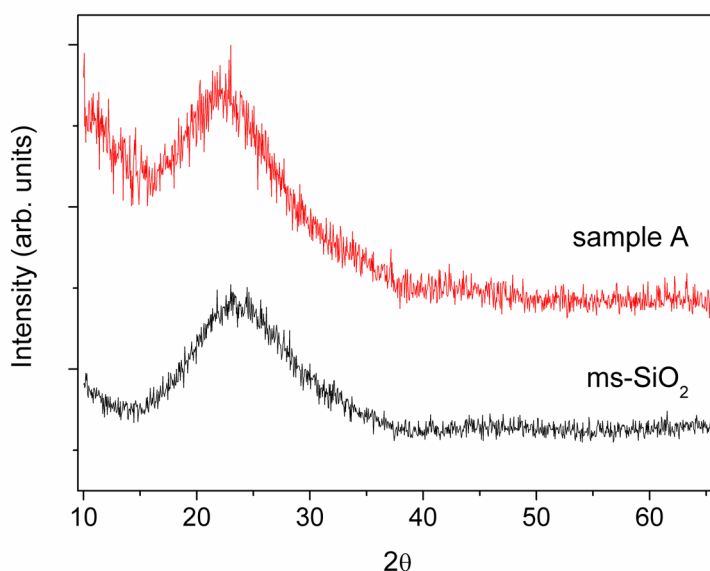


Figure 4.27 XRD patterns of sample A and of the undoped mesoporous silica (ms-SiO₂).

The XRD pattern of sample A (curve at the top) looks very similar to the one of the amorphous silica used for its preparation (curve at the bottom), since at first sight no additional peaks that could be assigned to a crystalline phase seem to emerge from the background curve of the amorphous silica. However, if carefully compared with the pattern of the undoped material, the pattern of sample A shows some small and just visible differences, such as a very weak and broad shoulder peak between 30° and 40° in 2θ values.

However, the very low intensity and the broadness of this peak do not allow any identification of the correspondent phase and therefore the XRD measurement could not add relevant information about the magnetic material embedded into the silica matrix, except for a further confirmation that the fraction of the latter in the nanocomposite is lower than expected, probably because of an inefficient impregnation of the mesoporous nanoparticles with the established amount of iron precursor.

Sample B

Sample B was prepared by impregnating the mesoporous silica nanoparticles after their hydrophobic surface functionalization ($\text{ms-SiO}_2\text{F}$), with the aim of promoting a better loading of iron precursor and hence of the final magnetic phase, especially from a quantitative point of view.

After the usual thermal treatment, the powdered sample, which appeared of an intense brick red – brown color, was first checked by visual means with the test of its magnetic properties in an ethanol suspension when in close proximity of a strong magnet (Fig. 4.28).

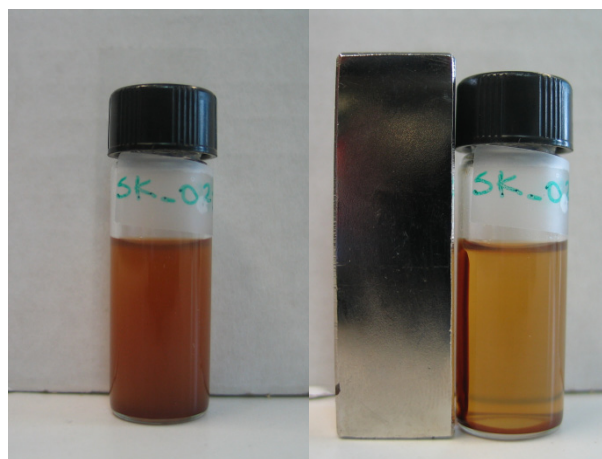


Figure 4.28 Images of sample B with powder dispersed in EtOH (left) and in presence of a magnet (right).

The result was encouraging, since, in comparison with sample A, a quicker response from sample B was observed and in less than one hour most of the

suspended powder migrated towards the magnet, though the liquid did not turn clear at all. Therefore, from this preliminary test the sample appeared to be loaded with a magnetic phase.

In order to get more information about the efficiency of the impregnation, a porosimetric analysis was performed as usual, by means of the N_2 adsorption/desorption measurement, which displayed, once again, a curve with the shape of a mesoporous material (type IV isothermal), notwithstanding the impregnation. Also the shape of the pore size distribution curve did not reveal any relevant changes with respect to the undoped mesoporous silica and to sample A. For these reasons, both the curves are not shown here.

However, the most interesting and significant data of the porosimetric measurements were the values of surface area ($660 \pm 10 \text{ m}^2/\text{g}$) and pore volume (ca. $0.9 \text{ cm}^3/\text{g}$), which both revealed a higher decrease (33% and 29% respectively) from the values of the unloaded silica with respect to sample A, thus indicating an increased fraction of loaded material inside the pores. Hence, being the amount of starting iron precursor unvaried between sample A and B, these results suggest an improvement in the impregnation process efficiency brought by the hydrophobic modification of the silica surface.

XRD analysis was performed on the sample for an investigation on the nature of the loaded phase and the resulting pattern is reported in Fig. 4.29, together with the patterns of the undoped amorphous silica $ms\text{-SiO}_2\text{F}$ and of pure metallic iron ($\text{Fe}(0)$), magnetite (Fe_3O_4) and maghemite ($\gamma\text{-Fe}_2\text{O}_3$) as references (PDF #060696, #19629, #391346 respectively). The two iron oxides have been taken as references since the pattern of sample B clearly showed two additional peaks (centered around 35° and 62.5° in 2θ values), emerging from the amorphous silica background, which are consistent with the presence of either magnetite or maghemite or a mixture of both, similarly to what happened in a previous study (see sample B in § 4.1.2). Also in this case, however, it is very hard to discriminate between the two iron oxides, due to the strong similarity of their XRD pattern and to the broadness of the correspondent peaks in the composite sample B.

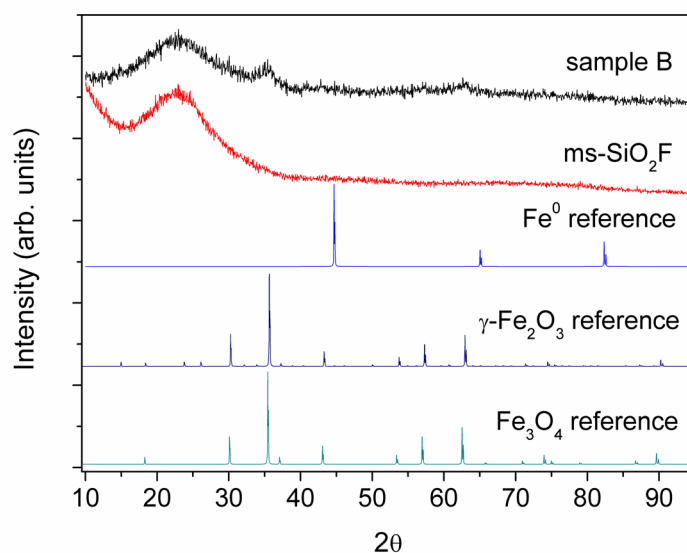


Figure 4.29 XRD patterns of: sample B, undoped mesoporous silica (ms-SiO₂F), Fe(0) (metallic iron), γ -Fe₂O₃ (maghemite) and Fe₃O₄ (magnetite) references from the literature (PDF #060696, #391346, #19629 respectively).

Anyway, at least three important observations could be done after the XRD measurement: (1) the magnetic phase that results to be present in the sample is not the desired one, *i.e.* metallic iron; (2) the higher intensity of the crystalline peaks with respect to the very weak signals in the pattern of sample A, confirmed the increase in the amount of loaded material that emerged also from the porosimetric analysis; (3) the broadness of the aforementioned peaks seems to qualitatively indicate the presence of relatively small nanocrystals in the nanocomposite and this is consistent with the idea that such nanocrystals have been embedded into the silica pores which limited their growth. The latter would be a further confirmation of a good quality of the impregnation which led to a satisfying homogeneity of the final nanostructure in the composite. In order to verify this hypothesis, TEM analysis was performed on sample B.

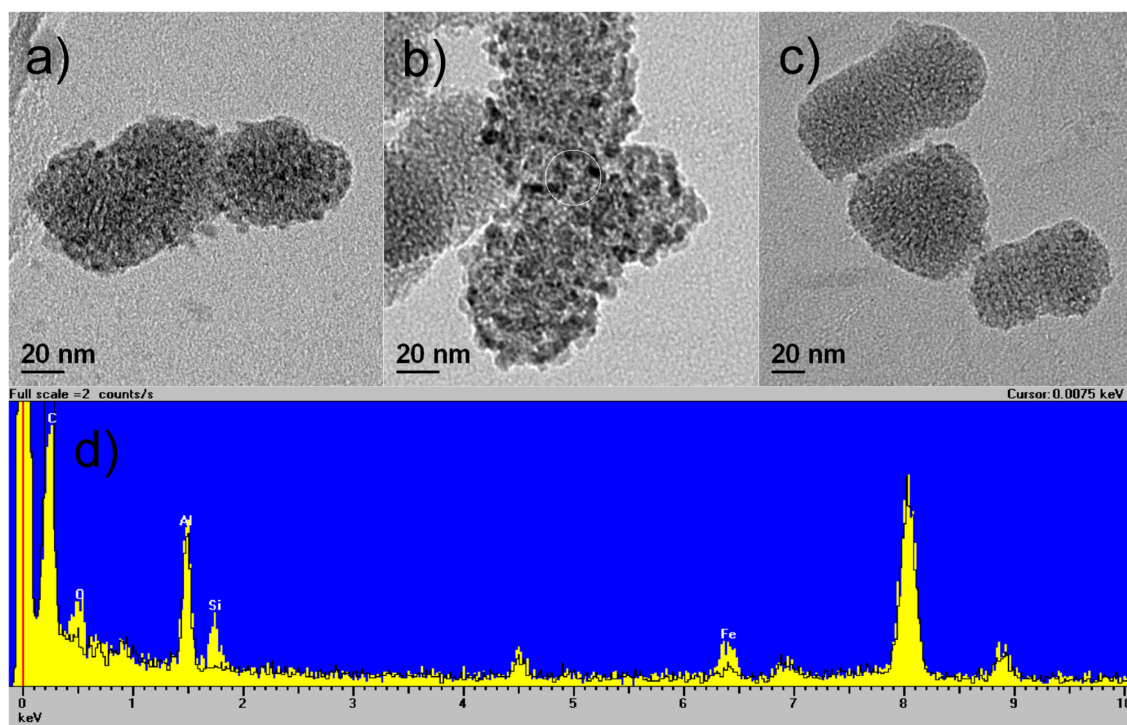


Figure 4.30 TEM micrographs (a-c) and EDS analysis (d) of circled area (b) of sample B.

The micrographs in Fig. 4.30a-b confirmed the presence of small and dark nanocrystals embedded into the silica nanoparticles, while no further material external to them was found during the analysis, as a confirmation of the good quality of the impregnation process. However, as depicted by the micrograph in Fig. 4.30c, some unloaded silica nanoparticles appeared and this fact indicates that the unequivocal enhancement in the quantity of loaded magnetic fraction, due to the hydrophobic functionalization, could further be improved, for example simply by increasing the starting amount of iron precursor and hence the nominal fraction of final magnetic material. Finally, as expected after the results of the XRD characterization, the EDS spectrum (Fig. 4.30d) of the circled area in Fig 4.30b confirmed the presence of Si, O and Fe, attributed to the silica matrix and the loaded iron oxide. Some impurities, coming probably from the tip sonicator which was employed for the preparation of the TEM samples, are responsible for the Al signal in the aforementioned EDS spectrum.

Sample C

The results that came out from the characterization of samples A and B justified the preparation of a further sample, in which, as described in § 4.2.1, the functionalized mesoporous silica $ms\text{-SiO}_2\text{F}$ was impregnated with a definitely higher amount of $\text{Fe}(\text{CO})_5$ in a different solvent (*n*-hexane) and in a more controlled and continuous inert atmosphere, in order to limit as much as possible the oxidation of iron. The change in the employed solvent was due to the necessity of avoiding the presence of water molecules that could be introduced in the material by the highly hygroscopic THF if not used in its anhydrous form, and that could render the environment less suitable to the hydrophobic precursor.

Following the usual thermal treatment, the obtained sample C consisted of a dark grey-black powder, therefore a more promising color than the previous ones for a correspondence with the desired composite material. The usual preliminary test of the magnetic properties proved to be very interesting, since this time the whole visible amount of the suspended powder migrated towards the magnet within several minutes (Fig. 4.31).

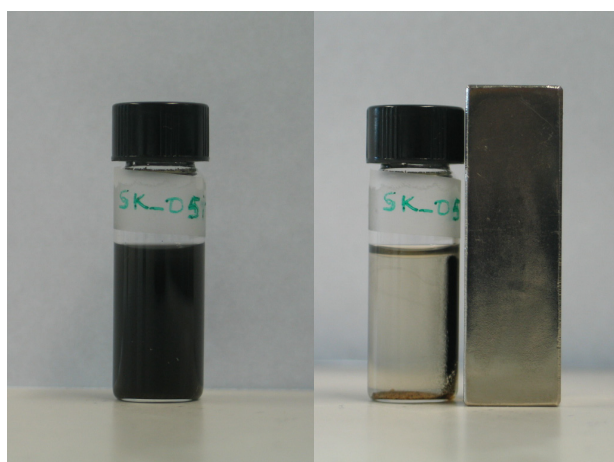


Figure 4.31 Images of sample C with powder dispersed in EtOH (left) and in presence of a magnet (right).

The check by visual means therefore showed a strong response of the sample to an external magnetic field and this was consistent with the potential presence of a strongly magnetic phase, like metallic iron, in the nanocomposite.

The porosimetric analysis did not exhibit any relevant differences from the previous samples (A, B and ms-SiO₂) in terms of the shapes of the N₂ adsorption/desorption and the pore size distribution curves (which therefore are not shown here). Also in this case the material maintained a high mesoporosity notwithstanding the heavily increased amount of iron precursor in the impregnation. This was confirmed also by the resulting values of the surface area ($580 \pm 15 \text{ m}^2/\text{g}$) and the pore volume (*ca.* $0.7 \text{ cm}^3/\text{g}$), which indicated a decrease from the initial conditions of the undoped silica host matrix (41% and 42% respectively) that was higher than the previous samples A and B but lower than expected considering the use of a huge amount of iron precursor. Hence, these data suggested the presence of the loaded phase both inside and outside the silica pores, *i.e.* the formation of a non uniform and homogeneous nanostructure in the composite, which was successively investigated by means of XRD analysis.

The XRD pattern of sample C is reported in Fig. 4.32, together with the patterns of the undoped silica ms-SiO₂F and some other iron-based phases as references. Four relatively intense and sharp peaks can clearly be discriminated from the amorphous background at around 30.25° , 35.55° , 57.1° and 62.7° in 2θ values. As discussed for the previous sample, they can be assigned to either magnetite or maghemite since the patterns of the aforementioned iron oxides almost coincide; or even a mixture of them could be present in the sample. However, contrary to the previous sample B, in this case the sharpness of these peaks in the nanocomposite pattern seems to indicate that the correspondent average size of the crystallites is too big to suppose an efficient embedding into the silica pores and therefore their formation should have occurred (totally or partially) outside the silica nanoparticles.

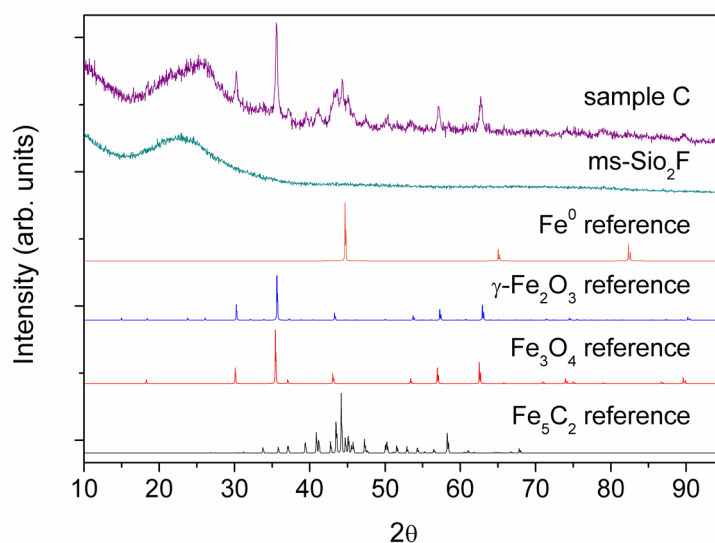


Figure 4.32 XRD patterns of: sample C, undoped mesoporous silica (ms-SiO₂F), Fe(0) (metallic iron), γ -Fe₂O₃ (maghemite), Fe₃O₄ (magnetite) and Fe₅C₂ (iron carbide) references from the literature (PDF #060696, #391346, #19629 and #361248 respectively).

Anyway, a further signal can be observed in the pattern of sample C, *i.e.* the broad peak centered at about 44.3° in 2θ values. At first sight, this signal could be attributed to the metallic iron, since its angular position is consistent with the main peak in the reference pattern of the aforementioned phase and its broadness could be caused by the small size of the crystallites and hence suggest their incorporation into the silica pores. But a more thorough research pointed out the resemblance of the examined signal to a group of sharp peaks that characterize the reference pattern of pure iron carbide Fe₅C₂ in the interval 39° – 50° in 2θ values, thus suggesting a high possibility of its presence in the sample. Of course, this matching could not exclude the potential presence of metallic iron too. Hence, further investigation was needed to determine the nature of the crystalline nanostructure in the nanocomposite.

Raman spectroscopy was employed for further study on sample C and the recorded spectra (between 100 and 1000 cm⁻¹ and between 0 and 3000 cm⁻¹) are shown in Fig. 4.33.

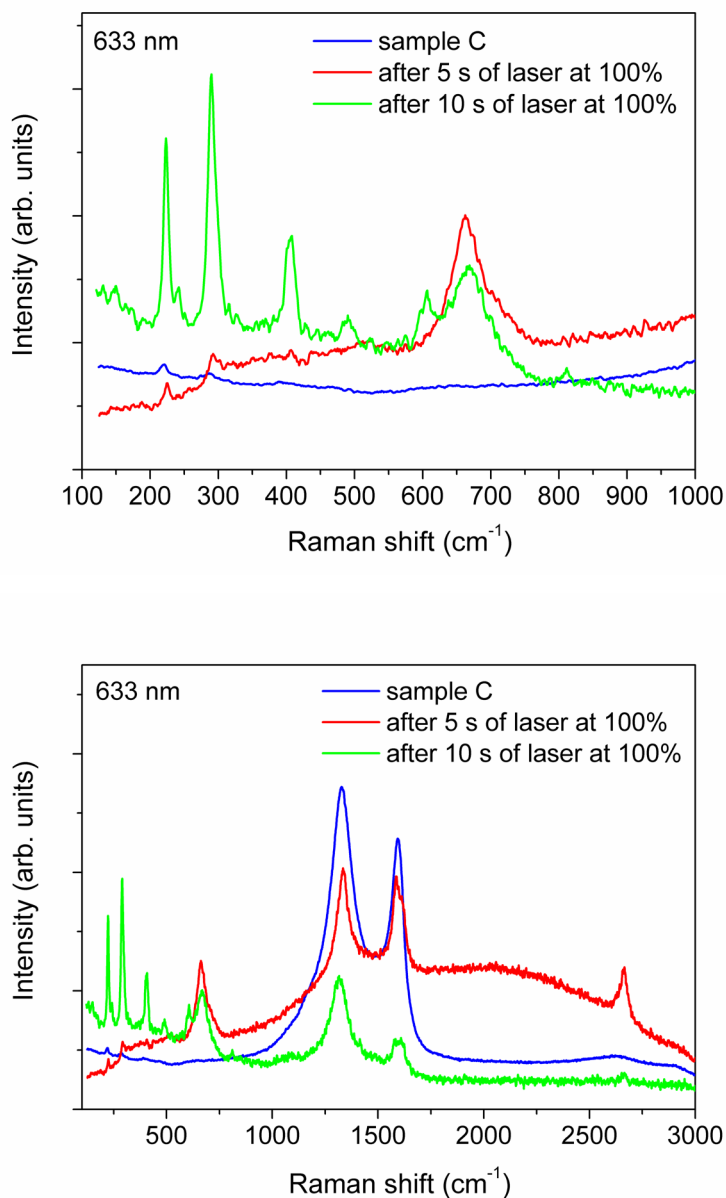


Figure 4.33 Raman spectra of sample C between 100 and 1000 cm⁻¹ (top) and between 0 and 3000 cm⁻¹ (bottom).

The Raman spectrum of sample C (blue curve) indicates the presence of carbon-based nanostructures, probably single or double-wall nanotubes, whose characteristic bands appear between 1000 and 1750 cm⁻¹. Fe(CO)₅ is often used as a precursor to obtain these particular nanostructures and therefore their

presence in the sample is not surprising in consideration of the huge amount of employed iron pentacarbonyl. It should be noted that the presence of both metallic iron and iron carbide, contrary to iron oxide, cannot be directly detected through Raman spectroscopy, since these two materials do not generate any signals in the spectrum. On the other hand, the spectrum did not even show any relevant traces of the magnetite and/or maghemite that were observed in the XRD analysis, probably because their nanocrystals, that resulted to have big size and therefore to have formed outside the silica matrix as previously discussed, were too few and probably not included in the very small fraction of sample that is examined during Raman analysis.

Anyway, the Raman analysis could indirectly confirm the presence of iron as element in the sample after the irradiation of the examined material by means of a laser at its maximum power (ca. 16 mW), since this treatment usually implies the oxidation of iron and therefore allows its detection.

In fact, in the Raman spectrum recorded after 5 s. of laser irradiation at 100% (red curve), the following main features can be noticed: (1) the typical bands of the nanostructured carbon have lower intensity than before, but at the same time a new signal appeared at about 2600-2700 cm^{-1} , which can be attributed to ordered systems such as nanotubes or graphene; (2) a characteristic band of the magnetite emerged at 660 cm^{-1} , thus indicating that iron was initially present in the material in non oxidized form which became iron oxide following the laser irradiation.

Finally, after 10 s. of laser treatment at 100% (green curve), the appearance of the strong signals between 200 and 400 cm^{-1} indicates that part of the magnetite transformed into hematite ($\alpha\text{-Fe}_2\text{O}_3$), as it is known to happen to this crystalline phase when subjected to laser irradiation in air.

In summary, the Raman spectroscopy, besides detecting the presence of carbon-based nanostructures deriving from the massive use of iron precursor, confirmed also an indication of the XRD analysis, namely the presence of iron in a non oxidized form, *i.e.* metallic or, more probably, carbide iron.

To obtain more information about the nanostructural nature and quality of the composite, TEM analysis was performed on sample C (Fig 4.34).

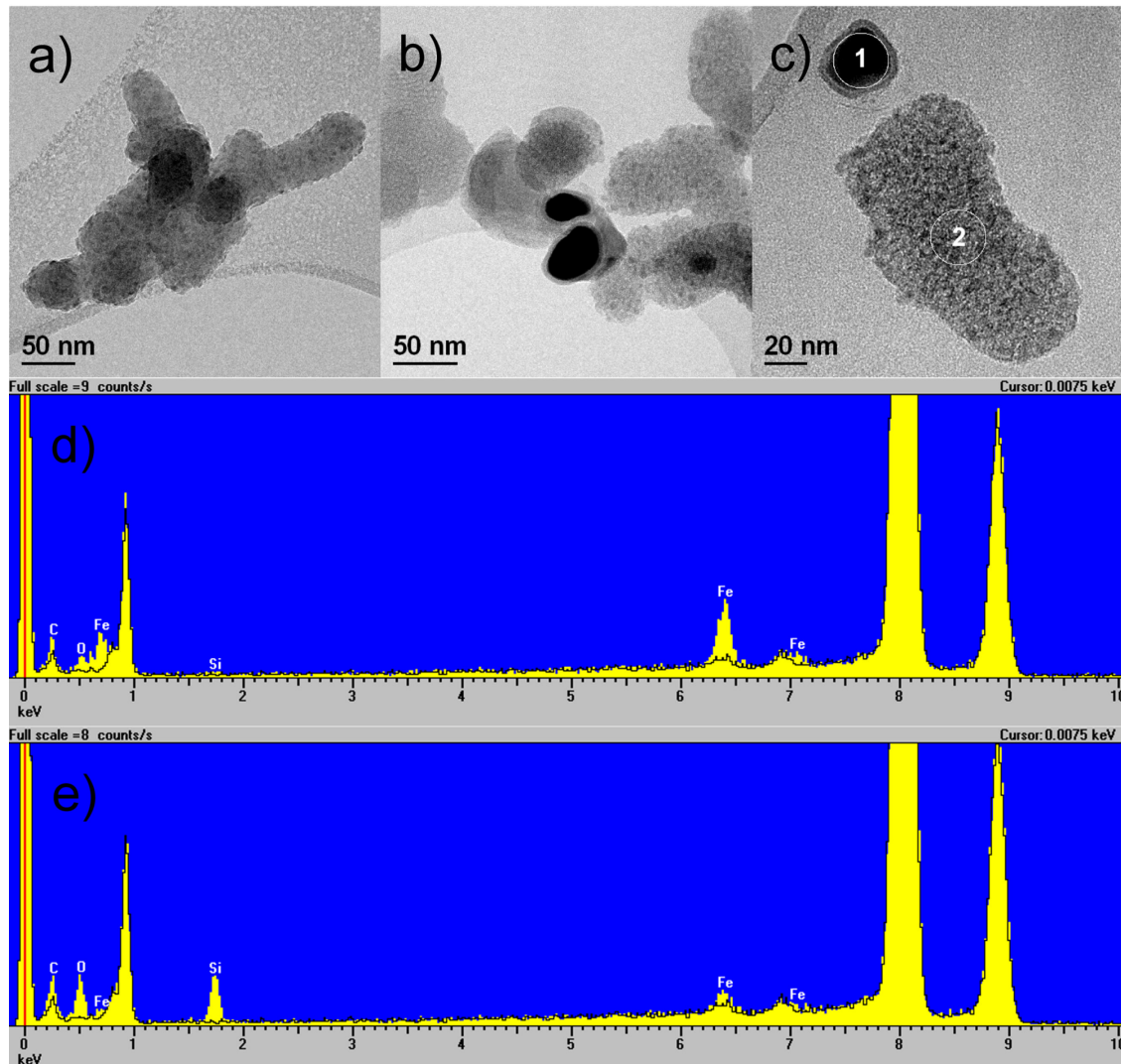


Figure 4.34 TEM micrographs (a-c) and EDS analyses (d, e) of circled areas n.1 and n.2 (c) of sample C.

The micrographs (Fig. 4.34a-c) show silica nanoparticles that are loaded with a high density of small (*ca.* 3 nm) nanocrystals; but, contrary to the previous samples, also some bigger (30-50 nm) nanocrystals, as suggested by the XRD analysis, have formed out of the silica matrix (dark structures in Fig. 4.34 b,c) and they resulted to be covered by a thin shell of undefined nature.

The EDS spectra in Fig. 4.34d and e, recorded respectively on a big dark nanocrystal (circled area n.1 in Fig. 4.34c) and on an impregnated silica nanoparticle (circled area n.2 in Fig. 4.34c), confirmed the presence of elemental Fe, C and O in both the cases (though the iron signal is more evident, as expected, in the first spectrum), while the signal of Si appeared only in the second spectrum, being attributed to the SiO_2 which is not present in the area n.1. These data are therefore consistent with the presence of iron oxide and/or iron carbide both inside and outside the silica matrix, even if also metallic iron cannot be excluded from the list of potentially present phases.

Even though they proved the non homogeneous and irregular nature of the nanostructure in the composite, the big dark nanocrystals that formed outside the silica pores were very useful, since they contributed to the determination of some of the present phases in the sample. By means of HRTEM (High Resolution Transmission Electron Microscopy) on the aforementioned nanocrystals, the interplanar distances of their crystalline structure could be easily measured and the obtained values, after being compared with the literature (PDF database), led to the identification of the correspondent phase.

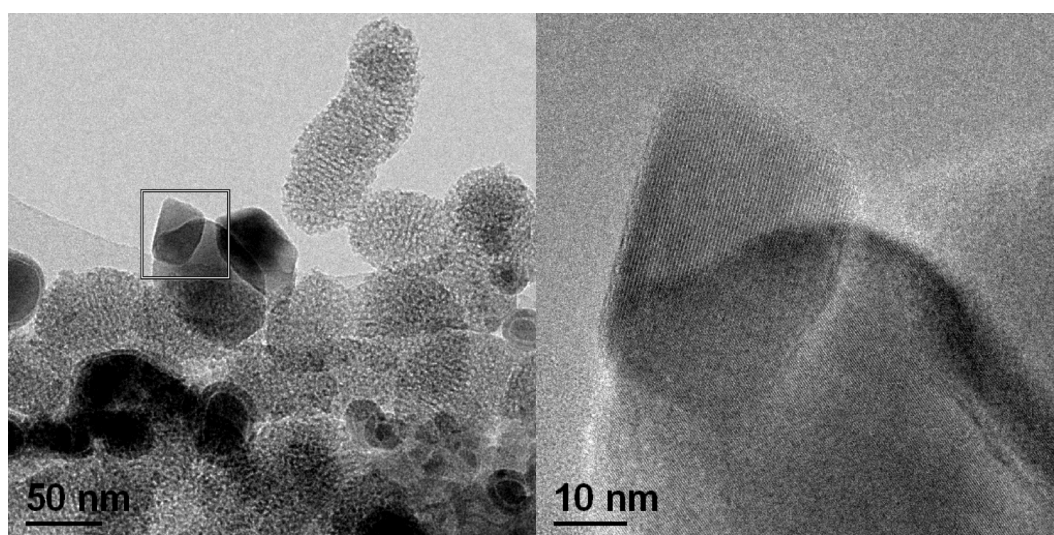


Figure 4.35 TEM micrographs of sample C: (left) a maghemite nanocrystal (squared area) and (right) its crystalline planes at high resolution.

The HRTEM analysis of the structure that is shown in Fig. 4.35 revealed that the sample contains maghemite (in agreement with the result of the XRD analysis), as evidenced by the comparison of the theoretical and experimental values of the interplanar distances (Tab. 4.4).

Table 4.4 Average values of the interplanar distances in the crystalline structure of maghemite (PDF #391346) and in the nanocrystal shown in Fig. 4.35.

Miller indices	theoretical interplanar distances of maghemite (Å)	observed interplanar distances (Å)
111	4.82	4.84
220	2.95	2.96
400	2.09	2.10

HRTEM analysis also confirmed the presence of iron carbide Fe_5C_2 in the sample, as revealed by the same examination of the interplanar distances (Tab. 4.5) in another structure appearing in Fig. 4.36.

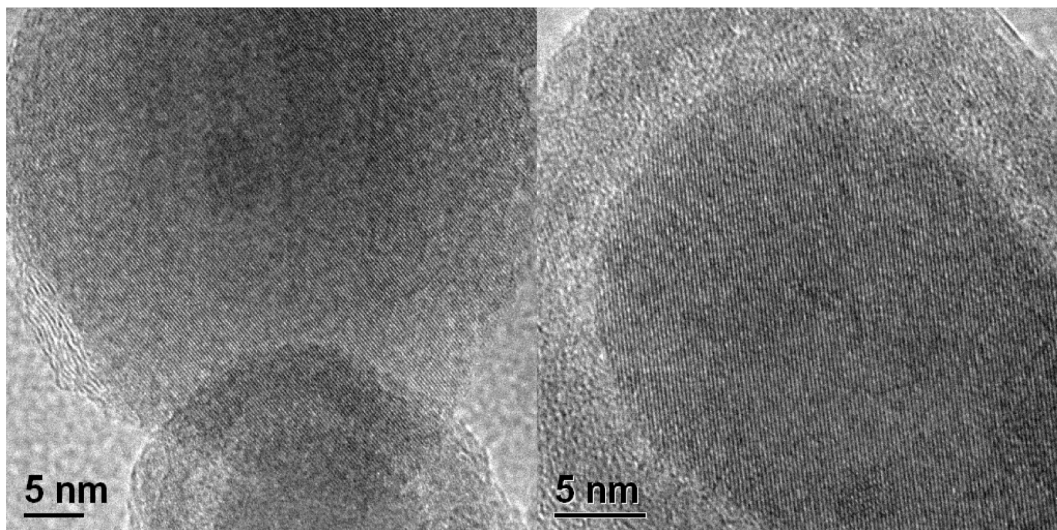


Figure 4.36 TEM micrographs at high resolution of a Fe_5C_2 nanocrystal in sample C.

On the contrary, no traces of metallic iron, whose crystalline structure has typically close packed planes that should be easily recognized with this kind of analysis, were detected in the sample.

Table 4.5 Average values of the interplanar distances in the crystalline structure of Fe_5C_2 (PDF #361248)³⁴ and in the nanocrystal shown in Fig. 4.36.

Miller indices	theoretical interplanar distances of Fe_5C_2 (Å)	observed interplanar distances (Å)
400	2.86	2.86
002	2.51	2.51
311	2.42	2.42
202	2.19	2.15

The TEM analysis therefore confirmed in general the prediction of the XRD measurement, though it could only determine the nature of the bigger nanocrystals, while the nature of the embedded ones can be only hypothesized as the same. Moreover, the carbon-based nanostructures that emerged from the Raman spectroscopy could not be observed here. This could be due to the employed procedure for the preparation of the TEM samples.

Anyway, notwithstanding the absence of metallic iron and a nanostructural disorder which was probably caused by the too heavy amount of iron precursor used in the impregnation, sample C resulted to contain at least two different phases ($\gamma\text{-Fe}_2\text{O}_3$ and Fe_5C_2) with potential magnetic properties. For this reason, after the promising test of the magnetic response (Fig. 4.31), further investigation on the magnetic properties of the composite was performed.

The presence of various magnetic phases and their superparamagnetic behavior were investigated by measuring the temperature dependence of the ZFC and FC magnetizations (Fig. 4.37). The ZFC curve does not present any maximum and the two curves do not joint at 300 K; this double experimental evidence indicated that most of the nanoparticles are not superparamagnetic at

room temperature. In fact, this was also confirmed by the open hysteresis loop that was recorded at 300 K (Fig. 4.38), while, as previously mentioned (see § 4.1.2) the superparamagnetism is associated to a lack of irreversible processes like open loops.

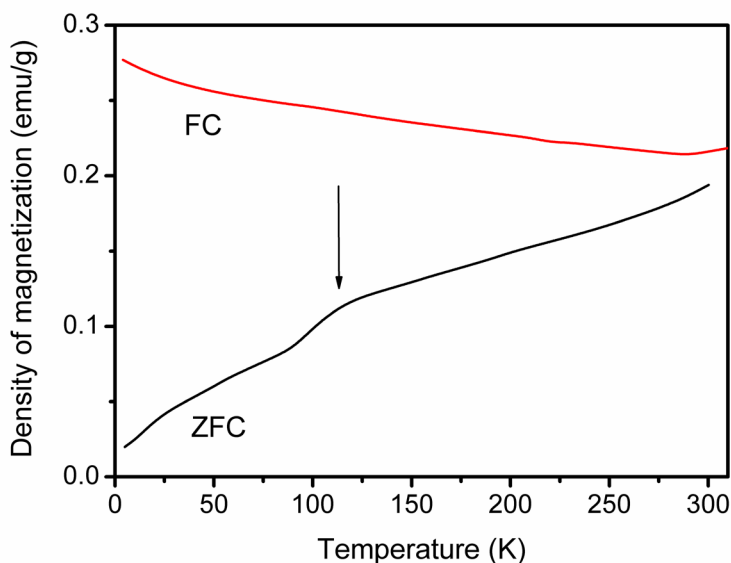


Figure 4.37 Temperature dependence of the ZFC and FC magnetization of sample C.

Moreover, the ZFC curve shows a broad peak at about 110-115 K, which a priori could hardly be assigned to a definite phase, but its position coincide with the Verwey temperature (T_V) of magnetite and so this peak should reasonably indicate the presence of the aforementioned phase.

The hysteresis loops of sample C at 3 K and 300 K are reported in Fig. 4.38. At 3 K, the density of magnetization of the composite, with a magnetic field of 5 T, is 17.5 emu/g, while a second measurement of a different fraction of the sample gave a lower value, 11 emu/g. However, the shape of the hysteresis loops as well as the ZFC and FC curves (not shown here) of this second fraction of sample did not change. This means that the magnetic material which is present in the two fractions of sample is the same, while the content of magnetic material is different, indicating that sample C is not homogeneous with

respect to its composition, as expected after the results of previous characterizations.

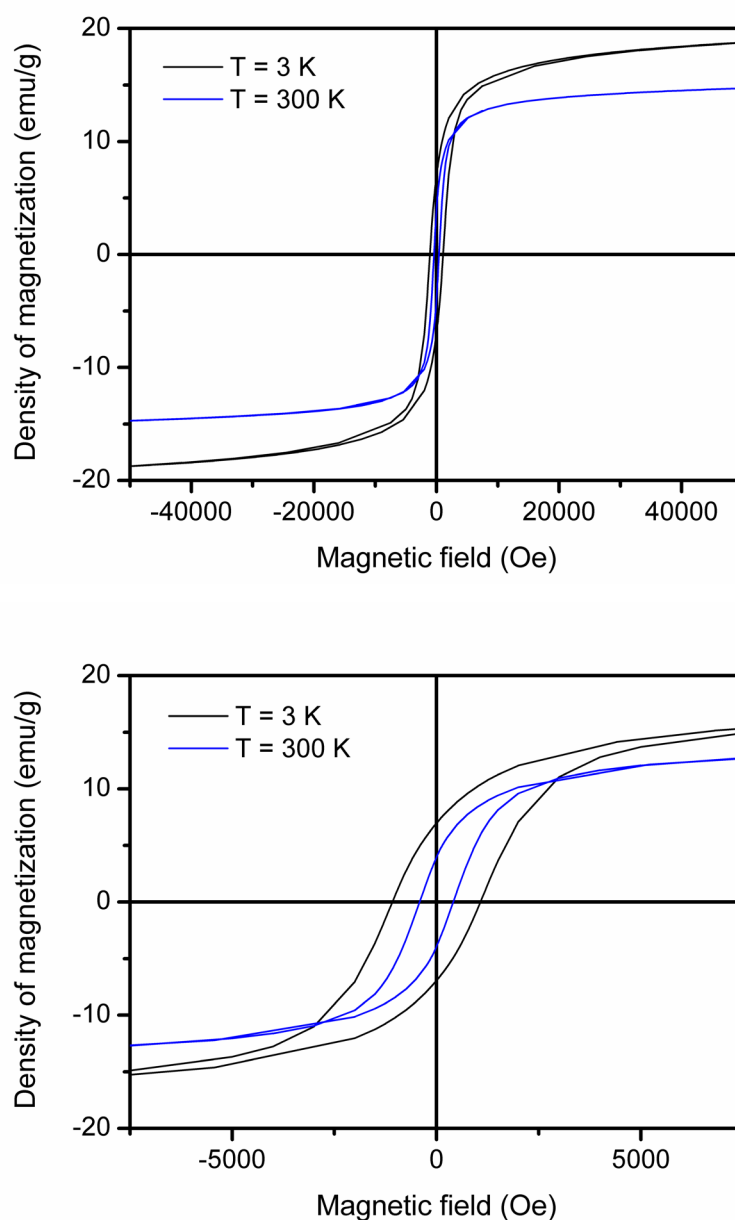


Figure 4.38 Hysteresis loops of sample C measured at 3 K and 300 K (top); details of the central part of the curves (bottom).

This lack of uniformity forbids to calculate the magnetization of the magnetic material, but, considering that the mass fraction of Fe on the total composite

should be *ca.* 0.5, the density of magnetization per gram of iron is around 35 emu/g (or alternatively 22 emu/g), a lower value if compared to those of magnetite (136 emu per gram of iron or, more known, 92 emu per gram of magnetite). Moreover, the shape of the hysteresis loops indicates that the density of the magnetization does not reach saturation even at high magnetic fields, a behavior that suggests the presence of some ions. If the measured magnetic moment were supposed to come totally from an iron oxide as magnetite, the small value of 35 emu/g would imply that approximately only the 25% of iron formed oxides, while the 75% remained in the form of poorly magnetic ions. But this hypothesis is not corroborated by the data. In particular, though it is difficult to quantify the magnetization of these ions, the very gentle slope of the magnetization at high fields indicates that the percentage of the aforementioned ions cannot be so high. Therefore, the low magnetization that was measured could be due to the presence of the Fe_5C_2 phase, even if the determination of its magnetic properties is not possible.

In Fig. 4.39, the variation of the magnetization with the temperature measured by applying a magnetic field of 5 T is reported.

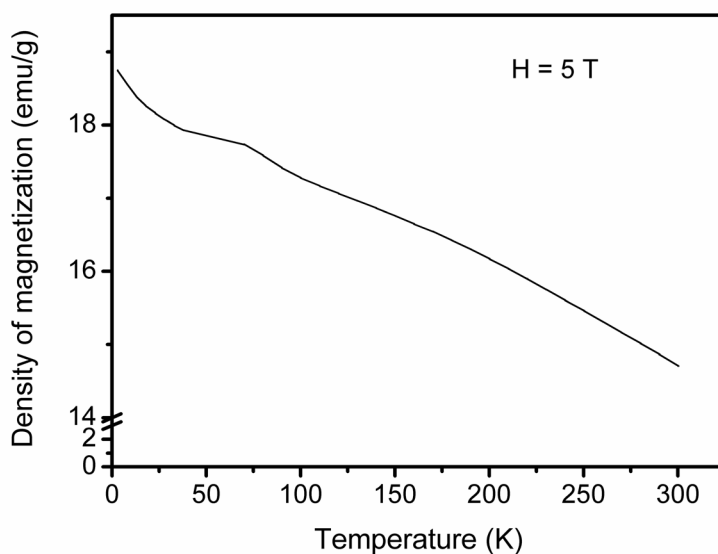


Figure 4.39 Variation of the magnetization in function of the temperature of sample C with an applied magnetic field of 5 T.

The curve is diverging below 25 K, with a typical shape of a $1/T$ trend that usually characterizes paramagnetic ions. Anyway this contribution is small. Above 25 K, the magnetization trend reasonably follows the Bloch's law:

$$M(T) = M_0 (1 - BT^{3/2})$$

which is characteristic of magnetic materials. The decrease of the magnetization from 3 to 300 K is around 20%, a value which is usually high for a bulk material and low for a nano one.

Finally, a measurement of the variation of the magnetization from 3 to 300 K at zero field after having saturated the sample with an applied magnetic field of 5 T at 3 K (ZFC method) and at 300 K (FC method), was performed.

The resulting curves (Fig. 4.40) are separated at low temperatures and joint just before the Verwey temperature T_v of the magnetite. This proves the presence of this oxide in the sample, in addition to the hypothesized Fe_5C_2 .

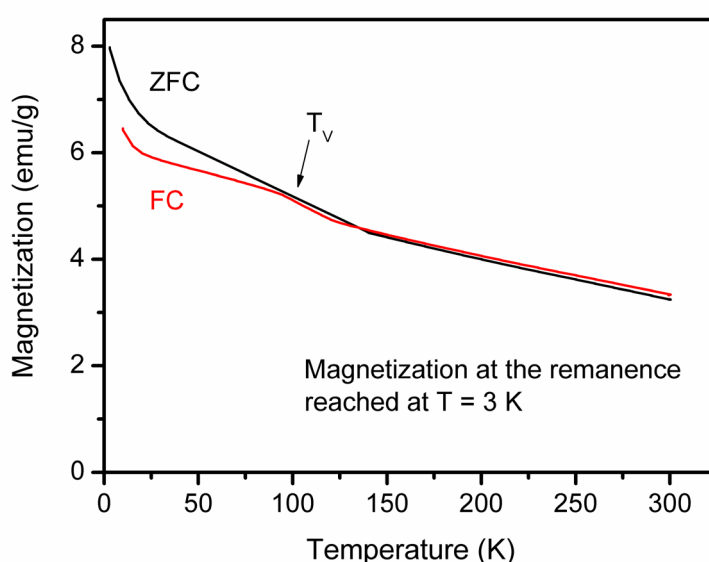


Figure 4.40 variation of the magnetization from 3 to 300 K at zero field after having saturated the sample with an applied magnetic field of 5 T at 3 K (ZFC method) and at 300 K (FC method).

In general, the magnetic characterization pointed out that this sample is much more magnetic than the composites of the previous study with iron oxide and cobalt-iron oxide (see § 4.1.2); the magnetic nanocrystals are bigger and with higher coercive fields. But the magnetic content is not homogeneous at all.

The sample contains magnetite nanocrystals and some clues indicate the presence of a phase with low density of magnetization and Curie temperature, which is consistent with the presence of iron carbide Fe_5C_2 . The presence in the sample of the maghemite crystals that were observed by means of the HRTEM analysis, was not detected through the magnetic measurements.

4.2.3 Conclusions

The aim of this study was the incorporation of metallic iron into a mesoporous silica matrix in order to obtain a nanostructured composite material with high magnetic properties. Three different ways were followed to this purpose, all based on the impregnation of the host matrix with iron pentacarbonyl followed by a thermal treatment in inert atmosphere.

The first two samples (A and B) were prepared by impregnating the mesoporous silica nanoparticles with a solution of the precursor in THF and this process was performed in air. The only difference between the two procedures was that in the second attempt a TMES functionalized silica was used, in order to improve the impregnation efficiency with a more hydrophobic environment. In both cases the obtained composites were not in agreement with the expectations, since they resulted to contain only iron oxide (probably a mixture of magnetite and maghemite) and their magnetic response seemed to be quite low. Anyway, the hydrophobic functionalization of silica in sample B brought to an increase in the quantity of loaded material with respect to sample A (indicated by the evaluation of its pore volume decrease after the impregnation, *ca.* three times higher than sample A), thus proving to be efficient in improving

the overall quality of the sample, though a presumably small fraction of silica nanoparticles still remained undoped.

A third attempt (sample C) consisted in the employment of a higher amount of precursor in a more appropriate solvent (*n*-hexane) and in an inert atmosphere (by means of the *cannula transfer* method) during the impregnation process, in order to limit as much as possible the iron oxidation in every step of the synthetic procedure.

This sample resulted to have a definitely stronger magnetic behavior, good stability and a different nanostructure, since its characterization evidenced the presence of different iron compounds, such as the usual magnetite and maghemite and an iron carbide, Fe_5C_2 , which is also known to have interesting magnetic properties. Therefore, the more controlled inert atmosphere and the cannula transfer method, as expected, gave a partial advantage. Unfortunately, no evidence of the zero-valent iron presence was found, but this could be also due to the its high chemical instability once formed, especially in nanosized materials. Moreover, the huge amount of precursor caused an irregular and heterogeneous nanostructure in the composite, since, together with an improvement in the quantity of loaded material (in the form of small nanocrystals) into the SiO_2 , the presence of bigger nanocrystals outside the host matrix was detected, accounting for a poor structural quality of the sample.

Ultimately, this study demonstrated the possibility to obtain, via the thermal decomposition of $\text{Fe}(\text{CO})_5$, a magnetic nanocomposite material based on a silica matrix containing iron oxide and iron carbide. One of its main advantages is represented by the retained mesoporosity of the final composite, which implies the possibility to load further materials, *e.g.* biomolecules or drugs, that could be useful for a wide range of biological applications. In perspective, the applied procedure for sample C, combined with a more appropriate amount of starting precursor, should produce a qualitatively better material, with nanostructural regularity and homogeneity, and thus promising for potential application in the biomedical field.

List of references:

- (1) Slonczewski, J. C. *Phys. Rev.* **1958**, *110*, 1341-1348.
- (2) Verma, S.; Pravarthana, D. *Langmuir* **2011**, *27*, 13189-13197.
- (3) Bozorth, R. M.; Tiltan, E. F.; Williams, A. J. *Phys. Rev.* **1955**, *99*, 1788-1798.
- (4) Fantechi, E.; Campo, G.; Carta, D.; Corrias, A.; de Julián Fernández, C.; Innocenti, C.; Pineider, F.; Rugi, F.; Sangregorio, C. submitted to *Journal of Physical Chemistry*.
- (5) Song, Q.; Zhang, Z. *J. Phys. Chem. B* **2006**, *110*, 11205-11209.
- (6) Baldi, G.; Bonacchi, D.; Innocenti, C.; Lorenzi, G.; Sangregorio, C. *J. Magn. Magn. Mater.* **2007**, *311*, 10-16.
- (7) Qiao, Z.-A.; Zhang, L.; Guo, M.; Liu, Y.; Huo, Q. *Chem. Mater.* **2009**, *21*, 3823-3829.
- (8) Parma, A.; Freris, I.; Riello, P.; Enrichi, F.; Cristofori, D.; Benedetti, A. *J. Lumin.* **2010**, *130*, 2429-2436.
- (9) del Monte, F.; Morales, M. P.; Levy, D.; Fernandez, A.; Ocaña, M.; Roig, A.; Molins, E.; O'Grady, K.; Serna, C. *J. Langmuir* **1997**, *13*, 3627-3634.
- (10) de Faria, D. L. A.; Venâncio Silva, S.; de Oliveira, M. T. *J. Raman Spect.* **1997**, *28*, 873-878.
- (11) Coey, J. M. D. *Magnetism and Magnetic Materials*; Cambridge University Press: Cambridge, U.K., 2010.
- (12) Kodama, R. H.; Berkowitz, A. E. *Phys. Rev. B* **1999**, *59*, 6321-6336.
- (13) *Surface Effects in Magnetic Nanoparticles*; Fiorani, D., Ed.; Springer: New York, 2005.
- (14) Machala, L.; Zboril, R.; Gedanken, A. *J. Phys. Chem. B* **2007**, *111*, 4003-4018.
- (15) Bean, C. P.; Livingston, J. D. *J. Appl. Phys.* **1959**, *30*, 120S-129S.
- (16) Dormann, J. L.; Fiorani, D.; Tronc, E. *Adv. Chem. Phys.* **1997**, *98*, 283-494.

- (17) Néel, L. *Ann. Geophys.* **1949**, *5*, 99-136.
- (18) Knobel, M.; Nunes, W. C.; Socolovsky, L. M.; De Biasi, E.; Vargas, J. M.; Denardin, J. C. *J. Nanosci. Nanotechnol.* **2008**, *8*, 2836-2857.
- (19) Stoner, E. C.; Wohlfarth, E. P. *Philos. Trans. R. Soc. London* **1948**, *Ser. A 240*, 599-642.
- (20) Pankhurst, Q. A.; Connolly, J.; Jones, S. K.; Dobson, J. *J. Phys. D: Appl. Phys.* **2003**, *36*, R167-R181.
- (21) Hatch, G. P.; Stelter, R. E. *J. Magn. Magn. Mater.* **2001**, *225*, 262-276.
- (22) Rietveld, H. M. *J. Appl. Cryst.* **1969**, *2*, 65-71.
- (23) Wang, Z.; Downs, R. T.; Pishedda, V.; Shetty, R.; Saxena, S. K.; Zha, C. S.; Zhao, Y. S.; Schiferl, D.; Waskowska, A. *Phys. Rev. B* **2003**, *68*, 094101.
- (24) Tung, L. D.; Kolesnichenko, V.; Caruntu, D.; Chou, N. H.; O'Connor, C. J.; Spinu, L. *J. Appl. Phys.* **2003**, *93*, 7486-7488.
- (25) Sorescu, M.; Grabias, A.; Tarabasanu-Mihaila, D.; Diamandescu, L. *J. Appl. Phys.* **2002**, *91*, 8135-8137.
- (26) Peddis, D.; Cannas, C.; Piccaluga, G.; Agostinelli, E.; Fiorani, D. *Nanotechnology* **2010**, *21*, 125705.
- (27) Khurshid, H.; Tzitzios, V.; Colak, L.; Fang, F.; Hadjipanayis, G. C. *J. Phys.: Conf. Ser.* **2010**, *200*, 072049.
- (28) Kim, H.-J.; Ahn, J.-E.; Haam, S.; Shul, Y.-G.; Song, S.-Y.; Tatsumi, T. *J. Mater. Chem.* **2006**, *16*, 1617-1621.
- (29) Eliseev, A. A.; Kolesnik, I. V.; Lukashin, A. V.; Tretyakov, Y. D.; Görnert, P. *Physica E* **2008**, *40*, 2531-2534.
- (30) Napolsky, K. S.; Eliseev, A. A.; Knotko, A. V.; Lukashin, A. V.; Vertegel, A. A.; Tretyakov, Y. D. *Mater. Sci. Eng. C* **2003**, *23*, 151-154.
- (31) Kim, J.-C.; Lee, J.-W.; Park, B.-Y.; Choi, C.-J. *J. Alloys Compd.* **2008**, *449*, 258-260.
- (32) Parma, A.; Freris, I.; Riello, P.; Cristofori, D.; de Julián Fernández, C.; Amendola, V.; Meneghetti, M.; Benedetti, A. submitted to *J. Mater. Chem.*

- (33) Grigorieva, N. A.; Grigoriev, S. V.; Eckerlebe, H.; Eliseev, A. A.; Napolskii, K. S.; Lukashin, A. V.; Tretyakov, Y. D. *J. Magn. Magn. Mater.* **2006**, *300*, e342-e345.
- (34) Retief, J. J. *Powder Diffraction* **1999**, *14*, 130-132.

CHAPTER 5

LUMINESCENT AND MAGNETIC MATERIAL

5.1 FeO_x/Eu(DBM)₃Phen@ms-SiO₂F luminescent and magnetic nanocomposite

The successful incorporation of luminescent materials, as well as magnetic nanocrystals, into a protective silica matrix encouraged the investigation on a bifunctional nanocomposite material with both magnetic and luminescent properties. The advantages of such a system, as discussed in the introduction, are largely employed nowadays in many fields of the biomedical sector.¹⁻⁵

To this purpose, the possibility to easily functionalize the surface of the mesoporous silica nanoparticles and to load them with desirable amounts of different functional materials through a multistep impregnation strategy resulted the chosen approach. From the varying assortment of luminescent and magnetic materials that were investigated, the selection of the most suitable for the impregnation of the host silica matrix was mainly based on the idea that a right compromise between the luminescent and magnetic efficiency should be found. In fact, an important drawback that could be related to a bifunctional luminescent and magnetic system is represented by the massive absorption of light by a typically dark magnetic phase, that could weaken the luminescence from the optically active species which are present in the same material.

Hence, a reasonable way to avoid, or at least reduce, this problem seemed to be the use of a strongly luminescent species with a very intense emission and high capability to absorb light, together with a less dark as possible magnetic material. For these reasons, the chosen materials to be impregnated inside the silica pores for the preparation of a bifunctional nanocomposite were the luminescent Eu(III)-complex Eu(DBM)₃Phen and the magnetic iron oxide FeO_x, that were both already studied in a silica based composite. In fact, the former was the luminescent material with the highest intensity of emission among the investigated ones, while the latter, once embedded into the silica pores, produced a nanocomposite that presented a dark red - brown color, instead of the dark grey - black color of other studied materials (e.g.

CoFe₂O₄@ms-SiO₂ in § 4.1 or sample C in § 4.2, both with better magnetic properties than FeO_x@ms-SiO₂).

The synthetic strategy for the preparation of the multifunctional nanocomposite was therefore based on a combination of the procedures that were previously followed for the preparation of the analogous luminescent or magnetic materials. In details, the presynthesized mesoporous nanoparticles were first impregnated with an appropriate amount of the magnetic nanocrystals (the same optimal nominal fraction that emerged from the FeO_x@ms-SiO₂ series of samples), then functionalized with APTES and finally impregnated again with the presynthesized and purified Eu(DBM)₃Phen complex (with the same nominal fraction of the previously investigated Eu(DBM)₃Phen@ms-SiO₂F sample).

5.1.1 Samples preparation

Synthesis of mesoporous SiO₂ nanoparticles (ms-SiO₂)

The synthesis of mesoporous silica nanoparticles was adapted from the procedure by Qiao et al.⁶ and has previously been reported in this thesis (see § 3.2.1).

Synthesis of FeO_x@ms-SiO₂ sample

This sample was prepared exactly like sample B of the correspondent FeO_x@ms-SiO₂ series, therefore with a 17% nominal weight fraction of impregnated iron oxide inside the silica pore network.

The sample was obtained by impregnating mesoporous SiO₂ nanoparticles (0.3 g) with an aqueous solution (4 mL) of Fe(NO₃)₃·9H₂O (0.328 g, 0.81 mmol) salt, whose quantity was calculated according to the desired nominal fraction. After stirring the mesoporous SiO₂ nanoparticles in iron nitrate solution overnight, the sample was dried by removing the solvent under reduced pressure. The impregnated silica powder was then annealed at 700 °C for 12 hours in air (first

oxidating thermal treatment) and at the same temperature for 12 hours in $N_2 + 5\% H_2$ gas atmosphere (second reducing thermal treatment).

Surface functionalization of $FeO_x@ms-SiO_2$ with APTES

The general procedure for surface functionalization with APTES,⁷ which has already been described (see § 3.1.1), was here applied to 0.2 g of the magnetic nanocomposite sample $FeO_x@ms-SiO_2$.

Synthesis and purification of $Eu(DBM)_3Phen$ complex

The synthesis of $Eu(DBM)_3Phen$ was adapted from the procedure by McGehee et al.⁸ and has previously been reported in this thesis, as well as the purification procedure (see § 3.3.1).

Synthesis of $FeO_x/Eu(DBM)_3Phen@ms-SiO_2F$ sample

The $FeO_x/Eu(DBM)_3Phen@ms-SiO_2F$ sample was prepared with a 7.5% nominal weight fraction of luminescent organic complex inside the silica matrix (the same fraction than sample $Eu(DBM)_3Phen@ms-SiO_2F$), thus excluding the weight of the magnetic fraction from the total weight of the final composite for the calculation of the needed amount of complex.

The sample was obtained by impregnating the powder of functionalized $FeO_x@ms-SiO_2F$ sample (0.240 g) with a 8mM solution of $Eu(DBM)_3Phen$ (0.016 g, 0.016 mmol) in DCM (1.99 mL), calculated according to the desired fraction of complex in the final nanocomposite. After stirring the functionalized and FeO_x -doped mesoporous SiO_2 nanoparticles in $Eu(DBM)_3Phen$ solution, the solvent was removed with the rotavapor and the dried powder was recovered and rinsed by repeated (2 times) DCM washing and centrifugation (30 min at 6 krpm), in order to remove the potential fraction of complex which could have remained outside the silica pores. Anyway, no relevant traces of complex were detected after each centrifugation in the liquid supernatant, monitored by means of UV-VIS absorption spectroscopy. The obtained sample,

$\text{FeO}_x/\text{Eu}(\text{DBM})_3\text{Phen}@ms\text{-SiO}_2\text{F}$ was dried under reduced pressure (10^{-1} mbar for 1 h).

5.1.2 Results and discussion

Mesoporous SiO_2 nanoparticles ($ms\text{-SiO}_2$)

For a better comparison with the previously discussed $\text{Eu}(\text{DBM})_3\text{Phen}@ms\text{-SiO}_2\text{F}$ composite, a fraction of the same mesoporous silica nanoparticles $ms\text{-SiO}_2$ that were employed in the aforementioned study, was here employed for the realization of the $\text{FeO}_x/\text{Eu}(\text{DBM})_3\text{Phen}@ms\text{-SiO}_2\text{F}$ composite. In this case the functionalization with APTES was preceded by the incorporation of iron oxide but for a comparison of the porosimetry between the two composites the sequence of the various synthetic steps should not have a particular significance. Therefore, the main features of the functionalized mesoporous silica nanoparticles $ms\text{-SiO}_2\text{F}$ that were used in the previous study can be considered as a reference here and are recalled in the following list:

- isolated and aggregated nanoparticles with spheroidal shape;
- nanoparticles' size: 60-70 nm;
- N_2 ads./des. isothermal curve: type IV (typical of a mesoporous material);
- surface area (B.E.T. method): $1090 \pm 10 \text{ m}^2/\text{g}$;
- pore volume: $1.4 \text{ cm}^3/\text{g}$;
- average pore diameter (B.J.H. method): ca. 2.8 nm;
- surface functionalization with APTES confirmed by IR spectroscopy.

$\text{FeO}_x/\text{Eu}(\text{DBM})_3\text{Phen}@ms\text{-SiO}_2\text{F}$ sample

Following incorporation of iron oxide, functionalization with APTES and impregnation with $\text{Eu}(\text{III})$ complex, the structural and morphological characterization of sample $\text{FeO}_x/\text{Eu}(\text{DBM})_3\text{Phen}@ms\text{-SiO}_2\text{F}$ was performed as usual by means of XRD, TEM and porosimetric analyses and IR spectroscopy.

The XRD pattern of $\text{FeO}_x/\text{Eu}(\text{DBM})_3\text{Phen}@ms\text{-SiO}_2\text{F}$ is reported in Fig. 5.1 together with those of $\text{Eu}(\text{DBM})_3\text{Phen}@ms\text{-SiO}_2\text{F}$ (see § 3.3.2) and sample B of the $\text{FeO}_x@ms\text{-SiO}_2$ series (see § 4.1.2) for a comparison.

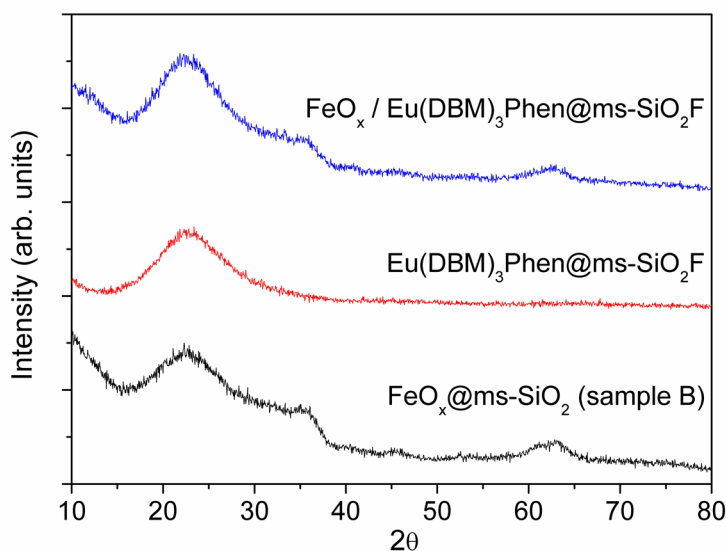


Figure 5.1 XRD patterns of samples $\text{FeO}_x@ms\text{-SiO}_2$ (sample B in § 4.1), $\text{Eu}(\text{DBM})_3\text{Phen}@ms\text{-SiO}_2\text{F}$ and $\text{FeO}_x/\text{Eu}(\text{DBM})_3\text{Phen}@ms\text{-SiO}_2\text{F}$.

As expected, the XRD pattern of the $\text{FeO}_x/\text{Eu}(\text{DBM})_3\text{Phen}@ms\text{-SiO}_2\text{F}$ multicomposite resulted to be totally similar to that of sample B (with same nominal weight fraction of iron oxide), being the only difference between them the presence in the former of APTES and $\text{Eu}(\text{DBM})_3\text{Phen}$ complex, both of which demonstrated absence of XRD signals in the $\text{Eu}(\text{DBM})_3\text{Phen}@ms\text{-SiO}_2\text{F}$ composite (see § 3.3.2). Hence, the only signals that emerge from the typical amorphous curve of the mesoporous silica are the same broad and weak peaks that were ascribed to the mixture of crystalline Fe_3O_4 (magnetite) and $\gamma\text{-Fe}_2\text{O}_3$ (maghemite) in the investigation on the $\text{FeO}_x@ms\text{-SiO}_2$ series (see § 4.1.2). Therefore, according to the observations that were done for samples B and $\text{Eu}(\text{DBM})_3\text{Phen}@ms\text{-SiO}_2\text{F}$, the XRD characterization of the multicomposite material suggested the efficient incorporation of both the iron oxide nanocrystals and the $\text{Eu}(\text{III})$ complex into the silica host matrix.

The same indications came from the TEM analysis. Representative micrographs of sample $\text{FeO}_x/\text{Eu}(\text{DBM})_3\text{Phen}@ms\text{-SiO}_2\text{F}$ are shown in Fig. 5.2a-c. These micrographs, just like those of sample B (see Fig. 4.2), demonstrate the presence of dark nanocrystals (ca. 3 nm size) embedded within the porous SiO_2 nanoparticles. An EDS spectrum of the circled area in Fig. 5.2a is shown in Fig. 5.2d. The elemental analysis identified the presence of Si, O and Fe, which is attributed to the amorphous SiO_2 matrix and iron oxide nanocrystals. On the contrary, the presence of complex inside the silica nanoparticles could not be demonstrated, neither with TEM micrographs nor by means of the EDS analysis, since the low amount of complex in the sample brings to a fraction of elemental europium in the examined area which is below the detection limit (ca. 2%wt) of this technique. Anyway, the TEM analysis confirmed the absence of complex, as well as iron oxide, outside the silica matrix.

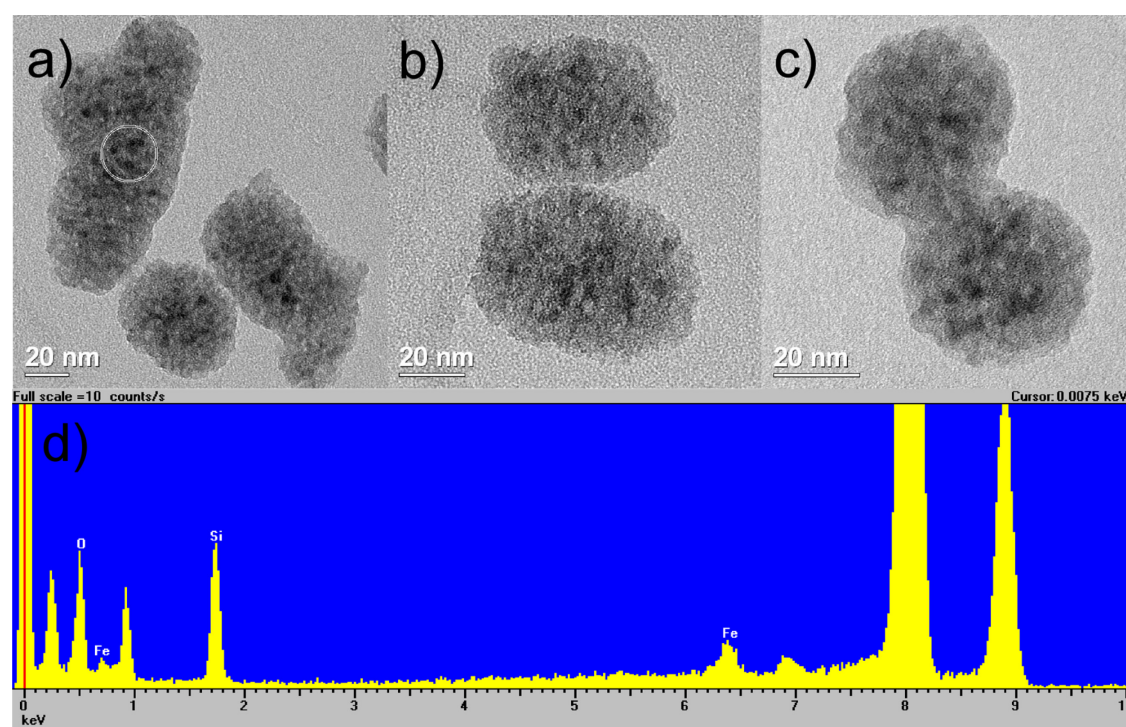


Figure 5.2 (a-c) TEM micrographs at different magnifications of sample $\text{FeO}_x/\text{Eu}(\text{DBM})_3\text{Phen}@ms\text{-SiO}_2\text{F}$ and (d) EDS analysis of circled area (a).

The N_2 adsorption/desorption isothermal curve of sample $FeO_x/Eu(DBM)_3Phen@ms-SiO_2F$ (Fig. 5.3) shows the typical shape of a mesoporous material (type IV isothermal), notwithstanding the functionalization with APTES (which did not cause significant modification of the porosimetry) and above all the double impregnation with the iron oxide and the Eu(III) complex. It is important to notice that the resulting decrease of the surface area and pore volume values ($520 \pm 10 \text{ m}^2/\text{g}$ and *ca.* $0.8 \text{ cm}^3/\text{g}$ respectively, to give correspondent reductions of 52% and 43% with respect to the starting values of $ms-SiO_2F$) is in agreement with the summed decreases of the respective values for sample B and sample $Eu(DBM)_3Phen@ms-SiO_2F$ of previous studies. In fact, after the impregnation the former showed a reduction of 30% and 22% in surface area and pore volume values (see § 4.1.2), while for the latter the diminution was 24% and 16% respectively (see § 3.3.2); if added together, these numbers give very close values to the aforementioned ones that were measured for the multicomposite. These porosimetric data indicate that both the impregnation steps were consistently performed; in line with the expectations, the resulting material can be considered as the sum of the previously discussed $FeO_x@ms-SiO_2$ (sample B) and $Eu(DBM)_3Phen@ms-SiO_2F$ materials. Also the pore size distribution curve (Fig. 5.4) featured the same usual profile that appeared in the previous studies for the undoped mesoporous silica, sample B and sample $Eu(DBM)_3Phen@ms-SiO_2F$ (see Figs. 3.18, 4.5 and 3.42 respectively), *i.e.* a narrow distribution that indicated an average pore size of *ca.* 2.7 nm. Overall, the porosimetric results for the $FeO_x/Eu(DBM)_3Phen@ms-SiO_2F$ sample proved valuable and confirmed the presence of loaded iron oxide and Eu(III) complex into the silica, while at the same time the retained mesoporosity could potentially allow for further modification of the composite.

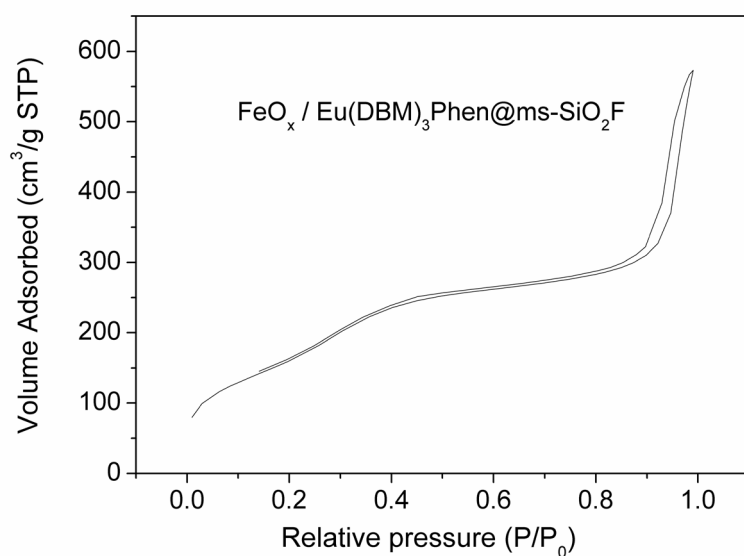


Figure 5.3 N₂ adsorption/desorption isothermal curve of FeO_x/Eu(DBM)₃Phen@ms-SiO₂F.

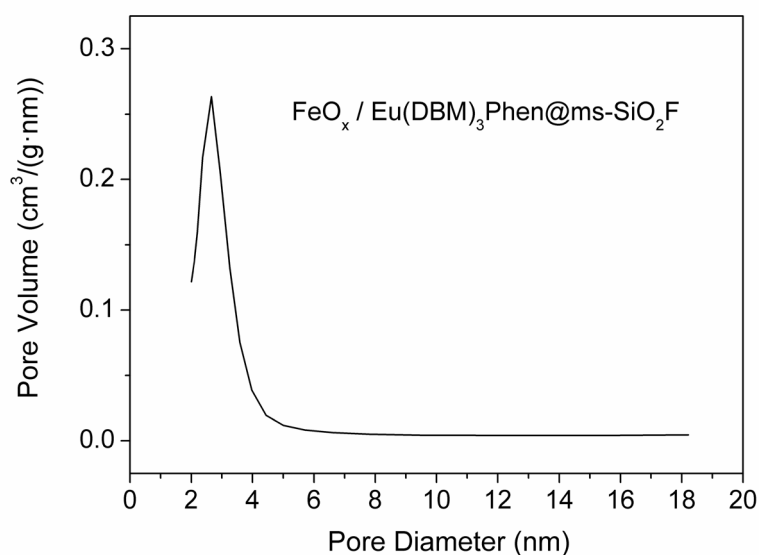


Figure 5.4 Pore size distribution curve of sample FeO_x/Eu(DBM)₃Phen@ms-SiO₂F.

The IR spectroscopy (Fig. 5.5) could not directly prove the qualitatively presence of iron oxide and complex in the FeO_x/Eu(DBM)₃Phen@ms-SiO₂F sample, since both these species could not be detected through IR

spectroscopy when embedded in small fractions into the silica matrix, as already discussed for samples B and $\text{Eu}(\text{DBM})_3\text{Phen}@ms\text{-SiO}_2\text{F}$. As a consequence, the IR spectrum of the multicomposite sample resulted to be almost identical to those of $\text{Eu}(\text{DBM})_3\text{Phen}@ms\text{-SiO}_2\text{F}$ and $\text{FeO}_x@ms\text{-SiO}_2\text{F}$, which in turn coincided with that of functionalized mesoporous silica $ms\text{-SiO}_2\text{F}$ prior to its impregnation (see Fig. 3.43). However, once again the comparison between the spectra of the material just before ($\text{FeO}_x@ms\text{-SiO}_2$) and immediately after ($\text{FeO}_x@ms\text{-SiO}_2\text{F}$) the functionalization procedure, qualitatively confirmed the attachment of APTES on the silica surface as previously mentioned.

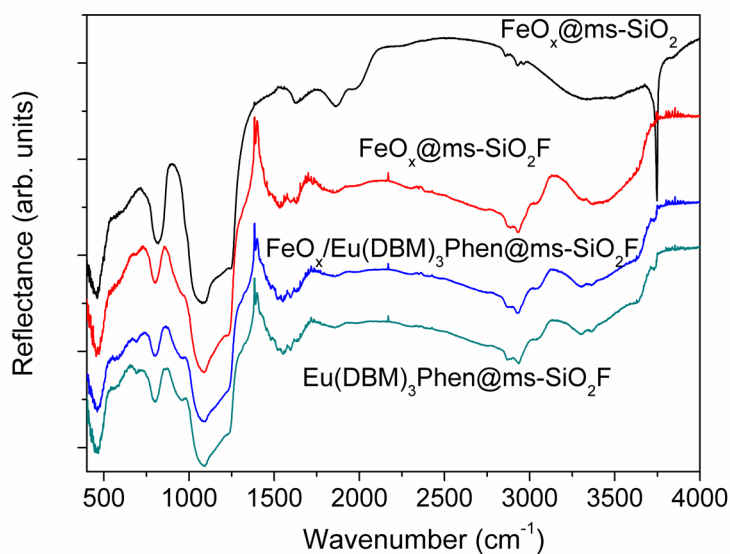


Figure 5.5 DRIFT spectra of samples: $\text{FeO}_x@ms\text{-SiO}_2$, $\text{FeO}_x@ms\text{-SiO}_2\text{F}$, $\text{FeO}_x/\text{Eu}(\text{DBM})_3\text{Phen}@ms\text{-SiO}_2\text{F}$ and $\text{Eu}(\text{DBM})_3\text{Phen}@ms\text{-SiO}_2\text{F}$.

Overall, the structural and morphological characterization of the multicomposite material pointed out the good regularity and homogeneity of the nanostructure and indicated the absence of residual traces of iron oxide crystals and of complex outside the silica nanoparticles.

The magnetic behavior of sample $\text{FeO}_x/\text{Eu}(\text{DBM})_3\text{Phen}@ms\text{-SiO}_2\text{F}$ was tested through the usual preliminary check by visual means that was performed by suspending the powders in ethanol and placing them in proximity of a strong magnet for several minutes (Fig. 5.6). The sample showed comparable magnetic behavior with the correspondent sample B (see Fig. 4.11), since also in this case almost the total visible amount of powder migrated towards the magnet within one hour.

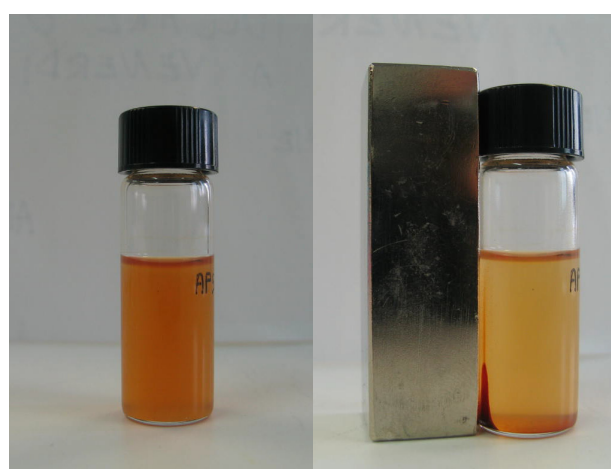


Figure 5.6 Images of sample $\text{FeO}_x/\text{Eu}(\text{DBM})_3\text{Phen}@ms\text{-SiO}_2\text{F}$ with powder dispersed in EtOH (left) and in presence of a magnet (right).

This result was expected, since the only difference between the two aforementioned samples is the presence of lanthanide complex in the multicomposite which should not cause any significant changes in the magnetic properties of the material with respect to sample B. Such magnetic properties have already been studied (see § 4.1.2) and for this reason the magnetic characterization of the multicomposite sample has not been performed.

On the contrary, in order to confirm the presence of complex inside the silica nanoparticles and to investigate the possible effect of its interaction with iron oxide on the luminescent properties, the optical characterization of sample $\text{FeO}_x/\text{Eu}(\text{DBM})_3\text{Phen}@ms\text{-SiO}_2\text{F}$ has been performed.

Thanks to the high intensity of the emitted luminescence under UV excitation, some optical microscopy photographs of $\text{FeO}_x/\text{Eu}(\text{DBM})_3\text{Phen}@ms\text{-}$

SiO₂F sample, with and without UV light as exciting source could be realized (see § 2.2), like for the Eu(DBM)₃Phen@ms-SiO₂F sample. In Fig. 5.7, four images of two powder fractions at different magnifications are shown and the intense red emission of the UV excited powders is clearly visible.

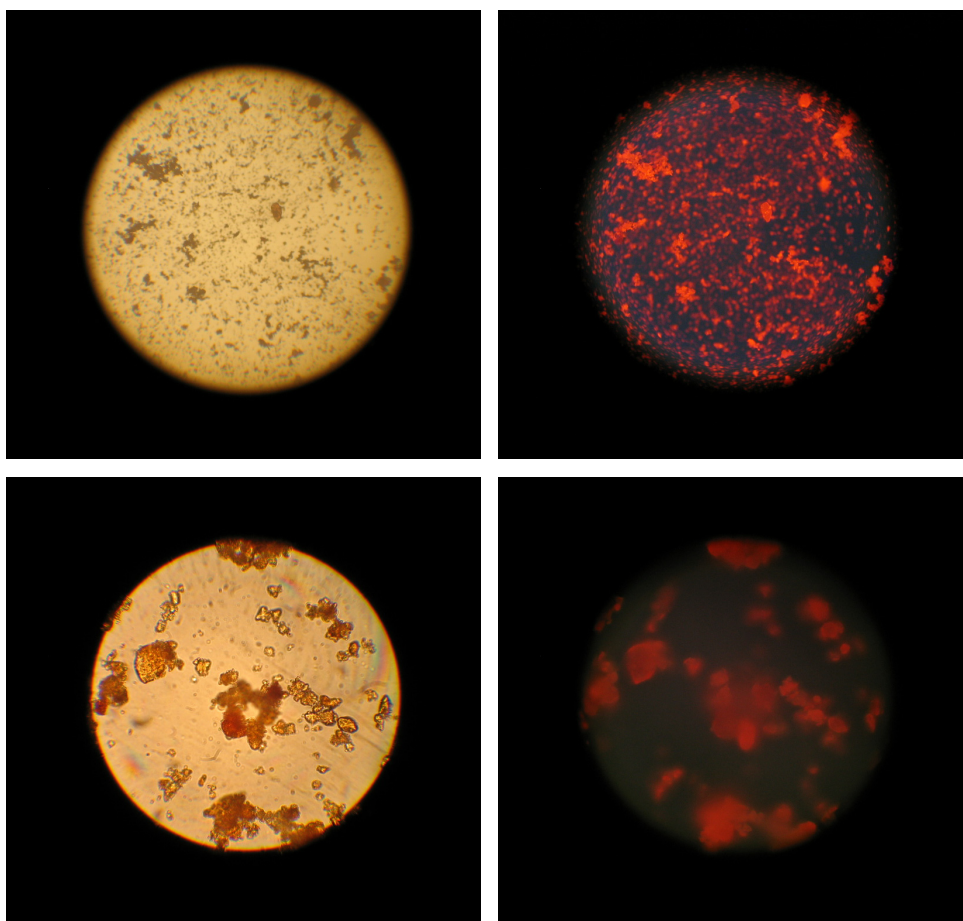


Figure 5.7 Optical microscopy photographs of sample FeO_x/Eu(DBM)₃Phen@ms-SiO₂F at different magnifications; two different powder fractions (top and bottom, respectively) in absence (left) and in presence (right) of UV excitation.

The luminescence excitation spectra of the FeO_x/Eu(DBM)₃Phen@ms-SiO₂F multicomposite, and of sample Eu(DBM)₃Phen@ms-SiO₂F for a comparison, are reported (normalized at their maximum value and shifted along the Y axis for a better visualization) in Fig. 5.8.

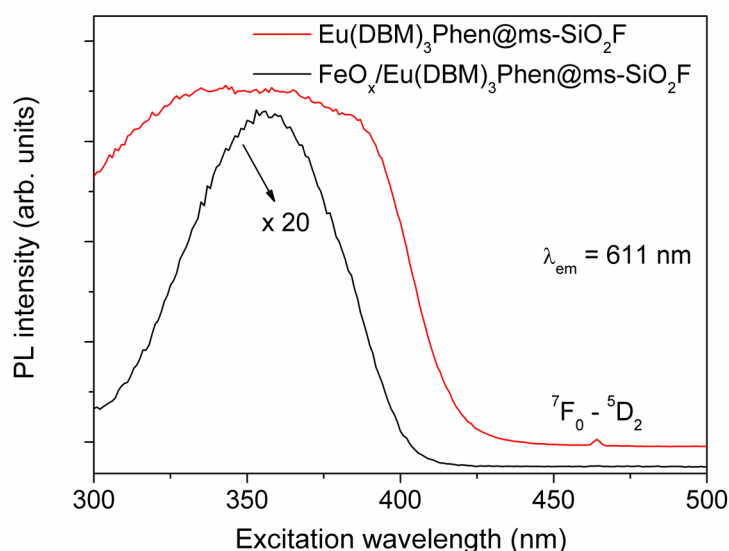


Figure 5.8 Luminescence excitation spectra at 611 nm emission for samples $\text{FeO}_x/\text{Eu}(\text{DBM})_3\text{Phen}@ms\text{-SiO}_2\text{F}$ and $\text{Eu}(\text{DBM})_3\text{Phen}@ms\text{-SiO}_2\text{F}$.

A strong decrease (ca. 20 times lower) in the intensity of the signal at the maximum position around 350 nm was measured in the multicomposite with respect to the $\text{Eu}(\text{DBM})_3\text{Phen}@ms\text{-SiO}_2\text{F}$ sample. Two evident changes affected also the shape of the spectrum of the multicomposite with respect to the previous material; in fact, the broad absorption band centered at 353 nm, which is attributed to the organic ligands ($\pi \rightarrow \pi^*$ transitions⁹) of the complex and to their antenna effect, has become sharper, while the sharp and weak peak at 464 nm that is ascribed to the ${}^7\text{F}_0 \rightarrow {}^5\text{D}_2$ transition of the Eu^{3+} ion has disappeared. The latter modification suggests that in the multicomposite the f–f inner-shell transitions are quenched through the non-radiative energy transfer from the higher excited states to some uncertain defect levels, substituting for the non-radiative relaxation to ${}^5\text{D}_0$.^{10–12}

In general, since the synthetic procedures and the morphological and structural analyses indicated that the two composites should contain nearly the same amount of complex, all these modifications are supposed to be caused by the presence of the iron oxide. Its interaction with the luminescent species in the

same host matrix could somehow introduce changes in the environment surrounding the europium complex. Anyway, the relevant reduction of the absorption efficiency both in terms of lowered intensity of the emission at 611 nm and of narrower spectral window of the absorption, was expected in the multicomposite in consideration of the massive absorption of light by the dark magnetic phase. The latter can weaken the luminescence from the optically active species and in this particular case reduce the antenna effect brought by the organic ligands of the complex.

In Fig. 5.9 the PL emission spectra under 353 nm excitation of $\text{FeO}_x/\text{Eu}(\text{DBM})_3\text{Phen}@ms\text{-SiO}_2\text{F}$ and $\text{Eu}(\text{DBM})_3\text{Phen}@ms\text{-SiO}_2\text{F}$ samples are shown (normalized at their maximum value and shifted along the Y axis).

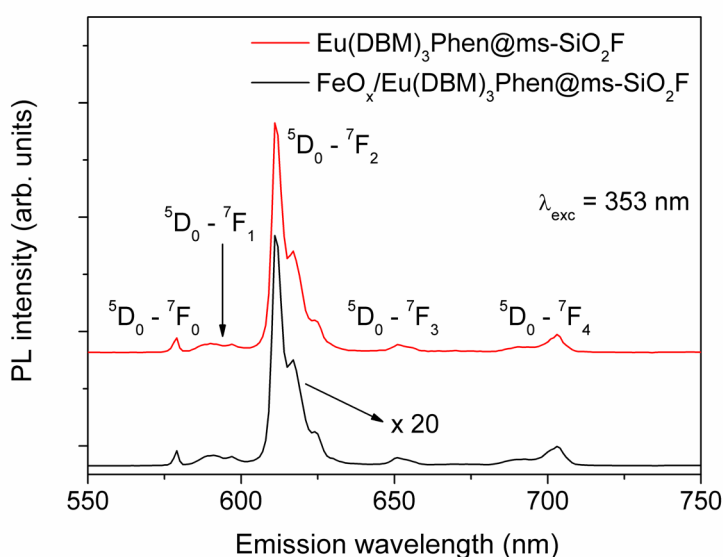


Figure 5.9 Luminescence emission spectra under 353 nm excitation for samples $\text{FeO}_x/\text{Eu}(\text{DBM})_3\text{Phen}@ms\text{-SiO}_2\text{F}$ and $\text{Eu}(\text{DBM})_3\text{Phen}@ms\text{-SiO}_2\text{F}$.

Apart from the aforementioned decrease of *ca.* 20 times in the maximum emission intensity, the spectrum of the multicomposite displayed the same emission profile than $\text{Eu}(\text{DBM})_3\text{Phen}@ms\text{-SiO}_2\text{F}$ sample and the same observations that were made about the PL spectrum of $\text{Eu}(\text{DBM})_3\text{Phen}@ms\text{-}$

SiO₂F sample can be repeated here. Therefore, all five signal at 579 nm, 591 nm, 611 nm, 652 nm and 703 nm that are associated to the typical $^5D_0 \rightarrow ^7F_j$ ($j = 0, \dots, 4$) transitions of Eu³⁺ showed an expected general broadening of the peaks with respect to those of the complex alone, that is ascribed to the enhanced disorder brought by the interactions with the silica host matrix, into which the complex is incorporated. The two spectra in Fig. 5.9 are close to a perfect match when superimposed and therefore also their *R* index values correspond. This fact indicates that the presence of the iron oxide should not affect the site symmetry of the Eu³⁺ ion in the multicomposite material.

The same PL emission measurement for FeO_x/Eu(DBM)₃Phen@ms-SiO₂F sample was also performed under 393 nm excitation wavelength. Apart from an obvious difference in the overall emission intensity with respect to 353 nm excitation, the aforementioned measurement gave a spectrum with identical profile in terms of shape, position and relative intensities of the peaks with respect to the previous and therefore it is not reported.

However, notwithstanding the highly disadvantageous presence of the magnetic phase from the optical point of view, the overall luminescent red emission of the multicomposite proved to be notable if compared to the previously studied inorganic luminescent materials measured under the same conditions, thanks to the intrinsic remarkable luminescent properties of the Eu(III) complex.

Finally, from the decay curve of the PL emission under 377 nm excitation of the multicomposite sample, the observed lifetime (τ_{obs}) could be calculated, at the same way as for the previously studied samples (see, for example, § 3.1.2). Fig. 5.10 displays the experimental decay curves (and their respective fits) of both FeO_x/Eu(DBM)₃Phen@ms-SiO₂F and Eu(DBM)₃Phen@ms-SiO₂F samples for a comparison.

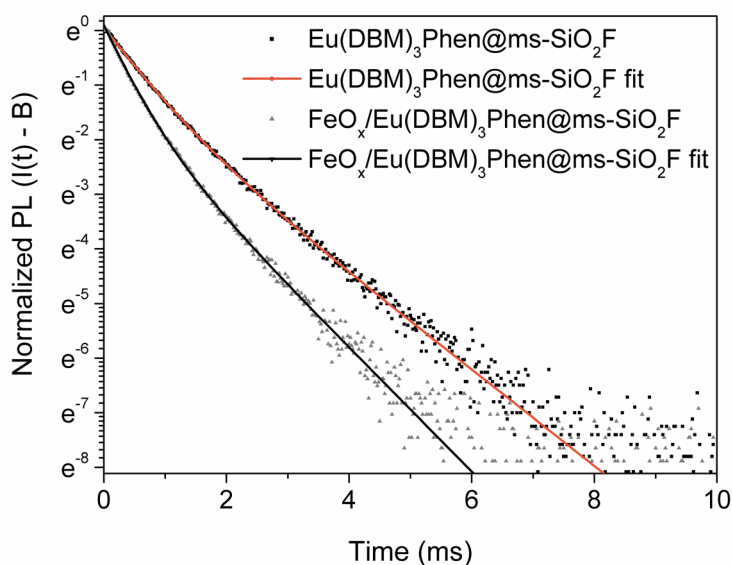


Figure 5.10 Time decay curves (MCSPC) and respective fits of samples $\text{FeO}_x/\text{Eu}(\text{DBM})_3\text{Phen}@ms\text{-SiO}_2\text{F}$ and $\text{Eu}(\text{DBM})_3\text{Phen}@ms\text{-SiO}_2\text{F}$. Intensity corrected using the background.

Contrary to the $\text{Eu}(\text{DBM})_3\text{Phen}@ms\text{-SiO}_2\text{F}$ sample, the multicomposite showed a decay curve whose shape is non-exponential and this trend could be attributed to the high degree of disorder affecting the sites in which the Eu^{3+} ions are accommodated or, more reasonably, to the presence of traps which act as quenching centers. A comparison with the curve of sample $\text{Eu}(\text{DBM})_3\text{Phen}@ms\text{-SiO}_2\text{F}$ clearly indicates that this phenomenon is strongly related to the presence of iron oxide in the material, because with its absence the shape of the decay curve is close to mono-exponential.

Moreover, the calculated effective lifetime T_{obs} for sample $\text{FeO}_x/\text{Eu}(\text{DBM})_3\text{Phen}@ms\text{-SiO}_2\text{F}$ was 0.60 ± 0.04 ms, a value that resulted to be a 30% lower than the calculated effective lifetime coming from $\text{Eu}(\text{DBM})_3\text{Phen}@ms\text{-SiO}_2\text{F}$ (0.87 ± 0.07 ms). The decrease of the effective lifetime can be ascribed to the introduction of the magnetic phase and the consequent increasing presence of defects or traps that can provide non-radiative recombination paths. On the other hand, the lifetime value of the

multicomposite still remained higher than that of the $\text{Eu}(\text{DBM})_3\text{Phen}$ complex (0.42 ± 0.03 ms, see § 3.3.2) and this result suggests that the luminescence stability of the complex was enhanced after its incorporation into the mesoporous silica, notwithstanding the presence of the iron oxide nanocrystals in the same host matrix.

Overall, the optical characterization, in agreement with the nanostructural investigation, confirmed the presence of the $\text{Eu}(\text{DBM})_3\text{Phen}$ complex, and indirectly of the iron oxide nanocrystals, embedded into the silica matrix and indicated a notable intensity of the luminescence emission in the material.

5.1.3 Conclusions

This study was performed with the purpose of obtaining, via a multiple step impregnation route, a multifunctional nanocomposite with both luminescent and magnetic properties and nanostructural homogeneity that, as discussed in the introduction, could be destined to the various applications that are based on this double functionality. The nominal loaded fractions of magnetic iron oxide and luminescent $\text{Eu}(\text{III})$ complex were determined on the basis of previous investigation and the overall amount of loaded material, as indicated by the porosimetric analysis, could allow the further introduction of additional materials in the same host matrix.

The characterization of the multicomposite $\text{FeO}_x/\text{Eu}(\text{DBM})_3\text{Phen}@ms\text{-SiO}_2\text{F}$ sample proved the realization of the aforementioned purpose, since the multicomposite material resulted to have regular morphology and nanostructure coming from an efficient impregnation of the silica nanoparticles with both the magnetic and luminescent materials, which were totally embedded into the host matrix. Due to the strong correspondence between the multicomposite and sample B in the study on the $\text{FeO}_x@ms\text{-SiO}_2$ composites, the magnetic properties are expected to be very similar to those of the latter, *i.e.* a magnetic material consisting in a mixture of Fe_3O_4 (magnetite) and $\gamma\text{-Fe}_2\text{O}_3$ (maghemite) nanocrystals with superparamagnetic behavior, quite high magnetic anisotropy,

large coercive fields and moderate density of magnetization and magnetic response to a magnetic field. Notwithstanding the detrimental (to the optical properties) presence of the aforementioned dark nanocrystals, the multicomposite showed an enhanced lifetime value with respect to the complex and, above all, a notable luminescent emission in the red range under UV excitation, as desired. Of course, the incorporation of the magnetic phase brought to a lowering of the efficiency in absorbing the excitation radiation and to an enhanced density of defects or traps in the host matrix, which were responsible for a decrease of the luminescent properties with respect to sample $\text{Eu}(\text{DBM})_3\text{Phen}@m\text{-SiO}_2\text{F}$.

List of references:

- (1) Huh, Y.-M.; Jun, Y.-wook; Song, H.-T.; Kim, S.; Choi, J.-sil; Lee, J.-H.; Yoon, S.; Kim, K.-sup; Shin, J.-S.; Suh, J.-S.; Cheon, J. *J. Am. Chem. Soc.* **2005**, *127*, 12387-12391.
- (2) Giri, S.; Trewyn, B. G.; Stellmaker, M. P.; Lin, V. S.-Y. *Angew. Chem., Int. Ed.* **2005**, *44*, 5038-5044.
- (3) Kim, J.; Lee, J. E.; Lee, J.; Jang, Y.; Kim, S.-W.; An, K.; Yu, J. H.; Hyeon, T. *Angew. Chem. Int. Ed.* **2006**, *45*, 4789-4793.
- (4) Sen, T.; Sebastianelli, A.; Bruce, I. J. *J. Am. Chem. Soc.* **2006**, *128*, 7130-7131.
- (5) Kumar, R.; Nyk, M.; Ohulchanskyy, T. Y.; Flask, C. A.; Prasad, P. N. *Adv. Funct. Mater.* **2009**, *19*, 853-859.
- (6) Qiao, Z.-A.; Zhang, L.; Guo, M.; Liu, Y.; Huo, Q. *Chem. Mater.* **2009**, *21*, 3823-3829.
- (7) Parma, A.; Freris, I.; Riello, P.; Enrichi, F.; Cristofori, D.; Benedetti, A. *J. Lumin.* **2010**, *130*, 2429-2436.
- (8) McGehee, M. D.; Bergstedt, T.; Zhang, C.; Saab, A. P.; O'Regan, M. B.; Bazan, G. C.; Srdanov, V. I.; Heeger, A. J. *Adv. Mater.* **1999**, *11*, 1349-1354.
- (9) Li, H.; Inoue, S.; Machida, K.-i.; Adachi, G.-y. *Chem. Mater.* **1999**, *11*, 3171-3176.
- (10) Qi, S.; Yin, W. *J. Mater. Sci.* **2011**, *46*, 5288-5293.
- (11) Zhang, H.; Song, H.; Dong, B.; Han, L.; Pan, G.; Bai, X.; Fan, L.; Lu, S.; Zhao, H.; Wang, F. *J. Phys. Chem. C* **2008**, *112*, 9155-9162.
- (12) Zhang, H.; Song, H.; Yu, H.; Bai, X.; Li, S.; Pan, G.; Dai, Q.; Wang, T.; Li, W.; Lu, S.; Ren, X.; Zhao, H. *J. Phys. Chem. C* **2007**, *111*, 6524-6527.

CHAPTER 6

GENERAL CONCLUSIONS

The main purpose on which my doctoral activity has been focused was the study of luminescent and/or magnetic composite systems that could be destined to a wide range of applications, mainly in the biomedical field (*e.g.* bioimaging, DNA microarray, hyperthermal therapy, contrast-enhanced magnetic resonance imaging (MRI), combined optical and magnetic resonance bioimaging) but not exclusively in this field. For example, even in the environmental or in the anti-counterfeit fields these materials should find potential application.

Of course, prior to dedicate most of the future attention to their final applications, the aforementioned materials needed a thorough investigation in order to optimize or improve their nanostructural and peculiar properties. The work that has just been presented in this thesis was meant to accomplish this goal, since it dealt with the synthesis and characterization of several luminescent or magnetic composite materials and ended with the study of a multifunctional luminescent and magnetic system. The latter can be seen as a sort of collage of the previous work and paved the way for a further and more exhaustive investigation on such multifunctional materials and their concrete applications.

My activity started with the study of luminescent nanophosphors made of Eu^{3+} -doped zirconia nanocrystals which were synthesized with the polyol method and embedded into a silica matrix by a Stöber route (§ 3.1). The results of this investigation definitely proved to be valuable. In fact, the best samples showed satisfying luminescent properties, in terms of emission intensity and above all duration of the effective lifetimes that were characterized by the highest values ($4 \div 5$ ms) among all the studied materials in this thesis. Furthermore, a comparative study on different samples allowed to determine the optimum annealing temperature (700 °C) to maximize not only the aforementioned optical properties, but also the nanostructural quality and the availability of superficial $-\text{OH}$ groups for efficient surface functionalization of the composites. Nevertheless, the strong aggregation of the silica nanoparticles containing the luminescent species brought to an irregular morphology of the

system, which could represent a drawback for those applications in which a good regularity in shape and size monodispersity are requested for the silica nanoparticles. Therefore, in perspective further investigation on the possibility to improve this aspect, mainly through an optimization of the synthetic procedure, would be needed.

However, the important information acquired from the aforementioned study, especially on the ideal calcination temperature, proved to be useful also in the subsequent investigation on luminescent composite systems consisting of lanthanide-doped zirconia nanocrystals hosted by a mesoporous silica matrix. Overall, from this point on, the use of mesoporous silica as a host structure became predominant in my doctoral activity, since it showed promise for a lot of different reasons, among which the most important was the possibility to load, via an easy impregnation route, a great variety and amount of materials (even more than one in the same host matrix) into the nanosized pores and to control the final composition of the system. Moreover, the surface of the resulting (multi)functional nanocomposites could be functionalized in an even more easy way than the previously studied system, since the huge surface area of the mesoporous silica matrix led to a remarkable availability of superficial –OH groups. Nevertheless, also the mesoporous silica nanoparticles, both when undoped and when hosting the functional materials, showed a certain tendency to aggregation, but their morphological regularity, though improvable with further investigation, seemed to be qualitatively better with respect to the previously used silica matrix.

As mentioned before, after being synthesized and characterized, the mesoporous silica nanoparticles were impregnated with different rare-earth doped zirconia nanocrystals (§ 3.2). Also in this case, a series of $\text{ZrO}_2:\text{Eu}^{3+}@ms\text{-SiO}_2$ composite systems with different loadings of the luminescent species was reproduced. These samples, that had a strong analogy with the crystalline phase and overall composition of those of the previously studied system, showed also very similar luminescent properties (*i.e.* comparable emission intensities and identical profiles of the emission and

excitation spectra), though a general diminution of the effective lifetime was found, probably because of a higher presence of defects or traps in this structure. Analogous investigation was performed also on a $\text{ZrO}_2:\text{Tb}^{3+}@m\text{-SiO}_2$ system, which showed higher lifetime values and a greater closeness to mono-exponential shape of the decay curves, together with a satisfying luminescent green emission. Both the europium and the terbium-based composite systems proved to be characterized by nanostructural regularity and order (thanks to the efficiency and reliability of the impregnation process) and they showed promise for the production of multicomposite materials, since the retained mesoporosity in the loaded samples could potentially allow for further modification of the composites. A preliminary study was also made on a third system, in which the zirconia nanocrystals were co-doped with erbium and ytterbium in order to give up-converting luminescence. The most important result of this study is represented not only by the effective up-conversion but also by the successful functionalization of the material, notwithstanding the elevated calcination temperature (1000 °C) that was necessary for an efficient luminescence. However, in this case a deliberately increased loading level of luminescent phase in the silica host matrix was meant to favor the up-conversion luminescence efficiency in spite of the nanostructural homogeneity and the retained mesoporosity. Therefore, further work for an optimization of the overall quality of the composite is necessary. Anyway this preliminary study demonstrated the possibility to produce nanostructured and functionalized composite systems with up-converting properties, that can represent an important way to overcome the drawback of the autofluorescence by the biological systems in the biomedical applications.

After showing promising features as a host matrix for inorganic luminescent species as the RE^{3+} -doped ZrO_2 nanocrystals, the mesoporous silica nanoparticles were also employed in the preparation of a luminescent nanocomposite material containing an optimized amount of $\text{Eu}(\text{DBM})_3\text{Phen}$ complex (§ 3.3). This work was performed in order to investigate the realization of luminescent nanomaterials that could give a stronger luminescence emission

than the inorganic species, while maintaining at the same time their chemical stability. This composite was characterized by a regular and homogeneous nanostructure and, thanks to the peculiar properties of the organic complex, it showed a more intense red emission and a stronger absorption efficiency with respect to the previously studied luminescent materials, while retaining a high level of mesoporosity. Therefore it resulted to be the most suitable for a further production of a bifunctional luminescent and magnetic composite. Anyway further investigation would be needed to deepen the role of APTES in terms of its interaction with the complex and subsequent effect on the optical properties and chemical stability of the composite, as well as a study involving the use of different rare-earth complexes in similar systems would be interesting.

The study of lanthanide-doped luminescent materials represented the main purpose also during my PhD abroad stage in Turku (Finland), but in this case, in order to expand the range of my experience and investigation, the involved research field was different. In fact, the whole activity concerned the study of $\text{Sr}_2\text{MgSi}_2\text{O}_7:\text{Eu}^{2+},\text{Dy}^{3+}$ persistent luminescence materials (§ 3.4). These materials consisted of microsized powders that were synthesized with the simple solid state reaction. The study of the $\text{Sr}_2\text{MgSi}_2\text{O}_7:\text{Eu}^{2+}$ system gave heterogeneous and unfulfilling results: the high doped samples, apart from showing poor luminescence properties, did not consist of the expected final composition, while the low doped samples showed good structural quality and UV excited luminescence properties, but their persistent luminescence resulted to have very weak intensity and duration. Definitely better results came out from the $\text{Sr}_2\text{MgSi}_2\text{O}_7:\text{Eu}^{2+},\text{Dy}^{3+}$ system, since all the samples showed an efficient persistent luminescence and a comparative study allowed to determine an optimal composition of $(\text{Sr}_{0.97}\text{Eu}_{0.01}\text{Dy}_{0.02})_2\text{MgSi}_2\text{O}_7$, both for the strength and the duration (more than 25 h) of the afterglow. The nanostructural and optical properties of these materials were studied during my stage with the purpose of continuing the investigation in Venice, especially with a look at the development of nanostructured long lasting luminescent materials with improved morphological regularity, that could be used, among others, in biomedical

imaging application. Additional work to this purpose have not been performed yet. Hence, future investigation on the possibility to work with persistent luminescence nanomaterials, for potential utilization not only in the biomedical field but also in the wide range of applications that characterize this class of materials, would be certainly interesting.

Parallel with the research activity on lanthanide-doped luminescent materials, the last part of my doctoral studies involved also an investigation on magnetic nanocomposites. A first study was dedicated to the synthesis and characterization of magnetic composites made of iron oxide and cobalt-iron oxide embedded into the mesoporous silica nanoparticles (§ 4.1). These materials were prepared via a wet impregnation procedure and a comparative study on a $\text{FeO}_x@\text{ms-SiO}_2$ series of samples with different loading levels allowed to determine the most recommended nominal fraction of loaded iron oxide (17%wt, *i.e.* sample B), in order to obtain the best structural and morphological homogeneity. In fact, in this sample the obtained mixture of crystalline and magnetic Fe_3O_4 (magnetite) and $\gamma\text{-Fe}_2\text{O}_3$ (maghemite) was completely embedded into the silica matrix. The magnetic properties of the composite were examined, before and after the reducing treatment, and they indicated superparamagnetic behavior, quite high magnetic anisotropy, large coercive fields and moderate density of magnetization and magnetic response to a magnetic field. An enhancement in the density of magnetization was observed following the reducing treatment, and attributed to an increase in the magnetic material content. Anyway, further studies would be needed to improve the effectiveness of the reducing thermal treatment, in order to obtain a crystalline phase entirely made of magnetite and to enhance the magnetic properties of the aforementioned composite. The magnetic properties of the $\text{CoFe}_2\text{O}_4@\text{ms-SiO}_2$ composite were found to be superior to those of the $\text{FeO}_x@\text{ms-SiO}_2$ material. The higher density of magnetization in the former was attributed to a higher content of magnetic material in the crystalline phase and could justify the greater efficiency observed in the magnetic separation of this material. Similarly to the previously studied luminescent materials, the facile

surface functionalization of both the $\text{FeO}_x@\text{ms-SiO}_2$ and $\text{CoFe}_2\text{O}_4@\text{ms-SiO}_2$ composites was demonstrated using APTES.

Afterwards, the research on magnetic materials continued with an investigation on the incorporation of metallic iron into a mesoporous silica matrix, in order to realize a nanostructured composite material with elevated magnetic properties (§ 4.2). This goal has not been accomplished yet, due to the difficulties in avoiding iron oxidation during the preparation of the composite, but this could be due to its high chemical instability once formed, especially in nanosized materials. Anyway, as a partial result, a promising material with a remarkable magnetic response was obtained at the end of the study, following an improvement in the synthetic procedure and in the employed materials. The magnetic characterization pointed out that this sample was more magnetic than the composites of the previous study with iron oxide and cobalt-iron oxide; the magnetic nanocrystals were bigger on average and with higher coercive fields. But the magnetic content of the composite was not homogeneous at all and for this reason a more complete characterization of the magnetic properties was not possible. The presence of different crystalline phases (magnetite/maghemite and also Fe_5C_2 iron carbide, which is known to have interesting magnetic properties) was demonstrated by the structural and morphological analysis, that indicated a nanostructural disorder and heterogeneity in the material. The huge amount of employed iron precursor accounts for the poor structural quality of the composite.

Nevertheless, the promising magnetic properties and the high chemical stability of this composite strongly encourage to dedicate further investigation on this kind of material, especially with the aim of improving its nanostructural regularity with a more controlled synthetic procedure. Of course, the realization of a magnetic composite based on the presence of metallic iron would still be desired in perspective and additional work is needed to this purpose.

Anyway, the investigation on all the aforementioned magnetic materials demonstrated the possibility to obtain magnetic nanocomposites based on iron oxide, cobalt-iron oxide or iron carbide embedded in a silica matrix. One of the

main advantages is represented by the retained mesoporosity of the final composites, which implies the possibility to load further materials. Among them, biomolecules or drugs could be useful for a wide range of biomedical applications, such as localized drug release, also combined with hyperthermal therapy; alternatively, luminescent species could be incorporated for the production of bifunctional composite materials. This second strategy was followed in the final part of my doctoral research, which led to the production of a luminescent and magnetic composite consisting of magnetic iron oxide and luminescent Eu(III) complex embedded, via a multiple step impregnation route, into the APTES-functionalized mesoporous silica (§ 5.1).

The $\text{FeO}_x/\text{Eu}(\text{DBM})_3\text{Phen}@ms\text{-SiO}_2\text{F}$ multicomposite material resulted to have regular morphology and nanostructure, coming from an efficient impregnation of the silica nanoparticles with both the magnetic and luminescent materials. Due to the strong correspondence between this multicomposite and sample B of the $\text{FeO}_x@ms\text{-SiO}_2$ series, the magnetic properties are expected to be almost identical to those of the latter. Notwithstanding the detrimental (to the optical properties) presence of the iron oxide nanocrystals, the multicomposite showed an enhanced lifetime value with respect to the complex and, above all, a notable luminescent emission in the red range under UV excitation, as desired. Nevertheless, the incorporation of the magnetic phase brought to a lowering of the efficiency in absorbing the excitation radiation and to an enhanced density of defects or traps in the host matrix, which were responsible for a decrease of the maximum emission intensity (*ca.* 20 times lower) and the effective lifetime (*ca.* a 30% lower) with respect to the analogous $\text{Eu}(\text{DBM})_3\text{Phen}@ms\text{-SiO}_2\text{F}$ composite without iron oxide.

In perspective, further research for a parallel improvement in the peculiar properties and overall qualities of the mono-functional luminescent or magnetic composites, as well as further investigation on alternative possible coupling of the studied luminescent and magnetic species, should provide a consequent enhancement in the overall quality of the bi-functional composite materials.

ACKNOWLEDGEMENTS

I wish to acknowledge, above all, my tutor and supervisor Prof. Pietro Riello, for giving me the possibility to work as a member of his group and guiding my research activity during these three years with numerous suggestions, constant help, passion and an ongoing motivating force that were of fundamental importance for the growth of my research spirit, especially in the beginning of my PhD career.

I owe the greatest gratitude to Dr. Isidora Freris (Isi), for being an irreplaceable master, teaching me everything with endless patience and reinforcing day after day my passion for the research with her good example. I received a continuous help, assistance in the laboratory and support from Isi, which I greatly appreciate.

I would like to acknowledge Prof. Alvisè Benedetti, for treating me like a son and for encouraging and advising me throughout my PhD. I would never have started the experience as a PhD student without his presence.

I am extremely grateful to Prof. Elti Cattaruzza for the important and useful indications which helped me to improve the quality of this doctoral thesis.

I also wish to thank Prof. Jorma Hölsä of the University of Turku and his research group (Dr. Mika Lastusaari, MSc Taneli Laamanen and MSc Marja Malkamäki) for greeting me and making me feel at home during my pleasant experience in Turku; I acknowledge for all that I learned and appreciated on persistent luminescence materials and their wonderful country.

I am grateful to a lot of people for their precious help and contribution to this work, in particular I kindly acknowledge: Dr. Francesco Enrichi of C.I.V.E.N. (Coordinamento Interuniversitario Veneto per le Nanotecnologie) for giving me the opportunity to carry out the luminescence measurements in his optics laboratory and for his assistance and helpfulness; Prof. Cesar de Julián Fernández (University of Florence) for performing the magnetic characterization and for his fundamental support in the discussion of the experimental data; Prof. Moreno Meneghetti and Dr. Vincenzo Amendola (University of Padua) for the Raman measurements and for their support in the discussion of the results; Dr.

Andrea Lausi for the synchrotron radiation XRD measurements at the Materials Characterization by X-Ray Diffraction (MCX) beamline at the Elettra Synchrotron source (Trieste); Mr. Davide Cristofori for the TEM analysis and for his immeasurable availability; Dr. Luca Bellotto for his precious advice and assistance; Prof. Elisabetta Zendri and her research group (Dr. Francesca Izzo, Dr. Manuela Sgobbi and Dr. Eleonora Balliana) for giving me the opportunity and assistance to carry out the TGA measurements; Prof. Loretta Storaro and her research group (Dr. Elisa Moretti, Mr. Aldo Talon, Mrs. Martina Marchiori) for carrying out the porosimetric analysis and for giving me the possibility to perform the DRIFT spectroscopy measurements; Mr. Tiziano Finotto and Mr. Loris Bertoldo for performing the XRD measurements and in general for their daily assistance and valuable help.

I would also like to mention and thank all my PhD colleagues during these three years, in particular: Marta, Chandrashekhar, Laura F., Laura A., Gloria and Marco.

Finally, I want to express the deepest gratitude to my dear parents, Barbara and Ivano, for always supporting and loving me, like only a wonderful parent can do, and for all the sacrifices they have made for me. To you I dedicate this thesis.

I am immensely grateful to my sweet love Clara, for loving me, believing in me, giving me encouragement when it was most required and for being an example to me for her passion, sense of duty and responsibility that she shows in her work.

I also wish to thank all the people and friends who encouraged me during these years, for their emotional support, entertainment and friendship.

APPENDIX

PUBLICATIONS IN INTERNATIONAL JOURNALS

Part of the work included in this thesis has been presented in the following publications:

- Parma, A.; Freris, I.; Riello, P.; Enrichi, F.; Cristofori, D.; Benedetti, A. *J. Lumin.* **2010**, *130*, 2429-2436.
- Parma, A.; Freris, I.; Riello, P.; Cristofori, D.; de Julián Fernández, C.; Amendola, V.; Meneghetti, M.; Benedetti, A. submitted to *J. Mater. Chem.*

Estratto per riassunto della tesi di dottorato

L'estratto (max. 1000 battute) deve essere redatto sia in lingua italiana che in lingua inglese e nella lingua straniera eventualmente indicata dal Collegio dei docenti.

L'estratto va firmato e rilegato come ultimo foglio della tesi.

Studente: ALVISE PARMA _____ matricola: 955601 _____

Dottorato: SCIENZE CHIMICHE _____

Ciclo: XXIV _____

Titolo della tesi³ : Synthesis and characterization of luminescent and magnetic materials for biological applications _____

Abstract:

This thesis was focused on the study of luminescent and/or magnetic nanocomposites that could be destined to biological applications. Luminescent composites based on a SiO₂ matrix doped with various lanthanide compounds (Eu(DBM)₃Phen, ZrO₂:RE³⁺, RE = Eu, Tb, Er/Yb) were investigated. These systems showed satisfying optical properties, morphological and structural regularity and efficient functionalization. Moreover, the possibility to obtain functionalizable nanocomposites with up-converting properties was demonstrated. Sr₂MgSi₂O₇:Eu²⁺,Dy³⁺ persistent luminescence materials were also studied. An optimal composition of (Sr_{0.97}Eu_{0.01}Dy_{0.02})₂MgSi₂O₇, both for the strength and the duration of the persistent luminescence, was determined.

Magnetic composites made of FeO_x and CoFe₂O₄ embedded into mesoporous SiO₂ were obtained and studied, while the incorporation of Fe(0) was not achieved. By selecting the most suitable luminescent and magnetic species in terms of desired coexistence, the production of a bifunctional luminescent and magnetic system (FeO_x/Eu(DBM)₃Phen@ms-SiO₂F) with regular morphology and nanostructure was obtained.

Estratto:

Questa tesi ha riguardato lo studio di materiali nanocompositi luminescenti e/o magnetici utilizzabili in applicazioni biologiche. Sono stati esaminati compositi luminescenti basati su una matrice di SiO₂ drogata con vari composti di lantanidi (Eu(DBM)₃Phen, ZrO₂:RE³⁺, RE = Eu, Tb, Er/Yb). Tali sistemi hanno mostrato proprietà ottiche soddisfacenti, regolarità morfologica e strutturale ed efficiente funzionalizzazione. E' stata inoltre dimostrata la possibilità di ottenere nano compositi funzionalizzabili con proprietà di *up-conversion*. Sono stati studiati anche materiali a luminescenza persistente di tipo Sr₂MgSi₂O₇:Eu²⁺,Dy³⁺. E' stata in particolare determinata una composizione ottimale, ovvero (Sr_{0.97}Eu_{0.01}Dy_{0.02})₂MgSi₂O₇, sia per quanto riguarda l'intensità che la durata della luminescenza persistente.

Sono stati ottenuti e studiati compositi magnetici costituiti da FeO_x e CoFe₂O₄ incorporati in SiO₂ mesoporosa, mentre l'incorporazione di Fe(0) non è avvenuta con successo. Selezionando, tra tutte quelle esaminate, le specie luminescenti e magnetiche più desiderabili in termini di coesistenza reciproca nello stesso materiale, è stato prodotto un sistema composito bifunzionale luminescente e magnetico (FeO_x/Eu(DBM)₃Phen@ms-SiO₂F) con morfologia e struttura regolari.

Firma dello studente

³ Il titolo deve essere quello definitivo, uguale a quello che risulta stampato sulla copertina dell'elaborato consegnato.



Università
Ca' Foscari
Venezia

DEPOSITO ELETTRONICO DELLA TESI DI DOTTORATO

DICHIARAZIONE SOSTITUTIVA DELL'ATTO DI NOTORIETA'

(Art. 47 D.P.R. 445 del 28/12/2000 e relative modifiche)

Io sottoscritto **Alvise Parma**

nat ^O a **Venezia** (prov.) il **20/01/1980**

residente a **Mestre** in **via A. Emo** n. **45**

Matricola (se posseduta) **955601** Autore della tesi di dottorato dal titolo:
..... **Synthesis and characterization of luminescent and magnetic materials for biological applications**

.....

.....

Dottorato di ricerca in **Scienze Chimiche**

(in cotutela con)

Ciclo **XXIV**

Anno di conseguimento del titolo **2012**

DICHIARO

di essere a conoscenza:

- 1) del fatto che in caso di dichiarazioni mendaci, oltre alle sanzioni previste dal codice penale e dalle Leggi speciali per l'ipotesi di falsità in atti ed uso di atti falsi, decado fin dall'inizio e senza necessità di nessuna formalità dai benefici conseguenti al provvedimento emanato sulla base di tali dichiarazioni;
- 2) dell'obbligo per l'Università di provvedere, per via telematica, al deposito di legge delle tesi di dottorato presso le Biblioteche Nazionali Centrali di Roma e di Firenze al fine di assicurarne la conservazione e la consultabilità da parte di terzi;
- 3) che l'Università si riserva i diritti di riproduzione per scopi didattici, con citazione della fonte;
- 4) del fatto che il testo integrale della tesi di dottorato di cui alla presente dichiarazione viene archiviato e reso consultabile via internet attraverso l'Archivio Istituzionale ad Accesso Aperto dell'Università Ca' Foscari, oltre che attraverso i cataloghi delle Biblioteche Nazionali Centrali di Roma e Firenze;
- 5) del fatto che, ai sensi e per gli effetti di cui al D.Lgs. n. 196/2003, i dati personali raccolti saranno trattati, anche con strumenti informatici, esclusivamente nell'ambito del procedimento per il quale la presentazione viene resa;
- 6) del fatto che la copia della tesi in formato elettronico depositato nell'Archivio Istituzionale ad Accesso Aperto è del tutto corrispondente alla tesi in formato cartaceo, controfirmata dal tutor, consegnata presso la segreteria didattica del dipartimento di riferimento del corso di dottorato ai fini del deposito presso l'Archivio di Ateneo, e che di conseguenza va esclusa qualsiasi responsabilità dell'Ateneo stesso per quanto riguarda eventuali errori, imprecisioni o omissioni nei contenuti della tesi;
- 7) del fatto che la copia consegnata in formato cartaceo, controfirmata dal tutor, depositata nell'Archivio di Ateneo, è l'unica alla quale farà riferimento l'Università per rilasciare, a richiesta, la dichiarazione di conformità di eventuali copie.

Data _____ Firma _____

AUTORIZZO

- l'Università a riprodurre ai fini dell'immissione in rete e a comunicare al pubblico tramite servizio on line entro l'Archivio Istituzionale ad Accesso Aperto il testo integrale della tesi depositata;
- l'Università a consentire:
 - la riproduzione a fini personali e di ricerca, escludendo ogni utilizzo di carattere commerciale;
 - la citazione purché completa di tutti i dati bibliografici (nome e cognome dell'autore, titolo della tesi, relatore e correlatore, l'università, l'anno accademico e il numero delle pagine citate).

DICHIARO

- 1) che il contenuto e l'organizzazione della tesi è opera originale da me realizzata e non infrange in alcun modo il diritto d'autore né gli obblighi connessi alla salvaguardia di diritti morali od economici di altri autori o di altri aventi diritto, sia per testi, immagini, foto, tabelle, o altre parti di cui la tesi è composta, né compromette in alcun modo i diritti di terzi relativi alla sicurezza dei dati personali;
- 2) che la tesi di dottorato non è il risultato di attività rientranti nella normativa sulla proprietà industriale, non è stata prodotta nell'ambito di progetti finanziati da soggetti pubblici o privati con vincoli alla divulgazione dei risultati, non è oggetto di eventuali registrazione di tipo brevettuale o di tutela;
- 3) che pertanto l'Università è in ogni caso esente da responsabilità di qualsivoglia natura civile, amministrativa o penale e sarà tenuta indenne a qualsiasi richiesta o rivendicazione da parte di terzi.

A tal fine:

- dichiaro di aver autoarchiviato la copia integrale della tesi in formato elettronico nell'Archivio Istituzionale ad Accesso Aperto dell'Università Ca' Foscari;
- consegno la copia integrale della tesi in formato cartaceo presso la segreteria didattica del dipartimento di riferimento del corso di dottorato ai fini del deposito presso l'Archivio di Ateneo.

Data _____ Firma _____

La presente dichiarazione è sottoscritta dall'interessato in presenza del dipendente addetto, ovvero sottoscritta e inviata, unitamente a copia fotostatica non autenticata di un documento di identità del dichiarante, all'ufficio competente via fax, ovvero tramite un incaricato, oppure a mezzo posta

Firma del dipendente addetto

Ai sensi dell'art. 13 del D.Lgs. n. 196/03 si informa che il titolare del trattamento dei dati forniti è l'Università Ca' Foscari - Venezia.

I dati sono acquisiti e trattati esclusivamente per l'espletamento delle finalità istituzionali d'Ateneo; l'eventuale rifiuto di fornire i propri dati personali potrebbe comportare il mancato espletamento degli adempimenti necessari e delle procedure amministrative di gestione delle carriere studenti. Sono comunque riconosciuti i diritti di cui all'art. 7 D. Lgs. n. 196/03.